Automated Quantitative Inspection

Of Nuclear Assets and Canisters

Euan Foster

Department of Electronic and Electrical Engineering

University of Strathclyde

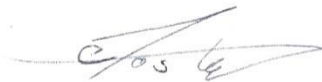A thesis submitted for the degree of

Doctor of Engineering

Oct 2022

Copyright

This thesis is the result of the author's original research. It has been composed by the author and has not been previously submitted for examination which has led to the award of a degree.

The copyright of this thesis belongs to the author under the terms of the United Kingdom Copyright Acts as qualified by University of Strathclyde Regulation 3.50. Due acknowledgement must always be made of the use of any material contained in, or derived from, this thesis.

Signed:

Date:

Acknowledgements

I am eternally grateful to Scottish education for providing me with a wealth of experiences few get to enjoy. To say I am proud to call this place home and have the University of Strathclyde as my home institution is an understatement. I am confident I will continue to look fondly upon these experiences for the remainder of my life.

Finally, I would like to thank my mother (Elizabeth), sister (Eilidh), grandparents (Dorothy and Ken), aunt (Karen), and cousins (Scott and Andrew), for playing a pivotal role in my upbringing and throughout my life to date. Without your mentorship and encouragement, instilling a strong work ethic and morals, this work would have not been possible.

Abstract

Structural integrity of nuclear assets and their associated infrastructure is key to national security, energy generation, and efficient deployment of capital. Furthermore, building nuclear infrastructure is inherently complex and it is common to seek extensions in asset and infrastructure lifetime as they age. Therefore, this thesis explores various Non-Destructive Evaluation (NDE) techniques to advance the inspection of nuclear canisters and their welds for three scenarios: 1) In-situ screening of legacy canisters sealed by Resistance Seam Welds (RSWs) while on a racking system with considerable accessibility constraints; 2) Ex-situ characterisation of legacy canisters sealed by RSWs; & 3) Inspection of fusion welds performed via Gas Tungsten Arc Welding (GTAW) for an upgraded canister of the future design at the point of manufacture.

For the in-situ scenario a unique ultrasonic guided wave, a Feature Guided Wave (FGW), was exploited to screen the legacy RSW. For the RSW, four weld-guided wave modes were identified, and the fundamental flexural (F_0) weld guided mode was down selected. Several Finite Element (FE) models explored applicable transduction strategies and documented reflection coefficients from transverse cracks. Multiple experiments were conducted on pseudo RSW structures as well as flat plate and cylindrical RSWs. For the pseudo weld experiments, it was shown that FGWs, like that of the analytical free plate counterparts, could easily be excited in flat plate-like features with traditional transduction techniques. For the flat plate RSW experiments, it was shown that reflections from 6.5 mm wide through wall and 1.00 mm deep defects could be observed with Signal to Noise Ratios (SNRs) of 16.33 dB and 8.21 dB respectively. Lastly, it was shown that for cylindrical canister like RSWs, reflections could also be observed from 1.00 mm deep defects with a SNR of 11.85 dB being reported. This work clearly showed the benefit of deploying such a system on-site at Sellafield as full circumferential screening of the RSW could be performed giving greater insight to the structural health of the canisters in-situ.

To address the ex-situ inspection of the legacy canister, an automated robotic eddy current system was developed. The data rich platform allowed for a complete digital

record to be established of the impedance data gathered and is well suited for further advancements in eddy current inversion to leverage in the future. The robotic deployment of the eddy current array was combined with force torque feedback and enabled major sources of noise, resulting from lift-off and wobble, to be reduced. Two different datasets were reported on. The first being eddy current scans of canister bodies with known stress corrosion cracks. All of the stress corrosion cracks were detected, and the resulting SNR of images generated from the impedance data was increased through post processing of the eddy current data. The second dataset is concerned with eddy current scans of RSWs. These scans make use of the aforementioned FGW, to localise defects and perform targeted raster scans in the area of concern. Basic inversion on the EDM notch width was shown to give results with 96.4% accuracy, and it was shown that time savings of up to ~95% could be realised by performing targeted eddy current raster scans. This work clearly shows the benefit of performing an ex-situ inspection in this manner due to the minimal levels of operator handling and time savings that can be realised on large production volumes like that at Sellafield.

Lastly, inspection of the envisaged canister of the future design at the point of manufacture was explored as it would enable operational efficiencies and the ability to be able to create a Non-Destructive Evaluation (NDE) digital twin to monitor the structural health of the component over its lifetime. Technically, inspecting welded components at the point of manufacture is challenging due to the elevated temperature and resulting thermal gradients in the component introducing beam bending effects due to refraction and positional inaccuracies in the ultrasonic data. A novel thermal compensation strategy was developed that leveraged thermal weldment simulations to correct for positional inaccuracies. Initially, the thermal compensation strategy was trialled on simulated data and the positional accuracy was shown to increase by at least 85%. Experimental results also showed a similar trend with a 63.6% improvement in reflector positional accuracy. The results show how high-quality ultrasonic images can be generated at the point of manufacture and how a similar strategy could be deployed to establish an inspection record from manufacture until the asset is retired.

Contents

List of Figures

xiii

List of Tables

Abbreviations

AC	–	Alternating Current
AGR	–	Advanced Gas-cooled Reactor
ALID	–	Absorbing Layers with Increasing Damping
CDT	–	Centre for Doctoral Training
COTS	–	Commercial Off The Shelf
DC	–	Direct Current
ECT	–	Eddy Current Testing
EMAT	–	Electro-Magnetic Acoustic Transducer
EPSRC	–	Engineering and Physical Sciences Research Council
FE	–	Finite Element
FFT	–	Fast Fourier Transform
FGW	–	Feature Guided Wave
FMC	–	Full Matrix Capture
GMAW	–	Gas Metal Arc Welding
GTAW	–	Gas Tungsten Arc Welding
GUI	–	General User Interface
HAZ	–	Heat Affected Zone
IP	–	Internet Protocol
KRC	–	Kuka Robotic Controller
MFFF	–	MOX Fuel Fabrication Facility

MFMM	–	The Multi-stencils Fast Marching Method
MMAW	–	Manual Metal Arc Welding
NDA	–	Nuclear Decommissioning Authority
NDE	–	Non-Destructive Evaluation
NDT	–	Non-Destructive Test
PAW	–	Plasma Arc Welding
PML	–	Perfectly Matched Layer
PWR	–	Pressure Water Reactor
RCNDE	–	Research Centre for Non-Destructive Evaluation
RSI	–	Robotic Sensor Interface
RSW	–	Resistance Seam Weld
SAFE	–	Semi-Analytical Finite Element
SAW	–	Submerged Arc Welding
SNM	–	Special Nuclear Material
SNR	–	Signal to Noise Ration
TCP	–	Transmission Control Protocol
TFM	–	Total Focusing Method
THORP	–	THermal Oxide Reprocessing Plant
ToF	–	Time of Flight
TRL	–	Technology Readiness Level
UAV	–	Unmanned Aerial Vehicle
WAAM	–	Wire Arc Additive Manufactured

SDH   –   Side Drilled Hole

UO_2 –   Uranium Oxide

Chapter 1

Introduction

Sellafield has its history rooted in the founding of the nuclear era dating back to the aftermath of the second world war in the 1950s. The site produced the Plutonium-239 used in the United Kingdom's first nuclear bomb and was also the location of the world's first commercial nuclear power station [1]. Currently, the site manages the vast majority of the United Kingdom's nuclear waste as well as reprocessing and storing spent nuclear fuel produced by exported British nuclear power plant designs abroad. With the recent nuclear disaster at Fukushima, Japan in 2011, and changing government policy, it is ever more vital to ensure safe and continued storage of nuclear assets to prevent environmental and financial loss, and to protect against severe health and safety incidents caused by failures in the storage of these assets.

1.1. Industrial motivation

In the UK, there are 15 active nuclear reactors that generate approximately 20-25% of the country's electricity [2]. Of these 15 nuclear power plants, many are ageing, and half of the current capacity is to be retired by 2025. As a result, the UK government is actively pursuing the development of next generation plants to raise output to approximately a third of the country's electricity demand by 2035 [3].

Of the 15 active reactors in the UK, 14 are Advanced Gas-cooled Reactors (AGRs) with the remaining being the country's sole Pressure Water Reactor (PWR) [3]. Additionally, due to the UK's role in the development of nuclear weapons, there are numerous legacy reactors that were developed for the dual purpose of producing weapon grade plutonium and generating civil energy. All these legacy reactors worldwide are now decommissioned but are known as MAGNOX reactors.

MAGNOX reactors used natural uranium as their fuel source, whilst PWR and AGR reactors use uranium oxide (UO_2) [4]. All of the aforementioned fuels make use of

fission reactions with the Uranium-235 isotope to generate energy. When approximately 3% of the Uranium-235 has been converted into fission products, the thermal reaction in the reactor has reduced in efficiency to warrant the removal of the fuel rods for reprocessing [5] to recover the remaining 97%. There are various approaches to nuclear fuel reprocessing throughout the world, and they vary from country to country with the most successful in terms of tons of fuel reprocessed per annum being the MELOX facility [6] in France, and the least being the MOX Fuel Fabrication Facility (MFFF) in the USA [7].

In the UK, to accommodate the two types of nuclear fuel used historically, there were two nuclear fuel reprocessing plants: - The MAGNOX Reprocessing Plant and the THermal Oxide Reprocessing Plant (THORP). The THORP facility was one of only two commercial nuclear reprocessing facilities in the world with the other being the previously mentioned MELOX facility in France. The THORP facility was shut in November 2018 siting 'a significant downturn' with many countries opting to store nuclear fuel over reprocessing, due to changing public and political opinion following the Fukushima incident in 2011 [5], [8], [9]. This loss of business coupled with excessive upgrade costs made the continual running of the THORP facility uneconomical. The MAGNOX plant has since also followed suits and shut in 2022 [10] .

This ultimately leaves the UK with no nuclear fuel reprocessing capability. At the same time, the UK government's policy still maintains its preference to reprocess spent fuel over disposal, putting the UK in a unique position, with a large stockpile of spent fuel due to previous reprocessing government policy, and no facility to reprocess in the future due to current policy. Professor Neil C Hyatt from the Immobilisation Science Laboratory at the University of Sheffield [11] has critiqued this approach [12]. However the only solution at present is to consider longer term storage than initially envisaged [13], placing emphasis on ensuring the integrity of the infrastructure associated with the temporary storage of these nuclear assets, as their lifetime is increased beyond the original design intent.

Sellafield Ltd., in the UK, is the site licensed company controlled by the Nuclear Decommissioning Authority (NDA), a government body in the UK created to decommission all legacy nuclear infrastructure, with its sole aim to manage the decommissioning of the Sellafield nuclear site in the Northwest of England over a 120-year period. The Sellafield site is the current storage location of all of the stockpiled spent fuel that is due to be reprocessed and they are stored in three variants of the same container, known as the Special Nuclear Material (SNM) packages, as outlined in Figure 1.
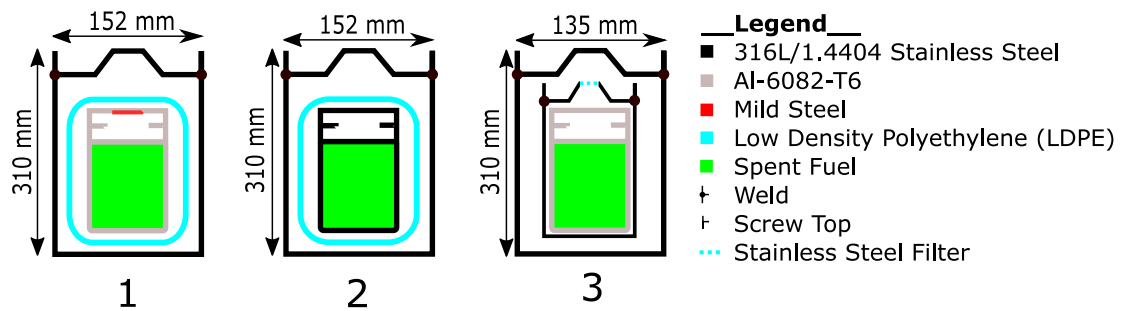
Figure 1: SNM variants: 1) Magnox canister; 2) Special material package canister, & 3) THORP canister

There is a wide body of academic work funded by Sellafield that aims to understand the structural health of the SNM canisters and their associated infrastructure as it ages [14]–[21]. One of these requirements is to understand the structural health of the weld that seals the canister body to the lid on the spent fuel canisters in the storage location as they are stored longer than initially envisaged. Each of the variants are made from the same 0.9 mm nominally thick 1.4404 stainless steel container and each have the same circumferential Resistance Seam Weld (RSW) to seal the canister body to the lid.

Figure 2 illustrates the RSW process, the resulting undulating RSW structure, a photograph, as well as a CAD schematic of the cylindrical RSW used on canisters to store nuclear material. It can be seen from Figure 2 (d) that the nuclear canister RSW is offset from the top of the canister body and can be thought of as a cylindrical lap joint. As the fusion and heat-affected zones are at the unification between the canister body and lid,

these zones become structurally critical in the resulting component. Being able to inspect these structurally important areas for defects after manufacture and while in service is of high priority for safety-conscious industries such as the nuclear industry [22]. This topic is covered in detail in Chapter 2.

(a)   (b)   (c)

(d)
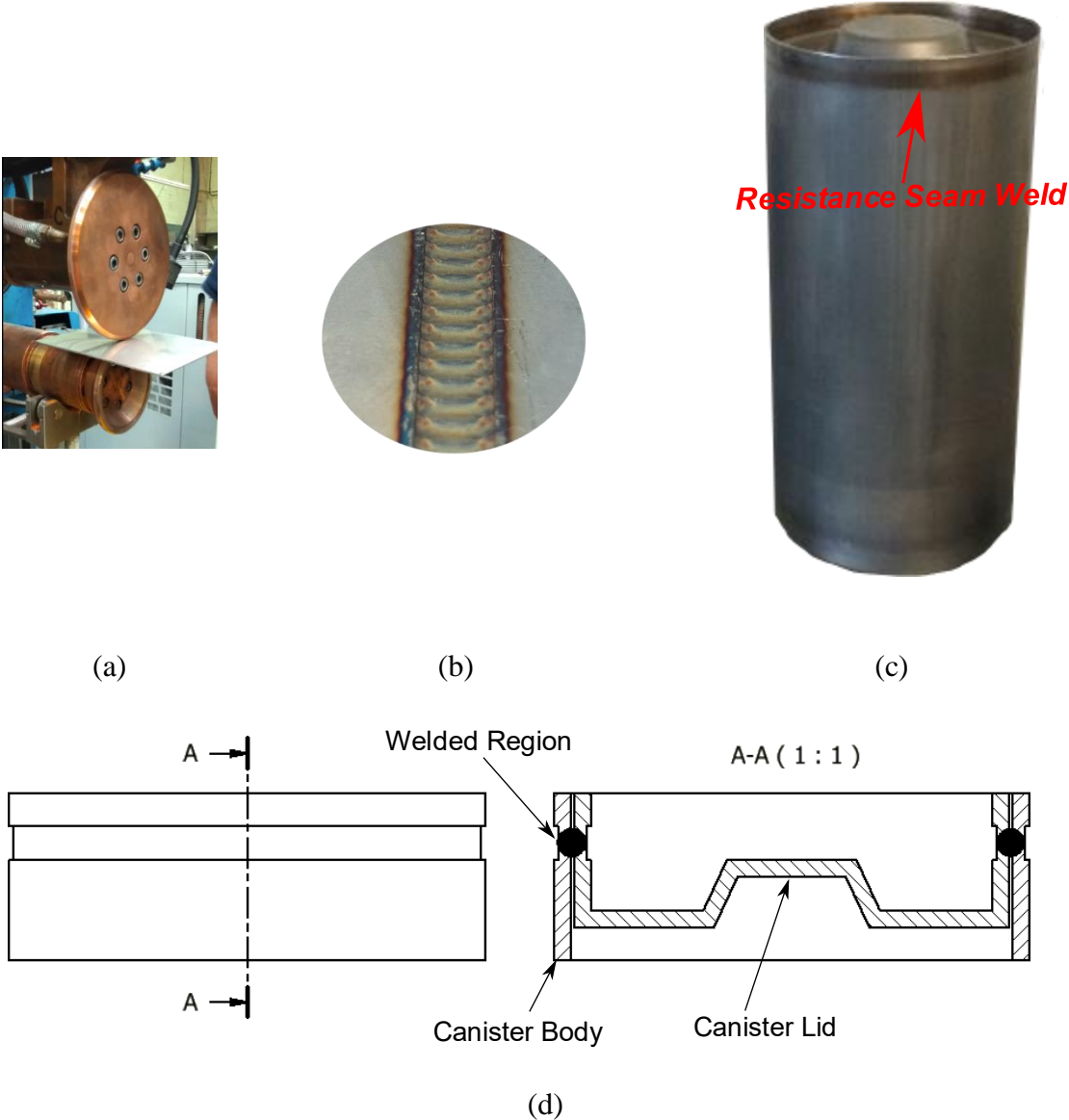
Figure 2: Resistance seam welds (a) Welding process, (b) Close-up of weld structure, (c) Welded cylindrical RSW canister, (d) CAD schematic and cross-sectional view of RSW canister

There is a desire to inspect these assets when they are in storage and when they have been removed from storage, via various applicable NDE techniques. These two scenarios will be referred to as the in-situ and ex-situ inspection scenarios here in. Figure 3 depicts a schematic of the storage system currently in use at Sellafield. It can be seen that access to the canisters can only be given through ports on one side of two concrete walls in the storage system. As such considerable accessibility challenges arise for the in-situ inspection scenario. Successful implementation of a novel NDE inspection regime will allow for any welds and canisters with defects to be identified in-situ, characterised further ex-situ, and priority given for contents to be reprocessed/repackaged.
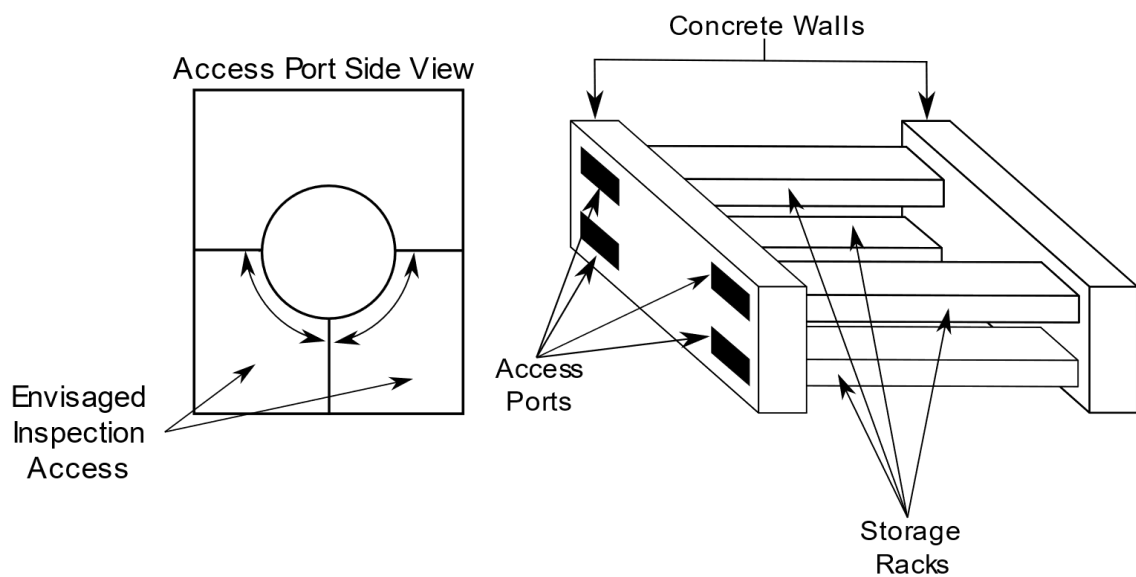
Figure 3: A schematic of the storage system used for the SNM packages

Furthermore, Sellafield has plans to alter the canister design to be more robust going forward in order to contain any future spent nuclear fuel for longer time periods associated with the current legacy design. This replacement canister design is known as the "canister of the future". Whilst many of the parameters for this design are not yet finalised, the material will remain 1.4404 stainless steel, the thickness of the canister will be increased to 3-10 mm, and the welding process will be changed to a Gas Tungsten Arc Welding (GTAW) process. The canister of the future is annotated in Figure 4. As safety and quality is paramount in the nuclear industry, there is a desire to create a "digital twin"

and perform inspection at the point of manufacture, as well as throughout the asset's lifetime. It is hoped that by performing inspections from the point of manufacture, defects can be corrected for in a more timely and cost-effective manner.
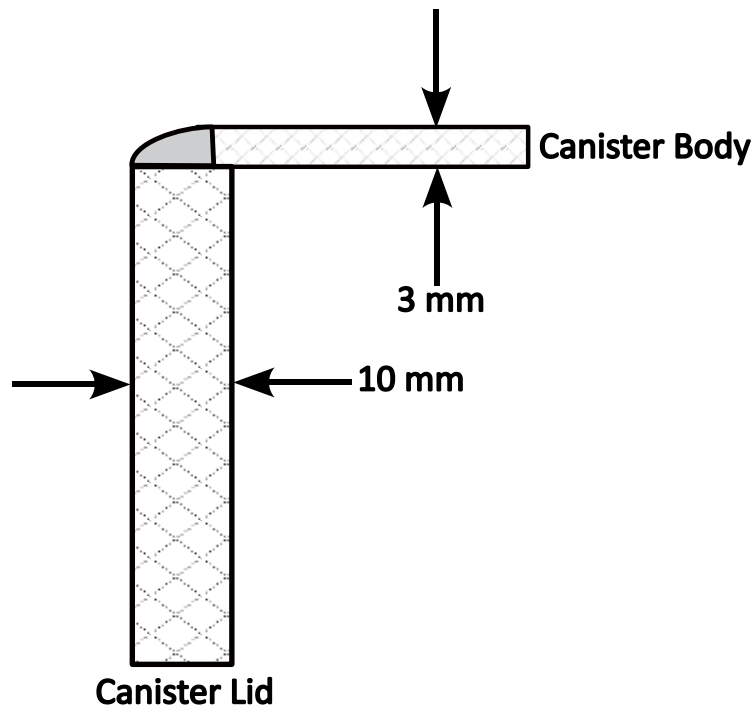
Figure 4: Annotation of the canister of the future

Therefore, the motivation of this thesis is to develop and further novel Non-Destructive Evaluation (NDE) techniques capable of inspecting the circumferential weld sealing the canisters in-situ and ex-situ for the existing legacy canister design, and at the point of manufacture for the canister of the future design. If possible, it would be beneficial to leverage any findings to inspect the entire canister body. With multiple tens of thousands of canisters expected to be stored over the next 35 years, efficient and accurate through-life inspection is essential.

1.2. Aims and objectives

The aims and objective can be summarised as the following:

1. To understand existing state of the art NDE techniques that are well suited to the in-situ, ex-situ, and point of manufacture inspection scenarios.

2. To develop an NDE technique capable of screening legacy canisters in-situ with considerable accessibility constraints.

3. To improve upon existing NDE techniques capable of characterising a large body of legacy canisters ex-situ.

4. To develop an NDE technique capable of inspecting and overcoming the environmental challenges at the point of manufacture.

1.3. Outline of thesis structure

The thesis is structured as follows:

- Chapter 2 provides an overview of fusion and resistance welding, as well as an outline of the currently available NDE techniques suitable for the inspection of the legacy canister as well as the canister of the future.

- Chapter 3 expands upon the overview of Feature Guided Waves (FGWs) given in Chapter 2 with application via numerical, simulation, and experimental methods. The numerical and simulated results are validated through the experiments, and a flexural FGW is shown to effectively screen RSWs for the first time.

- Chapter 4 explores the use of Eddy Current Testing (ECT) via sensor enabled automated robotic deployment. It is shown that automated ECT is well suited for the legacy canister design for inspecting both the canister as a whole and targeted inspection of the RSW.

- Chapter 5 outlines a compensation strategy used to correct for the thermal effects observed in ultrasonic datasets at the point of manufacture. The accuracy of this compensation strategy is documented, and it is shown to be able to perform accurate inspection at the point of manufacture for the canister of the future.

- Chapter 6 concludes the main findings of this thesis and documents any potential future work.

1.4. Contributions to academia and industry

The contributions produced from the fulfilment of this doctoral degree are as follows:

- The first use of an ultrasonic FGW on a RSW is demonstrated through numerical, simulation, and experimental methods. Numerically, a FGW is predicted through the use of the Semi-Analytical-Finite-Element (SAFE) method. The subsequent prediction is then validated via time-step Finite Element (FE) models. Finally, the FGW is demonstrated experimentally on a simplified "pseudo weld" and representative flat and cylindrical RSWs.

- An automated inspection framework for the intelligent eddy current inspection of positionally variant components, due to manufacturing tolerances, has been developed where a force-torque sensor is successfully deployed to correct for variations in wobble and lift-off experienced. Extensive software infrastructure was developed that allows for real-time acquisition and display of the eddy current data to the user, and further analysis in post-processing. Particular attention was given to develop the software infrastructure to a high standard. This effort assisted in many demonstrations on large grants (NEWAM – EPSRC grant no: EP/R027218/1, RoboWAAM EPSRC grant no: EP/P030165/1, & Remote Inspection of SNM Cans GC_253) and at the BINDT & Material Testing 2022 conferences.

- The automated eddy current deployment system was tested on two datasets. The first being the stress corrosion cracks. All cracks were detected and their SNRs were increased through novel post processing. The second datasets were on flat RSW samples. This was combined with the previous FGW work to allow for targeted eddy current inspection. By combining both the FGW and automated eddy current deployment strategy, time savings of up to 95% can be realised. These two datasets show the benefits of the former bullet point within a real world environment.

- Development of a compensation strategy to correct ultrasonic images in the presence of thermal gradients at the point of manufacture. It is shown that the proposed compensation strategy can increase reflector/defect positional accuracy by 63.6%,

providing a significant step towards industrially desirable inspection at the point of manufacture.

1.5. Lead author publications arising from this thesis

[1] **E. A. Foster**, R. Bernard, G. Bolton, J. C. Jackson-Camargo, A. Gachagan, E. Mohseni, and C. N. MacLeod, 'Inspection of nuclear assets with limited access using feature guided waves', *NDT E Int.*, vol. 131, no. 102695, Jun. 2022, doi: 10.1016/j.ndteint.2022.102695.

[2] **E. A. Foster**, G. Bolton, R. Bernard, M. McInnes, S. McKnight, E. Nicolson, C. Loukas, M. Vasilev, D. Lines, E. Mohseni, A. Gachagan, G. Pierce, and C. N. Macleod, 'Automated Real-Time Eddy Current Array Inspection of Nuclear Assets', *Sensors*, vol. 22, no. 16, Art. no. 16, Jan. 2022, doi: 10.3390/s22166036.

[3] **E. A. Foster**, N. E. Sweeney, E. Nicolson, J. Singh, M. K. Rizwan, D. Lines, G. Pierce, E. Mohseni, A. Gachagan, K. M. M Tant, and C. N. MacLeod, 'Thermal compensation of ultrasonic transmit and receive data for steel welded plates at the point of manufacture', *NDT E Int.*, Under Review.

1.6. Co-author publications arising from this thesis

1.6.1. Journal papers

[1] R. K. W. Vithanage, E. Mohseni, D. Lines, C. Loukas, **E. Foster**, C. N. MacLeod, S. G. Pierce, A. Gachagan, J. Ding, and S. Williams, 'Development of a phased array ultrasound roller probe for inspection of wire + arc additive manufactured components', *J. Manuf. Process.*, vol. 80, pp. 765–774, Aug. 2022, doi: 10.1016/j.jmapro.2022.06.045.

[2] R. Zimermann, E. Mohseni, R. K. W. Vithanage, D. Lines, **E. Foster**, C. N. Macleod, S. Gareth Pierce, G. Marinelli, S. Williams, and J. Ding, 'Increasing the speed of automated ultrasonic inspection of as-built additive manufacturing components by the adoption of virtual source aperture', *Mater. Des.*, vol. 220, p. 110822, Aug. 2022, doi: 10.1016/j.matdes.2022.110822.

[3] R. Domingo-Roca, **E. Foster**, and J. C. Jackson-Camargo, 'Acoustic bandgaps in polyatomic chains of 3D-printed resonators', *AIP Adv.*, vol. 11, no. 12, p. 125306, Dec. 2021, doi: 10.1063/5.0071874.

[4] M. Vasilev, C. MacLeod, W. Galbraith, Y. Javadi, **E. Foster**, G. Dobie, G. Pierce, and A. Gachagan, 'Non-contact in-process ultrasonic screening of thin fusion welded joints', *J. Manuf. Process.*, vol. 64, pp. 445–454, Apr. 2021, doi: 10.1016/j.jmapro.2021.01.033.

[5] E. Mohseni, Y. Javadi, N. E. Sweeney, D. Lines, C. N. MacLeod, R. K. W. Vithanage, Z. Qiu, M. Vasilev, C. Mineo, P. Lukacs, **E. Foster**, S. G. Pierce, and A. Gachagan, 'Model-assisted ultrasonic calibration using intentionally embedded defects for in-process weld inspection', *Mater. Des.*, vol. 198, p. 109330, Jan. 2021, doi: 10.1016/j.matdes.2020.109330.

[6] D. Lines, Y. Javadi, E. Mohseni, M. Vasilev, C. N. MacLeod, C. Mineo, R. K. Wathavana Vithanage, Z. Qiu, R. Zimermann, C. Loukas, **E. Foster**, G. Pierce, and A. Gachagan, 'A flexible robotic cell for in-process inspection of multi-pass welds', *Insight J. Br. Inst. Non-Destr. Test.*, vol. 62, no. 9, pp. 526–532, Sep. 2020, doi: 10.1784/insi.2020.62.9.526.

[7] E. Mohseni, C. Macleod, Y. Javadi, R. K. W. Vithanage, Z. Qiu, D. Lines, **E. Foster**, P. Lukacs, M. Vasilev, R. Zimermann, S. G. Pierce, and A. Gachagan, 'A Model-

Based Study of Transmit-Receive Longitudinal Arrays for Inspection of Subsurface Defects', *J. Nondestruct. Eval. Diagn. Progn. Eng. Syst.*, vol. 3, no. 3, Apr. 2020, doi: 10.1115/1.4046718.

[8] Y. Javadi, E. Mohseni, C. N. MacLeod, D. Lines, M. Vasilev, C. Mineo, **E. Foster**, S. G. Pierce, and A. Gachagan, 'Continuous monitoring of an intentionally-manufactured crack using an automated welding and in-process inspection system', *Mater. Des.*, vol. 191, no. 108655, Jun. 2020, doi: 10.1016/j.matdes.2020.108655.

[9] L. Asciak, J. Williams, **E. Foster**, L. Gilmour, L. Diaz-Garcia, H Mulvana, J. C. Jackson-Camargo, and R. Domingo-Roca, 'Towards an alternative to animal testing – 3D-printed multi-material tissue-mimicking microenvironments that replicate simplified solid tumours', *Nature Materials,* Under Review.

1.6.2.   Conference papers

[1] Y. Javadi, C. MacLeod, D. Lines, M. Vasilev, E. Mohseni, **E. Foster**, Z. Qiu, R. Vithanage, R. Zimermann, C. Loukas, G. Pierce, and A. Gachagan, 'In-process inspection of multi-pass robotic welding: 46th Annual Review of Progress in Quantitative Nondestructive Evaluation', Jul. 2019. Accessed: Aug. 19, 2022. [Online]. Available: http://event.asme.org/QNDE-2019

[2] E. Mohseni, Y. Javadi, D. Lines, R. K. Wathavana Vithanage, **E. Foster**, Z. Qiu, R. Zimermann, C. N. MacLeod, S. Pierce, A. Gachagan, G. Marinelli, J. Ding, and S. Williams, 'Ultrasonic phased array inspection of wire plus arc additive manufactured (WAAM) titanium samples', presented at the 58th Annual British Conference on Non-Destructive Testing, GBR, Nov. 2019. Accessed: Aug. 19, 2022. [Online]. Available: https://strathprints.strath.ac.uk/70520/

Chapter 2

Background research

It is evident that there is a need to understand the structural health of the weld that seals the SNM canisters at Sellafield and that these issues present complex commercial and academic problems. There is a requirement to understand the structural health of the welds that seal the canister lid to the body for three scenarios: 1) In-situ screening of legacy canisters sealed by RSWs while on a racking system with considerable accessibility constraints; 2) Ex-situ characterisation of legacy canisters sealed by RSWs; & 3) Inspection of fusion welds performed via Gas Tungsten Arc Welding (GTAW) for an upgraded canister of the future design at the point of manufacture. Therefore, this chapter is sectioned in two with the first section providing a comprehensive review of the welding techniques used at Sellafield, and the latter section providing a thorough review of relevant NDE inspection techniques well suited to the three issues faced at Sellafield.

Within the welding section, greater emphasis is placed on GTAW and RSW, as these welding techniques are either in use at Sellafield already or will be in the immediate future. The two processes use differing means to achieve a joint, and as such it can be concluded that RSW is well suited to forming a joint between two thin metals ($\sim < 2.00$ mm) while GTAW is well suited to forming a joint between two thick metals ($\sim \geq 2.00$ mm) [23]. While the joints formed between the two techniques are different, analogies could be made to the various defect types that are commonly associated with each welding process.

The second section presents a literature review of NDE techniques well suited to addressing the problems faced by Sellafield within the context of the relevant welding processes, and covers guided wave, eddy current testing and bulk ultrasonics. For the in-situ challenge, accessibility issues are present, and as such guided waves were explored in detail. It was found that a sub-category of guided waves known as Feature Guided Waves (FGWs) were well suited to screening the RSW on the legacy canister design. For

the ex-situ challenge, it was noted that due to the thin nature of the RSWs present, conventional ultrasonic methods could not be easily deployed. Eddy current testing was therefore opted for due to advances in eddy current array design and the ability of eddy currents to saturate the full thickness of the weld and canister body. For the canister of the future design, it was noted that the shift to GTAW produced significantly, thicker welds which was well suited to conventional ultrasonic testing. Various ultrasonic configurations were reviewed, and it was concluded that great benefits would be realised by performing ultrasonic inspection at the point of manufacture.

2.1. Welding

'Welding' as a term can be defined as the process by which two or more pieces of metal are united under the influence of heat to form a junction that is homogeneous. This definition encases all welding processes and does not define any method to achieve such a structure.

Generally, welding can be split into two categories – pressure and fusion [24]–[26]. Fusion welding uses heat and no application of force to liquefy and unite the two work pieces as solidification occurs. In contrast, pressure welding is defined as the union of two work pieces under high pressure where the junction is formed when the work pieces are in a plastic state. It is important to note that no liquefaction occurs in pressure welding.

Within each family, there are sub-categories ranging from very niche techniques like laser [27] & electron beam welding [28] to common techniques like Gas Metal Arc Welding (GMAW) [29] & Gas Tungsten Arc Welding (GTAW) [30]. Various differing welding techniques that correspond to differing categories and sub-categories are illustrated in Figure 5. As the work contained within this thesis is concerned with RSW & GTAW, more detail for these methods is given in Section 2.1.1 and Section 2.1.2, respectively. All other welding processes are outside the scope of this thesis and readers are referred to the "Welding processes handbook" by Klas Wernan [24] for further information and discourse.

Welding

Fusion Welding
- Power Beam Welding
  - Laser Welding
  - Electron Beam Welding
- Arc Welding
  - Gas Shielded Arc Welding
    - Gas Metal Arc Welding (GMAW)
    - Gas Tungsten Arc Welding (GTAW)
    - Plasma Welding (PAW)
  - Metal Arc Welding
    - Manual Metal Arc Welding (MMAW)
    - Submerged Arc Welding (SAW)
- Gas Welding

Pressure Welding
- Friction Welding
- Ultrasonic Welding
- Cold Pressure Welding
- Induction Welding
- Explosion Welding
- Magnetic Pulse Welding
- Resistance Welding
  - Spot Welding
  - Seam Welding
  - Projection Welding
  - Butt Welding
  - Flash Welding

s

Figure 5: An overview of welding processes categorised by process type

2.1.1.　Gas tungsten arc welding

GTAW is a fusion arc process, meaning the heat source is derived via an electric arc formed between a non-consumable electrode and material that is to be welded. The arc provides enough heat to melt the parent metal and consumable filler material, allowing the two parent metal sheets to be combined along a fused joint. A shielding gas, typically argon or helium, is used to shield the molten weld pool and protect against oxidisation. This differs from gas welding, where gas (usually acetylene) is burned to achieve the heat required to melt both the filler and parent material. Prior to the development of arc welding in the late 1920s, gas welded joints represented virtually all welds in commercial use. Since then, arc welding has gone on to supersede gas welding in almost all industrial use cases, due to its greater speed, better quality, wider range of materials that can be welded, and its ability to be controlled via automation [31], [32].

Arc welding is composed of two subcategories – metal arc welding and gas shielded arc welding. The major difference between metal arc welding and gas shielded arc welding is that the consumable electrode in metal arc welding is typically coated with a flux to provide the shielding gas required to protect against oxidation. For gas shielded welding processes, the electrode is always protected by a separate pressurised store of inert gas, enabling better protection against oxidation, and welding of non-ferrous metals such as aluminium and magnesium. The development of arc welding was primarily driven by the aerospace sector following the first world war as they sought to use light weight strong metals within their aircraft structures.

$$AE = \frac{VI}{T_s}$$

<div align="right">Eq. 1</div>

Within gas shielded arc welding, there are three sub-categories – GTAW, Gas Metal Arc Welding (GMAW), and Plasma Arc Welding (PAW). In all three a shielding gas is used, however in GMAW, the electrode is consumable, and this typically leads to spatter, caused by droplets of molten material, along the finished weld. GTAW and PAW

are very similar processes as they both use a non-consumable tungsten electrode. In general, PAW can reach far higher temperatures than GTAW due to the construction of the weld torch. In GTAW, the electrode is held externally by the torch, while in PAW the electrode is held inside the torch housing within a copper nozzle. This copper nozzle is designed to focus the electric arc and thus reach temperatures as high as $> 28,000^{\circ}$C compared to $< 19,000^{\circ}$C in GTAW. A comparison schematic between GTAW and PAW weld torches is given in Figure 6.
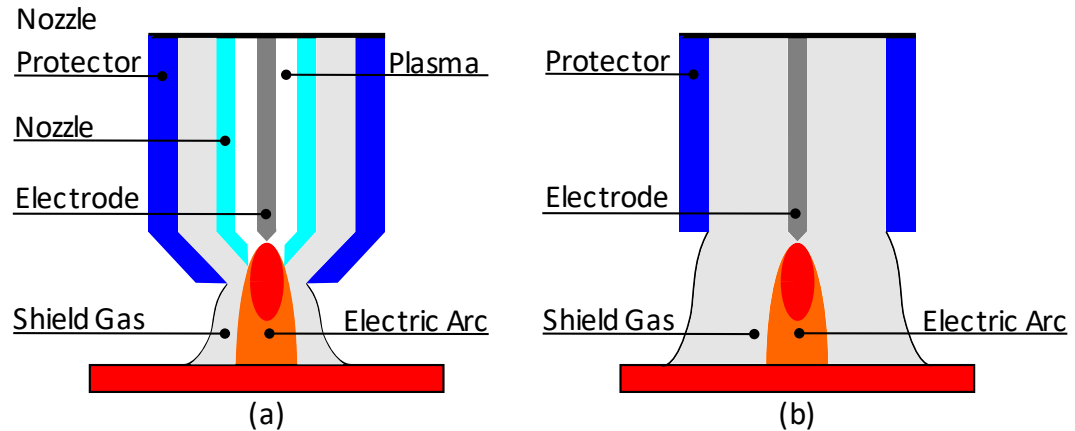
Figure 6: PAW and GTAW weld torch comparison. (a) PAW weld torch, (b) GTAW weld torch

PAW equipment can also perform cutting operations as well as welding operations due to the focused nature of the arc and the high associated temperatures. As the equipment used in PAW is significantly more complex, the cost associated with PAW is higher, leading to reduced uptake with most use cases being limited to exotic welds and operational efficiency (i.e. have the same PAW equipment perform both welding and cutting operations). This leads to GTAW being more common due to the economic advantages associated with equipment, its ability to be automated, and its ability to weld a wide range of light weight metals including stainless steel, aluminium, magnesium, and copper alloys.

In order to achieve high quality welds using arc welding processes, it is essential that the arc energy as denoted in Eq. 1 is controlled [18], where *AE* is the arc energy (kJ/m),

V is the welding voltage (V), *I* is the welding current (A), and T_s is the travel speed of the weld torch (m/s). In GTAW, a variable constant current power source is used and the distance between the non-consumable Tungsten electrode and the workpiece controls the arc voltage. In GMAW, a variable constant voltage power source is used while wire speed and contact tip to work distance to control arc current [24]. Control of the arc energy is typically performed through the use of highly sophisticated modern day power supplies [33], [34].

Whilst efforts to ensure high quality GTAW welds are usually taken, defects can still occur. The reasons why defects occur can be widespread from incorrect sample preparation to operator error and are due to process variability. Defects can manifest themselves in many differing ways. Figure 7 shows the most common defects associated with the GTAW process, including cracking, slag inclusion, porosity, lack of side wall fusion, undercut, and incomplete penetration.
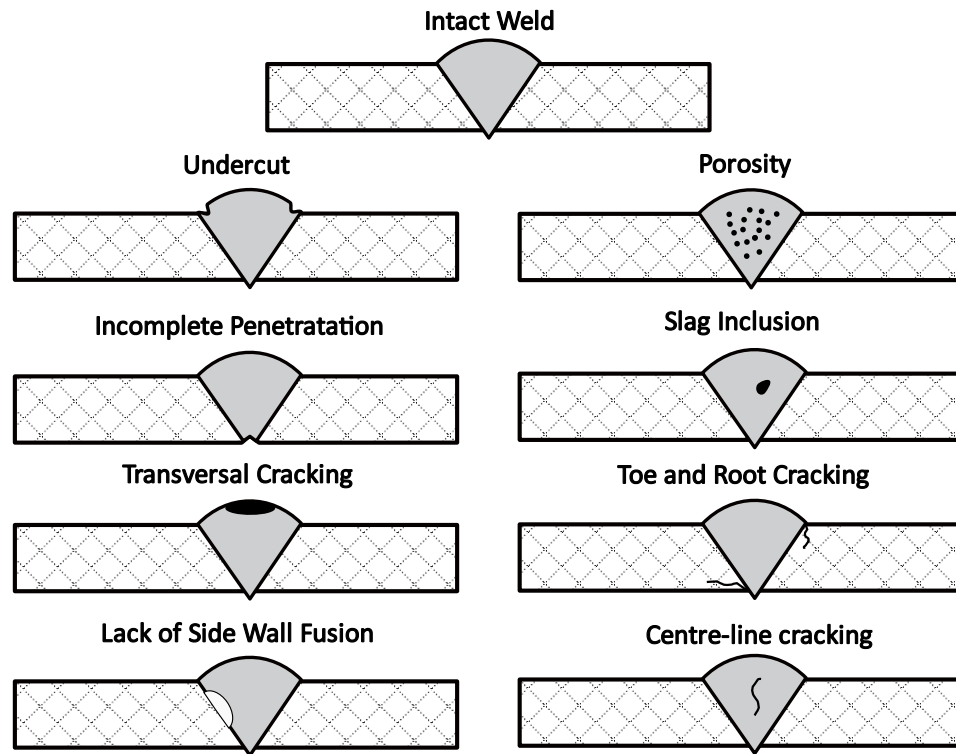
Figure 7: Common defects associated with GTAW showing undercut, porosity, incomplete penetration, slag inclusion, transversal cracking, toe and root cracking, lack of side wall fusion and centre-line cracking

There are a range of standards that govern GTAW welds and their inspection [35]–[42]. Industry standards dictate that inspection is carried out after the final deposition and when the sample has cooled to ambient temperature. As businesses seek continual improvements as they move towards Industry 4.0 [28], the time lost due to this practice is now undesirable and there is a desire to move inspection to the point of manufacture. Decreasing the time to inspect, so that inspection at the point of manufacture can be realised, is one topic this thesis explores in Chapter 5.

2.1.2.   Resistance seam welding

Resistance seam welding is a resistance welding process that falls under the family of pressure welding. In resistance welding, the work pieces are clamped together between

two electrodes. Plasticity is achieved by allowing high current to flow between the two electrodes via the work pieces. The highest point of resistance is located at the interface between the two work pieces directly under the electrodes, which raises the temperature of the junction to a plastic state. Furthermore, the pressure is commonly achieved via hydraulic or pneumatic actuators forcing the electrodes on to the two work pieces. This allows for a small volume of material to coalesce together and form what is known as a weld nugget. The amount of pressure and current applied varies drastically by material, thickness, electrode type, and type of resistance welding machine.

There are many processes that contribute to the wider family of resistance welding. These processes are related to each other by what join they form – see Figure 5. For brevity, this thesis is only concerned with resistive welded lap joints, and as a result spot and seam resistance welding. Spot welding is the most widely used example of lap joining via resistance welding. It is most commonly used in the automotive industry with a high degree of automation, achieving a high yield and low cost per weld in comparison to other welding methods [44]. Spot welding, as the name suggests, fuses together two sheets of metal at one point of contact to form a singular weld nugget. An example of a spot weld is illustrated in Figure 8.
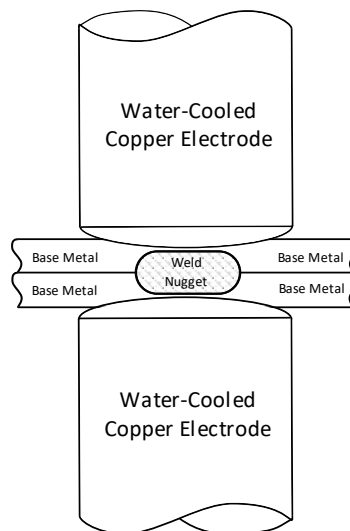
Figure 8: Spot weld illustration depicting two electrodes, two stock sheets, and a fused weld nugget [45] .

An analogous process to spot welding is seam welding, where the electrodes revolve to form a series of overlapping weld nuggets to create a continuous lap joint as illustrated in Figure 9. As resistive spot and seam welding are so similar, they will be interchangeably referred to herein. One major advantage that seam welding has over spot welding is its ability to form gas tight seals with a high rate of manufacture. For this reason, seam welding is commonly used in the manufacture of large pipes and canisters.
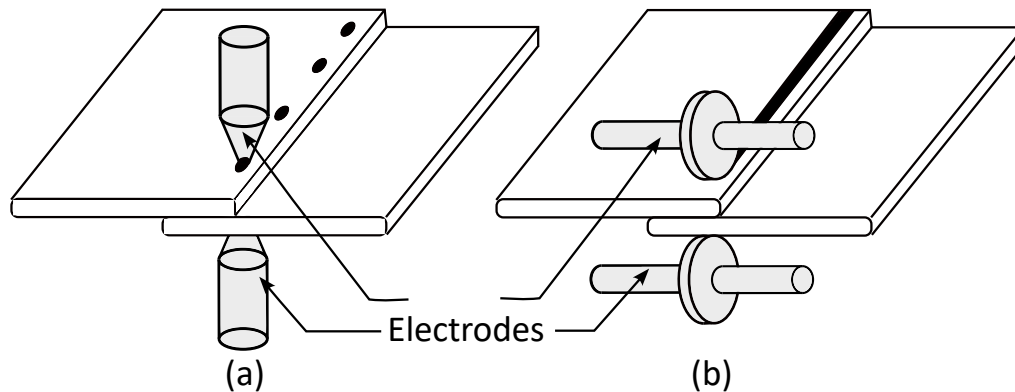
Figure 9: Spot V Seam Welding [46]

By considering a simple spot weld and the basic principles of the heat generation associated with the process, a better insight into what factors control the weld quality can be obtained. The fundamental and overriding principle in resistance welding is to deliver the maximum amount of heat energy to the weld zone in as little time as possible. This principle is described mathematically by Joules Law of Heating in Eq. 2:

$$Q = I^2 Z t$$

Eq. 2

From Eq. 2, it can be seen that the amount of heat, Q (W), produced is directly proportional to the square of the current, I (A), time, t (s), and impedance, Z (Ω) of the circuit connecting the two stock sheets. The time is defined to start and finish at the start and finish of the welding process. The current and time can be accurately adjusted via the welding control parameters. However, the impedance of the work pieces is fixed for a given thickness and material. Overall, the impedance can be further sub-divided into two

elements: the volumetric impedance of the material in the circuit, and the interfacial impedance at the contacting surfaces. Figure 10 illustrates the various resistive elements and shows the change in bulk and contact resistances over the weld process.
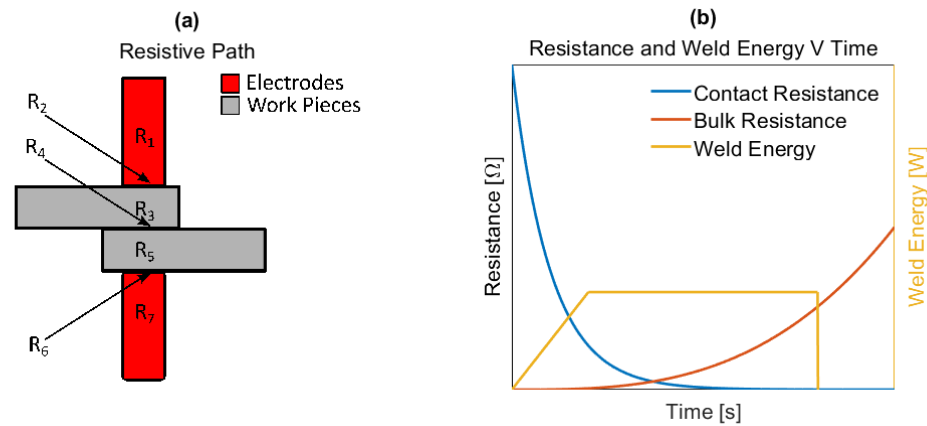
Figure 10: Resistive path of weld as well as the change in bulk and contact resistance over time

All materials oppose the flow of current to varying extents [47]. The type of current used has an impact on the volumetric impedance that is observed. In Direct Current (DC), the impedance is lower, due to the absence of electrical reactance, and the opposite is true for Alternating Current (AC). The impedance to direct current is known as the materials resistivity and is a proportional function of temperature. The volumetric impedance increases with temperature and is the major source of impedance at the end of the weld cycle (see Figure 10 (b)). Copper is used as the standard that other metals get compared due to its low resistivity, however, it is usually quoted in percentage terms of conductivity (the inverse of resistivity) [48]. By default, using this terminology, copper has a conductivity value of 100%, whereas steel is approximately 10% as conductive as copper. It can thus be extrapolated that for two plates of steel being spot welded together between two copper electrodes, the heat generated will be approximately 10 times greater in the steel, than in the copper. For this reason alone, it is common for electrodes to be made from copper alloys. It can also be concluded that resistance welding of copper stock is impractical, due to the heat generation at the fraying surfaces being insufficient to produce a well-formed weld [44].

At the interfaces of the electrodes and the two work pieces, the interfacial/contact impedance exists. There are a wide variety of factors that influence the interfacial impedance from material to pressure, and from contact area to surface condition. However, as a rough rule, it has been observed that the interfacial resistance is approximately proportional to the resistivity of the work pieces involved. Generally, the interfacial impedance is much higher than the volumetric impedance, and varies as a function of process defects (e.g. surface contamination, surface condition etc). As is shown in Figure 10 (b), the interfacial impedance decreases with temperature and is the major source of impedance at the initiation of the welding process.

Both the volumetric (R_1, R_3, R_5, & R_7 in Figure 10 (a)) and the interfacial impedances (R_2, R_4, & R_6 in Figure 10 (a)) are observed in series, and due to Ohm's Law, it is apparent that the greatest heat generation will occur at the fraying surfaces of the work pieces (R_4 in Figure 10 (a)). Furthermore, these impedances are dynamic and change throughout the welding cycle. This has practical implications for the design of the resistance welding machine and can be used to explain the cause of any potential defect which may occur.

A typical resistance seam or spot weld is completed over a cycle of 4 stages: 1) Clamping the work pieces between the electrodes at a specified pressure; 2) a timed passage of current whilst maintaining the specified pressure; 3) a dwell period at the specified pressure; rotation of the electrodes before repeating the previous two steps if a seam weld is being attempted; and finally, 4) a release of the fused work pieces from the electrodes. The weld schedule is usually provided by the machine manufacturer or determined experimentally for niche cases.

A single-impulse weld schedule is shown in Figure 11 (a) and can be detrimental under certain types of operating conditions, particularly when applied to welding of thin stock in a seam weld as utilised on the SNM canisters. The heat generated from the previous nugget can conduct into the weld zone of the next nugget giving a preheat effect. This can result in thermal run off making the weld reach melting point due to the increase in bulk resistance associated with temperature – refer to Figure 10 (b).
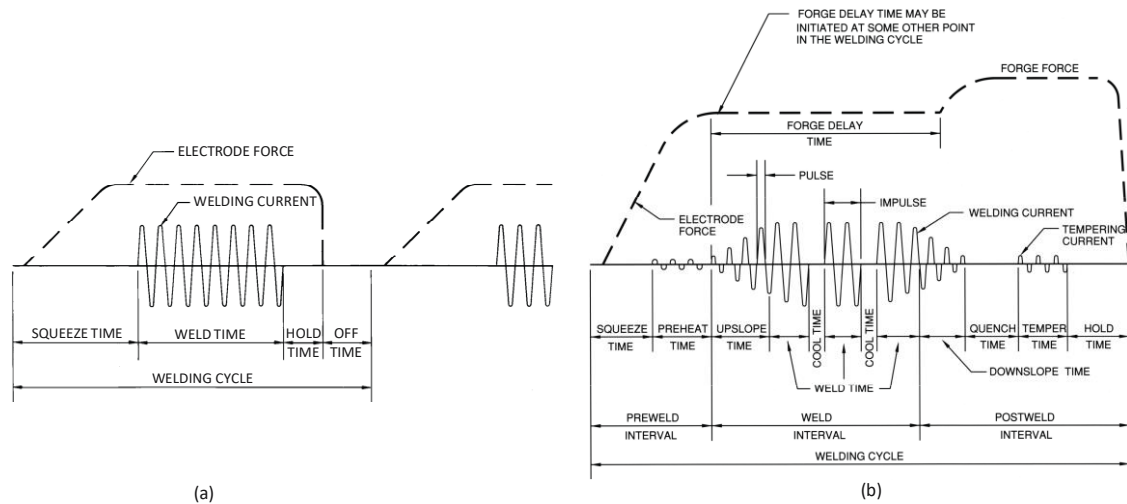
Figure 11: Resistance seam weld schedules: (a) Single-impulse weld schedule, & (b) Multi-impulse weld schedule with cool down periods between the weld impulse cycle [45].

Due to this issue, multi-impulse weld schedules have been developed. Figure 11 (b) shows a multi-impulse weld schedule. It can clearly be seen that there is a short cool time between the multiple impulses of current. This allows for some of the heat energy to conduct away from the weld zone between pulses causing a drop in temperature, and hence a drop in volumetric impedance. As a result, this prevents the effects of thermal run off, and allows the total impedance to be dominated by the interfacial impedance effectively focusing the temperature generation at the fraying surfaces of the work pieces. Better well-formed weld nuggets are usually obtained in multi-impulse weld schedules from the focusing of energy at the interfaces. These observations further underpin the fundamental principle of generating the maximum amount of heat in the shortest amount of time possible, as noted earlier in the chapter.

Both the Resistance Welding Manufacturers Alliance Resistance Welding Manual [44], and the American Welding Society Welding Handbook [49] provide suggested weld schedules for different resistance weld types, materials, and quality. For the welds in the SNM packages a multi-impulse weld is utilised to generate a gas tight seam with approximately 12-15 nuggets/inch, and this is broadly in line with these guidelines.

Defects in resistance seam welding occur in the fusion and/or the heat-affected zone and can occur at manufacture or while in service [50], [51]. The heat affected zone in welding is a non-molten area of metal that has undergone changes in its material properties due to being exposed to high temperatures. Oversized/undersized nuggets [52], voids/porosity [53], expulsion [54], and transversal cracking [55] are the most widely reported defects and are graphically illustrated in Figure 12. Transversal cracks are the most detrimental to the overall structure, and as such a screening technique to detect these types of defects in-situ is explored in Chapter 3, while detection of more generalised defects is explored ex-situ in Chapter 4.
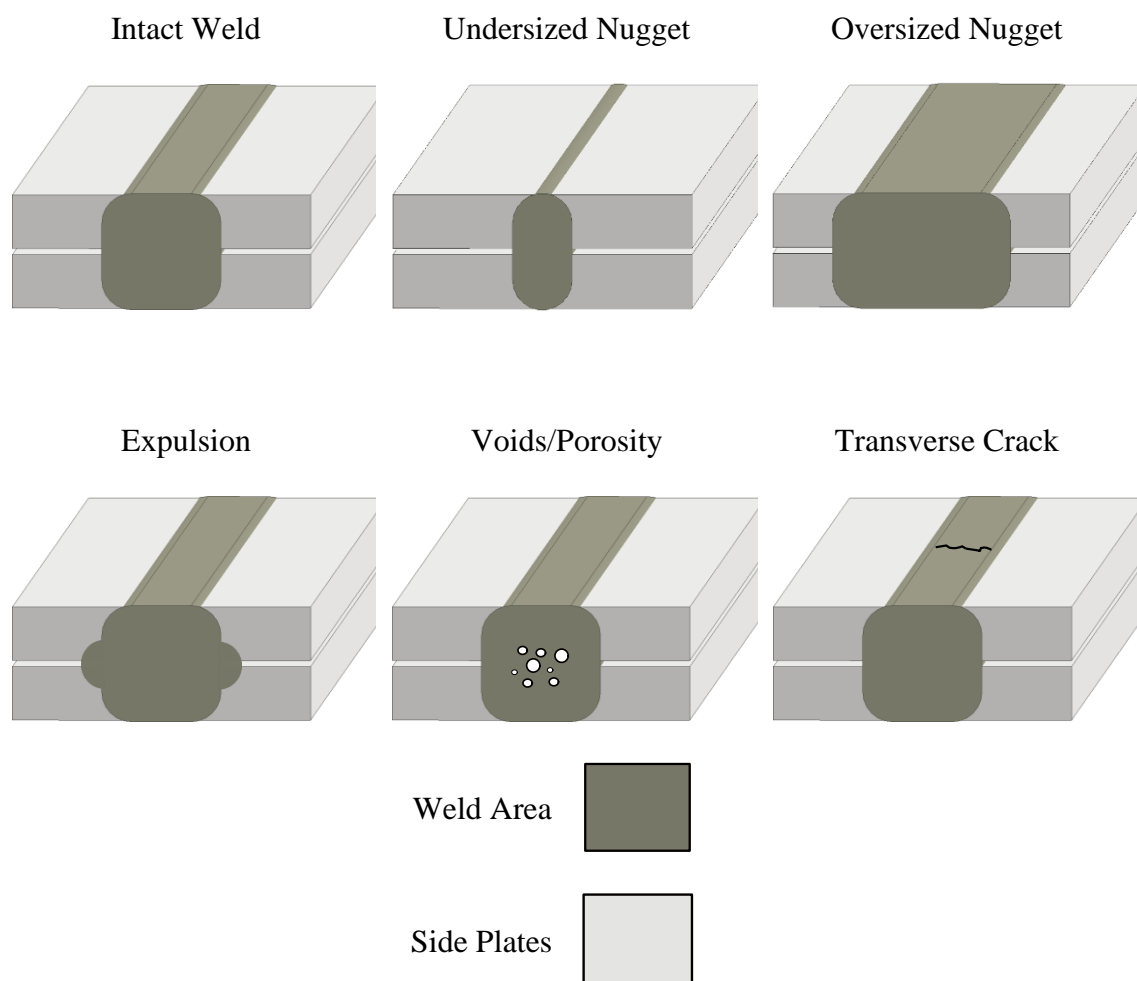
Figure 12: Illustrations of most common RSW defects in a cross-section view

2.2. Non-Destructive Evaluation

To determine the focus of key research areas, it was necessary to perform an overview of various NDE techniques suited to the three problems of; 1) In-situ screening of legacy canisters sealed by RSWs while on a racking system with considerable accessibility constraints; 2) Ex-situ characterisation of legacy canisters sealed by RSWs; & 3) Inspection of fusion welds performed via Gas Tungsten Arc Welding (GTAW) for an upgraded canister of the future design at the point of manufacture. Given that NDE is a wide topic area [56] and the industrial context of this thesis, focus was placed on the three specific NDE techniques that are well suited to the problems this thesis seeks to address. These are bulk ultrasound, guided ultrasonic waves and eddy current testing. Other techniques such as surface acoustic waves, magnetic particle testing, radiographic testing, penetrants testing, and thermography were also considered and dismissed as they were not well suited for a nuclear environment and/or didn't have the required detection capabilities. These techniques were thought to be best suited to address the challenges associated with the canister of the future, in-situ and ex-situ inspection challenges, respectively.

2.2.1.   Ultrasonic inspection

Ultrasonic inspection is the most common NDE method for weld inspection, due to its low cost, high accuracy, and its ability to detect volumetric and planar volumetric defects. Ultrasonic testing approximately accounted for 27% of the USD 6.3 billion NDE market in 2021 [57]. Recent developments in the sophistication of array technology have further increased adoption as the same arrays and array controllers can perform several inspection modes at once [58]. Ultrasonic waves can be classified as sound waves with a frequency greater than or equal to 20.00 kHz. However, for NDE applications it is common to use frequencies far greater with 1.00-10.00 MHz to allow detection and characterisation of millimetre scale defects.

There are various ultrasonic inspection modalities from bulk [59], to guided [60], to nonlinear [61]. This section is focused on bulk ultrasonic inspection with many of the

concepts being applicable to other ultrasonic inspection modes. In the industrial context of this thesis, bulk ultrasonic inspection is considered for the inspection problems associated with cannister of the future inspection challenge.

2.2.1.1. Wave propagation in bulk isotropic media

The theory of bulk wave propagation in infinite isotropic media is well documented [60], [62], [63]. Owing to this, only the principal equations of interest are outlined in this section. Isotropic solids are only considered as 1.4404 stainless steel has been shown to be isotropic in nature [64].

A common approach taken to deriving the wave equation of an infinite homogenous isotropic material is to consider an infinitesimal small parallelepiped whose faces are aligned with the global axes directions (1, 2, & 3). Each face of this parallelepiped has one direct stress and two shear stresses on it making a total of 18 stresses, denoted by σ, acting on the overall parallelepiped. This concept is quite abstract and for clarity it is annotated for only three faces in Figure 13.
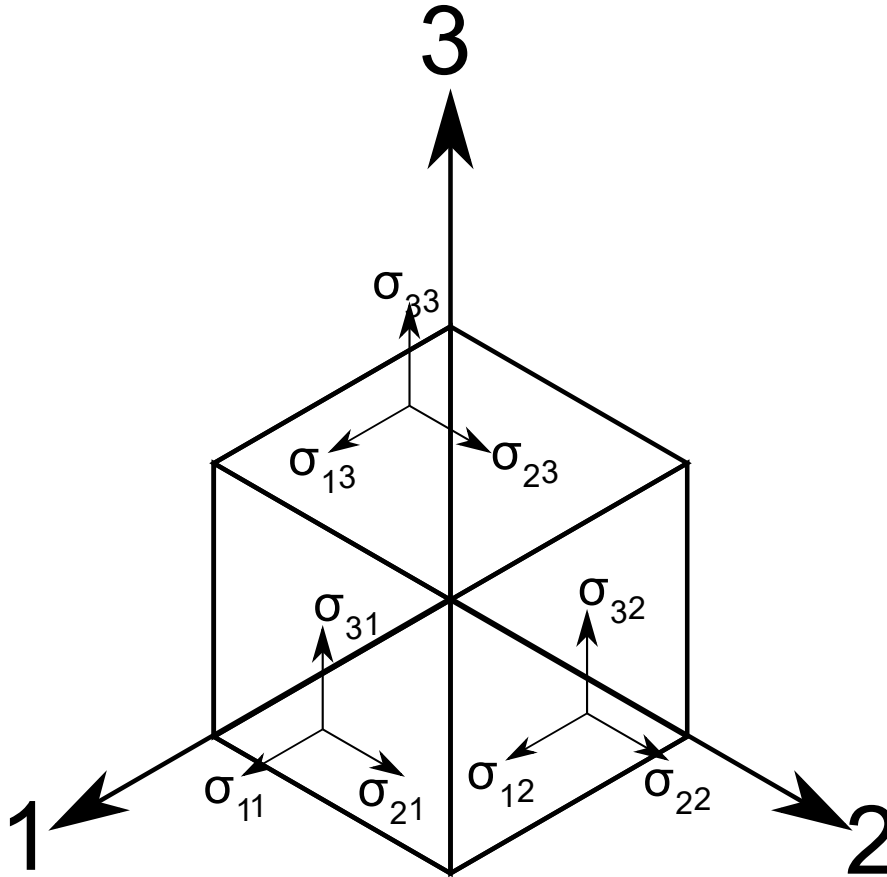
Figure 13: Infinitesimal parallelepiped with 9 components of stress acting on three faces

We can define the origin position with zero displacement as a vector position, $\boldsymbol{x} = (x_1, x_2, x_3)$, and the displaced position to be defined as $(x_1 + u_1, x_2 + u_2, x_3 + u_3)$ with the total displacement being contained within the vector $\boldsymbol{u}$. A nearby point close to the origin can be described with an un-displaced position of $(x_1 + \delta x_1, x_2 + \delta x_2, x_3 + \delta x_3)$ and a displaced position of $(x_1 + u_1 + \delta x_1, x_2 + u_2 + \delta x_2, x_3 + u_3 + \delta x_3)$. The change in displacement can therefore be written as:

$$\delta u_1 = \frac{\partial u_1}{\partial x_1}\delta x_1 + \frac{\partial u_1}{\partial x_2}\delta x_2 + \frac{\partial u_1}{\partial x_3}\delta x_3$$

$$\delta u_2 = \frac{\partial u_2}{\partial x_1}\delta x_1 + \frac{\partial u_2}{\partial x_2}\delta x_2 + \frac{\partial u_2}{\partial x_3}\delta x_3$$

Eq. 3

$$\delta u_3 = \frac{\partial u_3}{\partial x_1} \delta x_1 + \frac{\partial u_3}{\partial x_2} \delta x_2 + \frac{\partial u_3}{\partial x_3} \delta x_3$$

The stain, which is the geometrical measure of deformation representing the relative displacement between particles in a material, can then be related to the displacement. For small displacements, the change in displacement dominates and therefore the following can be stated in Eq. 4 for direct strains.

$$\epsilon_{11} = \frac{\partial u_1}{\partial x_1}, \epsilon_{22} = \frac{\partial u_2}{\partial x_2} \; \epsilon_{33} = \frac{\partial u_3}{\partial x_3}$$ Eq. 4

And for the shear strains and small displacements:

$$\epsilon_{23} = \frac{1}{2}\left(\frac{\partial u_2}{\partial x_3} + \frac{\partial u_3}{\partial x_2}\right), \quad \epsilon_{13} = \frac{1}{2}\left(\frac{\partial u_1}{\partial x_3} + \frac{\partial u_3}{\partial x_1}\right), \quad \epsilon_{12} = \frac{1}{2}\left(\frac{\partial u_1}{\partial x_2} + \frac{\partial u_2}{\partial x_1}\right)$$ Eq. 5

In the following sections ϵ_{ij} is utilised which defines the strain on the ith face in the jth direction. Now that the small displacements and strains are related on the parallelepiped, the strains can now be related to the stresses using Hooke's law:

$$\begin{pmatrix} \sigma_{11} \\ \sigma_{22} \\ \sigma_{33} \\ \sigma_{23} \\ \sigma_{13} \\ \sigma_{12} \end{pmatrix} = \begin{pmatrix} C_{11} & C_{12} & C_{13} & C_{14} & C_{15} & C_{16} \\ C_{21} & C_{22} & C_{23} & C_{24} & C_{25} & C_{26} \\ C_{31} & C_{32} & C_{33} & C_{34} & C_{35} & C_{36} \\ C_{41} & C_{42} & C_{43} & C_{44} & C_{45} & C_{46} \\ C_{51} & C_{52} & C_{53} & C_{54} & C_{55} & C_{56} \\ C_{61} & C_{62} & C_{63} & C_{64} & C_{65} & C_{66} \end{pmatrix} \begin{pmatrix} \epsilon_{11} \\ \epsilon_{22} \\ \epsilon_{33} \\ \epsilon_{23} \\ \epsilon_{13} \\ \epsilon_{12} \end{pmatrix}$$ Eq. 6

Where C is the stiffness matrix written in Voigt notation where the mapping of the tensor index becomes ($11 \Rightarrow 1, 22 \Rightarrow 2, 33 \geq 3, 23 = 32 \Rightarrow 4, 13 = 31 \Rightarrow 51, 12 = 21 \Rightarrow 6$) due to symmetry. With the fact that we are limiting our study to isotropic medium the following substitution can be made:

$$\begin{pmatrix} \sigma_{11} \\ \sigma_{22} \\ \sigma_{33} \\ \sigma_{23} \\ \sigma_{13} \\ \sigma_{12} \end{pmatrix} = \begin{pmatrix} \lambda + 2\mu & \lambda & \lambda & 0 & 0 & 0 \\ \lambda & \lambda + 2\mu & \lambda & 0 & 0 & 0 \\ \lambda & \lambda & \lambda + 2\mu & 0 & 0 & 0 \\ 0 & 0 & 0 & \mu & 0 & 0 \\ 0 & 0 & 0 & 0 & \mu & 0 \\ 0 & 0 & 0 & 0 & 0 & \mu \end{pmatrix} \begin{pmatrix} \epsilon_{11} \\ \epsilon_{22} \\ \epsilon_{33} \\ \epsilon_{23} \\ \epsilon_{13} \\ \epsilon_{12} \end{pmatrix} \qquad \text{Eq. 7}$$

Where λ and μ are the Lamé constants of the material, and are related to the Young's modulus, E, and the Poisson's ratio, v, by the following:

$$\lambda = \frac{Ev}{(1+v)(1-2v)} \qquad \qquad \text{Eq. 8}$$

$$\mu = \frac{E}{2(1+v)} \qquad \qquad \text{Eq. 9}$$

$$E = \frac{\mu}{\lambda + \mu}(3\lambda + 2\mu) \qquad \qquad \text{Eq. 10}$$

$$v = \frac{\lambda}{2(\lambda + \mu)} \qquad \qquad \text{Eq. 11}$$

The expansion of the matrix in Eq. 7, leads to the following expressions of the stresses:

$$\sigma_{11} = (\lambda + 2\mu)\epsilon_{11} + \lambda\epsilon_{22} + \lambda\epsilon_{33}, \qquad \sigma_{22} = \lambda\epsilon_{11} + (\lambda + 2\mu)\epsilon_{22} + \lambda\epsilon_{33}$$

$$\sigma_{33} = \lambda\epsilon_{11} + \lambda\epsilon_{22} + (\lambda + 2\mu)\epsilon_{33}, \qquad \sigma_{12} = \mu\epsilon_{12} \qquad \qquad \text{Eq. 12}$$

$$\sigma_{23} = \mu\epsilon_{13}, \qquad \sigma_{13} = \mu\epsilon_{13}$$
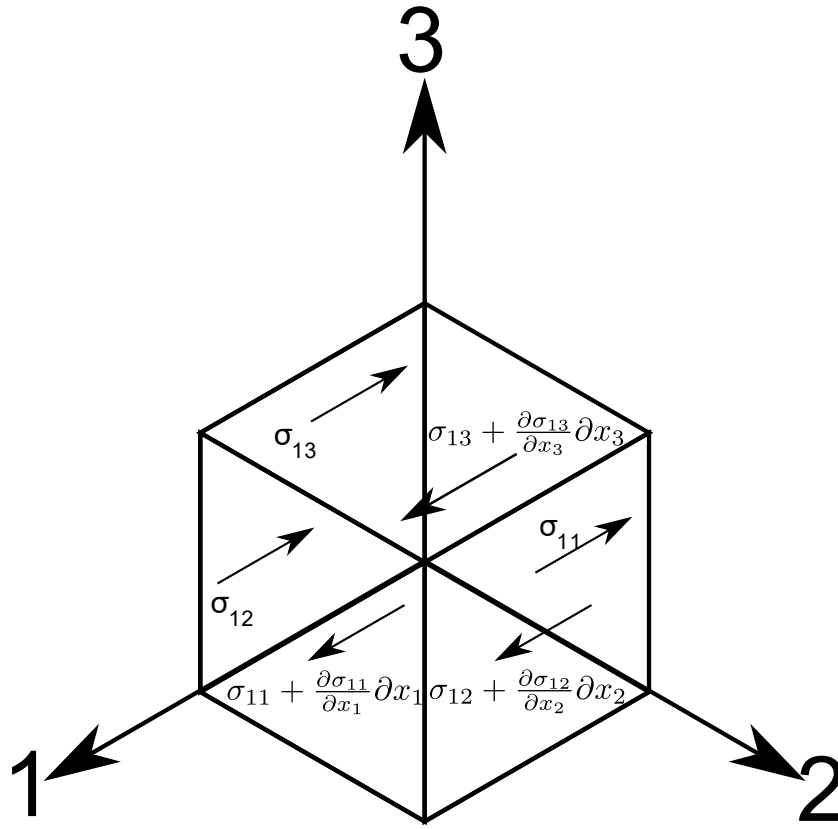
Figure 14: 6 Stresses acting along the X₁ Direction of the infinitesimally small parallelepiped

From which Newton's second law can be applied in each of the axes of the parallelepiped, to yield Euler's equation of motion (Eq. 13) [62].

$$
\left.\begin{array}{l}
\rho \dfrac{\partial^2 u_1}{\partial t^2} = \dfrac{\partial \sigma_{11}}{\partial x_1} + \dfrac{\partial \sigma_{12}}{\partial x_1} + \dfrac{\partial \sigma_{13}}{\partial x_1} \\[2ex]
\rho \dfrac{\partial^2 u_2}{\partial t^2} = \dfrac{\partial \sigma_{21}}{\partial x_2} + \dfrac{\partial \sigma_{22}}{\partial x_2} + \dfrac{\partial \sigma_{23}}{\partial x_2} \\[2ex]
\rho \dfrac{\partial^2 u_3}{\partial t^2} = \dfrac{\partial \sigma_{31}}{\partial x_3} + \dfrac{\partial \sigma_{32}}{\partial x_3} + \dfrac{\partial \sigma_{33}}{\partial x_3}
\end{array}\right\}
\qquad
\rho \left(\dfrac{\partial^2 \boldsymbol{u}}{\partial t^2} \right) = \nabla . \vec{\vec{\sigma}}
\qquad \text{Eq. 13}
$$

Substitution of Eq. 4 & Eq. 5 into Eq. 13 leads to Navier's Displacement Equation of motion shown in Eq. 14.

$$(\lambda + \mu)\nabla\nabla.\boldsymbol{u} + \mu\nabla^2\boldsymbol{u} = \rho\left(\frac{\partial^2\boldsymbol{u}}{\partial t^2}\right)$$

Eq. 14

This can be rearranged into another form shown in Eq. 15, which gives a more intuitive understanding of the wave propagation with terms being attributed to the dilation/compressional and rotational/equi-voluminal portions of the solution.

Dilatational   Rotational

$$[(\lambda + 2\mu)\nabla(\nabla.\boldsymbol{u})] + [(\mu\nabla)x\ (\nabla \times \boldsymbol{u})] = \rho\left(\frac{\partial^2\boldsymbol{u}}{\partial t^2}\right)$$

Eq. 15

Material damping can be accommodated in various ways, but for typical NDE applications, a damping model which describes a constant loss of displacement per wavelength travelled is used. This has often been used in many ultrasonic models [65]–[67].

Damping of the material replaces the Lamé constants with the following expressions:

$$\lambda = \lambda + \frac{\lambda'}{\omega}\ , \qquad \mu = \mu + \frac{\mu'}{\omega}\frac{\partial}{\partial t}$$

Eq. 16

Where μ' & λ' are the viscoelastic constants and ω is the angular frequency. If these constants are zero, then the material is purely elastic and there is zero damping. From this, Eq. 15 can be written as:

$$(\lambda + \mu)\nabla(\nabla.\boldsymbol{u}) + \mu\nabla^2\boldsymbol{u} + \left(\frac{\lambda' + \mu'}{\omega}\right)\nabla\left(\nabla.\frac{\partial\boldsymbol{u}}{\partial t}\right) + \left(\frac{\mu'}{\omega}\right)\nabla^2\frac{\partial\boldsymbol{u}}{\partial t} = \rho\left(\frac{\partial^2\boldsymbol{u}}{\partial t^2}\right) \qquad \text{Eq. 17}$$

Using Helmholtz decomposition, the three-dimensional vector equation of Eq. 17, can be expressed as a sum of the gradient of the compressional scalar potentials, ϕ, and the curl of an equi-voluminal vector potential, $\boldsymbol{\psi}$.

$$\boldsymbol{u} = \nabla\phi + (\nabla \times \boldsymbol{\psi}) \qquad \text{Eq. 18}$$

This expression along with the fact that $\nabla \times \boldsymbol{\psi} = 0$, can be substituted back into Navier's equation of motion (Eq. 14) along with the following identities:

$$\nabla.\nabla\phi = \nabla^2\phi, \quad \nabla^2(\nabla\phi) = \nabla(\nabla^2\phi), \quad \nabla.\nabla \times \boldsymbol{\psi} = 0$$

 The resulting equation is:

$$\nabla\left[(\lambda + 2\mu)\nabla^2\phi - \rho\left(\frac{\partial^2\phi}{\partial t^2}\right)\right] + \nabla \times \left[\mu\nabla^2\boldsymbol{\psi} - \rho\frac{\partial^2\boldsymbol{\psi}}{\partial t^2}\right] = 0 \qquad \text{Eq. 19}$$

Eq. 19 is satisfied if both terms vanish, which gives the following standardised equations:

$$\frac{\partial^2\phi}{\partial t^2} = c_1^2\nabla^2\phi \qquad \text{Eq. 20}$$

$$\frac{\partial^2 \boldsymbol{\psi}}{\partial t^2} = c_2^2 \nabla^2 \boldsymbol{\psi}$$

<div align="right">Eq. 21</div>

Where,

$$c_1 = \left(\frac{(\lambda + 2\mu) - i(\lambda' - 2\mu')}{\rho}\right)^{\frac{1}{2}}, \qquad c_2 = \left(\frac{\mu - i\mu'}{\rho}\right)^{1/2}$$

<div align="right">Eq. 22</div>

Or if the material is purely elastic,

$$c_1 = \left(\frac{\lambda - 2\mu}{\rho}\right)^{\frac{1}{2}}, \qquad c_2 = \left(\frac{\mu}{\rho}\right)^{1/2}$$

<div align="right">Eq. 23</div>

If the material is purely elastic, the constants c_1 & c_2 are real valued and equal the longitudinal and shear bulk wave velocities respectively. If the material is viscoelastic and contains damping, then these speeds are complex. If the damping is light, the real parts still approximate to the bulk wave velocities as previously mentioned.

2.2.1.2.   Attenuation of sound

Isotropic solids with no attenuation can be defined entirely by their density, and either their Young's modulus and Poisson's ratio, or their longitudinal and shear ultrasonic velocities. Ideal materials of this kind do not exist in nature, and therefore there is a need to describe the physical phenomenon of attenuation. There are various mechanisms that lead to attenuation of sound waves in materials, and it is not possible to incorporate every single mechanism into our mathematical understanding [68]. As a result, a general modelling approach is typically taken in which the amplitude of the sound wave decays in an exponential fashion according to the model used. The theoretical derivation provided in Chapter 2.2.1.1 allows for attenuation through damping but does not specify the model use to achieve this. Therefore, material damping that causes attenuation can be specified

in several ways. In each case the damping values are defined independently for the longitudinal and shear waves. Common ways of specifying damping are:

- **Hysteretic structural damping** in which a constant damping loss per wavelength travelled is specified and is expressed in units of Nepers per wavelength or dB per wavelength. A neper is an exponential decay constant as defined in Eq. 24.

$$A_{location2} = A_{location2}e^{-\alpha n}$$ Eq. 24

The amplitude of the wave, A, decreases by the factor of $e^{-\alpha n}$ if α is in nepers per wavelength and location 2 is n wavelengths downstream from location 1. This means that as the frequency of the wave is increased, the attenuation also increased per unit distance travelled as the wavelength decreases. Hysteretic structural damping is the *de-facto* description and is compatible with the derivations presented in Section 2.2.1.1.

- **Hysteretic damping (per meter) damping** is an adaptation of hysteretic structural damping where the bulk attenuation is defined as a loss per unit distance at a given frequency for convenience. It is common to have to convert this to attenuation to a loss per wavelength to conform the derivations presented in Section 2.2.1.1.

- **Kelvin-Voigt viscous damping** is defined by a dashpot damping model, where the damping force is proportional to the particle velocity. This results in a model that has higher attenuation as a function of frequency than in hysteretic damping. Unlike hysteretic damping, the loss per wavelength is now no longer constant but increases linearly with frequency. Modern composites and polymer materials are materials that experience considerable viscoelastic damping [59], and as this thesis is primarily focused on inspecting 1.4404 stainless steel, this damping model is out of the scope of this thesis.

2.2.1.3.   Wave refraction, reflection, and mode conversion

When an ultrasonic wave intercepts a distinct interface between two media of differing physical properties, a change in direction is observed. This change in direction is what is known as refraction. In general, highly dissimilar materials produce greater refraction angles while the opposite is true for similar materials. Snell's Descartes [62] law as depicted in Eq. 25 describes this phenomenon, where c_1 & c_2 are the ultrasonic wave speeds of medium 1 and 2 respectively, θ_i is the angle of incidence, and θ_r is the refracted angle.

$$\frac{Sin(\theta_i)}{c_1} = \frac{Sin(\theta_r)}{c_2}$$

Eq. 25

Additionally, if refraction occurs at a solid interface below the critical angle, it is accompanied by mode conversion. Figure 15 shows a schematic of a longitudinal incidence wave mode converting and refracting into a shear and longitudinal wave. Like with all waves undergoing refraction critical angles can occur where the refracted angles of the longitudinal and shear waves reach 90°. The critical angle of the longitudinal wave mode is widely exploited within NDE to allow for inspection with just the shear wave alone in the component [69] .
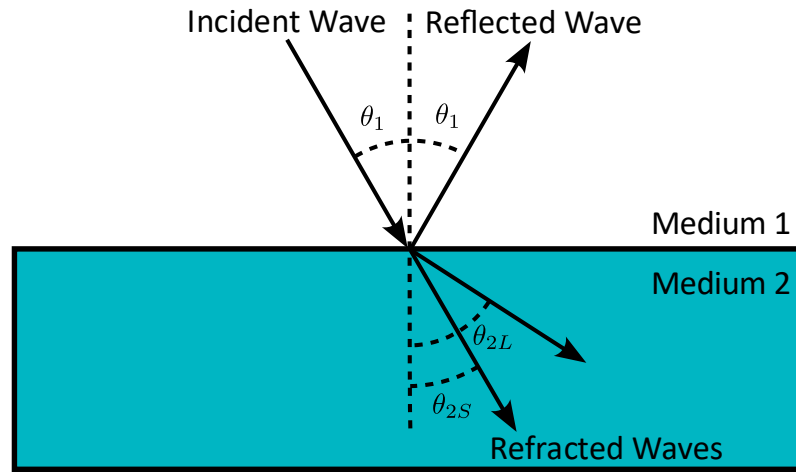
Figure 15: Schematic showing a longitudinal wave reflecting, refracting and mode converting at an interface between two media.

For normal incidence, the amount of energy transmitted between the two media is governed by their associated acoustic impedance ($z = \rho c$). Acoustic impedance can be thought of analogously to electrical impedance [70] and is a measure of how ease sound propagates through each medium. Like electrical impedance, the sound wave will take the path of least resistance and most of its energy will be transfers to the medium of lowest impedance. For normal incidence, the reflection coefficient at an interface can be described by Eq. 26, and the transmission coefficient at a boundary can be described by Eq. 27.

$$R = \frac{z_2 - z_1}{z_1 + z_2}$$
Eq. 26

$$T = \frac{2z_2}{z_1 + z_2}$$
Eq. 27

The aforementioned applies well to a boundary with two distinct media of differing material properties. For media that exhibit a gradual change in material properties, solutions to the Eikonal equation are required [71] or discretised ray-tracing algorithms are utilised [72].

While there are other niche ultrasonic wave types, such as Rayleigh waves, guided waves, and non-linear acoustics, the large majority of ultrasonic testing makes use of bulk ultrasonic waves to infer structural health using the properties described in this section.

2.2.1.4. Phased arrays

Phased array ultrasonic transducers containing numerous piezoelectric elements housed within a single housing have become increasingly popular in many Non-Destructive Evaluation (NDE) applications due to their flexibility, quality, and reduced inspection times [58], [73]. Flexibility in the acquisition of data is ensured since the same array can be used for various differing inspections, while flexibility in post-processing arises from the variety of imaging algorithms that can be applied to the rich ultrasonic datasets acquired by arrays.

Individual element generation parameters such as the voltage, delay, or excitation signal can be controlled independently allowing for a wide array of inspection modes to be performed. Beam forming, where a sub-aperture of many elements is fired in sync with one another, is the simplest inspection mode and produces a plane wave. Plane wave imaging algorithms can be used to create images from the datasets they use with the advantage of high Signal to Noise Ratios (SNRs) and framerates [74]. If a specific location is to be inspected, the beam can be focused onto a single point by varying the time delays between the elements in the array. Synthetic aperture techniques can be used to create focused images from these datasets [75]. Likewise, ultrasonic beams can be steered to specific locations across a series of angles to form sectorial images of the component under inspection [76]. These three inspection modalities are illustrated in Figure 16.
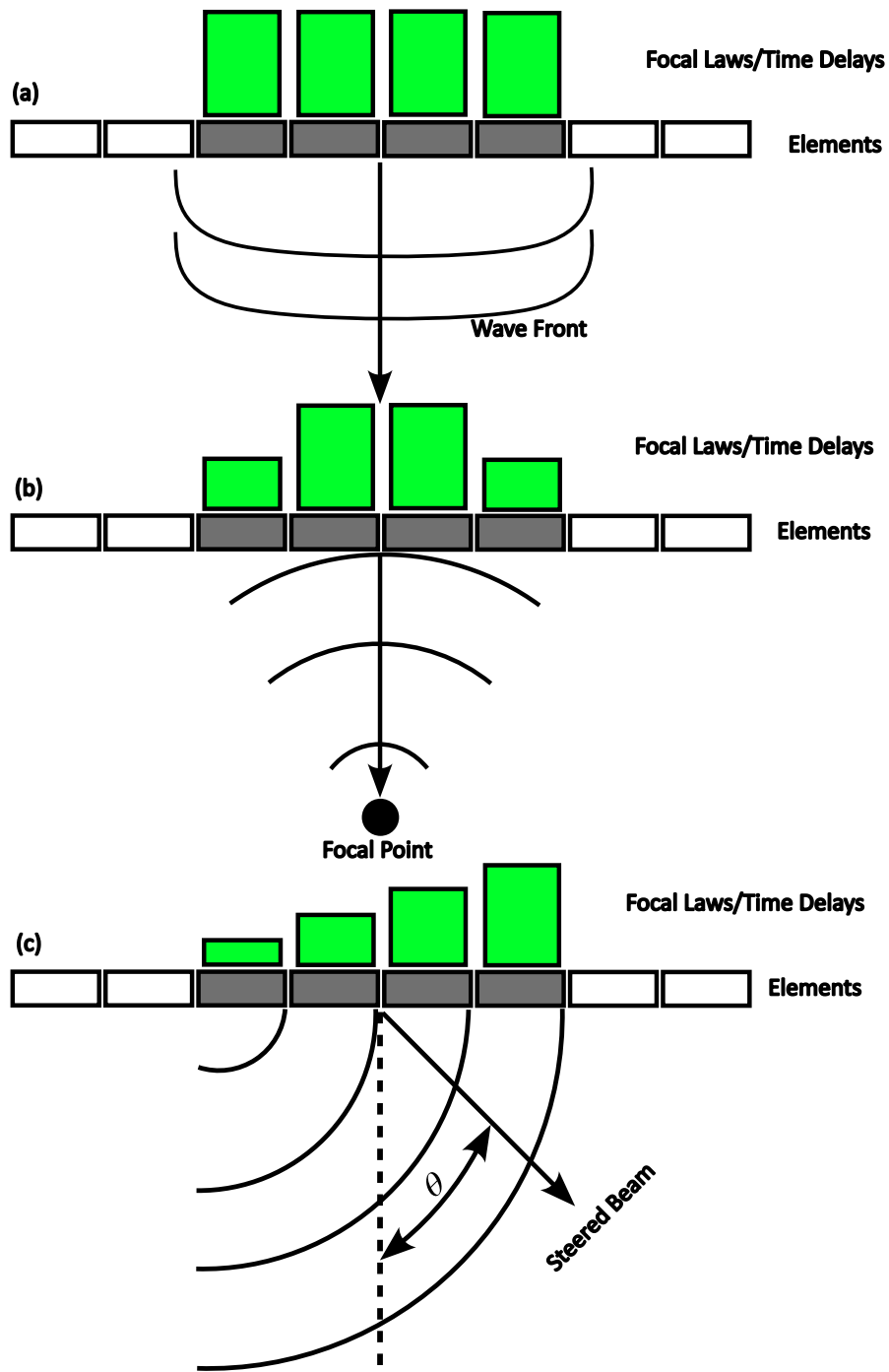
Figure 16: Illustrations of standard array imaging techniques, where elements are represented by white/greyed rectangles and focal laws/time delays between elements are represented by green rectangles. (a) Plane wave inspection where all elements in the sub-aperture are fired simultaneously, (b) Focused inspection where element in the sub-

More recently, Full Matrix Capture (FMC) datasets have become increasingly popular as the cost of array electronics continues to decrease and the speed of computation increases. FMC datasets are a complete set of time domain data that is acquired from all combinations of transmit/receive elements, to create an N^2 matrix of A-scan data.

As complete information about the wavefront is captured in FMC datasets, they have widely become the *de facto* standard to which imaging algorithms are applied [77]. It is often necessary for these imaging algorithms to incorporate some element of *a priori* knowledge in order to accurately detect and characterise any present defects. One such imaging algorithm is the Total Focusing Method (TFM) [78]. In TFM, *a priori* knowledge of the ultrasonic velocity within the component is used in a forward model to create a Time of Flight (ToF) map from each transmit/receive pair to each pixel in the imaging domain. The amplitude corresponding to each of the times in the ToF map is extracted, and the results from every transmit/receive pair in the FMC dataset are then summed. This creates an image that is synthetically focused across the entire domain, leading to increased defect detection and improved characterisation [79]–[82]. Issues occur when inspecting welds, especially so in austenitic welds, where large grains in the weld and HAZ, create larger amounts of attenuation and scatter. Typically, the images formed from these components have large amounts of noise present and supressing these issues is an active area of research [80]–[83].

The TFM is mathematically described in Eq. 28 for a single homogenous domain, where x_{s_x} and y_{s_y} are the x and y coordinates of the transmitting ultrasonic array element, x_{r_x} and y_{r_y} are the x and y coordinates of the receiving ultrasonic array element, x_i and y_i are the x and y coordinates of the imaging domain, $A_{s_{x,y}r_{x,y}}$ is the amplitude associated of the transmit and receive pair under consideration, c is the ultrasonic velocity of the domain and $I(x_i, y_i)$ is the image pixel value at each x and y coordinate of the imaging domain. Additionally, the TFM is visually depicted in Figure 17.

$$I(x_i, y_i) = \left| \sum_{s_{x,y}=1}^{N} \sum_{s_{x,y}=1}^{N} A_{s_{x,y}r_{x,y}} \left(\frac{\left(\sqrt{(x_{s_x} - x_i)^2 + (y_{s_y} - y_i)^2} + \sqrt{(x_{r_x} - x_i)^2 + (y_{r_y} - y_i)^2} \right)}{c} \right) \right| \quad \text{Eq. 28}$$
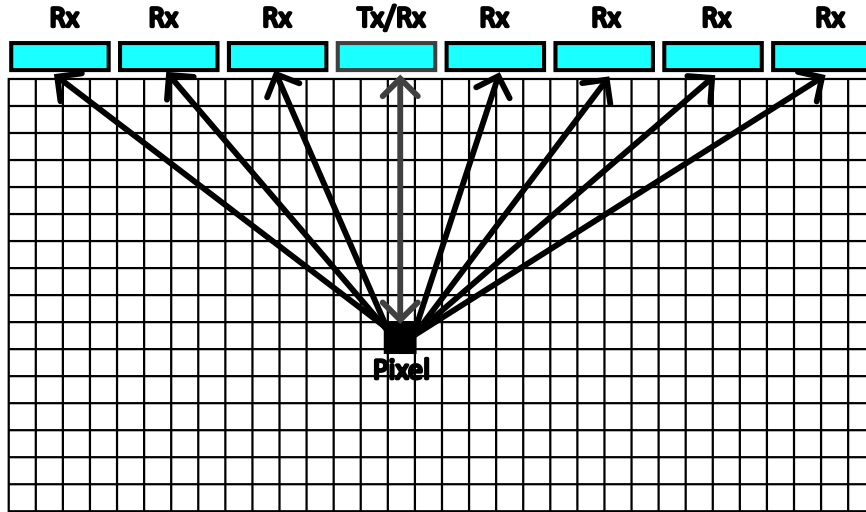
Figure 17: Illustration of the Total Focusing Method (TFM).

Bulk ultrasound from a phased array can be used for a wide range of NDT activities, including weld inspection, thickness measurements, corrosion mapping and inspection of pressure vessels. It is apparent that bulk ultrasonic inspection offers a lot of benefits due to its maturity, and wide array of post processing techniques that can be used to perform inversion of the physical internal structure of the component [82], [84]. However, inspection of thin metal presents various issues such as ringdown [85], frequency choice, and guided wave effects dominating the propagation [86]. Due to this, industry standards recommend that bulk ultrasonic inspection of welds is carried out on thicknesses of ≥ 8.00 mm [37]. In the industrial context of this thesis, it is therefore useful to consider bulk ultrasonic inspection for the challenges associated with the cannister of the future as thicknesses are predicted to as high as 10.00 mm – see Figure 4.

2.2.2.   Guided waves

The propagation of bulk waves in unbounded media, as described in Section 2.2.1.1, is solely dependent on the material properties, and as such their acoustic velocity is constant. In contrast, when waves are transmitted along bounded structures, frequency-dependent dispersive characteristics can be observed due to the resulting interference occurring from successive reflections at each boundary. For a plate structure, this phenomenon is illustrated in Figure 18. These waves are therefore guided by the structure in which they are present in, and as such they are referred to as guided waves and wave guides respectively [60]. The way in which these wave structures interfere, and move can then be categorised into several different families. Typically, their vibrational patterns become increasingly complex as the frequency is also increased. Dispersion curves are commonly used to characterise and understand more about guided waves.
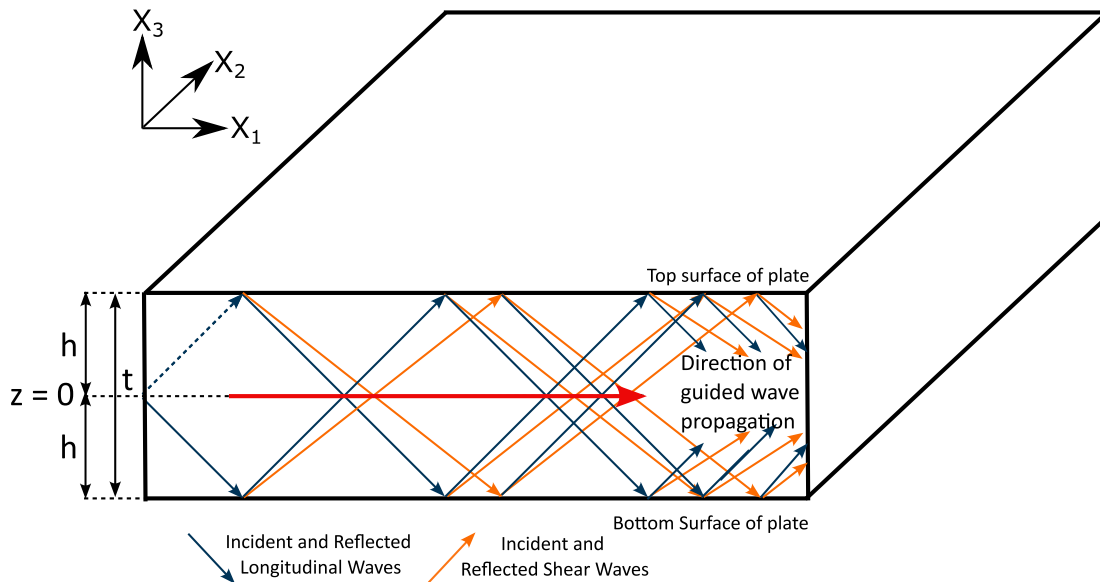
Figure 18: Schematic of guided wave propagation resulting from total internal reflection

The vast majority of guided waves are dispersive meaning that their phase and group velocities are a function of frequency. Phase velocity describes the speed at which an individual phase within a broadband wave packet moves at and is described by Eq. 29

$$V_{ph} = \frac{\omega}{k}$$ Eq. 29

Where ω is the angular frequency and k is the real wavenumber. To describe the speed at which a guided wave packet travels at, the term group velocity is used, as shown in Eq. 30.

$$V_{gr} = \frac{\partial \omega}{\partial k}$$ Eq. 30

For isotropic free plates, guided waves can be classified into three families: 1) anti-symmetric Lamb waves, 2) symmetric Lamb waves, and 3) shear horizontal waves. All Lamb waves are characterised via their mode shapes about the mid-plane of the plate structure. Symmetric Lamb waves are characterised by a vibrational pattern predominantly in the radial plane parallel to the direction of propagation. Anti-symmetric modes are characterised by a vibrational pattern that is predominantly out of plane. Both symmetric and anti-symmetric modes are denoted by S_i and A_i $(i = 0,1,2,3 \dots)$, respectively. The third family of plate guided wave modes are shear horizontal and they are characterised by a vibrational pattern in the x_1-x_2 plane perpendicular to the direction of travel.

2.2.2.1. Lamb waves

The equations that describe bulk longitudinal and shear motion in an infinite isotropic solid can be expanded upon to derive the equations that govern Lamb wave propagation and their dispersive properties. The approach defined by Rose [60] is used herein. Lamb waves comprise of both shear and longitudinal motion giving rise to elliptical particle motion. Eq. 20 & Eq. 21 from Section 2.2.1.1 can be rewritten to give Eq. 31 and Eq. 32 for purely isotropic media:

$$\nabla^2 \phi - \frac{1}{c_L^2} \frac{d^2 \phi}{dt} = 0 \qquad\qquad \text{Eq. 31}$$

$$\nabla^2 \psi - \frac{1}{c_S^2} \frac{d^2 \psi}{dt} = 0 \qquad\qquad \text{Eq. 32}$$

The equations can then be further simplified to ignore motion in the x_2-direction due to the elliptical motion associated with Lamb waves:

$$\frac{\partial^2 \phi}{\partial x_1^2} + \frac{\partial^2 \phi}{\partial x_3^2} = \frac{1}{c_L^2} \frac{d^2 \phi}{dt}, \text{ governing longitudinal waves} \qquad\qquad \text{Eq. 33}$$

$$\frac{\partial^2 \psi}{\partial x_1^2} + \frac{\partial^2 \psi}{\partial x_3^2} = \frac{1}{c_T^2} \frac{d^2 \psi}{dt}, \text{ governing shear waves} \qquad\qquad \text{Eq. 34}$$

Another important point to note is the elliptical motion allows for plane strain to be assumed so that the displacements and stresses can be written as the following:

$$u_1 = u = \frac{\partial \phi}{\partial x_1} + \frac{\partial \psi}{\partial x_3} \qquad\qquad \text{Eq. 35}$$

$$u_2 = v = 0, \qquad\qquad \text{Eq. 36}$$

$$u_3 = w = \frac{\partial \phi}{\partial z} - \frac{\partial \psi}{\partial x} \qquad \text{Eq. 37}$$

$$\sigma_{31} = \mu \left(\frac{\partial u_3}{\partial x_1} + \frac{\partial u_1}{\partial x_3} \right) = \mu \left(\frac{2\partial^2 \phi}{\partial x_1 \partial x_3} - \frac{\partial^2 \psi}{\partial x_1^2} + \frac{\partial^2 \psi}{\partial x_3^2} \right) \qquad \text{Eq. 38}$$

$$\sigma_{33} = \lambda \left(\frac{\partial u_1}{\partial x_1} + \frac{\partial u_3}{\partial x_3} \right) + 2\mu \frac{\partial u_3}{\partial x_3} = \lambda \left(\frac{\partial^2 \phi}{\partial x_1^2} + \frac{\partial^2 \phi}{\partial x_3^2} \right) + 2\mu \left(\frac{\partial^2 \phi}{\partial x_3^2} - \frac{\partial^2 \psi}{\partial x_1 \partial x_3} \right) \qquad \text{Eq. 39}$$

General plane wave solutions in the form defined in Eq. 40 & Eq. 41 can then be assumed. These solutions describe travelling waves in the x_1-direction and standing waves in the x_3-direction.

$$\phi = \Phi(x_3)e^{i(kx_1 - \omega t)} \qquad \text{Eq. 40}$$

$$\psi = \Psi(x_3)e^{i(kx_1 - \omega t)} \qquad \text{Eq. 41}$$

The following solutions can also be assumed for the expressions in the thickness direction to give:

$$\Phi(x_3) = A_1 \sin(px_3) + A_2 \cos(px_3) \qquad \text{Eq. 42}$$

$$\Psi(x_3) = B_1 \sin(gx_3) + B_2 \cos(gx_3) \qquad \text{Eq. 43}$$

Where $A_1, A_2, B_1, \& B_2$ are arbitrary amplitude constants, $p^2 = \frac{\omega^2}{c_L^2} - k^2$ and $q^2 = \frac{\omega^2}{c_T^2} - k^2$. With all this result, Eq. 35-Eq. 39 can be rewritten as Eq. 44-Eq. 47. Note that the time dependent of the plane wave solution, $e^{i(kx - \omega t)}$, is omitted for simplicity.

$$u_1 = ik\phi + \frac{d\psi}{dz} \qquad \text{Eq. 44}$$

$$u_3 = \frac{d\phi}{dz} - ik\psi \qquad \text{Eq. 45}$$

$$\sigma_{31} = \mu\left(\frac{2ikd\Phi}{dx_3} + k^2\Psi + \frac{d^2\Psi}{dx_3^2}\right) \qquad \text{Eq. 46}$$

$$\sigma_{33} = \lambda\left(-k^2\Phi + \frac{d^2\Phi}{dx_3^2}\right) + 2\mu\left(\frac{d^2\Phi}{dx_3^2} - ik\frac{d\Psi}{dx_3}\right) \qquad \text{Eq. 47}$$

It is then possible to split the functions into odd and even functions about $z = 0$ corresponding to the sine and cosine terms giving rise to symmetric and antisymmetric solutions. Symmetric motion about the mid plane of the plane is described through cosine terms in the u_1 displacement and sine terms in the u_3 displacement. The opposite is true for antisymmetric waves. This leads to the following displacement terms:

Symmetric waves

$$u_1 = ikA_2\cos(px_3) + qB_1\cos(gx_3) \qquad \text{Eq. 48}$$
$$u_3 = -pA_2\sin(px_3) - ikB_1\sin(gx_3) \qquad \text{Eq. 49}$$

Antisymmetric waves

$$u_1 = ikA_1\sin(px_3) - qB_2\sin(gx_3) \qquad \text{Eq. 50}$$

$$u_3 = pA_1\cos(px_3) - ikB_2\cos(gx_3) \qquad \text{Eq. 51}$$

The stresses can also similarly be rewritten as:

Symmetric waves

$$\sigma_{31} = \mu(-2ikpA_2\sin(px_3) + (k^2 - g^2)B_1\sin(gx_3)) \qquad \text{Eq. 52}$$

$$\sigma_{33} = -\lambda(k^2 + p^2)A_2 \cos(px_3) - 2\mu[p^2 A_2 \cos(px_3) + ikgB_1 \cos(gx_3)] \qquad \text{Eq. 53}$$

Antisymmetric waves

$$\sigma_{31} = \mu[2ikpA_1 \cos(px_3) + (k^2 - g^2)B_2 \cos(gx_3)] \qquad \text{Eq. 54}$$

$$\sigma_{33} = \lambda(k^2 + p^2)A_1 \sin(px_3) - 2\mu[p^2 A_1 \sin(px_3) - ikgB_2 \sin(gx_3)] \qquad \text{Eq. 55}$$

The boundary conditions for Lamb waves in that the stresses, σ_{31} & σ_{33}, must be equal to zero at $\pm h$, can then be applied. This can be applied to equations Eq. 52-Eq. 55 to give a pair of equations with two unknown constants each, i.e. A_2 & B_1 for symmetric modes, and A_1 & B_2 for antisymmetric modes. Each system of equations for each wave mode can then be non-trivially solved by assembling them in a matrix format and taking the determinant. For symmetric waves this is shown in Eq. 56 & Eq. 57.

$$\begin{bmatrix} -2\mu ikp\sin(ph) & \mu(k^2 - g^2)\sin(gh) \\ -\lambda(k^2 + p^2)\cos(ph) - 2\mu p^2 \cos(ph) & 2\mu ikgB_1 \cos(gh) \end{bmatrix} \begin{bmatrix} A_2 \\ B_1 \end{bmatrix} = \begin{bmatrix} 0 \\ 0 \end{bmatrix} \qquad \text{Eq. 56}$$

$$\begin{aligned} &-4k^2 pq\mu \sin(ph)\cos(gh) \\ &\quad + (k^2 - g^2)(\lambda k^2 + \lambda p^2 + 2\mu p^2)\sin(gh)\cos(gh) = 0 \end{aligned} \qquad \text{Eq. 57}$$

Eq. 57. can then be further simplified as is stated in Eq. 58. Note that the denominator can be further simplified with the use of Lame parameters, λ and μ, and their relationship to the longitudinal and shear velocities as defined in Eq. 23 in Section 2.2.1.1. This simplification is given in Eq. 59.

$$\frac{\tan(gh)}{\tan(ph)} = \frac{4k^2 pg\mu}{(\lambda k^2 + \lambda p^2 + 2\mu p^2)(k^2 - g^2)} \qquad \text{Eq. 58}$$

$$\frac{\tan(gh)}{\tan(ph)} = -\frac{4k^2pg}{(g^2-k^2)^2}$$

Eq. 59

A similar process can be followed for antisymmetric waves to give the expression in Eq. 60.

$$\frac{\tan(gh)}{\tan(ph)} = -\frac{(g^2-k^2)^2}{4k^2pg}$$

Eq. 60

The dispersion relationships documented in Eq. 59 & Eq. 60 can only be solved numerically [60], [65] and it has been shown that there are an infinite number of wave numbers that satisfy them. If the wavenumber value is real, imaginary or complex, various real-world applications can be inferred. If the wavenumber is complex, the time harmonic element of the dispersion relationship, which was omitted from the above derivation, can be written as the following:

$$e^{i(kx_1-\omega t)} = e^{i(k_r x_1-\omega t)}e^{-k_{im}x_1}$$

Eq. 61

This gives rise to three distinct regimes of k_{im} that describe different types of Lamb waves. If $k_{im} > 0$, this, then describes an evanescent Lamb wave that exponentially decays with distance. If $k_{im} < 0$, this, then describes a Lamb wave that grows exponentially with distance. For $k_{im} = 0$, this describes all Lamb waves useful to NDE.

In order to predict the dispersive properties of these guided waves various analytical solvers are available [87]–[89] and perform solutions to the equations covered in this subsection.

49

2.2.2.2.   Shear horizontal guided waves

Another family of guided waves have also been shown to exist called shear horizontal waves. These waves can be similarly derived but assume no displacement in the x_1 and x_3 directions and neglect any compressional scalar potential ($\phi = 0$). This leads to Eq. 20 from Section 2.2.1.1 vanishing and & Eq. 21 being rewritten as:

$$\frac{\partial^2 \psi}{\partial t^2} = c_T^2 \left(\frac{\partial^2 \psi}{\partial x_2^2} \right) \qquad \text{Eq. 62}$$

A similar general plane wave solution to that of subsection 0 can also be taken in Eq. 63, where k_{x_1} is the wavenumber in the propagation direction:

$$\psi = \Psi(x_3) e^{i(k_{x_1} x_1 - \omega t)} \qquad \text{Eq. 63}$$

The component related to the thickness direction, x_3, can be assumed to take the form of:

$$\Psi(x_3) = A sin(k_{x_3} x_3) + B cos(k_{x_3} x_3) \qquad \text{Eq. 64}$$

Where like subsection 0, A & B are arbitrary constants and k_{x_3} is the through thickness wavenumber. Applying the boundary conditions at $x_3 = T$ & $x_3 = 0$ yields:

$$A cos(k_{x_3} T/2) - B sin(k_{x_3} T/2) = 0 \qquad \text{Eq. 65}$$

$$A cos(k_{x_3} T/2) + B sin(k_{x_3} T/2) = 0 \qquad \text{Eq. 66}$$

The system of equations represented by Eq. 65 & Eq. 66 can be solved to give:

$$\cos(k_{x_3}T/2)\sin(k_{x_3}T/2) = 0$$

Eq. 67

Which can only be satisfied if:

$$k_{x_3} = \frac{\pi n}{T} \quad (n = 0,1,2,3,\dots)$$

Eq. 68

The wavenumber can be related to the shear bulk wavenumber as stated in Eq. 69. This in combination with the fact that the wavenumber from the shear waves can be described as (ω/c_T) leads to Eq. 70

$$k_{x_3}{}^2 = k_T^2 + k_{x_1}^2$$

Eq. 69

$$k_{x_1}^2 = \left(\frac{\pi n}{T}\right)^2 - \left(\frac{\omega}{c_T}\right)^2$$

Eq. 70

From the expression given in Eq. 70, and the fact that $k_{x_1} = \frac{\omega}{c_p}$, the frequency, f, thickness, T, dependent phase velocity of shear horizontal waves can be found from Eq. 71.

$$c_p(fT) = \pm 2c_T \left(\frac{fT}{\sqrt{4(fT_0)^2 - n^2 c_T^2}}\right)$$

Eq. 71

This expressing can then be derived further to give an expression for the group velocity of the wave pulses to as shown in Eq. 72.

$$c_g = c_T \sqrt{1 - \frac{\left(\frac{n}{2}\right)^2}{(fT_0 c_T)^2}} \qquad \text{Eq. 72}$$

As with Lamb waves, in order to predict the dispersive properties of these guided waves various analytical solvers are available [87]–[89] and perform solutions to the equations covered in this subsection.

2.2.2.3.   Dispersion curves

The phase and group velocity solutions for a 1.00 mm thick 304 stainless steel plate are shown in Figure 19. For each guided wave family there are an infinite number of modes that exist, and they are sequentially numbered in the order they appear in the dispersion curves from low to high frequency. The SH_0 wave mode is unique in the fact that it is completely non-dispersive and has a constant group and phase velocity over its entire frequency spectra when propagating on a flat plate. All other modes for a flat plate in free space have differing amounts of dispersion across their frequency range. However, it is common to use certain transduction techniques to excite only one mode, or at least as few modes as possible, at a frequency where the dispersion effect is minimal.
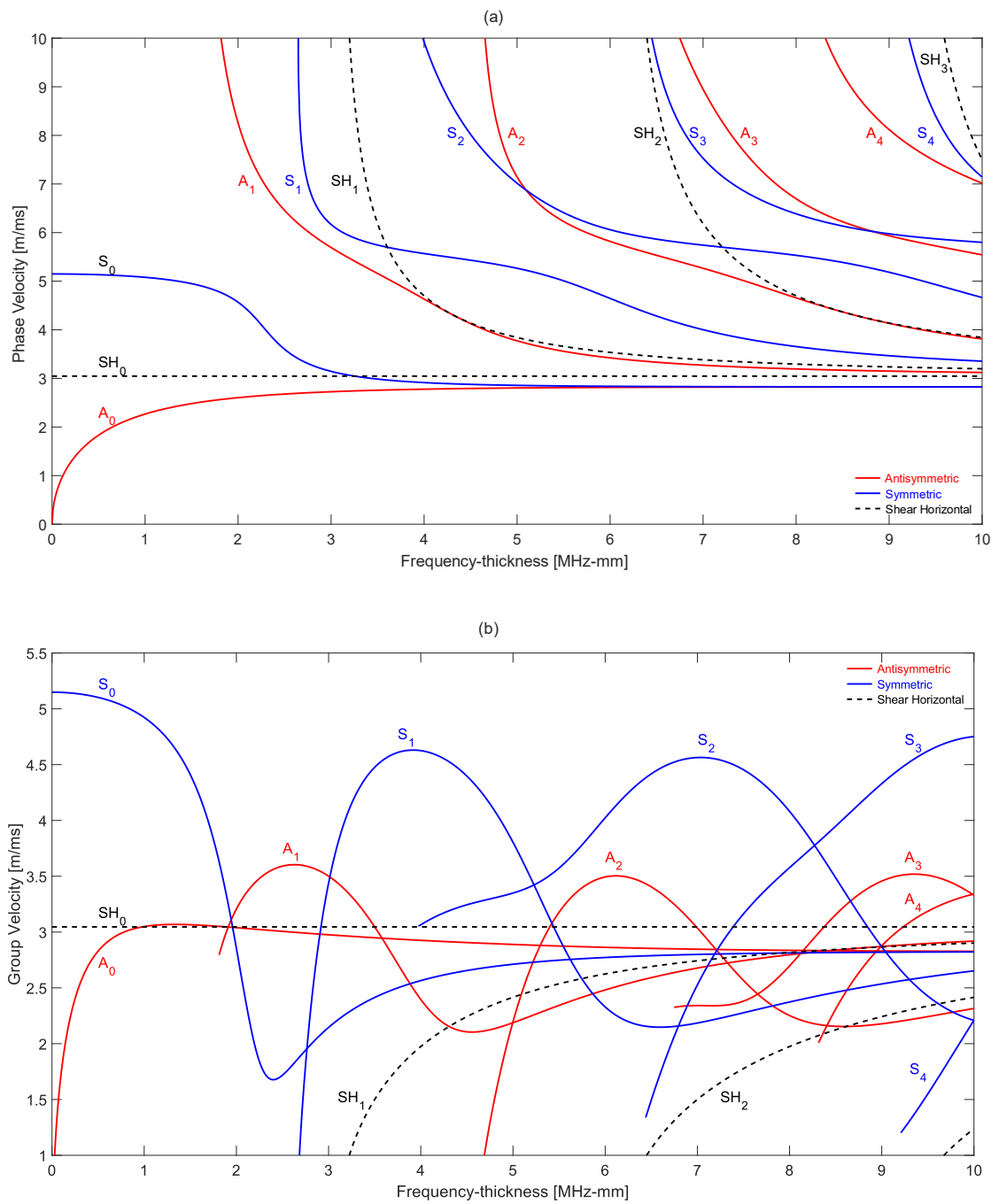
Figure 19: Dispersion plots of a 1.00 mm steel plate in free space – (a) phase velocity dispersion plot, & (b) group velocity dispersion plot.

To show the effect of dispersion, Dispersion Calculator [89] was used to simulate the signal of the fundamental symmetric, anti-symmetric, and shear horizontal modes after 200.00 mm propagation on 1.00 mm 304 stainless steel plate from a 5 cycle Hann windowed 1.50 MHz excitation signal, with results shown in Figure 20. It can be seen that there is a large amount of dispersion in the symmetrical wave mode, while there is little in the anti-symmetric mode and none in shear horizontal mode. This result is mirrored in the group velocity denoted for these modes in Figure 19 where the larger the gradient of change in the group velocity corresponds to a larger dispersion effect.
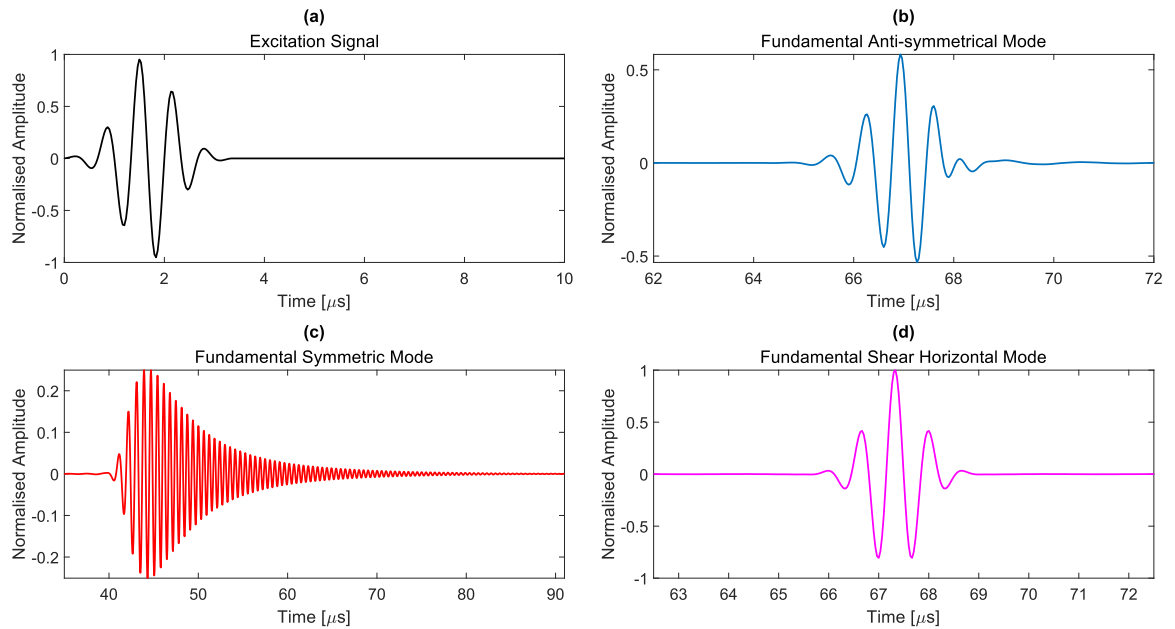
Figure 20: Illustrations of the dispersion effect. (a) 1.50 MHz 5-cycle Hann windowed excitation signal, (b) Fundamental anti-symmetric mode after 200.00 mm of propagation in 1.00 mm steel plate, (c) Fundamental symmetric mode after 200.00 mm of propagation in 1.00 mm steel plate, & (d) Fundamental shear horizontal mode after 200.00 mm of propagation in 1.00 mm steel plate.

As alluded to earlier, most practical guided wave systems tend to use modes with little or no dispersion to make signal interpretation easier [90]. With that said, dispersion effects can be compensated for as the underlying physics is well understood [91]. Many guided wave systems now exist including evaluating pipeline corrosion [92], the quality of adhesive bonds [93], and tomographic inspection [94]–[96].

2.2.2.4.   Mode Shapes

Mode shapes of guided waves are the distributions of the wave field quantities, such as displacements, stresses, or power flow, over the cross section of the waveguide itself. The displacement mode shape is by far the most common field variable that is used, as it allows classification of the guided wave, and insights into suitable transduction techniques to generate the wave mode under consideration.

The displacement mode shapes of the fundamental symmetric, anti-symmetric, and shear horizontal wave modes at 0.50 MHz for a 1.00 mm 304 stainless steel plate are shown in Figure 21. The displacement mode shapes are obtained from Eq. 48-Eq. 51 for Lamb waves and Eq. 63 for shear horizontal waves. It is observed that the fundamental anti-symmetric mode is dominated by out-of-plane displacement in the x_2 direction with a low amount of in-plane displacement in the x_1 direction. In contrast to this, the fundamental symmetric mode is dominated by in-plane displacement in the x_1 direction, while the fundamental shear horizontal mode is dominated by in-plane displacement in the x_3 direction. It is also important to note that the mode shape of a guided wave may vary with frequency. An example of this is observed in the fundamental symmetric mode where the in-plane displacement in the x_1 direction becomes more confined to the outer surfaces as the frequency is increased and eventually acts like a Rayleigh wave [97].

Furthermore, the stress mode shapes are also important to consider with respect to NDE applications, where high stress concentrations in the cross-section give a good indication of sensitivity to defects in that region [98]–[101]. Exact sensitivities of different wave modes to different defects can be determined through either experiments or simulation. Figure 22 shows the stress mode shapes of waves propagating in a 1.00 mm 304 stainless steel plate in free space at 0.50 MHz. It is observed that the fundamental anti-symmetric mode has two significant stress components in the $\sigma_{x_1 x_1}$ axial stress, and $\sigma_{x_2 x_1}$ shear stress. It can also be seen that the fundamental symmetric mode is dominated by the $\sigma_{x_1 x_1}$ along the propagation direction and that the fundamental shear horizonal wave mode is dominated by $\sigma_{x_3 x_1}$ shear stress component. The differing signs associated

with the stresses indicate that they are in compression or tension for negative and positive stresses respectively.
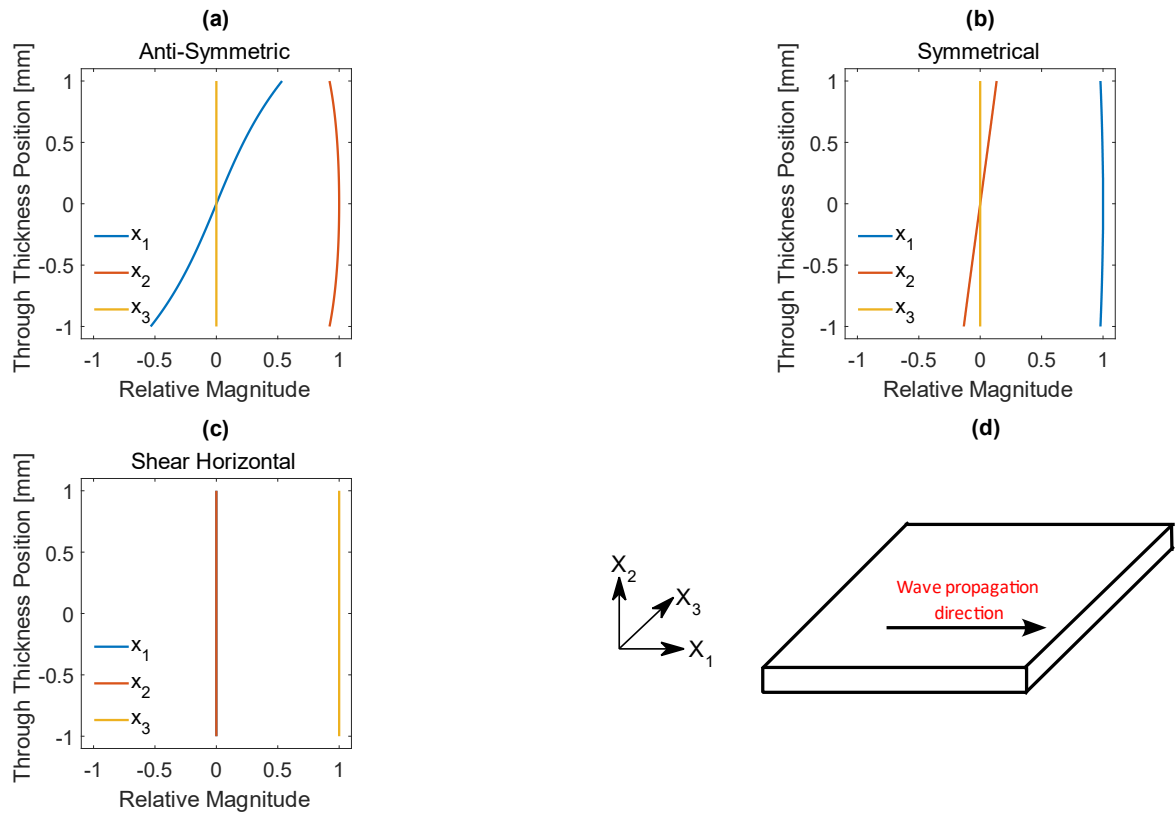
Figure 21: Displacement mode shapes of the fundamental wave modes at 0.50 MHz in a 1.00 mm steel plate – (a) displacement mode shape of the fundamental anti-symmetric mode, (b) displacement mode shape of the fundamental symmetric mode, (c) displacement mode shape of the fundamental shear horizontal mode, & (d) schematic of the steel plate with illustrated co-ordinate system.
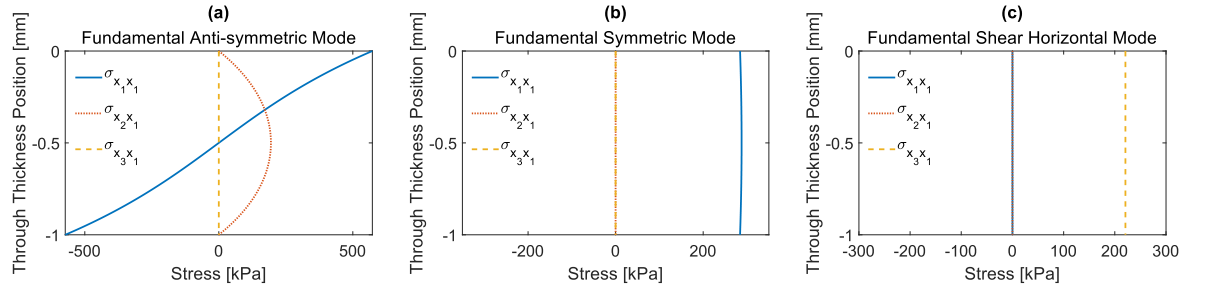
Figure 22: Stress mode shapes of the fundamental anti-symmetric, symmetric, and shear horizontal wave modes at 0.50 MHz is a 1.00 mm thick plate.

2.2.2.5.   Attenuation of guided waves

Attenuation of guided waves, is for the most part, accurately described with the same models and theory associated with bulk waves as given in Section 2.2.1.2. Like with bulk waves, a perfectly elastic system in a vacuum will experience zero attenuation. Attenuation models have been developed to cover two different scenarios: 1) materials that have their damping defined in their viscoelastic material properties [102], [103]; and 2) multi-layered structures that radiate/leak energy from one medium to another [104], [105]. Both of these scenarios can be described through an exponential decay of the wave amplitude as it propagates. This exponential decay is typically described through a complex wave number as is shown in Eq. 73, where the real component corresponds to the wavenumber of the propagating wave ($k' = 2\pi/\lambda$) and the imaginary part corresponds to the attenuation in Nepers per meter.

$$\boldsymbol{k} = \boldsymbol{k}' + i\boldsymbol{k}'', \boldsymbol{i} = \sqrt{-1} \qquad \text{Eq. 73}$$

From the introduction of the complex wave number, the general one dimensional wave equation can be expanded and allow for the separation of the harmonic propagation and the exponential decay to be clearly shown in Eq. 74.

$$u = Ae^{i(kx-\omega t)} = Ae^{ik'x-\omega t}e^{-k''x}$$

Eq. 74

In order to model materials that have damping present, it is common to define a complex 4th order stiffness tensor as is given in Eq. 75, where the subscript refer to the components that comprise the overall vector. Materials that exhibit large damping are carbon or glass fibre reinforced plastics.

$$C^*_{ijkl} = C'_{ijkl} - iC''_{ijkl}, \qquad i = \sqrt{-1}$$

Eq. 75

The aforementioned hysteretic and Kelvin-Voigt models summarised in Section 2.2.1.2 can also be used to accurately describe attenuation losses due to damping in guided waves. However, these models rely entirely on the viscoelastic definition of the materials stiffness vector and neglect any leakage of guided waves in layered structures [106]–[108]. A waveguide immersed with in a layered structured can experience attenuation in the form of leakage, as energy from the guided wave is transmitted across the interfaces into the surrounding medium. This phenomenon is graphically illustrated in Figure 23, and Snell's law can be used to define the angle of leakage as in Eq. 76.

$$\theta_{leak} = \sin^{-1}\left(\frac{V_m}{V_{ph}}\right)$$

Eq. 76

V_m is the bulk velocity of the surrounding material, and V_{ph} is the phase velocity of the guided wave. It can be seen that the leakage angle becomes imaginary if the phase velocity is smaller than the bulk velocity of the surrounding medium. Due to the leakage angle becoming non-real it is rendered physically meaningless and represents a non-leaky guided wave in a layered structure. It can be said that a guided wave in a layered structure

will not leak if its phase velocity is less than the bulk velocity of the surrounding material. Additionally, if the waveguide is undamped, the guided wave will propagate with zero attenuation, and the term 'non-leaky' can be used to describe such a mode.
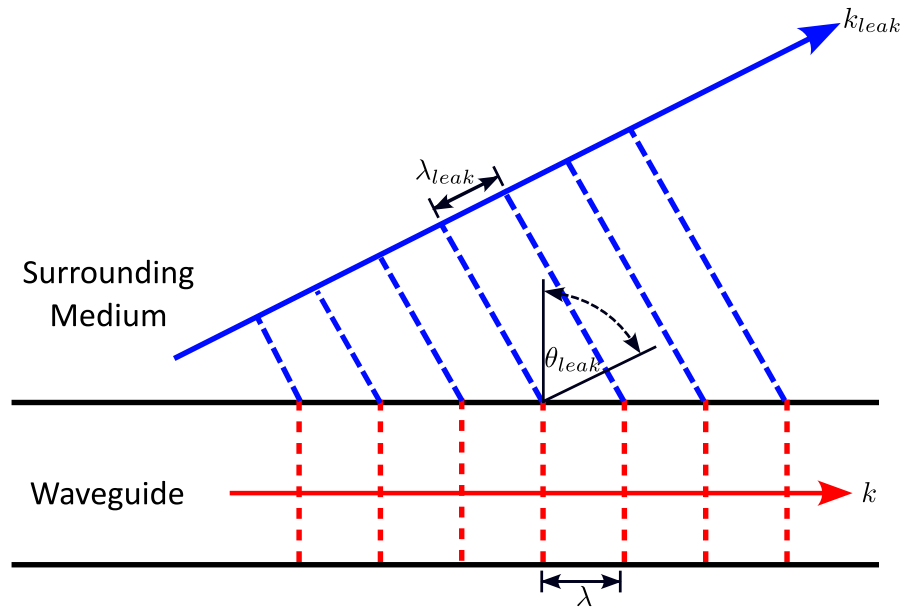
Figure 23: Illustration of the energy leakage associated with guided wave propagation in layered structures.

2.2.3.   Feature guided waves

Guided waves are predominantly defined by the geometry of the overall structure and as such it is common to represent their dispersion properties as a function of frequency thickness – see Figure 19. However, if the cross-sectional topology changes sharply around a structural feature (i.e. a stiffener or weld), an energy trapping effect is observed, in which a guided wave propagates only along the structural feature itself. These structural features act as local waveguides and confine the guided wave energy within them, making them useful for inspecting these structural features. This subsection of guided waves are referred to as Feature Guided Waves (FGWs) and were first observed via experimentation on fusion welds [109], [110]. The initial work exploited a compressional longitudinal mode and showed that FGWs maintain their energy confinement enabling longer

inspection of their structural feature when compared to comparable guided waves in their flat plate counterparts. Following on from the initial discovery, a shear type wave mode was also found to be confined within the same fusion weld geometry, and had the additional benefits of being non-leaky and almost non-dispersive in nature [111]. [112]. This phenomenon can be explained due to the change in geometry of the local feature, creating guided wave modes that possess similar mode shapes but different phase velocities to that of the adjacent structure, due to the total internal reflection of the wave as it propagates along the feature [62]. An illustration of this effect is provided in Figure 24. Details of what feature guided waves exist is a structure are calculated by the Semi-Analytical Finite Element (SAFE) method and this is covered in Section 2.2.3.1.
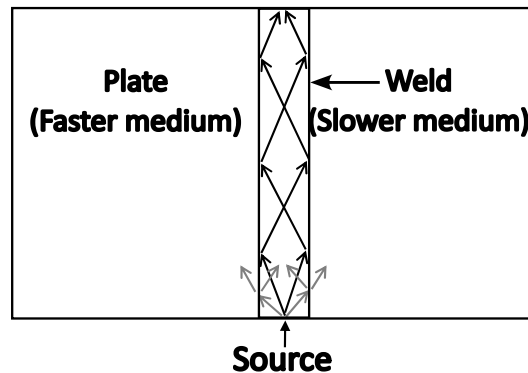
Figure 24: Illustration of the energy trapping effect cause by the total internal reflection due to the difference in phase velocities between the structural feature and surrounding plate [111].

FGWs have been demonstrated to exist in many structures including fusion welds [111], [113]–[115], bends [116]–[118], seal fins [119] and stiffeners [112]. For the purpose of this overview, a fusion weld will be used to demonstrate the fundamental concepts associated with FGWs. Fan & Lowe [113] initially discovered four fundamental mode shape categories (flexural, torsional, longitudinal, & shear horizontal) for a fusion

weld and these are shown in Figure 25. Like conventional guided waves, the fundamental FGWs were classified by their vibrational pattern shown in their displacement mode shape. It can be seen that the mode shapes of the weld guided longitudinal, flexural, and shear horizontal modes are similar to the fundamental symmetric, anti-symmetric, and shear horizontal wave modes found in a flat plate. While the reported torsional wave mode has no flat plate counterpart and is more akin to axial pipe guided wave modes.
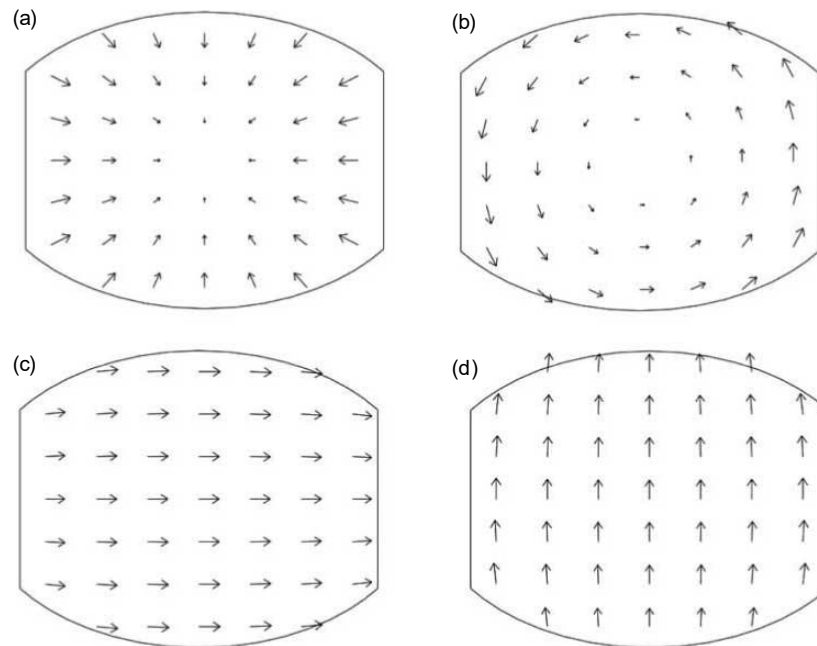
Figure 25: Modes shapes of the fundamental weld guided modes at 100.00 kHz: (a) longitudinal mode, (b) torsional mode, (c) shear horizontal mode, and (d) flexural mode where arrows represent the displacement vector observed in the cross-section [111].

Figure 26 shows the dispersion curves for the fundamental weld guided modes contrasted with the fundamental guided wave modes for a 6.00 mm thick steel plate denoted by dashed lines. It is observed that the fundamental shear horizontal and longitudinal weld guided modes propagate at a slower speed compared to the fundamental

shear horizontal and symmetric flat plate wave modes, respectively. They are therefore trapped within the weld and exhibit very low attenuation as they are non-leaky. Conversely, the fundamental flexural wave mode has a higher phase velocity than the fundamental anti-symmetric flat plate wave mode, and therefore is not trapped and represents a leaky wave mode.
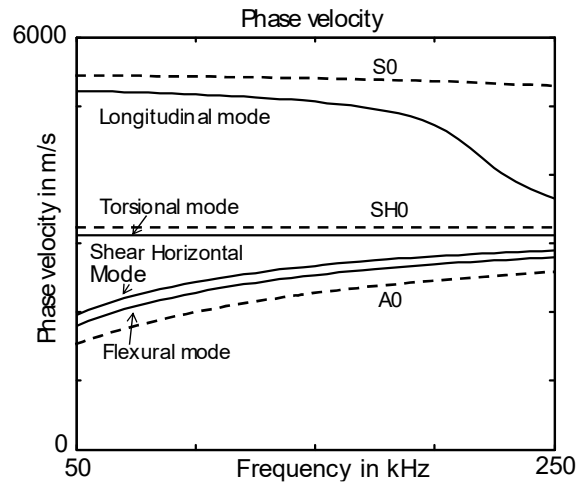
Figure 26: Phase velocity dispersion curves for fundamental fusion weld guided waves modes for a 6.00 mm thick steel plate [111].

FGWs are highly attractive for quick timely inspection of defects in and around key structural features over long distances, as their associated energy trapping effect allows for long wave propagation than is typically associated with conventional plate guided waves. Niche applications for guided waves exist and range from thickness mapping [120] to guided wave tomography [94], [95] and from focused guided waves [121], [122] to surface wave inspection [123]–[125]. However, guided wave testing in general is deployed primarily as a screening tool to locate defective regions [90] and this restriction also applies to FGWs. While novel techniques have been developed to increase the type and size of defects that can be detected [115], screening of key structural features remains the primary goal of FGW testing. In the context on the in-situ inspection challenge as outlined in Chapter 1, it is clear that a FGW on the RSW would provide a great benefit

and allow for full circumferential screening on the weld and identify any potential defective canisters for repackaging and containment.

2.2.3.1.   Semi-analytical finite element method

In order to understand the dispersive multi-modal nature of waveguides it is essential that modal studies are performed. Proper understanding of these factors allows for suitable wave modes, operational frequencies, and transduction techniques to be selected. For simplistic waveguides such as a plate or a cylinder, analytical solutions that describe their dispersion characteristics exist. For waveguides with irregular cross-sections, analytical solutions bespoke to that geometry need to be developed and this is often a prohibitively complex exercise to perform. To overcome this difficulty, numerical methods have been developed that can be applied to both simple and complex irregular cross-sections. One such method is the Semi-Analytical Finite Element (SAFE) method which was originally developed in the 1970s [126], [127]. It has since gained increasing popularity as the technique is applied to more complex and industrially relevant problems. The SAFE method has been used to develop inspection techniques for railway tracks [128], [129], beams [130], stiffeners [131], as well as damped leaky irregular waveguides [132], [133].

The SAFE method solves the quadratic eigenvalue problem [134] of a solid with a constant arbitrary cross-section and assumes a harmonic oscillation along the direction of propagation. As a result, the SAFE method only requires the discretisation of the 2D cross-section while still providing three displacement components. Castaings and Lowe [133] developed the SAFE method to incorporate leaky guided waves along an elastic waveguide with an arbitrary cross-section radiating into a solid of infinite extent.
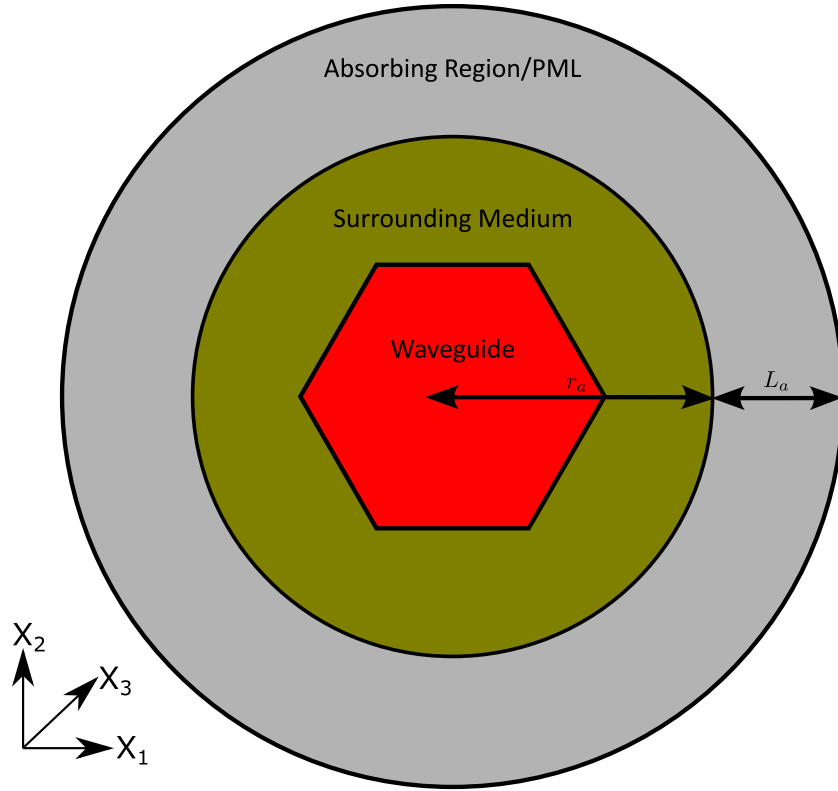
Figure 27: Schematic of a 2D SAFE model of waveguide immersed in an infinite surrounding medium and absorbing or perfectly matched layers (PML)

By considering a wave propagating in a solid waveguide of constant cross-section that does not vary along its length, as shown in Figure 27, the mathematics behind the SAFE method can be understood. The harmonic displacement within the waveguide is given by Eq. 77

$$u_i(x_1, x_2, x_3, t) = U_i(x_1, x_2)e^{I(kx_3 - \omega t)}, \qquad I = \sqrt{-1} \qquad \text{Eq. 77}$$

Where k is the complex wavenumber, $\omega = 2\pi f$ is the angular frequency, U_i is the initial displacement, t denotes time, and the $i = 1, 2, 3$ subscript denotes the

coordinate index as illustrated in Figure 27. For a general material, the equation of dynamic equilibrium is given by Eq. 78.

$$\sum_{i,j,k=1}^{3} \left[C_{ijkl} \frac{\partial^2 u_j}{\partial x_k \partial x_l} \right] + \rho \omega^2 u_i = 0, \qquad i = 1,2,3$$

Eq. 78

Where C_{ijkl} is the stiffness tensor and ρ is the density. By substitution of Eq. 77 into Eq. 78, the quadratic eigenvalue problem can be stated in Eq. 79.

$$C_{ijkl} \frac{\partial^2 U_j}{\partial x_k \partial x_l} + I \left(C_{i3jk} + C_{ikj3} \right) \frac{\partial (k U_j)}{\partial x_k} - k C_{i3j3} \left(k U_j \right) + \rho \omega^2 \delta_{ij} U_i = 0$$

Eq. 79

Where δ_{sr} is the Kronecker delta (when $s = r, \delta_{sr} = 1 \ otherwise \ \delta_{sr} = 0$) and with summation over the indices $j = 1, 2, 3$ and $k, = 1, 2$. This equation can be solved by various means, but the simplest solution is to make use of commercial FE solvers [135]. In order to do so the input formalisation must be in the form stated in Eq. 80.

$$\nabla \cdot \left(c \nabla \tilde{U} + \alpha \tilde{U} - \gamma \right) - \beta \nabla \tilde{U} - \alpha \tilde{U} + \lambda d_a \tilde{U} - \lambda^2 e_a \tilde{U} = 0$$

Eq. 80

In Eq. 80 all matrix coefficients can be complex valued, and $\hat{U} = (U_1, U_2, U_3, V_1, V_2, V_3)$ represent the set of variables to be solved for, with $V_i = k U_j$. The complete implementation is given by Predoi *et al.* and Zuo *et al.* [136], [137], as well as being summarised in Appendix A.

To describe the infinite surrounding material immersing the waveguide, absorbing regions or Perfectly Matched Layers (PMLs) are used to limit the computation domain.

Both techniques have been applied throughout literature with PMLs showing an increase in computational efficiency [133], [137].

For the case where an absorbing region is used, the viscoelasticity of the stiffness matrix increases with length whilst maintaining the same mass density and elastic properties as the medium in which it is attached to. This is described mathematically in Eq. 81.

$$C_{ija} = C'_{ij}\left[1 + I\alpha\left(\frac{(r - r_a)}{L_a}\right)^3\right] + IC''_{ij}, \qquad I = \sqrt{-1}$$

<div align="right">Eq. 81</div>

Where C_{ija} is the stiffness tensor of the absorbing region itself, C'_{ij} is the stiffness of the medium the absorbing region is attached to, C''_{ij} is the viscoelasticity of the material that the absorbing region is attached to, r_a is the inner radius of the absorbing region, L_a is the radial length of the absorbing region, r is the radial position within the absorbing region $(r > r_a)$, and α is the coefficient used to define the viscoelasticity at the outer limit of the absorbing region. Typically, the α coefficient must be optimised in order to reduce reflections from the boundaries, while also avoiding sharp changes in acoustic impedance which may also generate additional unwanted reflections [138]. As a rough rule of thumb, for effective absorption, the length of the absorbing region should be 2-3 times the longest wavelength of any radiated wave throughout the entire frequency spectra of the problem under consideration, and α can take on values between 1 and 4 for high and low frequencies, respectively [138].

An alternative approach to absorbing regions are PMLs. In PMLs the acoustic impedance matches perfectly with that of the material is joined to [139], [140]. This allows for almost all propagating waves of non-tangential angles of incidence and non-zero frequencies to be absorbed, due to their similar acoustic impedances. By introducing the

PMLs, the real coordinates of the physical equations are extended into the complex domain allowing standing waves to be absorbed [141].

The aim of SAFE method is to determine propagating waves within the waveguide under consideration. To this effect, the eigenvalue solutions of the SAFE method are the complex wavenumbers with the real elements representing the angular wavenumbers and the imaginary components representing the attenuation coefficients, due to leakage into the surrounding material. The SAFE method is a frequency domain problem, and in order to document the entire dispersive characteristics of each wave present, it is necessary to repeatedly solve the SAFE model over a frequency range of interest.

By solving the SAFE model repeatedly for each frequency, many solutions are generated and thus the need to intelligently examine the solutions arises. An important parameters is exploited: the Poynting vector. Poynting theorem has its origin in electromagnetism and describes the power flow associated with an electromagnetic field [142]. Auld adapted this theory for acoustics and formulated the acoustic Poynting vector which described the power flow density of an acoustic wave [62]. The Poynting vector is a highly useful quantity and can be used for investigating guided wave energy, field normalisation, and excitability [60]. The Poynting vector is a complex value and can be calculated by Eq. 82.

$$\boldsymbol{P} = -\frac{\boldsymbol{v}^*\sigma}{2}$$

Eq. 82

Where $\boldsymbol{v}^*$ is the conjugate of particle velocity vector and σ is the cartesian 3x3 stress tensor. The velocity vector and stress at each nodal location are returned in the SAFE method, therefore calculating the Poynting vector at each nodal position can easily be accomplished prior to solving, generating a power flow distribution over the cross-section of the SAFE problem. In relation to FGWs, it is useful to look at the time averaged power flow in the axial direction of propagation which is given by Eq. 83.

$$P_{x_3} = -Re\left[\left(\frac{I\omega}{2}\right)(U_1^*\sigma_{31} + U_2^*\sigma_{32} + U_3^*\sigma_{33})\right] \qquad \text{Eq. 83}$$

where σ_{31}, σ_{32} and σ_{33} are the components of axial stress; U_1^*, U_2^* and U_3^* are the complex conjugates of displacement. To obtain the averaged domain axial power flow, it is necessary to integrate over the domain of interest according to the following, where S denotes the cross-sectional area.

$$\overline{P_{x_3}} = \int_s \frac{\left|P_{x_3}\right| ds}{\int_s ds} \qquad \text{Eq. 84}$$

Suitable FGW modes are identified where the average power flow is higher in the feature of interest than that of the surrounding structure [137]. The power flow ratio that describes this scenario can be calculated by the following formula:

$$\eta = \frac{\overline{P_{x_3}}_{guide}}{\overline{P_{x_3}}_{total}} \qquad \text{Eq. 85}$$

Another noteworthy difference in problems suited to SAFE modelling is group and energy velocity. As previously stated in Eq. 30, group velocity describes the speed at which a guided wave packet travels at. This definition only applies in undamped waveguides free of attenuation and leakage. In the presence of attenuation and leakage, the energy velocity must be used to describe the speed at which a wave packet travels at. The definition of energy velocity, V_e, is stated in Eq. 86, and it is dependent on the power flow in the wave propagation direction and the energy density of the wavefield [60].

$$V_e = \frac{\int_\Omega \boldsymbol{P}\, \hat{\boldsymbol{x}}_3 d\Omega}{\frac{1}{\mathrm{T}}\int_T (\int_\Omega e_{tot}\, d\Omega)dt} \qquad \text{Eq. 86}$$

Ω denotes the domain of interest, $\hat{\boldsymbol{x}}_3$ is the unit vector in the propagation direction, $\frac{1}{\mathrm{T}}\int_T (.)dt =< (.) >$ is the time average integral over one period, T, $\boldsymbol{P}$ is the real component of the time averaged Poynting vector given by Eq. 82, and e_{tot} is the total energy density of the system which is the sum of the potential and kinetic energy. Eq. 87 & Eq. 88 describe the time averaged kinetic and potential energy components respectively, where C_{ijkl} is the elastic stiffness tensor. Like the Poynting vector, the potential and kinetic energy can be calculated at each nodal point after the SAFE method has been executed, enabling the dispersive energy velocity to be understood for any FGW.

$$< e_k >_t = \frac{\omega^2}{4}\rho \boldsymbol{u}^T \boldsymbol{u} \qquad \text{Eq. 87}$$

$$< e_p >_t = \frac{1}{4}\boldsymbol{\epsilon}^T C_{ijkl}\boldsymbol{\epsilon} \qquad \text{Eq. 88}$$

2.2.4.   Eddy current testing

Eddy current testing is the most widely used of all the electromagnetic NDE techniques [143]. Eddy currents occur when a conducting material is in the presence of a time varying magnetic flux density and sets up its own magnetic flux via an eddy current to oppose the flux that caused them. The secondary magnetic field associated with the eddy current not only opposes the primary magnetic field, but also reduces the range of the primary magnetic field when compared to an undisturbed case. This effect is shown in Figure 28.

Primary magnetic field → induce a voltage to the sample's surface and forming current loops

The defect interrupt the eddy currents flow → lowering the secondary electromagnetic field → Increasing the flux net over the coil

The impedance variation is monitored in eddy current testing

Putting a defect in the sample
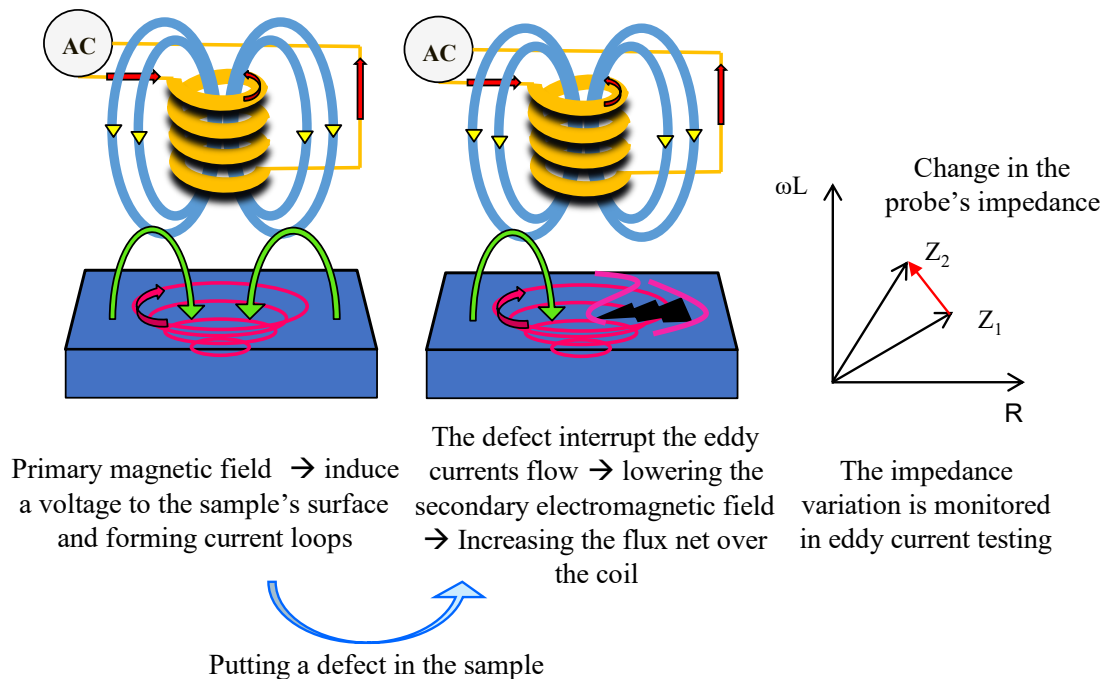
Figure 28: Eddy current generation and detection with and without a defect being present

"Near-field" is the term used to describe the range of the primary magnetic field. However, the electromagnetic perturbation allows for a diffuse electromagnetic wave to also propagate that can allow for interactions with defects that are out with the range of the near-field. This region is known as the remote-field.

Frequency of the excitation signal dictates the skin depth of the eddy current and the resulting sensitivity to defects. There are various eddy current configurations that

interact in the near-field or remote-field and make use of a single-frequency, multi-frequency, or pulsed excitation signal.

In the context of this thesis remote-field testing is ill suited to the inspection problems under consideration given the size of the SNM packages [144]. Again, pulsed eddy current testing is not well suited to the challenges of this thesis as it is typically used on thicker components to infer wall-thickness and is less mature than other eddy current techniques [145]. As a result, single-frequency and multi-frequency excitation near field eddy current testing are only explored in this thesis. Furthermore, eddy current arrays that exploit the near-field have gained traction in recent year, and as a result an overview of array technology is also given. Finally, eddy current testing is non-contact and therefore alleviates the problems associated with coupled techniques and smooth surface finishes in the case of piezoelectric ultrasonic testing.

2.2.4.1.   Electromagnetic Theory

In 1865, James Clerk Maxwell formulated the four underlying equations that describe electromagnetism [146] – Ampére's Law, Faraday's Law, Gauss' Law for electrical charges, and Gauss' Law for magnetic monopoles . In this section these equations are stated in their differential form. Ampére's Law is stated in Eq. 89, where $\boldsymbol{H}$ is the magnetic field, $\boldsymbol{J}$ is the current density, and $\boldsymbol{D}$ is the electrical displacement field:

$$\nabla \times \boldsymbol{H} = \boldsymbol{J} + \frac{\partial \boldsymbol{D}}{\partial t} \qquad \text{Eq. 89}$$

Faraday's law is denoted in Eq. 90, where $\mathbf{E}$ electric field, and $\boldsymbol{B}$ is the magnetic flux density. The electric field is related to the electrical displacement field by two constitutive equations: 1) $\boldsymbol{D} = \epsilon\boldsymbol{E}$, where ϵ is the electrical permittivity; & 2) $\boldsymbol{J} = \sigma\boldsymbol{E}$ where σ is the electrical conductivity. Likewise, the magnetic flux density is related to the magnetic field via $\boldsymbol{B} = \mu\boldsymbol{H}$ for conductive materials, where μ is the magnetic permeability, which in turn is the product of the material's relative magnetic permeability, μ_r, and the magnetic permeability of free space, μ_0.

$$\nabla \times \boldsymbol{E} = -\frac{\partial \boldsymbol{B}}{\partial t} \qquad \text{Eq. 90}$$

Gauss' law for electrical charges is given in Eq. 91 where q is the electric charge density.

$$\nabla . \mathbf{D} = q \qquad \text{Eq. 91}$$

Finally, Gauss' law for magnetic monopoles is stated in Eq. 92.

$$\nabla \cdot \mathbf{B} = 0 \qquad\qquad \text{Eq. 92}$$

Faraday's law states that a time varying magnetic field will always be accompanied by a non-conservative spatially varying electric field, and vice versa. It also states that a changing magnetic field will induce an electrical current in a nearby conductor which is referred to as an "eddy current". The direction of the current flow in the eddy current is such that its corresponding magnetic field will act to oppose the changing magnetic field that produced it according to Lenz's law [147]. From the time derivative within Faraday's law, it can be seen that the amplitude of the eddy current is proportional the rate of change of flux, hence electromagnetic induction becomes increasingly effective as the frequency of the field is increased.

Typically, sinusoidal time varying currents are used in practical set ups, and thus it is useful to consider the time-harmonic solution of Maxwell's equations to gain further insight into electromagnetic wave propagation. Complex notation can be used to describe the time varying electrical and magnetic fields, $\mathbf{E} = \boldsymbol{E}_0 e^{i\omega t}$ & $\mathbf{H} = \mathbf{H}_0 e^{i\omega t}$, where ω is the angular frequency and complex amplitude of $\boldsymbol{E}_0$ & $\boldsymbol{H}_0$, respectively. Substitution of these expressions in to Eq. 89 and Eq. 90 yields Eq. 93 & Eq. 94 where $k_e^2 = i\omega\mu(\sigma + i\omega\epsilon)$.

$$(\nabla^2 + k_e^2)\boldsymbol{E} = 0 \qquad\qquad \text{Eq. 93}$$

$$(\nabla^2 + k_e^2)\boldsymbol{H} = 0 \qquad\qquad \text{Eq. 94}$$

For all frequencies relevant to electromagnetic NDE (typically 10.00 kHz-MHz), σ is generally much greater than $\omega\epsilon$, inferring that the electromagnetic wavenumber, k_e, is complex and has both imaginary and real parts of magnitude, $k_e = \sqrt{-i\omega\mu\sigma}$. As a result,

the solutions to Eq. 93 & Eq. 94 for a plane wave propagating into a conductor in the z-direction are given in Eq. 95 & Eq. 96.

$$\mathbf{E} = E_0 e^{k_e x} e^{i(k_e x - \omega t)} \mathbf{e_x} \qquad \text{Eq. 95}$$

$$\mathbf{H} = H_0 e^{k_e x} e^{i(k_e x - \omega t)} \mathbf{e_y} \qquad \text{Eq. 96}$$

These electrical and magnetic field waves propagate orthogonal to one another and are transversely polarised with respect to the propagation direction. From these solutions, it is observed that the amplitude of this wave decays exponentially as it propagates through the conductor. The skin depth can thus be defined and is stated in Eq. 97 where $f = \frac{\omega}{2\pi}$.

$$\delta = \frac{1}{k_e} = \frac{1}{\sqrt{\pi f \mu \sigma}} \qquad \text{Eq. 97}$$

The skin depth describes the distance in the conductor where the amplitude of the propagating wave falls to $\frac{1}{e}$ ($\sim$37%) of its original value. It can be seen that the skin depth is inversely proportional to the square root of σ, μ, and f. The skin depth is therefore much smaller for materials that are highly conductive and magnetically permeable, as these materials allow for larger amplitude eddy currents to be formed, and as a result create a greater flux to oppose the flux that produced them. This is somewhat offset in practice by lowering of the frequency of the excitation flux.

2.2.4.2.   Eddy Current Arrays

One of the biggest enhancements in eddy current technology over the past decade is the development of eddy current arrays [148]. Eddy current arrays allow for increased productivity and enhanced probability of detection for surface inspection. When compared to manual single coil eddy current inspection, staff costs and complexity associated with any scanning fixture present a high economic barrier, which is significantly reduced with eddy current arrays [149]. Other visual surface inspection techniques such as dye penetrant and magnetic particle inspection require development and set up time, disposal of waste, and provide data that can only be displayed through photographic means allowing for subjectivity in operator interpretation.

Eddy current arrays can allow for instantaneous clean inspection of the components surface in a data-rich digital format. The coils can often be flexibly mounted and conform to undulations in the component surface to allow for more accurate results [150], [151]. Moreover, robotic deployment for the eddy current arrays allows for repeatable results with less noise [152] while maintaining the flexibility of being able to program a robot for various inspections of differing components. Furthermore, the probability of detection is enhanced in arrays through the various transmit and receiver pairs that can be deployed.

Figure 29 shows an example eddy current array being with axial and transversal transmit receive combinations. As can be seen in Figure 29 (b) for the axial configuration, coils in the array are excited in one column and reception of the impedance data is performed across the array in the second column. Conversely, the transversal configuration documented in Figure 29 (c) shows coils being excited and reception of the impedance data being performed within the same vertical column of coils.
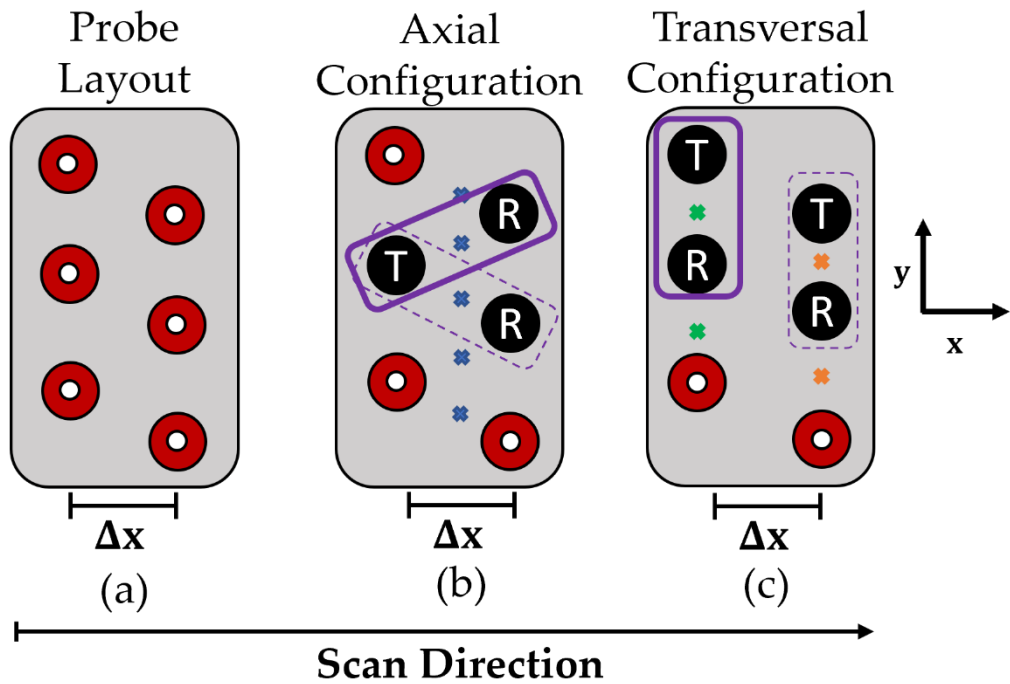
Figure 29: Eddy current array transmit and receive configurations. (a) Generic Eddy current array layout with two vertical columns of coils. (b) Axial transmit and receive configuration where x (in blue) correspond to the transmit/receive pair centres of the excited eddy current channels in the test part. (c) Transversal transmit and receive configuration where x (in green) correspond to the transmit/receive pair centres of the excited eddy currents in the test part resulting from the first/odd column of coils, and where x (in orange) correspond to the transmit/receive pair centres of the excited eddy currents in the test part resulting from the second/even column of coils.

The coil firing sequence is changed between the axial and transversal configurations to achieve greater sensitivity to differing defect orientations. With reference to the coordinate system in Figure 29, a larger change in impedance would be observed for a defect that is aligned with the X-axis for a transversal configuration over that of an axial configuration. This is due to the defect more severely intercepting the eddy current that exists between the two transmit and receive coils in the transversal configuration over that of the axial configuration. This greater compression of the eddy currents caused by the defect presence will have a large effect on the electromagnetic field and by proxy the sensed change in impedance. The opposite can be said to be true for a defect aligned in

the Y-direction. For further reading, Ye *et al.* [153] provide a thorough theoretical and experimental investigation of this phenomenon.

Additionally, Eddy current modelling has lagged ultrasonic modelling, due to the complex mathematics describing the physics of eddy currents testing. As a result, inverting physical characteristics of a component from the impedance data acquired is less mature when compared to ultrasonic testing. Due to increases in computational power, advances in inversion techniques are being made [154], but again in comparison to ultrasound lacks a standardised dataset or protocols such as FMC and the MFMC file format [155] for these techniques to be performed on. Overcoming, these issues is key for further uptake of eddy current array testing, but there is optimism that this will be achieved in the short-medium term.

In the industrial context of this thesis, eddy current array testing is well suited to the ex-situ inspection challenge. The vast majority of eddy current arrays make use of the near-field allowing for the resulting eddy current to saturate thin-walled components such as the resistance seam welds on the legacy canister. As arrays allow for higher scanning rates and greater area coverage, this is also of value as there are a large quantity of canisters already in storage. Finally, the ability to robotically deploy eddy current arrays is well suited to the nuclear industry as exposing staff to unnecessary radioactive doses is desirable when inspecting nuclear assets such as the SNM packages.

2.2.5.   NDE in Welds

The history of NDE in general has been driven by the need to improve quality control on production lines. At first the introduction of NDE was done as a reactionary measure but overtime as techniques have become better understood NDE has been introduced in a proactive manner. The first such example of NDE occurred in Hartford, Connecticut, USA. Following a boiler explosion in March of 1854, the State of Connecticut passed the "Boiler Inspection Law" that mandated annual visual inspections from certified inspectors. This is widely viewed as the first example of NDE in relation to how it is used today [156].

NDE as an industry remained quite primitive, primarily relying on visual and penetrant testing, until the first and second world wars required a step change in quality control for manufactured goods. In the 1920s in the USA, Dr H. H. Lester at Watertown Arsenal [157] began work on radiographic inspection of castings, welds, and armour plate to improve the quality of materials used by the army [158]. At roughly the same time, the first electro-magnetic technique was developed by Dr Elmer Sperry and H. C. Drake to detect discontinuities in railroad tracks [159]. Finally, at the tail end of the 1920's S. Y. Sokolov in Russia, first conducted experiments on cast iron and steel samples in which ultrasonic waves were used to detect for flaws [160]–[163]. These three methods – radiography, electromagnetic, and ultrasonic – would come to dominate NDE and NDE in welds specifically as the technology matured over time.

Radiographic testing makes use of gamma rays or X-rays in the electromagnetic spectrum as they attenuate through the inspection medium, and advances in these techniques have been widely tied to the development of more powerful sources and sophisticated acquisition hardware. Like ultrasonic NDE, the advancements in radiographic NDE is closely tied to advances medical radiographic testing [ref]. Radiographic testing primarily makes use of X-rays produced via cathode ray tube as it is portable proving that there is access to power infrastructure. The limiting factor in radiographic testing was initially the power of the source. In 1912, X-rays sources could

operate up to 100,000 volts [164]. By 1922, the power of these sources had increased to 200,000 volts, and by 1931, General Electric produced a 1,000,000-volt X-ray source allowing for thick steel components to be inspected [165]. At the same time, in 1931, the American Society of Mechanical Engineers (ASME) approved X-ray inspection of fusion welds in pressure vessels. Today, computed tomography X-ray machines, can acquire a full 3D volumetric data of the component under inspection with various standards specific for welding [166], [167]. Radiographic testing tends to be less commonly used to inspect welds due to health and safety concerns, and the associated down time when performing on-plant inspection.

Moreover, eddy current testing has also been used to predominantly inspect the surface of components due to the exponential decay in signal strength from the surface. The theory governing eddy current testing is covered in subsection 2.2.4, and it is highly complex. Due the complexity associated with electromagnetic and eddy current testing, this has limited development of this technique to recent times. While portable ultrasonic flaw detectors were available in the 1960s, equivalent eddy current kit was not available till the late 1980s. Much of the modern developments can be attributed to Dr Friedreich Foerster, who developed the impedance plane display and formulated the Law of Similarity [159]. The impedance plane display especially aided the adoption of eddy current testing as it allowed for a standardised display of complex eddy current signals for the first time. Inverting out physical features from eddy current signals is an active area of research and eddy current arrays are increasingly being commercialised. Various standards for eddy current inspection of welds now exist [39], [168].

Finally, ultrasonic NDE of welds is the most commonly used NDE method today due to its ability to screen the entire internal volume and lack of health and safety concerns. A lot of ultrasonic NDE has its roots from sonar applications where various militaries around the world made use of differing technique to maps the battlefield effectively. In the 1940s an ultrasonic Pulse-echo system was developed in the UK by D. O. Sproule [169] while a pitch-catch system was developed in the USA by F. Firestone [169]. From these initial single element demonstrations, rapid increase of use followed in the welding,

aerospace and foundry industries. The following research centred on accurate defect sizing. C. Abrahams established the -6dB or -20dB drop method to identify the longitudinal and vertical extents of reflectors [159]. Krautkramer in Germany developed the distance gain amplitude system to compare reflector amplitudes at different depths [170]. While in the USA, a similar approach was developed called the Distance Amplitude Correction (DAC) [171]. These two approaches enabled reproducible reporting of ultrasonic inspection. In 1977, Silk developed the Time-of-Flight Diffraction (TOFD) technique to display the top and bottom edges of defects to allow for more accurate sizing [172]. In the 1980s, the first industrial ultrasonic phased array transducer was developed which allowed for beams to be focused and steered. It also enabled a huge amount of data to be gathered and display in various formats. The theory underpinning ultrasonic wave propagation along with the benefits of phased array transducers is covered in subsection 2.2.1. Today, TOFD and phased array inspection are by far in a way the most common ways to inspect welded components, and various different standards exist on how to use these techniques appropriately [36]–[38], [173].

2.3. Summary

This literature review has explored the welding techniques that form the overall desired structures to be inspected in line with the industrial challenges faces by Sellafield in the storage of their SNM packages. Currently, there are areas for improvement in their approach to determining the weld quality in their current legacy design as well as their inspection approach being undefined for the canister of the future.

For the in-situ inspection challenge severe accessibility challenges limit the problem scope and thus techniques that provide inspection of inaccessibly. Guided waves were therefore a key focus due to their ability to provide large coverage from a single excitation point. During the literature review, Feature Guided Waves (FGWs) were found to be an ideal candidate for screening of the RSW while in-situ and were down selected for further study and examination.

For the ex-situ inspection challenge, accessibility issues were not present so other NDE methods were considered. The thin thickness of the RSW and canister body was a deterrent to using conventional ultrasound and therefore surface inspection modalities were considered. It was found that eddy current technology allowed for inspection of the RSW and potentially the canister body as the eddy currents themselves could saturate the thin canisters.

For the canister of the future inspection challenge, thicker walls are envisaged opening up the potential of conventional bulk wave ultrasonic inspection. An opportunity was identified to bring the inspection process to the point of manufacture to create an NDE digital twin from the point of construction to the end of its design life.

This chapter has highlighted the potential for several techniques to be used to address the SNM package weld inspection problems faced by Sellafield. These techniques are explored in detail in the following chapters.

Chapter 3

In-situ inspection using feature guided waves

As demonstrated from the literature review in the previous chapter, it is clear that exploitation of a FGW in the RSW of the legacy SNM package would be highly beneficial to ensure the structural health of the RSW joint and expand coverage to the entire circumference of the weld in-situ. Additionally, it was demonstrated that the theory behind FGW discovery and exploitation is complex, and care must be taken to ensure that the theory is applied in the correct manner. This chapter is therefore sectioned in to two where the first replicates previously published work covering modal and time step FE simulations of a fusion weld. Through this literature replication confidence was gained in deploying the theoretically complex SAFE method, and further adaptation to the RSW along with subsequent experimentation was de-risked.

The second section explores adapting the SAFE method, FE simulations, and experimentation to the RSW used in the legacy SNM canister design. The SAFE method revealed four suitable wave modes. An anti-symmetric flexural RSW guided mode was down-selected due to its ease of excitation, intense energy concentration around the RSW, low dispersion and attenuation. Simulations and experimental tests were conducted on transversal defects reported in the literature to be the most common and detrimental to overall structural integrity. Three-dimensional FE simulations were conducted to explore the sensitivity of the flexural FGW to transversal cracks of differing dimensions. Experimental results on simplified and realistic geometries to transversal crack defects of ≥ 1.00 mm deep show the efficacy of using this method to efficiently screen nuclear canister RSW joints for such defects in-situ.

3.1. Literature replication

One of the most recent publications in the study of FGWs was done be Yu *et al.* [115]. In this work, the widely exploited shear horizontal FGW associated with a fusion weld was expanded upon and made use of higher order FGW shear modes at a frequency of 500kHz in combination with a novel signal processing technique. The SAFE method and time step finite element analysis was carried out to document the dispersive nature of the weld guided shear horizontal waves and their reflection coefficients to certain defects. It was found that the SH_1 and SH_3 weld guided waves modes had reflection coefficients of 9.99% and 7.41% respectively. The SH_1 wave mode was selected for experimentation due to its' higher reflection coefficient. The novel signal processing technique superimposed different signals at multiple locations to significantly increase the reflection of the SH_1 wave mode. The larger reflection allowed the detectable defect size to drastically decrease.

Operating at high frequencies presents two challenges when it comes to guided waves and FGWs in particular. For guided waves in general, working at higher frequencies induces many modes in the waveguide. As a result, the received signals are complex to interpret, and thus a need to deploy niche signal processing techniques arises. The signal processing technique deployed by Yu *et al.* [115] makes use of a laser Doppler vibrometer to collect the received signals. Given the tight space constraints for the envisaged for deployment at Sellafield, the use of a laser Doppler vibrometer is not feasible. Therefore the signal processing technique used by Yu *et al.* [115] cannot be leveraged in our study.

For FGWs, a higher number of solutions are generated by the SAFE method when operating at high frequencies, and care must be taken in identifying and classifying wave modes correctly. This latter point is of importance in relation to performing the SAFE method on the RSW geometry used at Sellafield, as proper mode identification and classification is key for accurate experimentation.

Additionally, the work performed by Yu *et al.* [115] explored the reflectivity of certain modes to a 2 mm deep 5mm wide transverse crack positioned 500 mm axially away from the source on the top surface of the weld via computational three-dimensional explicit finite element (FE) simulations. Several displacement monitors on the weld allowed for a 2D-FFT to be performed [174] and enabled the calculation of reflection coefficients for various defects. It was shown that at 500.00 kHz the weld guided SH_1 and SH_3 modes had reflection coefficients of 9.96% and 7.41% respectively. Following on from this, the SH_1 weld guided mode with its greater interaction with defects, was exploited in the novel signal processing technique. In the context of the in-situ inspection problem faced at Sellafield, performing a similar reflectivity study is of benefit to document the response from differing defects prior to experimentation.

For the in-situ inspection challenge, accurate SAFE results for correct mode selection and understanding of wave mode sensitivity to various defect geometries are similarly important. Thus, the SAFE and FE results documented by Yu et al. [108] were initially replicated prior to adapting the work for a RSW.

3.1.1.   Modal analysis of the fusion weld using SAFE approaches

3.1.1.1.   SAFE modelling

To predict what FGWs are present with in a fusion weld waveguide, the SAFE method was applied. The fusion weld waveguide with a height of 13.46 mm in the centre and width of 17.20 mm is shown in Figure 30. It is acknowledged that this example is significantly thicker than the geometry of the legacy canister design., however, it still represents a useful case to document prior to exploring FGWs in the legacy canister RSW.
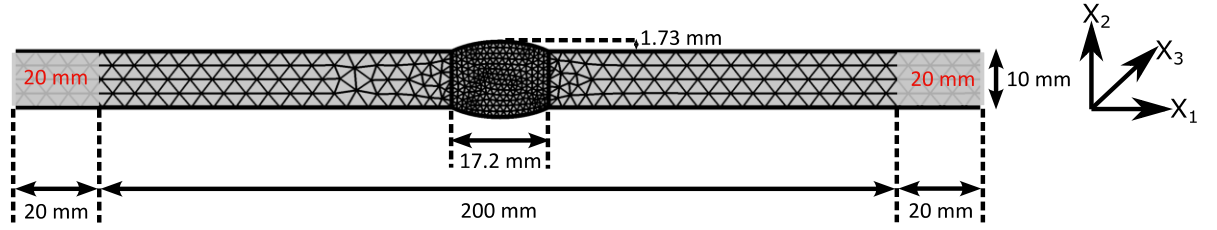
Figure 30: Schematic of the fusion weld model complete with PML regions

A PML region of 20.00 mm was used in order to absorb leaking plate waves and to subdue any radiative modes. The PML was defined via a continuous parabolic function as shown in Eq. 98, where $\widehat{\gamma_1} = 3 + 12i$ is the absorption rate of the PML; d_{x1} is the interface between the weld side plates and PML regions; and L_{pml} is the length of the PML region.

$$\gamma_1(x_1) = \begin{cases} 1 & , \quad \text{if } |x_1| \le d_{x1} \\ 1 + \widehat{\gamma_1}\left(\dfrac{|x_1| - dx_1}{L_{pml}}\right)^2 & , \quad \text{if } |x_1| \ge d_{x1} \end{cases} \qquad \text{Eq. 98}$$

The domain was meshed with 1600 quadratic triangular Lagrangian elements with local refinement around the weld region. Moreover, the model was solved from a minimum frequency of 50.00 kHz to a maximum frequency of 1.00 MHz in steps of 10.00 kHz with the following elastic constants being employed: $\rho = 7932.00 \frac{kg}{m^3}$, $E = 216.92 \, GPa$, $G = 84.3 \, GPa$ [109], [115]. The SAFE method was implemented on the commercial FE package, COMSOL [175] using the guidelines by Zuo *et. al* [137].

3.1.1.2.   Identification and categorisation of SAFE solutions

Through the SAFE method numerous complex wavenumber solutions were produced, and the need to classify what wave mode family they belong to arose.

According to Eq. 83, the time averaged power flow in the axial direction (i.e. the acoustic Poynting vector in the wave propagation direction) for every solution was calculated at each nodal position of the mesh. This can be used in combination with Eq. 84 to calculate the average power flow over the entire waveguide and the fusion weld feature within the same waveguide. With the axial power flow for the entire waveguide and the fusion weld feature calculated, it was then possible to filter modes by the ratio of the two as defined by Eq. 99. A weld guided solution was identified when a peak in this power flow ratio was observed, as it demonstrates that the wave energy is significantly higher in the weld than the surrounding plates.

$$\eta = \frac{\overline{P_{x_3\,guide}}}{\overline{P_{x_3\,total}}} \qquad\qquad \text{Eq. 99}$$

Upon filtering, various weld guided modes were identified. Figure 31 shows contour plots of the axial power flow and displacement mode shapes of various identified weld guided modes. As is evident, different wave modes have differing energy concentration effects in both the weld and Heat Affected Zone (HAZ). It is clear that different modes with their unique energy concentration effects would be useful to interrogate and screen differing parts of the weld and HAZ. To classify these wave modes and give insights into relevant transduction techniques, the displacement mode shapes were used. Shown in Figure 31 is the displacement mode shapes characterised by the orthogonal displacement components along the centre line in the x_2 direction. Figure 31 (a) shows a mode that is dominated by displacement in the x_1 direction and was denoted as a shear horizontal weld guided mode (SH-type). Additionally, Figure 31 (b) shows a wave mode that is dominated by displacement in the x_2 direction and was denoted as a flexural weld guided mode (F-type). Moreover, Figure 31 (c) shows a wave mode that is dominated by displacement in the x_1 direction but is rotational in nature so was deemed the torsional weld guided mode (T-type). Finally, Figure 31 (d) shows a mode shape that is dominated by displacement in the x_3 direction and was termed as the longitudinal weld guided mode (L-type).
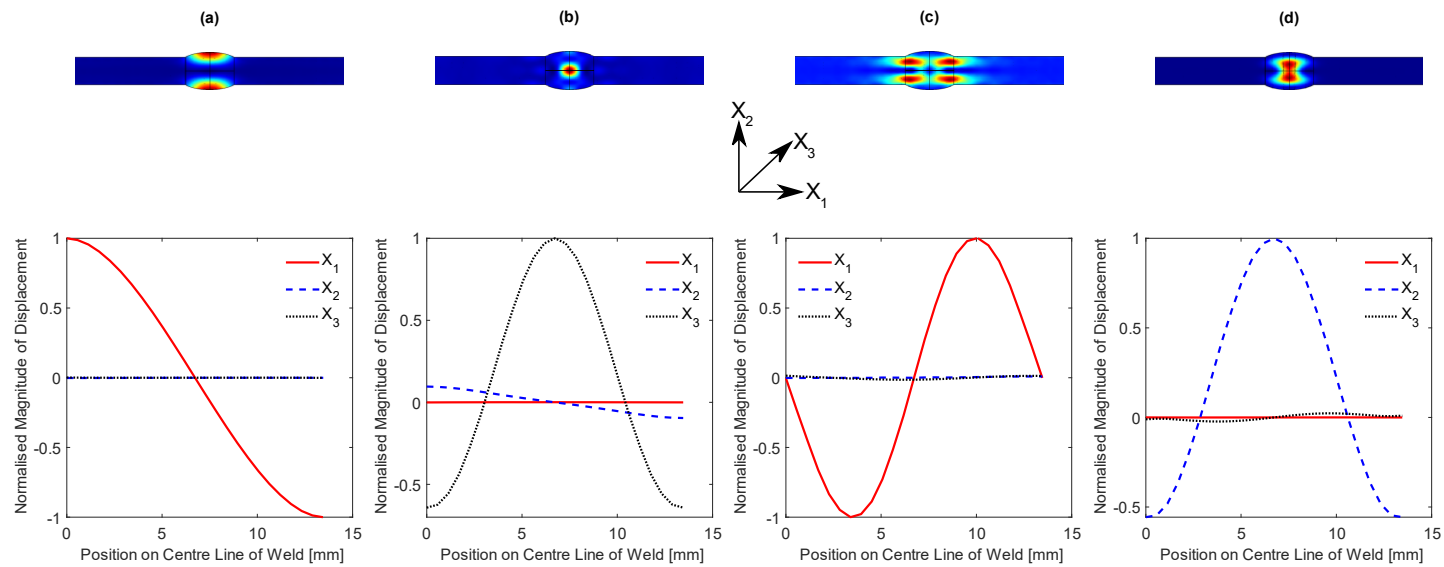
Figure 31: Axial power flow contour plots and displacement mode shapes for various weld guided modes: (a) Shear horizontal weld guided mode at 400.00 kHz, (b) Longitudinal weld guided mode at 320.00 kHz, (c) Torsional welded guided mode at 380.00 kHz, & (d) Flexural weld guided mode at 410.00 kHz. The colour coding represents the relative amplitude of the axial power flow of each guided mode (blue: low to red: high).

In the work performed by Yu et al. [115], the shear horizontal wave mode family was selected to be further exploited due to the large body of work published in the literature on this wave mode [109], [113], [114]. To further exploit this type of wave mode, a series of shear horizontal weld guided modes are documented in Figure 32. Figure 32 shows contour plots for the axial power flow and displacement mode shapes for a series of shear horizontal weld guided waves. It can be seen that these modes propagate with their energy confined along the centre line of the weld thickness (x_2 direction – see Figure 31). The fundamental shear horizontal weld guided wave mode discovered by Fan and Lowe [113] is not shown in Figure 32, but is denoted as the SH_0 weld guided mode, while the SH_{1-6} weld guided modes are shown. It is observed from the displacement mode shape that when the order of the SH weld guided mode is odd, an antisymmetric motion is observed, and when the order is even, a symmetric motion is observed. Noteworthily, these two patterns lead to out of phase and in phase displacement at the weld cap and root, which instantly gives insight into transduction strategies that could be used to excite different modes preferentially.
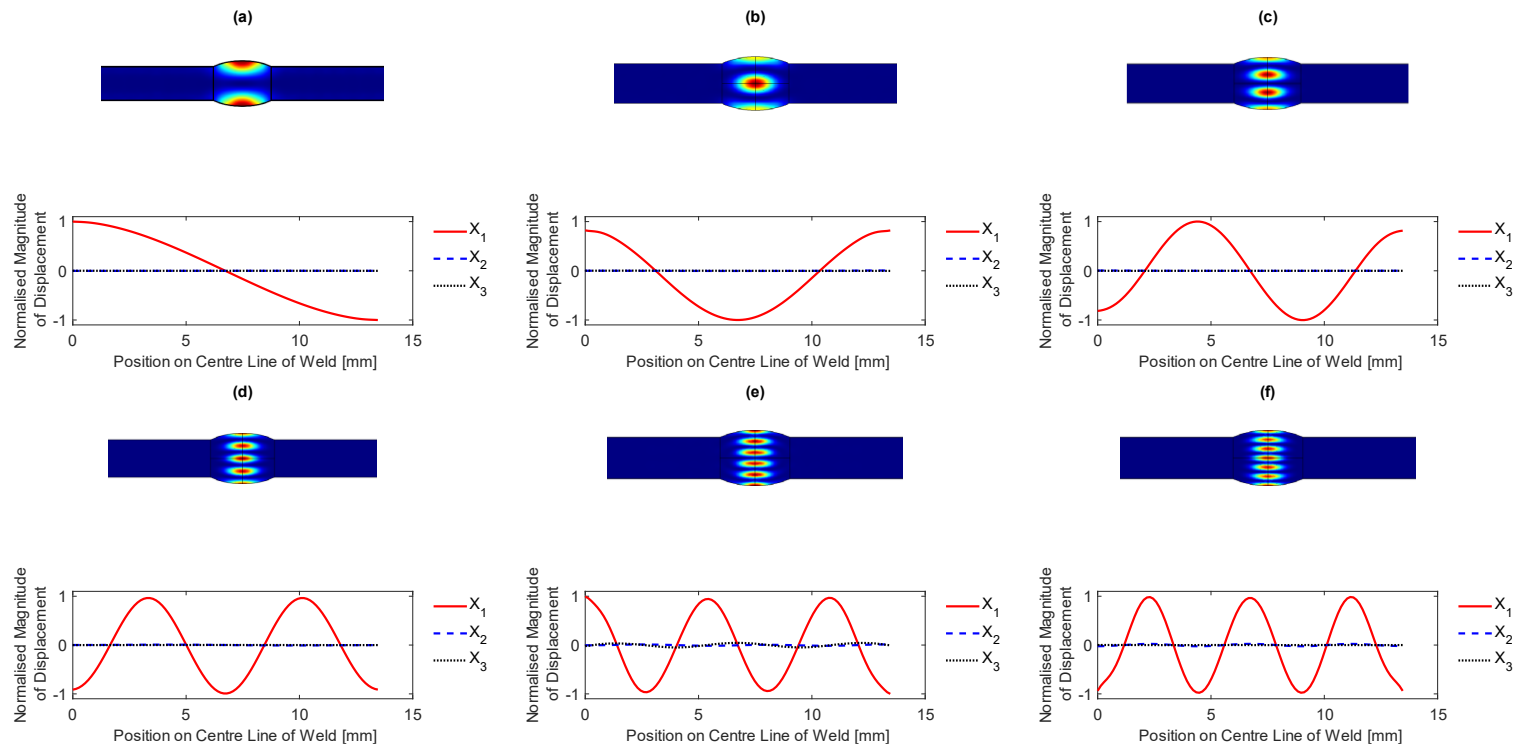
Figure 32: Axial power flow contour plots and displacement mode shapes for the shear horizontal weld guided modes at 1.00 MHz. (a) SH₁ weld guided mode, (b) SH₂ weld guided mode, (c) SH₃ weld guided mode, (d) SH₄ weld guided mode, (e) SH₅ weld guided mode, & (f) SH₆ weld guided mode

To best exploit the identified SH weld guided modes, the phase and energy velocity as well as the attenuation dispersive properties calculated from the SAFE method were examined and are shown in Figure 33. All modes except the fundamental shear horizontal weld guided mode can be seen to exhibit a cut-off frequency when the phase velocities asymptotically tend to infinity. Additionally, all modes except the SH_0 and SH_1 weld guided modes, generally propagate with high attenuation at their cut-off frequencies, indicating larger energy leakage from the weld which is averse to long range inspection. It was therefore concluded that to best exploit these family of SH weld guided wave modes, modes that exhibit little dispersion and attenuation above their cut-off frequencies should be selected.
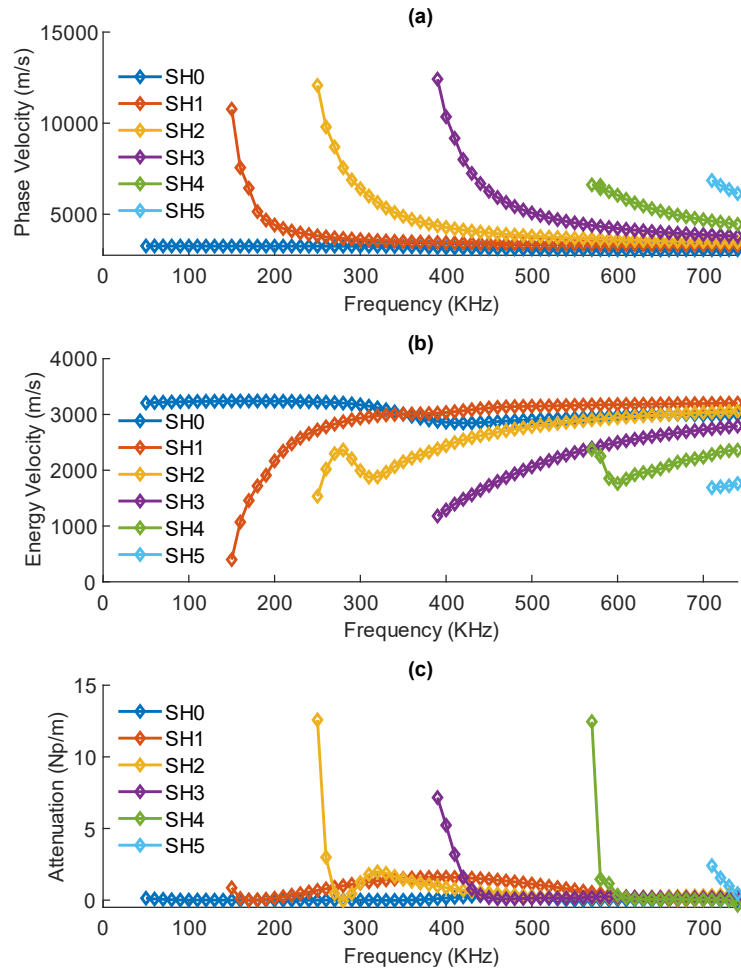
Figure 33: Dispersion characteristics from 50.00-750.00 kHz of the identified shear horizontal weld guided modes (a) Phase velocity of identified shear horizontal weld guided modes, (b) Energy velocity of identified shear horizontal weld guided modes, & (c) Attenuation of identified shear horizontal weld guided modes.

91

3.1.2. Evaluation of modal analysis via 3D finite element analysis

In the work performed by Yu et al. [115], several FE models that studied effective transduction strategies and reflections from defects were solved. These FE models were replicated on the accelerated high-fidelity GPU-based FE package, Pogo [176], while PogoPro visualised the field outputs and MATLAB performed the analysis of the time and field histories. The same cross-sectional geometry in the SAFE analysis was used with the overall domain being $900\,\text{mm} \times 340\,\text{mm} \times 13.46\,\text{mm}$. Absorbing Regions with Increasing Damping (ALID) [177] were applied at the boundaries to limit the computational domain and absorb any leaking waves. The domain was meshed with C3D8R 8-node brick elements with an element size in the transverse direction of 0.50 mm in the weld region and 1.00 mm in the adjacent plates and absorbing regions. Likewise, a 0.50 mm element size was applied to all regions in the lateral and axial directions. The meshing was accomplished in ABAQUS [178] and imported into Pogo. A schematic of the model domain and a close-up of the mesh is shown in Figure 34.
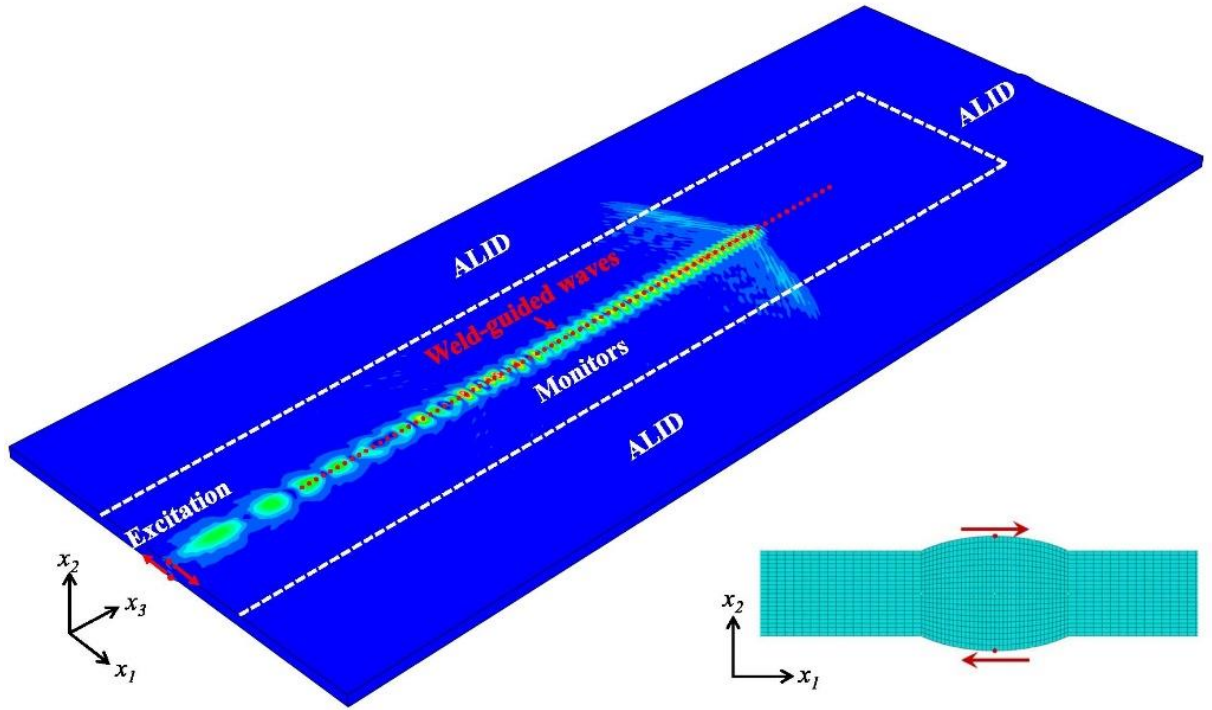
Figure 34: Schematic of the 3D FE model of a welded steel plate with containing absorbing layers with increasing damping (ALID) at the domain extremities; shear excitations at the weld cap and root, along with monitors along the weld bead; colour coding denotes the relative amplitude of the resultant displacement of propagating weld-guided modes (blue: low to red: high) [115]

The models were excited by selecting a node at the top and bottom of the centre of the fusion weld and applying an oscillating shear force in phase and out of phase for each model respectively. The oscillating shear force took the form of a sinc function with a cut off frequency of 1.30 MHz to achieve a broadband excitation as defined in Eq. 100.

$$f(x) = 2f_c sinc(2f_c x) = \frac{2f_c \sin(2f_c x)}{f_c x} \qquad \text{Eq. 100}$$

Several displacement monitors logged the displacement on the central position on the upper surface of the weld in the x_1 direction from $x_3 = 100\ mm$ to $x_3 = 700\ mm$ in steps of $1\ mm$. The resulting array of displacements was analysed using a two-dimensional Fast Fourier Transform (2D-FFT) [60], [174]. It should be noted that the data was Hann windowed in both the space and time dimensions prior to performing the 2D-FFT to suppress discontinuities caused by the signal not being an integer number of periods for all wavenumbers present. Figure 35 shows the sinc excitation signal in the time and Fourier domain as well as the normalised wavenumber-frequency spectra on a dB scale for the models subject to in phase and out of phase shear forces respectively.
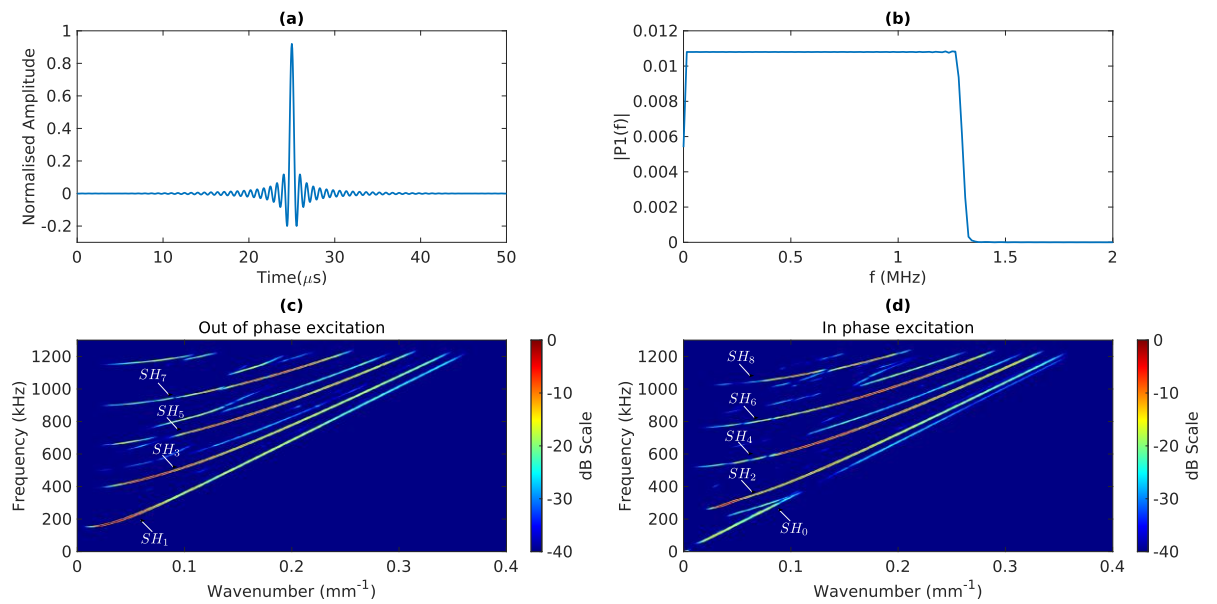
Figure 35: Excitation signal properties and normalised wavenumber-frequency spectra: (a) Time domain representation of sinc function (b) Single-sided Fourier domain representation of sinc signal (c) Normalised wavenumber-frequency spectra of measured wave signals along the weld subject to out of phase shear force, & (d) Normalised wavenumber-frequency spectra of measured wave signals along the weld subject to in phase shear force at the cap and root of the weld

It is also evident in Figure 35 (c) and (d) that it is not difficult to achieve selective excitation of differing SH weld guided waves. From Figure 35 (c), it can be seen that a series of odd order SH weld guided waves (SH_1, SH_3, SH_5, SH_7) are generated by an out

of phase excitation on the weld cap and root. While, in Figure 35 (d), it can be seen that a series of even order SH weld guided waves ($SH_0, SH_2, SH_4, SH_6, SH_8$) are generated by an in phase excitation on the weld cap and root. It is also observed that Figure 35 (c) and (d) additional modes are excited and these are thought to be the torsional wave modes previously described in Section 3.1.1.2 due to their similar mode shapes. None the less, it is clear that the dominant waves excited are the SH weld guided modes and that this transduction technique is well suited to experimental deployment.

Following on from the successful generation, it was useful to explore the sensitivity of these modes to defects. To this extent, a zero-width crack that was 5.00 mm long in the transverse x_1 direction and 2.00 mm deep in the x_2 direction was made in the mesh by disconnecting adjacent nodes in the axial direction where $x_3 = 500.00\ mm$. Like the previous models, displacement monitors logged the displacement on the central position on the upper surface of the weld in the x_1 direction from $x_3 = 100.00\ mm$ to $x_3 = 400.00\ mm$ in steps of $1.00\ mm$. The model was excited using the same singular nodes at the top and bottom of the weld cap and root respectively with a 5 cycle Hann windowed 500.00 kHz toneburst signal. The 2D-FFT method was used to calculate the reflection coefficient to the defect by making use of the amplitude noted at the corresponding positive and negative wavenumbers as they represent the incident and reflected waves respectively – see Figure 36. It is noted that the frequency-wavenumber spectra was normalised against the maximum amplitude modulus across the full spectra on a dB scale. With transmitted and reflected wave modes separated, it is then possible to calculate the reflection coefficient according to Eq. 101 [112].

$$R(f_0) = 10^{\frac{A_r - A_i}{20}}$$

Eq. 101

Where $A_r\ and\ A_i$ are the reflected and incident amplitudes in dB space for a positive and negative wavenumber of identical magnitude. Figure 36 shows the

normalised frequency-wavenumber spectra and it was calculated that SH_1 and SH_3 weld guided waves had a reflection coefficient of 9.99% and 7.34% respectively at 500.00 kHz. It is evident from Eq. 101 that this calculation could be repeated over the full frequency spectrum and obtain a reflection coefficient at all frequencies excited if necessary.
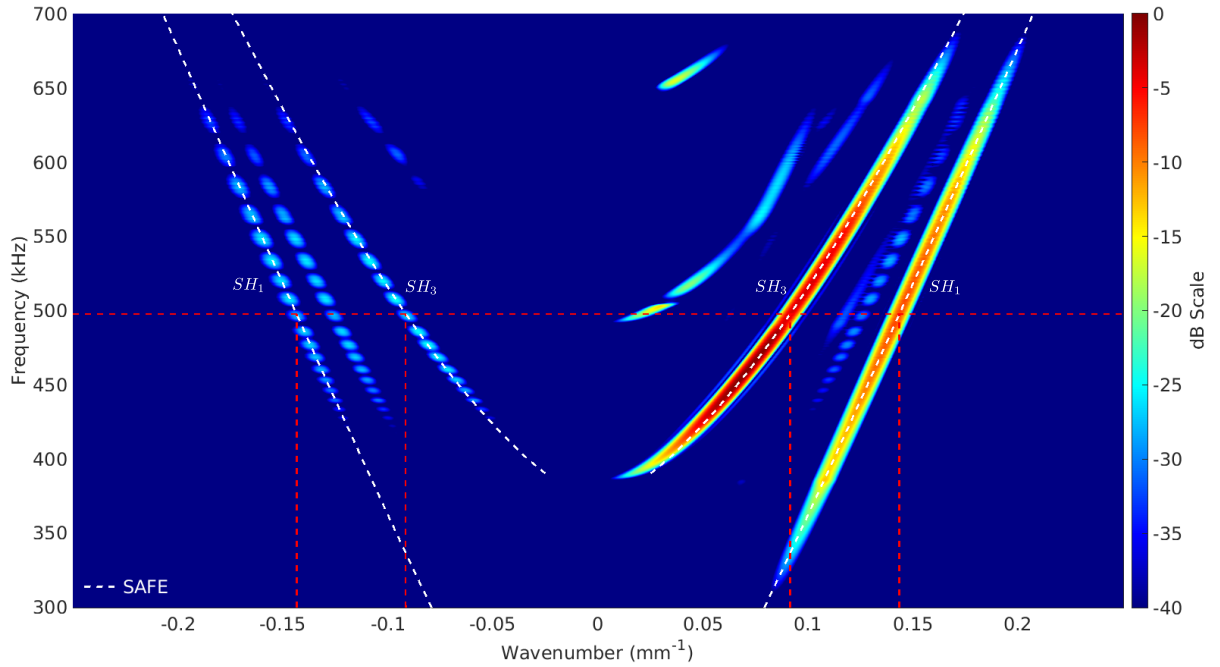
Figure 36: Normalised wavenumber-frequency spectra of measured wave signals along

Through the use of the 2D-FFT method, it has been shown that the SH_1 weld guided wave mode has a greater sensitivity to defects and was thus selected for experimental investigation in the work performed by Yu *et. Al* [115].

3.1.3.   Summary of literature replication

This literature replication has demonstrated that the SAFE method and relevant FE models can be used to predict the existence of FGWs within a fusion weld and study how they interact with differing defects. All of the FGW modes reported in the literature were replicated in this section as demonstrated in Figure 31 and Figure 32. Moreover, their dispersive properties were also accurately determined in Figure 33. Finally, accurate 3-dimensional FE models and post processing showed that similar reflection coefficients could be obtained. The weld guided SH_1 and SH_3 wave modes reported a reflection coefficient of 9.99% and 7.34% respectively. In the literature, these reflection coefficients were reported to be 9.96% & 7.41%, which represents an error of less than 1%.

This extensive effort has validated the complex simulation tools and post processing techniques required to predict the existence of FGWs and was based lined to state-of-the-art literature published with in the last three years. The modelling performed was theoretically complex and this thorough approach was vital to ensuring that adaptation to the inspection of the RSW used at Sellafield was successful.

3.2. Feature guided wave analysis of the RSW

3.2.1.   Modal analysis of the RSW joint using SAFE approaches

3.2.1.1.   SAFE modelling

In order to discover and exploit a FGW confined to the RSW sealed legacy canister used at Sellafield, the SAFE method was performed. AS previously demonstrated, the SAFE method solves the quadratic eigenvalue problem of a solid with a constant arbitrary cross-section and assumes a harmonic oscillation along the direction of propagation. As a result, a number of eigenvalue roots must be specified prior to the solving the model. The eigenvalue search was performed with a centre root search around $k = \frac{2\pi f}{c_T}$, and the number of roots was gradually increased to 700 until no additional modes of interest were returned, thus indicating convergence had been met. The SAFE method applied to a flat plate was used for this cylindrical structure. It has been shown within literature [60], [179], [180] that the dispersion relationships for flat plates match that of circumferential propagation under certain geometric conditions. These conditions include the inner to outer radius ratio being approximately equal to one and the thickness to radius ratio being less than 10%. The proposed canister structure fits well within these criteria; therefore, the solutions produced by this flat plate analysis were applied to the curved canister structure.

A schematic of the simplified RSW cross section used in the SAFE model is shown in Figure 38 where the weld's length is extended along the x_3 direction which is perpendicular to the 2-dimensional domain of the problem. The model contains three distinct regions. The central region is the RSW, which has a thickness and width of 1.53 mm and 6.50 mm, respectively. Either side of the RSW are the un-welded stock sheets which are 0.90 mm thick, separated by a very small (0.05 mm) air gap. This simplified geometry was extracted from an X-ray CT scan of a RSW sample, shown in Figure 37,

where undulations in the weld were noted to occur ~6.00 mm in the axial direction. Finally, at the perimeter of the model, there is an 11.00 mm wide Perfectly Matched Layer (PML). This is in line with the guidance given by Zuo *et al.* [137], where the minimum angular wavenumber in the frequency range of interest is the dominant factor in determining the PML length. By introducing the PMLs, the real coordinates of the physical equations are extended into the complex domain allowing standing waves to be absorbed. Therefore, standing non-propagating waves are not present in the solutions generated by the SAFE model. Nyugen *et al.* provide further information on how PMLs are practically implemented within SAFE modelling [140].
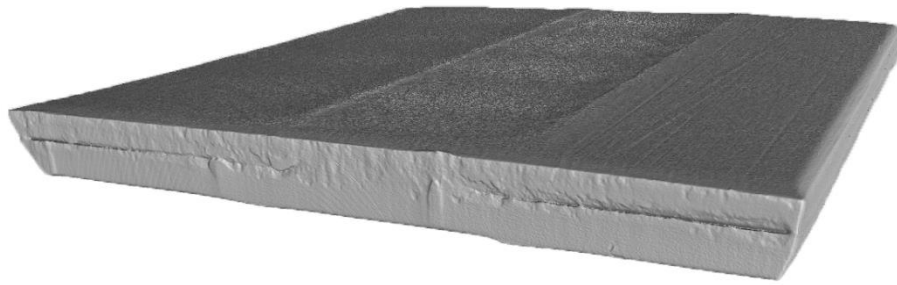
Figure 37: Isometric view of CT scan of RSW coupon

The entire geometry was assigned the elastic moduli associated with 1.4404 stainless steel [181] ($\rho = 7958.00 \frac{kg}{m^3}, E = 194.62\ GPa, G = 75.2\ GPa$). The mesh was composed of 1710 quadratic triangular Lagrangian elements, and the model was solved from a minimum frequency of 50.00 kHz to a maximum frequency of 1.00 MHz in steps of 10.00 kHz to ensure resolution and accuracy over a suitable frequency window.
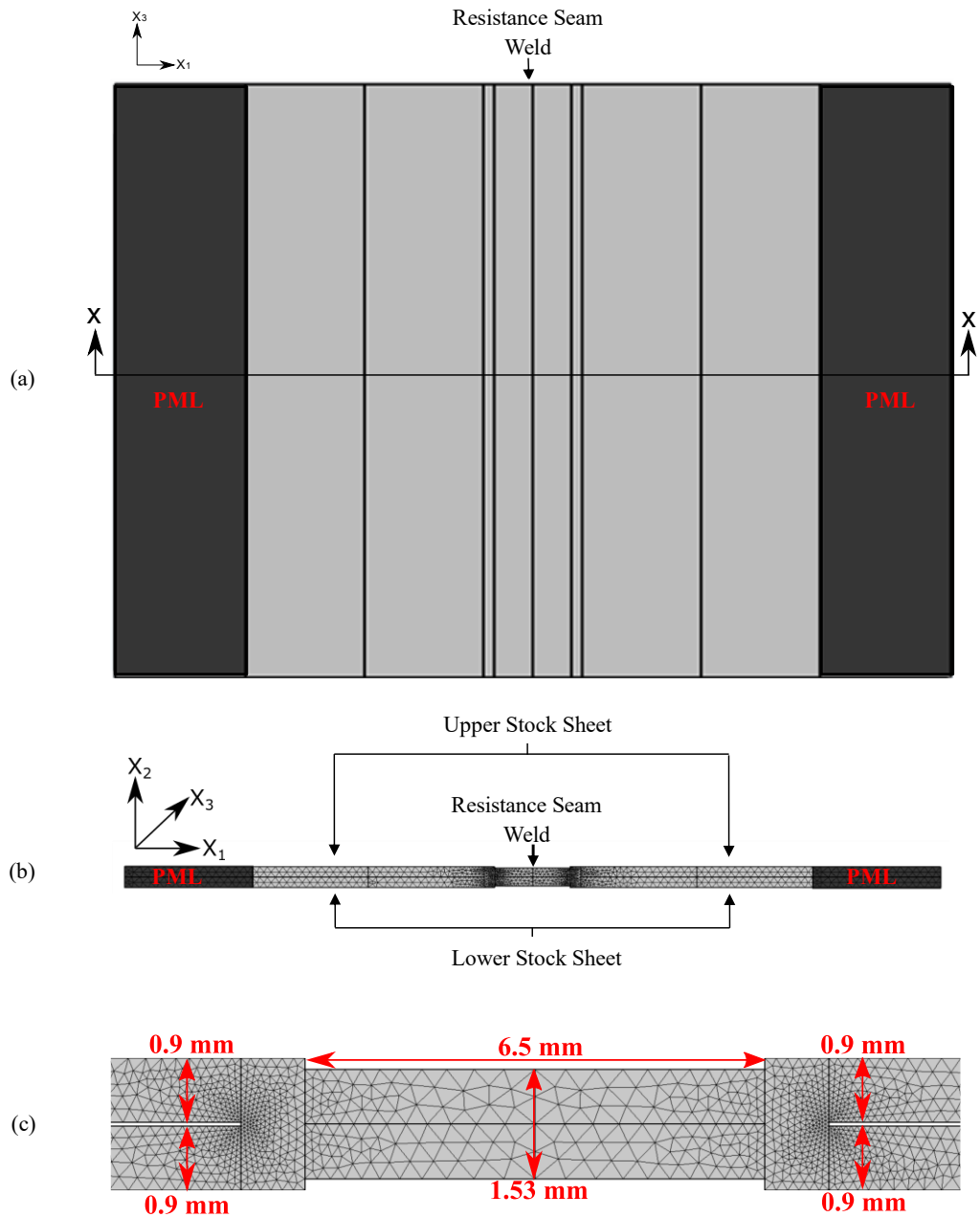
Figure 38: Schematic of SAFE model geometry (a) Plan view of RSW component with cross-sectional arrows. (b) 2-Dimensional cross-sectional view of the discretised SAFE model geometry detailing the RSW and stock sheets. Stock sheets either side of the weld are separated by a 0.05 mm air gap. (c) Detailed view of the 2-Dimensional cross-sectional discretised SAFE model geometry detailing relevant dimensions taken from the CT scan.

3.2.1.2.　　FGW mode selection

To select a suitable FGW mode and operational frequency for inspection, the modal solutions generated by the SAFE method were investigated. The axial component of the time averaged power flow in the x_3 direction was calculated at the nodal points of the mesh for every solution via Eq. 83 and Eq. 84. Suitable FGW modes are identified where the average power flow is higher in the feature of interest than that of the surrounding structure as detailed in Eq. 99.

Figure 39 shows the power flow ratio, produced by Eq. 99, for all eigenvalue solutions given from the SAFE model at 100.00 kHz. It can clearly be seen that when there is strong energy confinement in the RSW, the power flow ratio peaks and subsequently can be used to filter out solutions that are not weld guided as established by Zuo *et al.* [137]. By leveraging this property in combination with a proprietary algorithm, automatic detection of unique FGW modes and their corresponding dispersive properties was performed across the entire frequency spectrum of this problem.
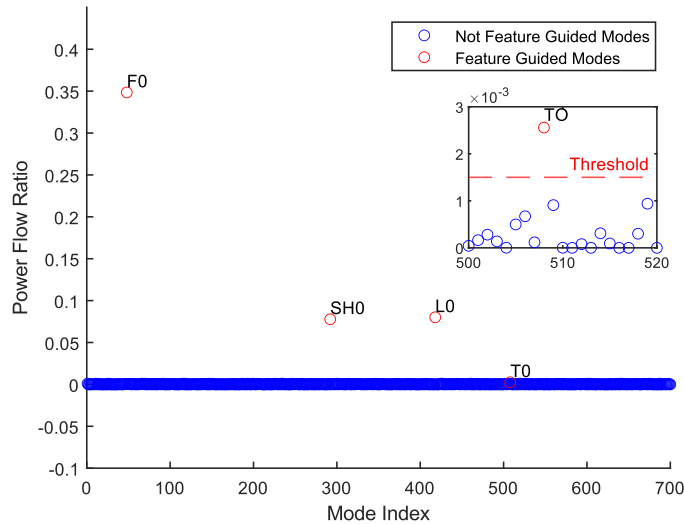
Figure 39: Power flow ratio at 100.00 kHz with 700 eigenvalues

Figure 40 shows the axial power flow, normalised orthogonal displacements, and vibrational pattern (indicated by arrows) that contribute to the through thickness mode shapes of the four-wave modes identified from this analysis at various frequencies. These details allow the identified wave modes to be classified based on the dominant displacement of their mode shape and vibrational pattern. For instance, Figure 40 (c) shows a mode shape dominated by the shear displacement component and was hence classified as the fundamental Shear Horizontal (SH_0) weld guided mode. Figure 40 (i) shows a mode shape dominated by the axial displacement component and was classified as the fundamental Longitudinal (L_0) weld guided mode. Figure 40 (f) shows a mode shape dominated by the shear displacement component but has a rotational vibrational pattern and was denoted as the fundamental Torsional (T_0) weld guided mode as a result. As torsional wave modes predominantly exist only in pipes, this result is more characteristic of a pipe rather than that of a plate. Lastly, Figure 40 (l) shows a mode shape dominated by the vertical displacement component and was termed the fundamental Flexural (F_0) weld guided mode.
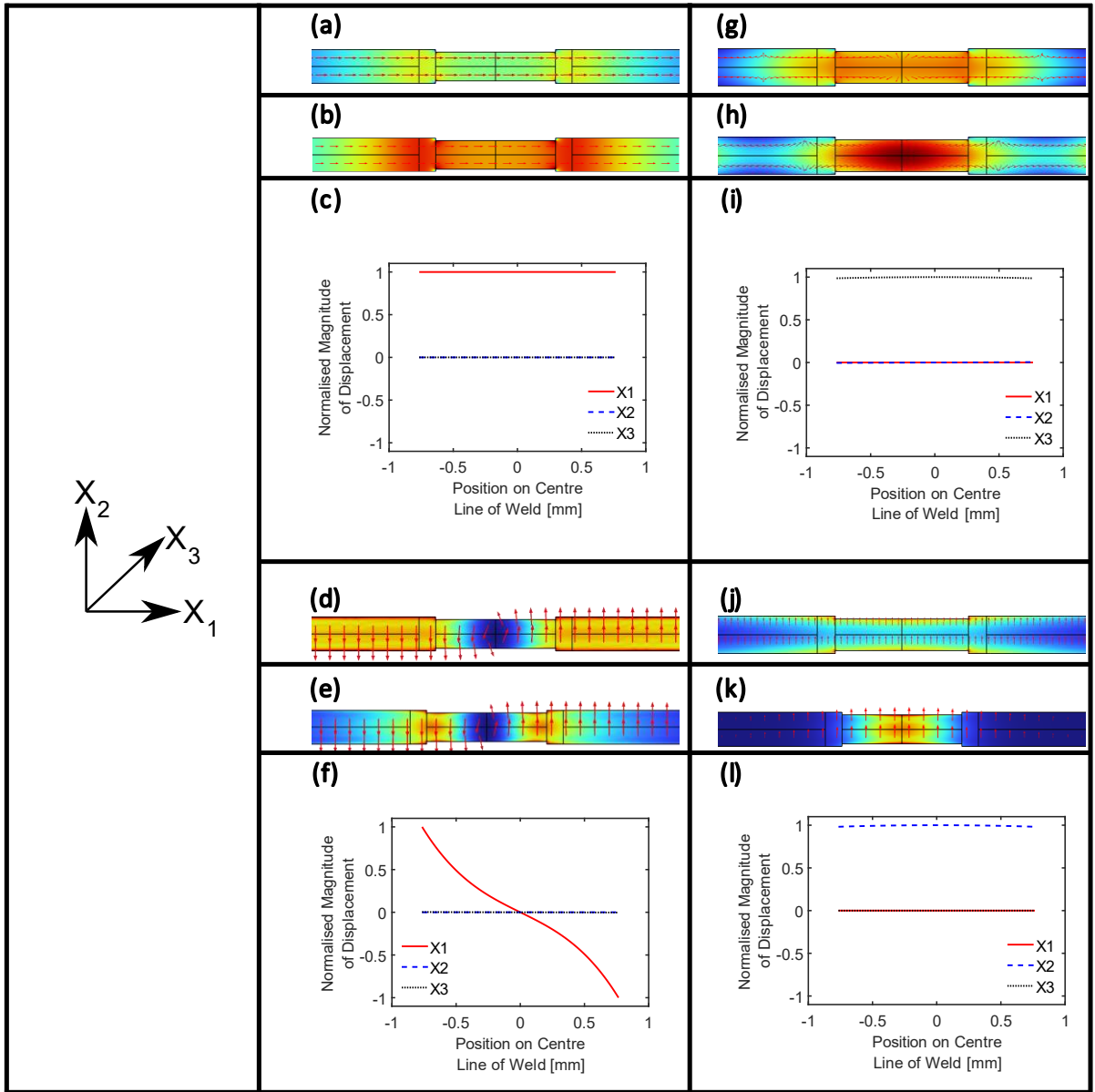
Figure 40: Axial power flow contour plots, vibrational pattern (indicated by arrows) & mode shapes of weld guided wave modes predicted by the SAFE method (a) SH_0 like power flow at 400.00 kHz ($\alpha = 0.15\ Np/m$), (b) SH_0 like mode power flow at 900.00 kHz ($\alpha = 0.015\ Np/m$), (c) SH_0 like mode shape at 400.00 kHz, (d) T_0 like mode power flow at 600.00 kHz ($\alpha = 0.27\ Np/m$), (e) T_0 like mode power flow at 900.00 kHz ($\alpha = 1.89x10^{-4}Np/m$), (f) T_0 like mode shape at 600.00 kHz, (g) L_0 like mode power flow at 270.00 kHz ($\alpha = 0.54\ Np/m$), (h) L_0 like mode power flow at 400.00 kHz($\alpha = 0.47\ Np/m$), (i) L_0 like mode shape at 270 kHz, (j) F_0 like power flow at 60.00 kHz ($\alpha = 0.077\ Np/m$), (k) F_0 like power flow at 900.00 kHz ($\alpha = 0.00\ Np/m$), (l) F_0 like mode shape at 60.00 kHz. The colour coding represents the relative amplitude of the axial power flow of each guided mode at particular frequencies (blue: low to red: high)

Figure 40 also shows how the attenuation of the identified wave modes is characterised by changes in the axial power flow over the frequency spectrum of this problem. Figure 40 (a), (d), (g) & (j) show points of relatively high attenuation of the fundamental SH_0, T_0, L_0, and F_0 weld guided modes, respectively – see Figure 41. While Figure 40 (b), (e), (g) & (k) show points of relatively low attenuation of the fundamental SH_0, T_0, L_0, and F_0 weld guided modes respectively. It can be seen that as the attenuation decreases, a stronger energy trapping effect is observed on the aforementioned contour plots. Figure 41 shows the variations in phase velocity, energy velocity, and attenuation of the wave modes identified with analytical solutions superimposed for a free plate of the same thickness as the weld. The F_0, SH_0, and L_0 weld guided modes are shown to be highly similar to that of the A_0, SH_0, and S_0 analytical free plate solutions for both phase and energy velocity. However, greater differences are observed in their energy velocity dispersion curves due to the presence of increased attenuation for the leaky weld guided modes compared to that of their analytical counterparts. A trend also observed in the literature [113], [133] and the work reported within this study is that any plate-like feature with a consistent but different thickness to that of the surrounding structure possesses similar FGWs to that of their analytical free plate counterparts. Therefore, it is expected that well documented traditional guided wave transduction techniques can also be utilised to successfully create the FGW of choice. Furthermore, it is hypothesised that this trend will hold for other components with similar plate-like features.

The attenuation dispersion curve shown in Figure 41 (e) is quite different from what one may expect when considering the analytical equivalents shown in Figure 41 (f). This result may appear counterintuitive initially, but several other FGW studies have reported similar attenuation characteristics. Manogharan *et al.* [117] reports a fundamental shear horizontal bend guided mode in which attenuation decreases as frequency increases - a trend that is also observed in this study. While Ramdhas *et al.* [116] report an antisymmetric bend mode that also exhibits low attenuation. Furthermore, Castaings and Lowe [133] report a highly unique attenuation dispersion curve for a weld guided S_0 mode that exhibits zero attenuation except from two distinct peaks. Their work demonstrates

and explains that due to the Snell Descartes Law [62] the weld guided S_0 mode cannot radiate as either the SH_0 or A_0 mode of the adjacent plates at particular frequencies. This is due to the phase velocity of the SH_0 mode of the adjacent plates being larger than that of the S_0 weld guided mode, and the A_0 mode of the adjacent plates having a mode shape that is too dissimilar to that of the S_0 weld guided mode. By using the same logic and applying it to the work present within this study, it can be said that the F_0 weld guided mode, with its' low phase velocity can only radiate as the A_0 mode of the adjacent plates. Moreover, the F_0 weld guided mode and A_0 mode of the adjacent plates possess highly similar mode shapes and therefore, the low attenuation characteristic of the F_0 weld guided mode in Figure 41 (e) is expected and confirmed with variations in the axial power flow illustrations shown in Figure 40.

As has been highlighted in the previous paragraphs, the F_0 weld guided wave mode possesses the highest axial power flow confined to the RSW region. On average, the power flow ratio of the F_0 weld guided is 5.25 times higher than the next highest wave mode identified implying that it would also have the largest reflection from defects. Due to the manufacturing process, this result was not unexpected as the geometry change is most significant in the weld's vertical axis, giving rise to a more substantial energy trapping effect. For experimental applications, a frequency of 1 MHz is recommended due to the abundance of commercially available transducers with this centre frequency and the lower dispersion characteristics observed at higher frequencies. In summary, the F_0 weld guided wave mode, with its high energy confinement in the RSW along with its low attenuation and low dispersion at higher frequencies, made it the most suitable candidate for screening of nuclear grade RSWs.
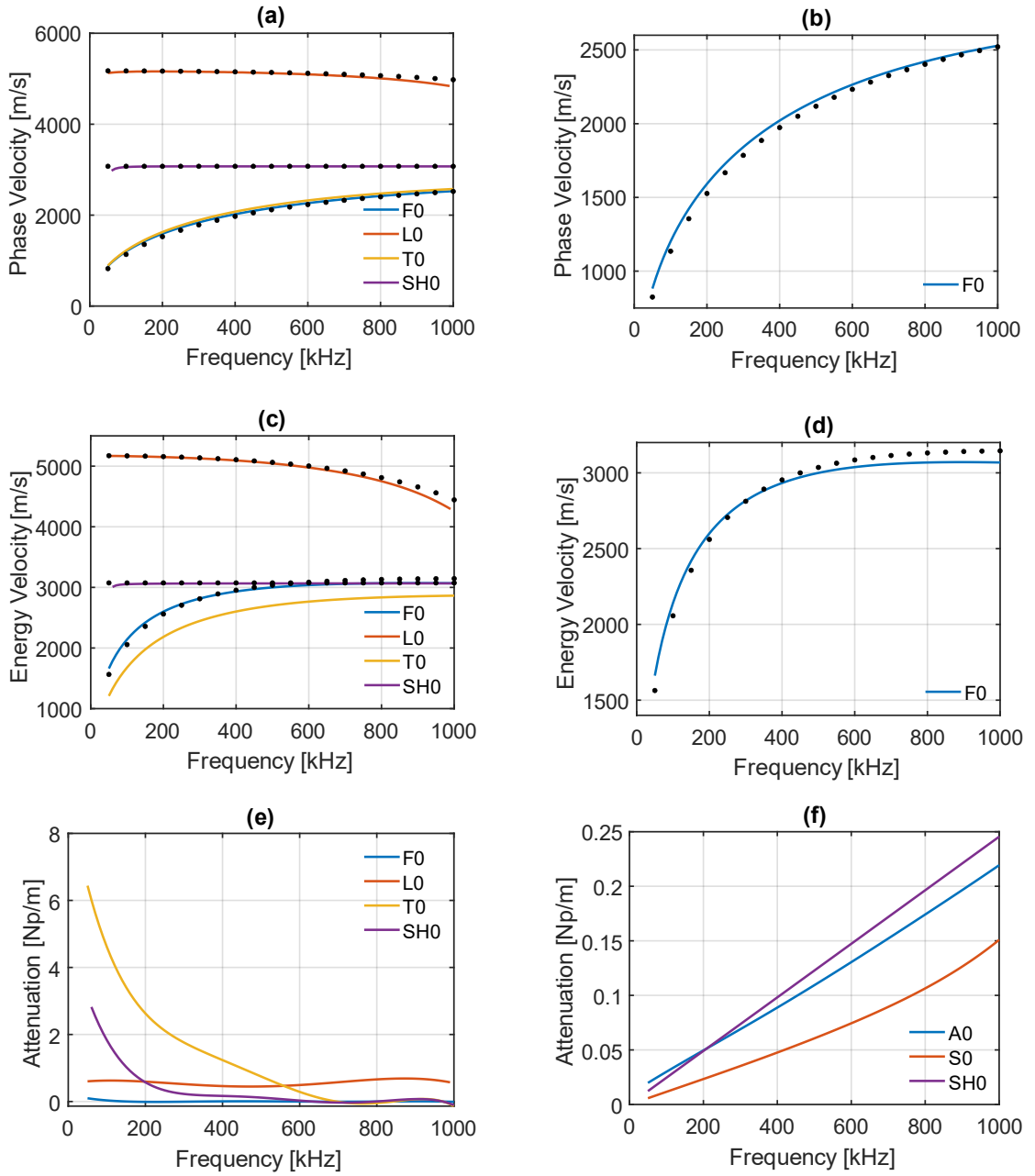
Figure 41: Dispersion characteristics of identified weld guided modes and their analytical counter parts for a free plate of the same thickness as the weld (1.53mm, ρ=7958 kg/m3, E=194.62 GPa, G=75.2 GPa, $\alpha_L = 0.002$ Np/λ, $\alpha_T = 0.004$ Np/λ) (a) Phase velocity of all weld guided modes, (b) Phase velocity of F0 weld guided mode (c) Energy velocity of all weld guided modes, (d) Energy Velocity of F0 weld guided modes, (e) Attenuation of all weld guided modes automatically detected from the SAFE solutions, (f) Attenuation of conventional analytical solutions for a free plate of the same thickness as the weld. Where (•••) represent conventional analytical solutions of the S0, SH0 & A0 modes propagating along a free plate of the same thickness as the weld.

3.2.2. Evaluation of modal analysis via 3D finite element analysis

3.2.2.1. SAFE and FE comparison

Several three-dimensional explicit FE simulations were performed on the accelerated high-fidelity GPU-based FE package Pogo [176] to further verify the predictions from the SAFE method, investigate suitable transduction techniques, and gain insight into defect sensitivity. PogoPro visualised the field outputs while MATLAB performed the analysis of the time and field histories.

Figure 42 shows a schematic of the FE model domain and a snapshot of the displacement field magnitude, where the flexural FGW confined to the RSW can be clearly seen. Figure 42 also depicts energy radiating from the FGW on the RSW and a faster plate-guided wave in the un-welded side sheets. Other similar publications have noted similar results [114] and also note that low attenuation of a FGW is accompanied by an angle of radiation of ~90° [133].

The FE model used the same geometry described in Section 3.2.1, and the overall domain was 128.30x1.85x550.00 mm. The internal utility, pogoMesh, discretised the domain and the resulting mesh comprised of 43,747,000 C3D6R 6 node triangular prism elements with an average size of 0.2.0 mm. The C3D6R element was chosen due to its ability to mesh complex structures and due to the fact that it has been extensively used within literature to effectively simulate such problems [182]–[184]. The mesh size of 0.20 mm was chosen as it was smaller than $1/20^{th}$ of the shortest wavelength in the medium [185]. In addition, a 50.00 mm Absorbing Region with Increasing Damping (ALID) [177] was applied at the boundaries of the plate to limit the extent of the domain and effectively apply an unbounded boundary condition. A high-performance computer that contains two Nvidia GeForce RTX 3090 graphics cards solved each model in approximately 10 minutes.
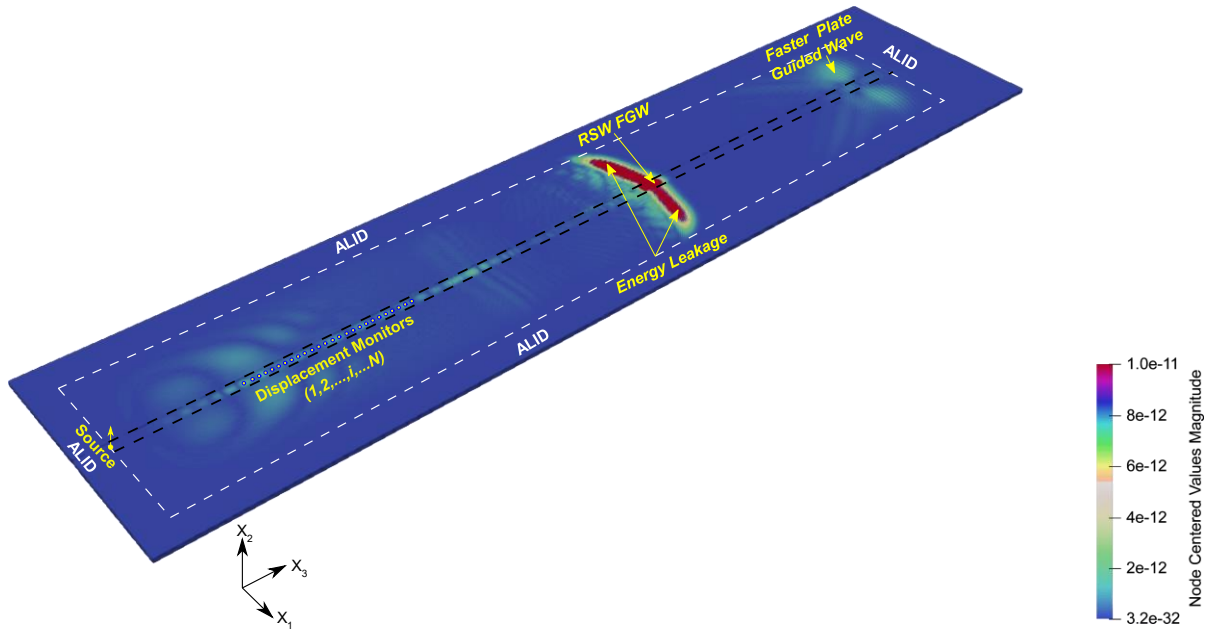
Figure 42: 3D FE model schematic from a 5 cycle Hann windowed 1 MHz excitation signal showing the displacement field magnitude of the FGW travelling up the RSW surrounded by absorbing layers with increasing damping (ALID)

The initial models were excited at a broad range of frequencies utilising a sinc function with a cut-off frequency of 1.3.0 MHz. The properties of the sinc function are shown in Figure 35 (a) and (b). This function was applied on a singular node in the x_2 direction on the upper surface of the welded pocket to successfully launch the F_0 weld guided mode. Several displacement monitors logged the displacement on the central position on the upper surface of the weld in the x_2 direction from $x_3 = 100 \, mm$ to $x_3 = 500 \, mm$ in steps of $1 \, mm$. The resulting array of displacements was analysed using a two-dimensional Fast Fourier Transform (2D-FFT) [60], [174]. It should be noted that the data was Hann windowed in both the space and time dimensions prior to performing the 2D-FFT to suppress discontinuities caused by the signal not being an integer number of periods for all wavenumbers present. The resulting spectra comprised of wavenumber-frequency data and is shown in Figure 43 normalised by the maximum modulus on a dB scale.

The wideband excitation of the sinc function is clearly shown, and good alignment with the predictions from the SAFE model is observed. Additionally, other studies have shown that the excitation technique utilised in this model to generate such anti-symmetric flexural Lamb-like wave modes is well suited to experiments that employ the angle-incidence method as their transduction technique [186], [187].
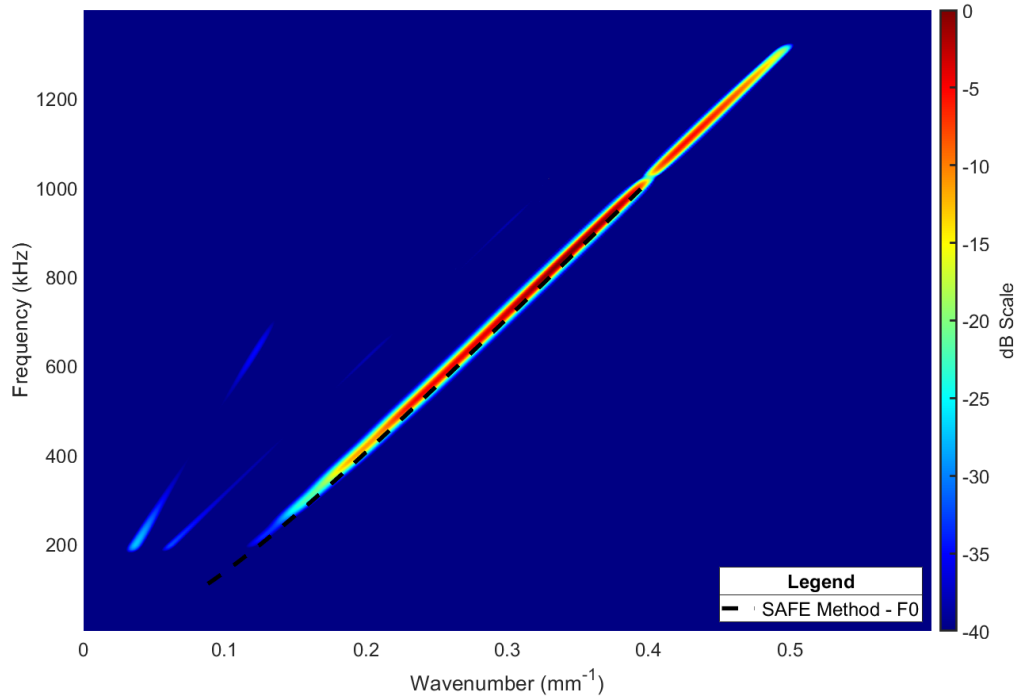
Figure 43: Normalised wavenumber-frequency spectra of FE simulation with no defect present excited by a broadband sinc signal with a 1.3 MHz cut off frequency. The SAFE solutions are overlayed on top of the spectra in black.

To further confirm the energy concentration effect, the same model was run with a 5 cycle 1 MHz Hann windowed excitation signal and studied in depth. The entire displacement field history at each nodal point was logged as well as the displacement time histories at the monitor points from $x_3 = 100.00 \ mm$ to $x_3 = 500.00 \ mm$ in steps of $1.00 \ mm$. Figure 44 shows an A-scan taken in the centre of the simulated plate at $x_3 = 225.00 \ mm$ and clearly show the flexural weld guided mode as the dominant mode

excited. The propagation time of ~$68\mu s$ agrees with the SAFE energy velocity of 3068.40 m/s to cover a 225.00 mm transit.
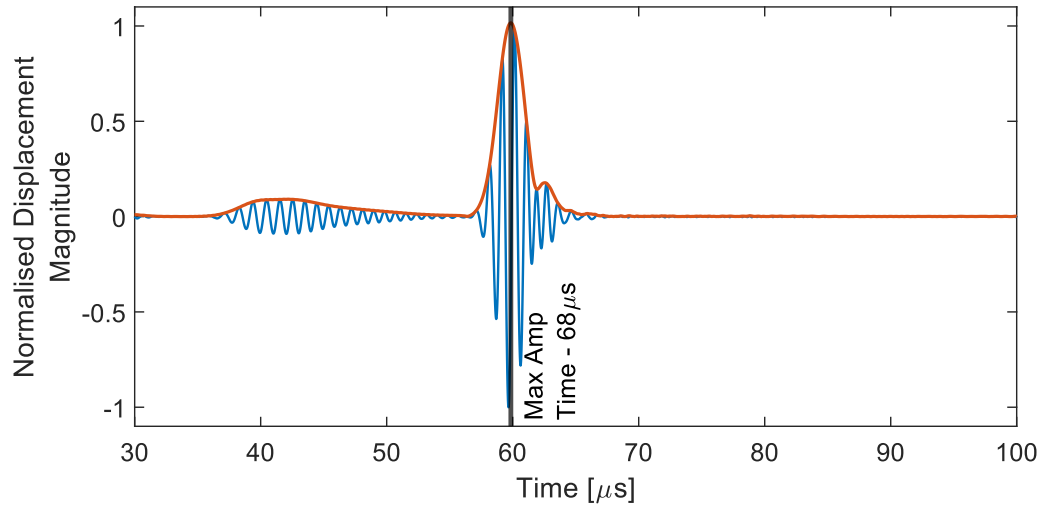
Figure 44: A-scan of the displacement field at $x_3 = 200$ mm

Figure 45 (a) shows the displacement field of a $x_{1,2}$ cross-sectional plane at a position of $x_3 = 225\ mm$ at 68 μs in time. The strong energy concentration effect of the fundamental flexural weld guided mode can be observed along with the radiated A_0 wave in the stock side sheets. Moreover, Figure 45 (b) plots the variation in the displacement field at the centre of the upper stock sheet. It can be seen that the displacement field exhibits a periodicity outwith the central welded region of 2.309 mm. As shown by Castaings and Lowe [133], this periodicity is indicative of the wavelength of the acoustic field being radiated from the FGW as it propagates along the feature. For a wavelength of 2.31 mm at 1 MHz this gives a speed of 2309.39 m/s which approximately matches the phase velocity for the A_0 mode for a 0.90 mm steel sheet at 2306.51 m/s. These results confirm that the high energy concentration and low attenuation properties of the flexural weld guided wave mode predicted from the SAFE modelling in Section 3.2.1.1 & 3.2.1.2 are indeed observed in these initial time step FEA models and are in line with previously published literature.
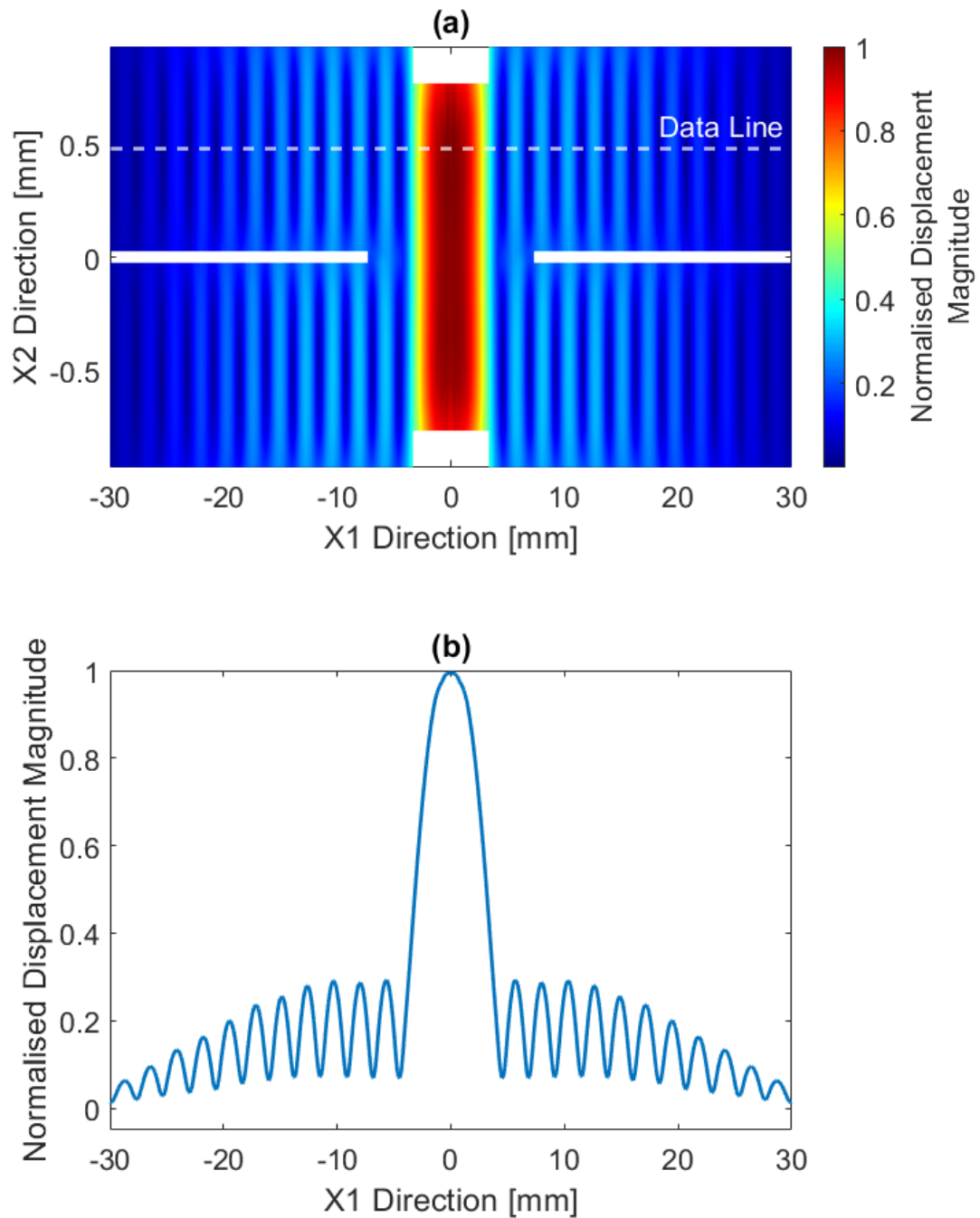
Figure 45: Displacement field at $x_3 = 200$ mm at 68 μs from $-30 \leq x_1 \leq 30$mm (a) Contour plot of the entire $x_{1,2}$ plane displacement field from $-30 \leq x_1 \leq 30$mm (b) Normalised displacement field across the centre of the upper stock sheet from $-30 \leq x_1 \leq 30$mm indicated by the dashed white line in Figure 45(a).

3.2.2.2.   Defect reflectivity

With successful models predicting and showing the presence of the fundamental flexural weld guided mode within the RSW, it was necessary to evaluate its sensitivity to defects. Therefore, various transversal cracks were introduced into the model by disconnecting adjacent nodes perpendicular to the crack extent. This location corresponded to a half circumferential transit of ~225.00 mm and was viewed as the maximum distance a defect could be from the transducer.

The same central node on the upper surface of the welded pocket was excited with a 5-cycle Hann-windowed 1.00 MHz toneburst signal. Likewise, displacement monitors logged the displacement from 100.00 mm to 200.00 mm in steps of 1.00 mm. An expansion of the 2D-FFT method previously defined in Eq. 101 was employed to generate the images denoted in Figure 43. As can be seen, both positive and negative wavenumbers are present within the spectra representing transmitted and reflected waves, respectively. With transmitted and reflected wave modes separated, it is then possible to calculate the reflection coefficient according to Eq. 101. Table 1 summarises the reflection coefficients obtained from several FE models where the crack width and height were modified. It can be concluded that the crack depth is the dominant factor when determining the reflection coefficient. Deeper cracks consistently produced significantly higher reflections. This trend is illustrated visually between Figure *46* (b) & (c) in the frequency wavenumber spectra.

Table 1: Crack dimensions and their corresponding reflection coefficients

Crack Dimensions	Reflection Coefficient
Full Width, Full Depth – 6.5x1.53 mm	19.11%
Full Width, Half Depth – 6.5x0.765 mm	11.45%
Half Width, Full Depth – 3.25x1.53 mm	16.33%
Half Width, Half Depth – 3.25x0.765 mm	7.82%
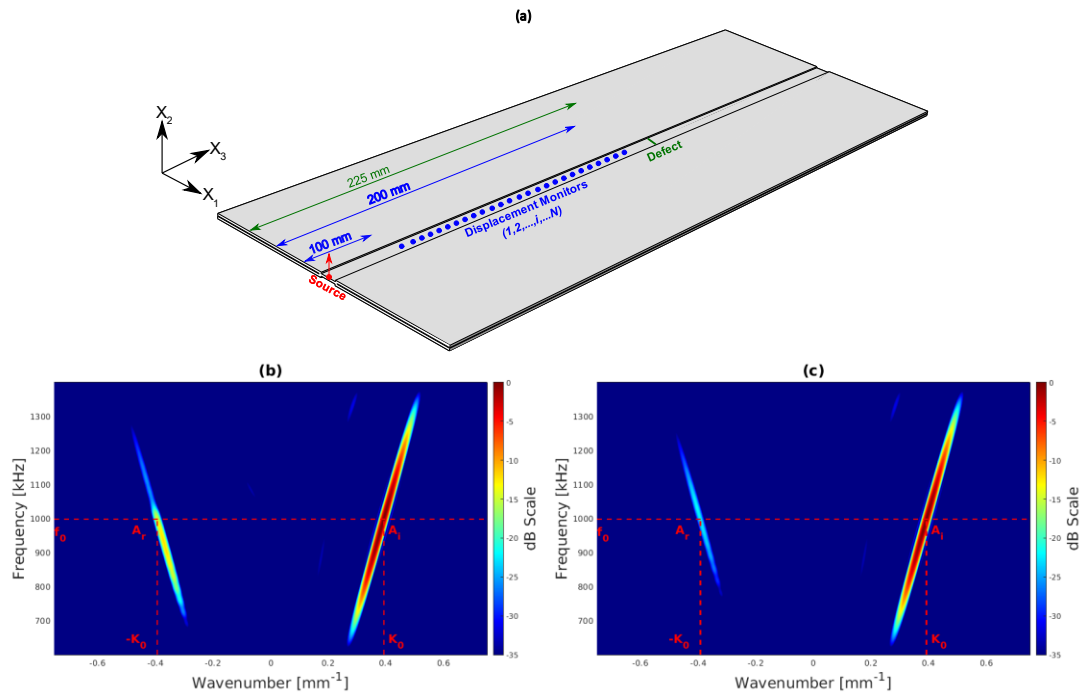
Figure 46: (a) Schematic of FE model utilised to study the interaction of the Fo RSW guided mode with defects, (b) Frequency-wavenumber spectra for a 5 cycle Hann-windowed 1.00 MHz excitation and 6.50x1.53 mm (full width full depth) crack at 225.00 mm (c) Frequency-wavenumber spectra for a 5 cycle Hann-windowed 1.00 MHz excitation and 6.50x0.77 mm (full width half depth) crack at 225.00 mm

3.2.3.   Experimental validation

Several experiments were undertaken to initially verify the successful generation of the predicted flexural FGW and subsequently evaluate the efficacy of using this FGW to screen for defects. A flow chart of the experiments conducted with the hypotheses they were testing and the findings they generated is illustrated in Figure *47*.

Hypotheses	Experiment	Findings
The angle-incidence method will create flexural anti-symmetric Lamb waves only in 5 mm centre section	**Pseudo Weld**	Angle-incidence method does create anti-symmetric lamb waves **only** on the 5 mm centre section with strong correlation to analytical solvers
The Angle-incidence method will produce a flexural FGW in the RSW / The predicted SAFE dispersion relationships will have close alignment to what is observed experimentally / A reflection will be observed from a transversal crack in the flat sheet RSW	**Flat RSW**	Successful generation of flexural FGW only in the RSW / Experimentally observed dispersion relationships were found to be different to what was predicted by SAFE due to undulating weld geometry / Successful detection of a transversal crack in the flat sheet RSW
A reflection will be observed from a transversal crack in the cylindrical RSW.	**Cylindrical RSW**	Successful detection of a transversal crack in the cylindrical RSW

Increasing Complexity

Figure 47: Experimental flow chart showing the series of experiments undertaken

Firstly, a machined aluminium pseudo weld was manufactured and experimented on. This simplified geometry removed the possibility of any unforeseen interactions with the undulating nature of the RSW and the propagating wavefront (See Figure 2(b)), while also removing any challenges associated with wave propagation within the core material [188]. Then, with further confidence developed in the experimental approach, additional experiments of increasing complexity were conducted on flat and cylindrical stainless steel RSWs representative of the welds utilised on nuclear canisters.

3.2.3.1.   Pseudo weld

A simplified weld was machined from 6082-T6 aluminium with the geometry shown in Figure 48.

Plan View

Displacement Monitor Zone - Side Plate

Displacement Monitor Zone - Pseudo Weld

Centre Line Displacement Monitors for 2D FFT

50   40   50   5 15

500

Side View

Front View
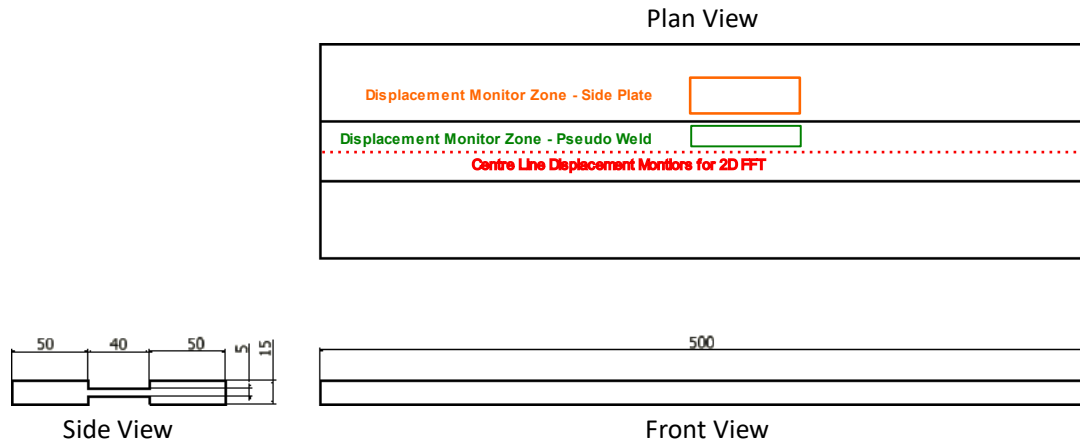
Figure 48: Pseudo weld 3rd angle projection schematic in mm

This component was manufactured to test the previously mentioned hypothesis raised initially in Section 3.2.1.2, that FGWs like that of their flat plate counterparts would be generated in a component where the thickness changes abruptly to a consistent value at the topological feature of interest. These experiments also confirmed if the angle-incidence technique was a viable transduction method in creating Lamb-like FGWs, as theorised in Section 3.2.2. To prove these two points, the material used was not of concern and aluminium was selected due to its' low attenuation and scattering properties. The geometry was also further simplified to remove the presence of air gaps in the side plates due to time and economic constraints. Therefore, it was expected that only Lamb-like wave modes would be created in the centre 5.00 mm thick pseudo weld region.
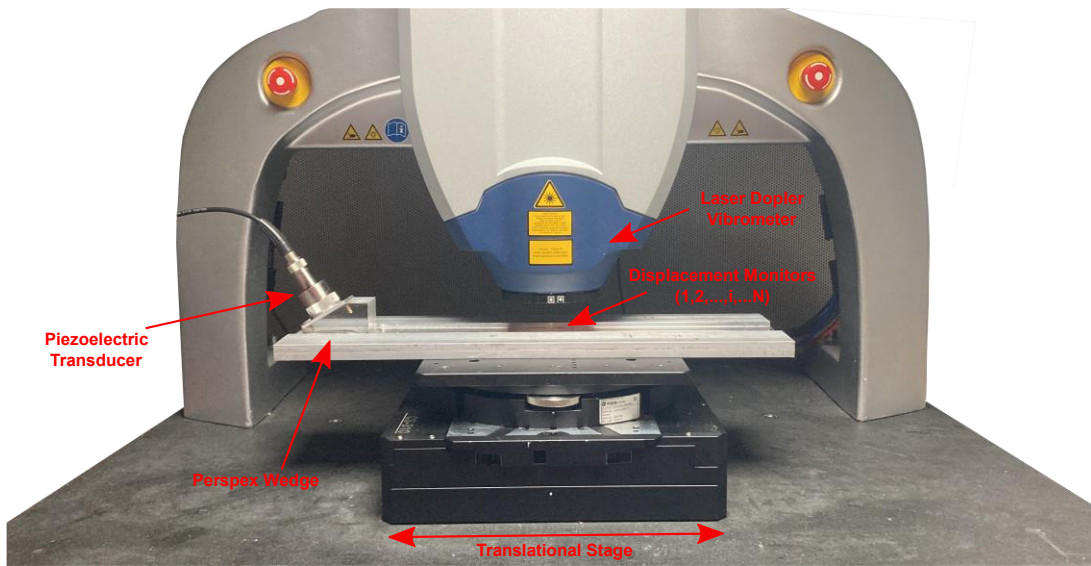
Figure 49: Pseudo weld experimental set up

A Perspex wedge with a 30-degree angle was machined and is shown along with the experimental set-up in Figure 49. As this experiment was intended to show that Lamb waves are only generated in the pseudo weld, the angle of the wedge was not optimised. A commercially available Olympus, 1-inch diameter, piezoelectric transducer (Part No: A301S-SU, Item Number U8421001) was pulsed with a 5-cycle Hann-windowed wave at 500.00 kHz using the Wavemaker Duet pulser from Macro Design Ltd. Gel couplant [189] was applied between the transducer and wedge as well as between the wedge and sample. Two displacement monitoring zones were set up: one on the pseudo weld and the other on the thicker side plates. The displacement in both zones was monitored using a Polytec MSA-100-3D laser Doppler vibrometer, animated and is available via the supplemental data in [190]. From Figure 50 it is clear that there is a strong wavefront generated only within the pseudo weld region. Only noise is present in the thicker side sheets. Figure 50 shows A-scans from the pseudo weld and thicker side sheets normalised to the maximum value observed across both signals. Again, it can be seen that a strong wavefront is generated in the welded region with only noise present in the thicker side sheets. This result gives a strong indication that a flexural FGW had been successfully generated.
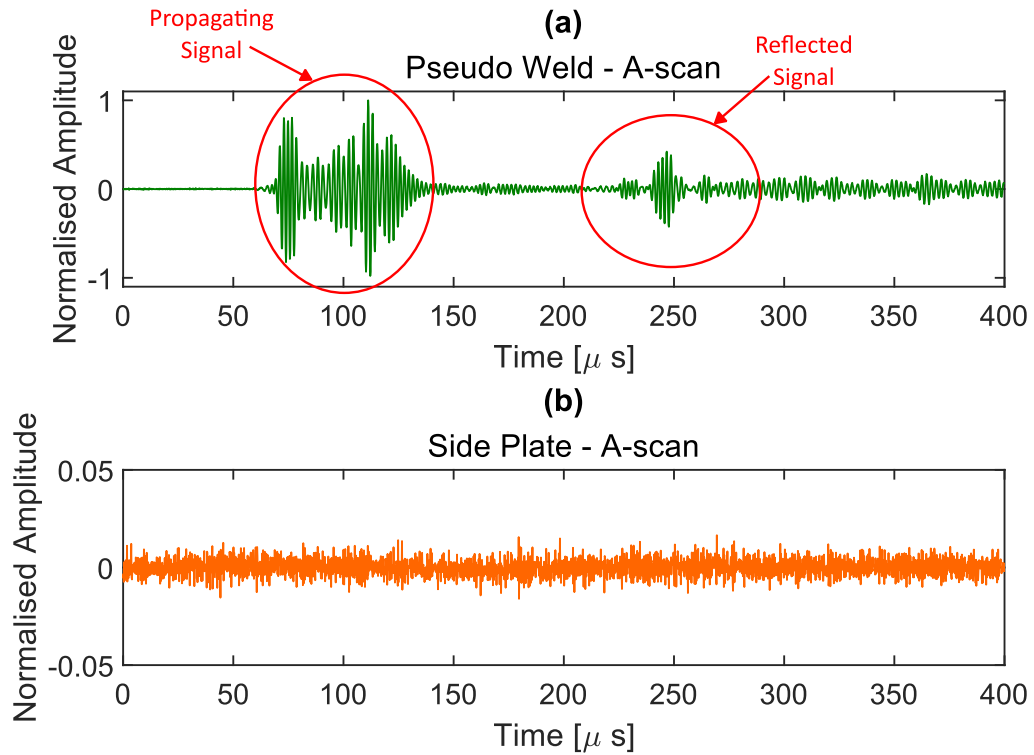
Figure 50: A-Scans from pseudo weld and side sheets (a) A-scan on 5.00 mm thick pseudo weld (b) A-scan on 15.00 mm thick side sheet

To further confirm and expand our findings, the same piezoelectric transducer was pulsed with a 5-cycle Hann-windowed wave packet from 200.00 kHz to 900.00 kHz in steps of 100.00 kHz. For each frequency, the Polytec MSA-100-3D laser Doppler vibrometer monitored the centre line displacements along the weld from 200.00-300.00 mm in front of the transducer location in steps of 0.30 mm. Each signal was normalised and superimposed at each location, creating one array of displacements for all frequencies. The resulting array was analysed using the aforementioned 2D-FFT method and compared to the Lamb wave analytical solutions for a 5.00 mm thick aluminium free plate generated by the computational solver, Disperse [87], in Figure 51.

Figure 51 shows strong alignment between the experimental data and analytical solutions. It is noted that due to the frequency-thickness product at 500.00 kHz with the unoptimised wedge angle, multiple Lamb wave modes are excited. Furthermore, the amplitude observed in the spectra increases as the dispersion curves approach the wedge's

117

excitation curve and the transducer's centre frequency. This result confirms that the angle-incidence method is a suitable transduction technique to excite flexural Lamb-like FGWs.
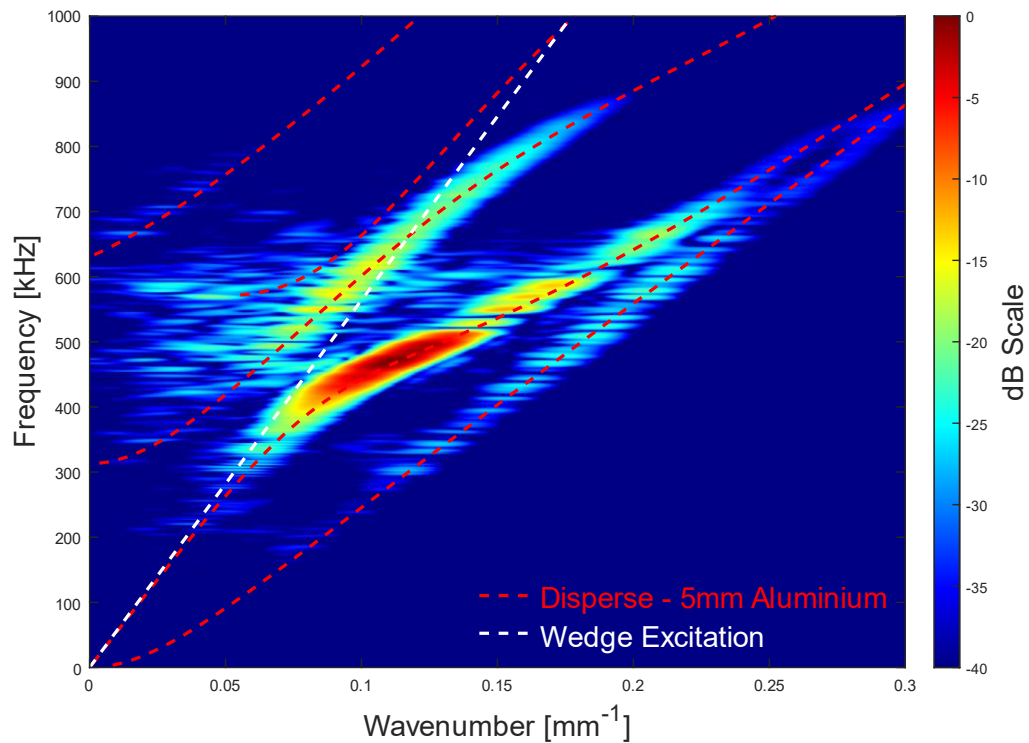
Figure 51: Frequency-wavenumber spectra for superimposed data on the pseudo weld

These observations also have broader implications that could be exploited. For example, other similar structures that contain flat plate-like features could use the dispersion relationships from analytical solvers (i.e. Disperse [87], GUIGUW [88], Dispersion Calculator [89]), avoiding the need to run a complex SAFE model to predict, excite and launch FGWs of their own. Hence, this approach could be applicable to I-beam structures and other similar metallic extrusions.

3.2.3.2. Resistance seam weld

3.2.3.2.1 PFTE wedges

With confidence in the transduction technique, further vibrometry and pulse-echo experiments on flat and curved canister-like RSW samples were conducted. A pulse-echo experimental set-up was chosen to be integrated as it is believed to best mimic a real-world inspection scenario where access to complex equipment, like a laser Doppler vibrometer, is cost-prohibitive. To facilitate these experiments, two wedges were manufactured with and without a curved bottom surface from PTFE with a 30-degree angle to conform to the angle-incidence transduction formula – see Eq. 102. The wedges are shown in Figure 52.
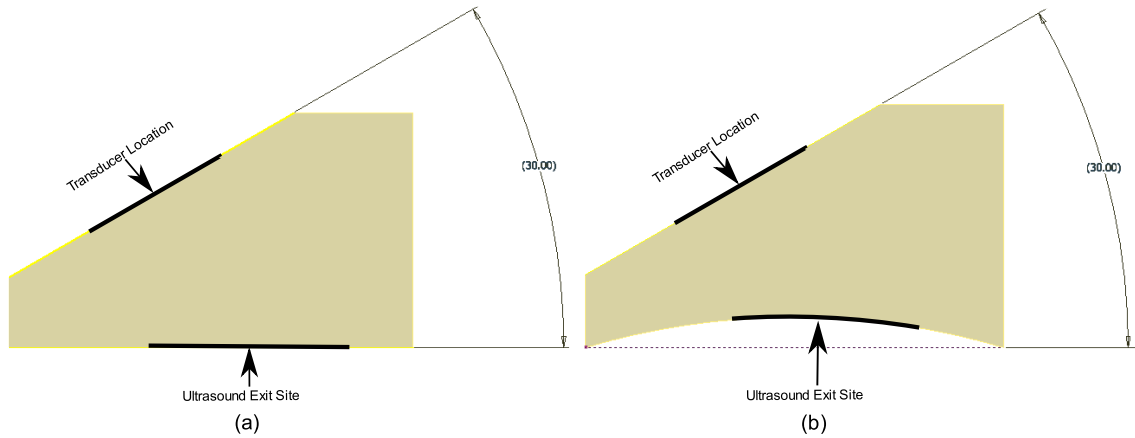
Figure 52: Schematic of PTFE wedge (a) PTFE wedge for flat RSW samples, (b) PTFE wedge for curved canister-like RSW samples

PTFE was chosen due to its low longitudinal wave speed of ~1,400.00 m/s and the low F_0 phase velocity of 2524.00 m/s at 1.00 MHz, making any resulting wedge easily manufacturable. The angle-incidence method is described mathematically in Eq. 102, where v_l is the longitudinal speed of sound of the wedge, v_{ph} is the phase velocity of the guided wave being excited, and θ is the wedge angle.

$$\theta = \sin^{-1}\left(\frac{v_l}{v_{ph}}\right) \qquad \text{Eq. 102}$$

Both wedges feature a polyurethane-based AptFlex F48A absorber (see Figure 55) from Precision Acoustics [191] to limit any amount of reflected sound within the wedge interfering with the signal from the sample itself.

To confirm the performance of the wedge and absorber, a simple A-scan into air was performed. A commercially available Olympus, 0.5-inch diameter, dual-element piezoelectric transducer (Part No: DHC703-RM, Item Number: U8452055) was excited with a 1.00 MHz 5 cycle Hann-windowed wave packet in a pulse-echo configuration. This dual-element transducer was selected due to its' lower ring down in a pitch-catch configuration when compared to an equivalent single-element transducer in a pulse-echo configuration. In addition, the effects of any electromagnetic interference present in the pulser's electronic systems are also significantly reduced with the transmit and receive channels separated. The receiver had 40.00 dB amplification, and A-scans with 64 averages at a sampling rate of 100.00 MHz were acquired via a standard oscilloscope (Tektronix DPO 4054B). Gel couplant [189] was applied between the transducer and wedge as well as between the wedge and sample.

Figure 53 shows A-scans of the excitation signal, the received A-scan from the flat wedge, and the received signal from the curved wedge, along with a snapshot of the experimental set up. Reverberations are denoted for the first $60\mu s$. As a result, multiple peaks are expected to be observed from any interaction with defects, back wall reflections, and full circumferential transits. These reverberations are not expected to be an issue to effectively screen RSW joints and highlight areas for further in-depth inspection via other NDE modalities, as it is envisaged that there will always be sufficient spatial resolution from the transducer to the defect location. This is also shown to be the case with other similar studies in literature [119]. The reverberations observed may be further suppressed, if necessary, via more advanced transducer and wedge design and are the subject of future work.
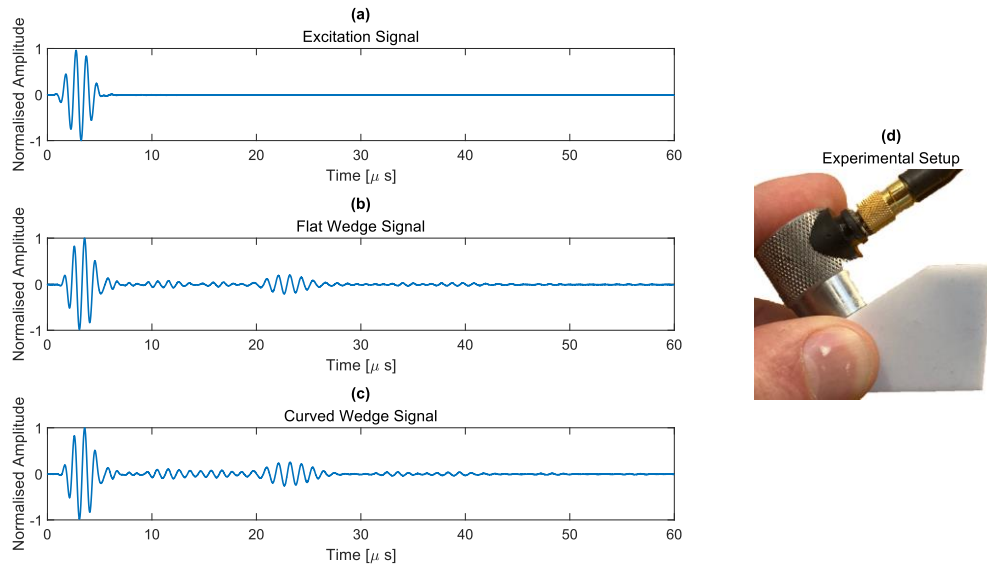
Figure 53: Illustration of simple wedge A-scan experiment, (a) Normalised 1.00 MHz 5 cycle Hann windowed excitation signal, (b) Normalised A-Scan from flat bottomed wedge held in air, (c) Normalised A-scan from curved bottom wedge held in aid, (d) Photo of simple experimental set-up

3.2.3.2.2   Flat plate resistance seam welds

To confirm the dispersive relationship of the RSW joint, a further vibrometry experiment was undertaken on flat RSW samples. The RSW samples comprised of two 0.90 mm thick long 1.4404 stainless steel sheets fused together to a standard used in fabricating canisters. Due to size and economic constraints, the sample used in this experiment was only 200.00 mm in length. A series of displacement arrays generated by the Laser Doppler vibrometer were gathered from 200.00 kHz to 900.00 kHz in steps of 100.00 kHz from 50.00 mm to 150.00 mm in front of the transducer in steps of 0.30 mm. As before, each signal was normalised, superimposed, and analysed via the 2D-FFT technique. Figure 54 shows the resulting frequency wavenumber spectra normalised against the maximum amplitude in a dB scale.
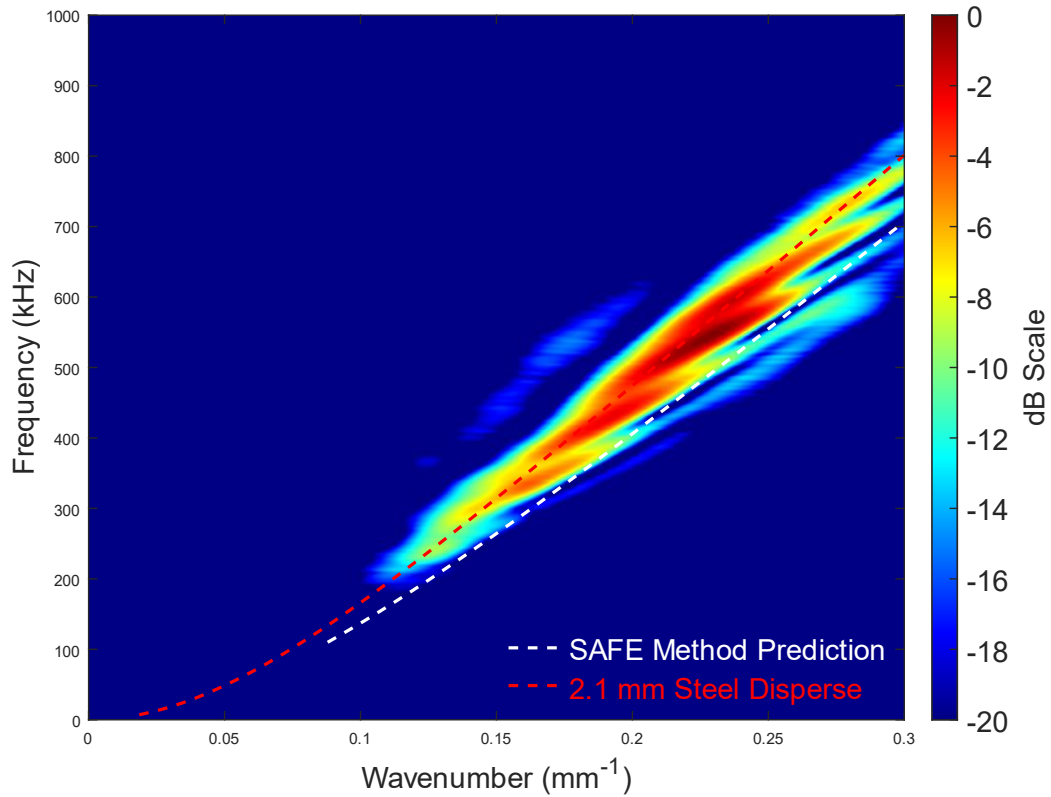
Figure 54: Frequency-wavenumber spectra for superimposed data on a flat RSW sample

It can be seen in Figure 54 that the predicted SAFE results are offset from the experimental data, and the experimental data more closely aligns with the analytical solution for the fundamental antisymmetric 2.10 mm steel free plate. The thickness of the analytical solutions was iteratively changed while keeping the material properties constant until good agreement was observed between experimental and analytical datasets. This shift is thought to be due to the undulating nature of the RSW (see Figure 2 (b)), which could not be modelled by the SAFE method. However, even with this slight shift, it can be seen that one flexural mode is excited in the RSW.

With the real-world dispersion relationship better understood, experiments were conducted on flat 0.9-meter long RSWs with and without defects. For the defective samples, the defects were represented by a 6.50 mm wide (x_1 direction) by 0.50 mm tall

(x_3 direction) through-thickness and 1.00 mm deep (x_2 direction) transversal EDM notches in separate samples at an axial position of 500.00 mm. The receiver had 40.00 dB amplification, and A-scans with 64 averages were acquired at a sampling frequency of 100.00 MHz for both defective and defect free flat RSW samples. Gel couplant [189] was applied between the transducer and wedge as well as between the wedge and sample. The experimental set up is shown in Figure 55.
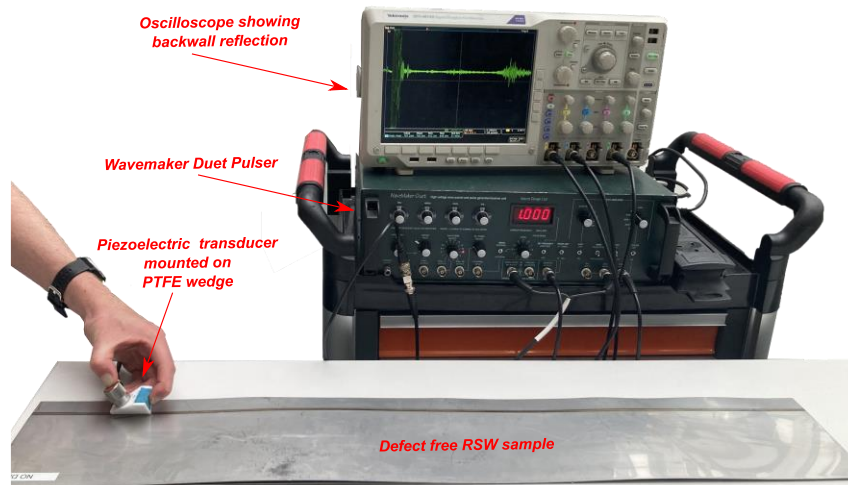
Figure 55: Experimental set up on a defect-free RSW sample

Figure 56 shows the resulting A-scans, with strong reflections observed in both the through wall and 1.00 mm defective time series at ~375.00 μs along with a significantly dampened back wall reflection. It is also noted that the back wall is observed in the defect free time trace to occur at ~700.00 μs, giving a velocity of ~2,500.00 m/s in agreement with the predicted velocities stated in Section 3.2.1.2. All signals were normalised to the maximum amplitude observed after the first 60.00 μs reverberation zone detailed in Section 3.2.3.2.1.

The signal to noise ratios (SNRs) for both defective time series was calculated by computing the ratio of the summed squared magnitude of the signal to that of the noise. First, an envelope was calculated over the entire signal using local maxima separated by

900 samples. The signal was taken to be the signal amplitude between where the envelope value drops to 25% on either side of the maximum envelope value reported at ~375 μs. While the noise was taken to be an equal number of samples as the signal beginning 150 μs. SNRs of 16.33 dB and 8.21 dB were reported for the through wall and 1.00 mm deep defects, respectively. Measurements were also attempted against 0.50 mm and 0.25 mm deep defects, but the reflection was not readily distinguishable from the noise floor. This serves to indicate a practical limit of the technique that may be addressed in future work. Furthermore, the results reported in Table 1 also indicate that the "half depth" defects modelled are close to the practical limit of the hardware used in this experiment. However, defects of ≥ 1.00 mm can be clearly seen in the defective time series, demonstrating the efficacy of using this flexural FGW mode to screen for defects on flat RSW plates.
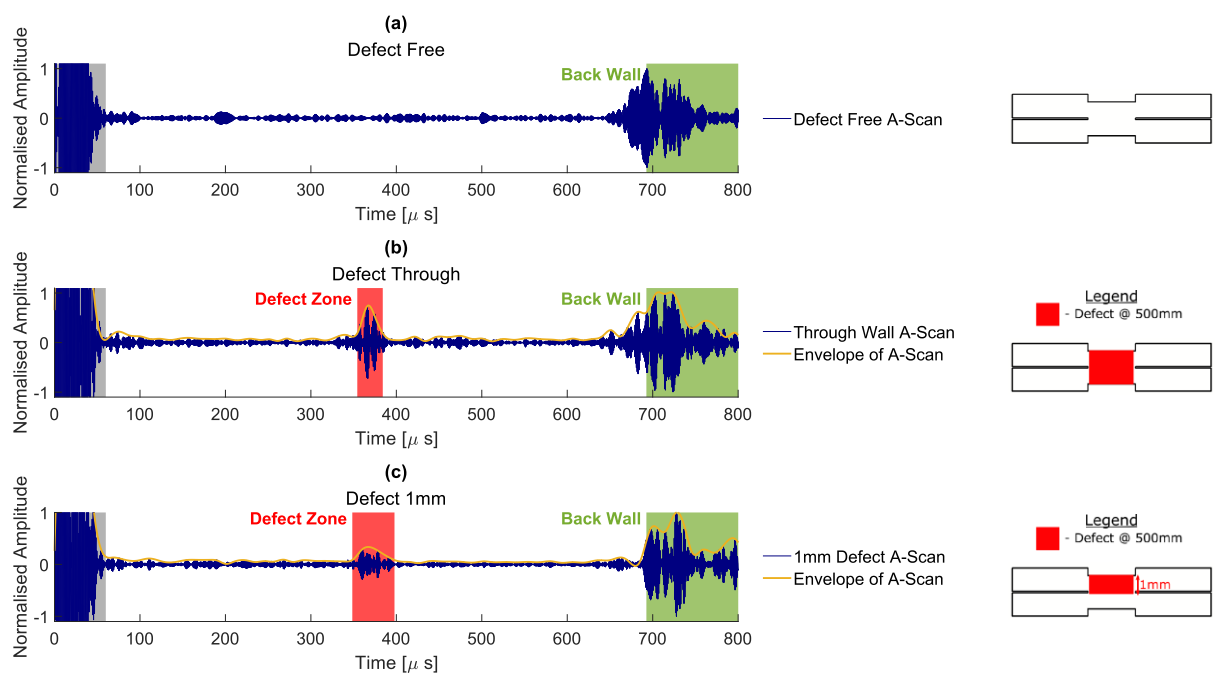
Figure 56: Normalised A-Scans on defect-free and defective flat plate RSW samples (a) Normalised A-scan for a defect-free flat RSW sample, (b) Normalised A-scan for a through wall defective flat RSW sample, (c) Normalised A-scan for a 1.00 mm deep defective flat RSW sample.

3.2.3.2.3   Cylindrical resistance seam welds

Expanding upon the flat plate experiments, cylindrical RSWs were experimented on with and without a defect. Like with the flat RSW samples, a 6.50 mm wide by 0.50 mm tall by 1.00 mm deep transversal EDM notch was created to represent a crack in one location of the cylindrical samples, as it was shown to be the smallest detectable defect. Care was taken in the position of the transducer relative to the EDM notch to avoid mistaking a full circumferential transit as a defect located diametrically opposite the transducer location. As a result, the transducer was positioned at approximately a quarter of the circumference from the EDM notch. The same 1.00 MHz Olympus transducer (Part No: DHC703-RM, Item Number: U8452055) was pulsed with a 5 cycle 1.00 MHz Hann-windowed wave packet, and A-scans were collected with 64 averages at a sampling frequency of 100.00 MHz and 40.00 dB of amplification. Gel couplant [189] was applied between the transducer and wedge as well as between the wedge and sample.
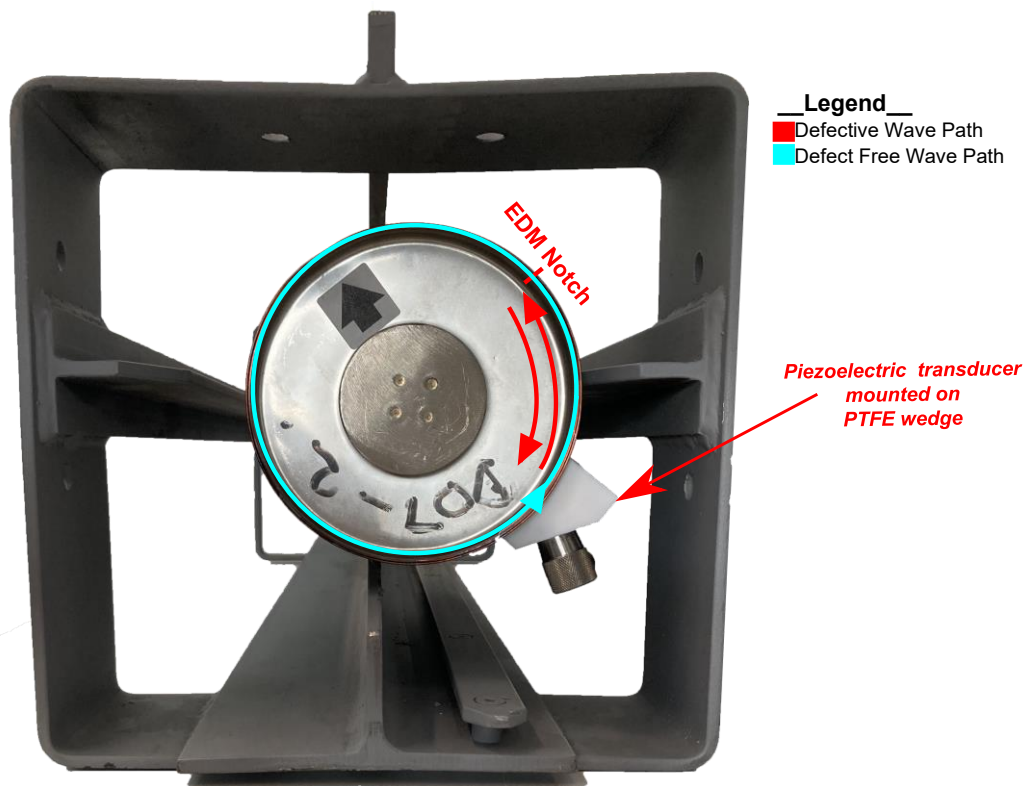
Figure 57: Experimental Set up on cylindrical RSW

Figure 58 shows the acquired A-scans for defect-free and defective cylindrical RSWs. In the defect-free time series, a full circumferential transit is observed at ~180 μs. In the defective time series at ~115 μs, a strong reflection is observed from the EDM notch and is accompanied by a large reduction in the full circumferential transit. Like in Section 3.2.3.2.2, the SNR of the defective time series was calculated. An envelope was calculated over the full signal using local maxima separated by 450 samples. The signal was taken to be the signal amplitude between where the envelope value drops to 25% on either side of the maximum envelope value reported at ~115.00 μs. While the noise was taken to be an equal number of samples at the signal beginning at 180.00 μs. A SNR of 11.85 dB was reported and is in good agreement with the SNR reported to the same 1.00 mm deep defect in Section 3.2.3.2.2. Additional samples with defects at different positions were not possible due to sample availability but will be considered as part of future work.

It is also noted that to provide full circumferential coverage, two inspection locations are required. If only one inspection location is utilised, 'blind spots' are created by the transducer ring-down time from the wedge into the sample and from a defect diametrically opposite from the transducer location, which could appear as a full circumferential transit.

Regardless of these two limitations, it is clear from the acquired data that this technique could be used to screen the quality of RSWs whilst in storage and facilitate further detailed inspection of any defective welds identified.
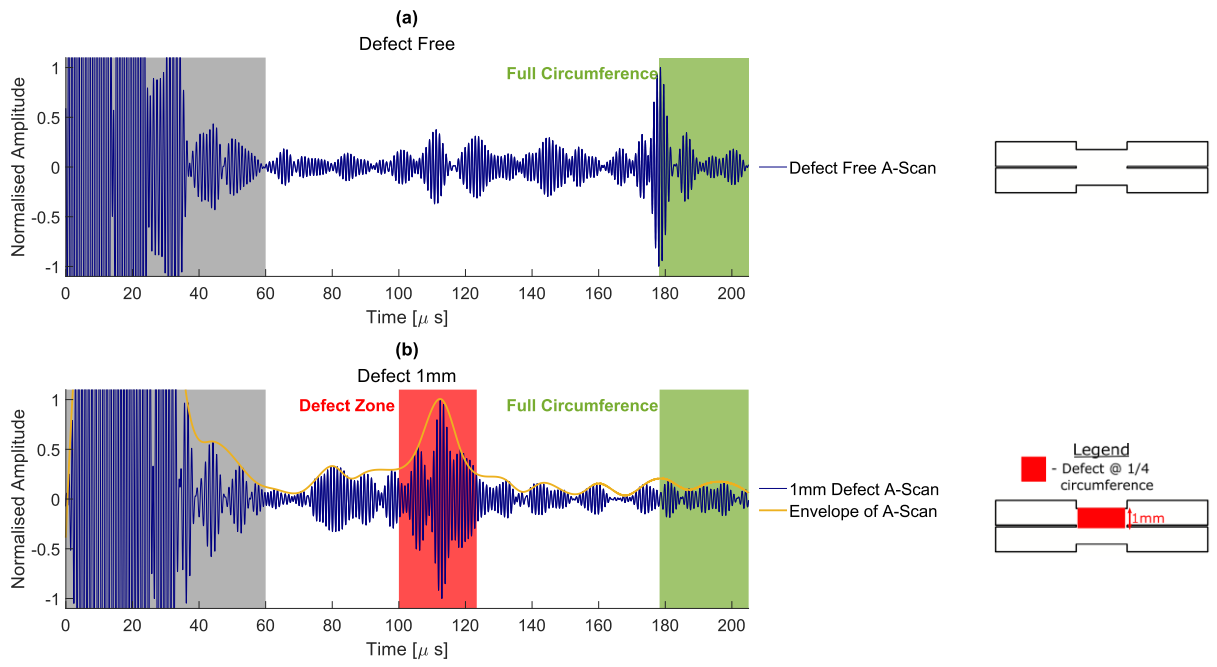
Figure 58: A-Scans on defect-free and defective Cylindrical RSWs

3.3. Summary

This chapter has practically deployed the SAFE method to two differing geometries. To develop confidence in the use of the SAFE method an extensive literature replication on a fusion weld was undertaken. Initial mode identification revealed the same four modes reported in the literature along with successive higher order FGWs. The dispersion properties calculated from the SAFE method was also studied and the same dispersive properties were observed. The SAFE results were validated through FE simulations and the interaction with defects were studied. Reflection coefficients for the SH_1 & SH_3 weld guided modes were reported to 9.99% and 7.34% respectively and were within 1% of the values reported in the literature.

The second section of this chapter explored the use of FGWs for the targeted screening of nuclear grade RSW joints through the SAFE method. Four weld-guided wave modes were identified. Through down selection, the fundamental flexural (F0) weld guided mode, with the average power flow ratio being on average 5.25 times higher than the next highest wave mode, was selected for further study. Several FE models were developed and confirmed the prediction from the SAFE model that a flexural FGW would exist within the RSW. Furthermore, the FE models also investigated the defect sensitivity of the F0 mode to transversal cracks concluding that the defect depth was the primary driver behind strong reflections. Several experiments were conducted on defective and defect-free pseudo RSW structures, flat plate and cylindrical RSWs. For the pseudo weld experiments, it was shown that FGWs, like that of the analytical free plate counterparts, could easily be excited in flat plate-like features with traditional transduction techniques. For the flat plate RSW experiments, it was shown that reflections from through wall and 1.00 mm deep defects could be observed with SNRs of 16.33 dB and 8.21 dB being respectively reported. Lastly, it was shown that for cylindrical canister like RSWs, reflections could also be observed from 1.00 mm deep defects with a SNR of 11.85 dB being reported. These results show the potential of using flexural FGWs to screen RSW joints.

Chapter 4

Ex-situ inspection via automated real time eddy current testing

Unlike the in-situ inspection covered in Chapter 1, there are no accessibility constraints regarding the legacy canister sealed with RSWs when they have been removed from their storage racking. This in turn opens up more inspection modalities that can be used to scan both the RSW and the canister body. As covered in Chapter 2, the thin nature of the RSWs make it well suited to near field eddy current testing.

This chapter presents a robotically deployed real time eddy current array inspection system to address the ex-situ inspection of the legacy SNM canister. The data rich platform allows for a complete digital record to be established of the impedance data gathered and is well suited for further advancements in eddy current inversion to leverage in the future. The robotic deployment of the eddy current array is combined with force torque feedback and enables major sources of noise, resulting from lift-off and wobble, to be reduced. The software infrastructure associated with the eddy current data acquisition is configurable so that different arrays can be used, while the software infrastructure regarding the robotic path planning and control is configurable for different components.

Two different datasets are reported on. The first being eddy current scans of canister bodies with known stress corrosion cracks. All of the stress corrosion cracks were detected, and the resulting SNR of images generated from the impedance data is increased through post processing of the eddy current data. The second dataset is concerned with eddy current scans of RSWs. These scans make use of the FGW, documented in Chapter 3, to localise defects and perform targeted raster scans using the eddy current array in the area of concern. For an operator such as Sellafield, automated and targeted inspection of assets is of value given the health and safety concerns associated with operator handling of radioactive goods, and the large number of assets that are required to be inspected.

4.1. Introduction

The global NDE market size has been valued at USD 6.3 billion in 2021 with a predicted compound annual growth rate (CAGR) of 13.66% from 2022-2029 to hit a total market value of USD 16.66 billion [57]. This high level of growth can be attributed to the rise of "NDE 4.0", in which greater connectivity across the manufacturing supply chain is sought through the integration of connected sensors of which NDE techniques play a role [43]. To deliver this level of interconnectivity, it is now commonplace to see automated robotic delivery of NDE [192]–[195].

The vast majority of the NDE market is based around volumetric inspection of high value infrastructure and components, like automotive/aerospace components or public rail infrastructure, primarily through the use of radiographic and ultrasonic testing [57]. Due to this popularity, the automation of volumetric techniques is the most mature in the NDE industry. Further growth in the automation of volumetric NDE is expected to lag behind other NDE techniques, as innovation has shifted towards more novel and complex delivery of volumetric NDE as well as incorporating advanced imaging and post processing techniques. Examples of these trends include performing volumetric inspection at the point of manufacture for high value components [196]–[201], performing aerial Unmanned Aerial Vehicle (UAV) based volumetric inspection [202]–[205], optimising the amount of data gathered [206], [207], and deploying machine/deep learning in the analysis of the datasets generated [84], [208], [209].

By contrast, the automation of surface inspection is far less mature and from 2022-2029 it is predicted to have the highest CAGR of any NDE technique due to the increased adoption of Eddy Current Testing (ECT) [57]. Of the 'big 5' NDE techniques, eddy current, magnetic particle, and penetrant testing have been shown to be able to detect surface breaking flaws, where others in the 'big 5' (bulk ultrasound and radiographic) struggle [143].

Eddy currents are induced in a sample according to Faraday's Law of Induction [210] when a coil carrying an alternating current produces an alternating magnetic field

and the conductive sample lies within this magnetic field. The induced eddy current in the sample is of opposite phase to that of the coil and sets up its own magnetic field to oppose that of the coil. The eddy current density, $J(z)$, decays exponentially with depth z in an isotropic material, and the sensed impedance is directly proportional to the current density [211]:

$$J(z) = J_0 \exp\left(-\frac{z}{\delta_{sd}(1 + i)}\right)$$

Eq. 103

In the presence of a defect, the current density is altered and this change in current density can be sensed as a change in impedance in the component. The magnitude of the eddy current density decays exponentially and when it falls to $1/e$ of its surface value, the depth at which this occurs is known as the standard depth of penetration, δ_{sd}. The standard depth of penetration is dependent on the frequency of the voltage in the coil, the magnetic permeability, and the electrical conductivity of the component, and is widely viewed as the deepest depth a meaningful change in impedance can be sensed. Due to the exponential decay associated with eddy currents, they are ideally suited to detecting surface breaking defects. This is in direct contrast with bulk ultrasound where the front wall echo typically masks any shallow defects within a component. With correct eddy current probe design and frequency selection, an eddy current can be created that has a standard depth of penetration greater than or equal to the thickness of some thin-walled components, like the canisters used in the storage of low-level nuclear waste.

Magnetic particle testing is restricted to the use of ferromagnetic metals and requires the component to be magnetized/de-magnetized frequently. While penetrant testing is not restricted to any material but it requires the component to be coated in a penetrant and developer, which is frequently undesirable. Both magnetic particle and penetrant testing are subject to great operator error and do not produce discrete data points as a sensor is rastered across the component's surface making automation unfeasible.

131

However, these drawbacks do not exist for ECT, and hence ECT is well suited for automation. As society moves towards Industry 4.0, automation is becoming increasingly important in surface inspection in the immediate future.

In comparison to volumetric techniques, ECT does not suffer from the health and safety concerns associated with radiographic inspection. Additional technical requirements may also prohibit the use of other inspection modalities. For example, multi-angle accessibility requirements and part size limitations may make computed tomography radiographic testing unfeasible. While for ultrasonic inspection, environmental factors may deter the use of couplant. ECT has a significant advantage as single sided access is all that is required, and no couplant is needed to perform an inspection.

Reuse and sustainable business practices are the main drivers behind the increased adoption of ECT, as detecting surface breaking flaws that occur in operation is becoming increasingly important to prolong the safe operation of key assets for industries such as nuclear and aerospace. Furthermore, due to the lower market size, robotic delivery of ECT is far less common with only a few primitive integration efforts being reported in the literature [212]–[215]. To keep pace with the high throughput demands of modern production/maintenance lines, increased robotic deployment of ECT is necessary and vital to capitalise on this demand.

This chapter presents, for the first time, the automated deployment of an eddy current array, via a flexible robotic cell complete with force-torque control, to scan a canister typical of the ones used in the storage of spent nuclear fuel. Previously this was not able to be performed due to the immaturity and variation seen in eddy current array designs, and the lack of technology capable of integrating these two technologies.

Table *2* shows a comparison between previously published papers that feature robotically deployed inspection via an eddy current array and this work. Real-time adaptive control of a 6-axis robotic arm (KUKA Quantec Extra HA KR-90 R3100 [216]) and an external rotary stage (KUKA DPK-400 [217]) with force-torque compensation was accomplished using a framework described in previous work [31]. Force-torque compensation allowed for constant lift-off of the eddy current array during the inspection. This was intentionally done as it has been shown that robotically delivered eddy current inspection offers far less noise when compared to that of manual eddy current inspection [152]. A commercial 32 element padded eddy current array from EddyFi (Part No: ECA-PDD-034-500-032-N03S [218]) with a centre frequency of 500.00 kHz and an operating frequency range of 100.00-800.00 kHz, along with a 64 element Eddyfi Ectane 2 controller [219] were used to perform scans of a 1.4404 stainless steel nuclear grade canister body as well as the welds that seal the canister to the lid. Extensive software infrastructure coupled with the Eddyfi Ectane 2 Software Development Kit (SDK) allowed for the impedance data to be logged and analysed in real time. All data was stored in a proprietary binary file format to allow for further post-processing in MATLAB.

It is envisaged that studies like this will progress eddy current testing to match the level of flexibility and quality enjoyed in the post-processing of ultrasonic datasets [78], [155].

Table 2. Comparison between previously published robotically deployed eddy current inspections and this work

	Mackenzie et al., 2009 [212]	Summan et al., 2016 [213]	Morozov et al., 2018 [214]	Zhang et al., 2020 [215]	This Work
Adaptive Motion	✖	✖	✖	✖	✓
Eddy Current Array	✖	✓	✖	✓	✓
Image Compensation	✖	✖	✖	✖	✓

Where ✓ denotes yes and ✖ denotes no.

4.2. Hardware & experimental summary

Figure 59 shows the experimental hardware used in the automated deployment of the eddy current system. In order to scan cylindrical components, a mechanical chuck on top of a KUKA DPK-400 external rotary stage that has an angular resolution of 0.009° is used. It is noted that the robotic framework has the ability to scan flat samples by moving the array relative to the sample, as well as the ability to scan cylindrical samples by moving the sample relative to a stationary array. The padded eddyfi eddy current array (Part No: ECA-PDD-034-500-032-N03S) is mounted in a bespoke 3D printed housing which is in turn secured to a IP-65 rated gamma force-torque sensor from ATI Industrial Automation [220]. To move the sensor to the start of the motion path for inspection, the eddy current array, 3D printed housing and force-torque sensor assembly, are mounted to the flange of a KUKA KR-90 robot. Both the KR-90 and DPK-400 external rotary stages are controlled via a KRC 4 controller [221].
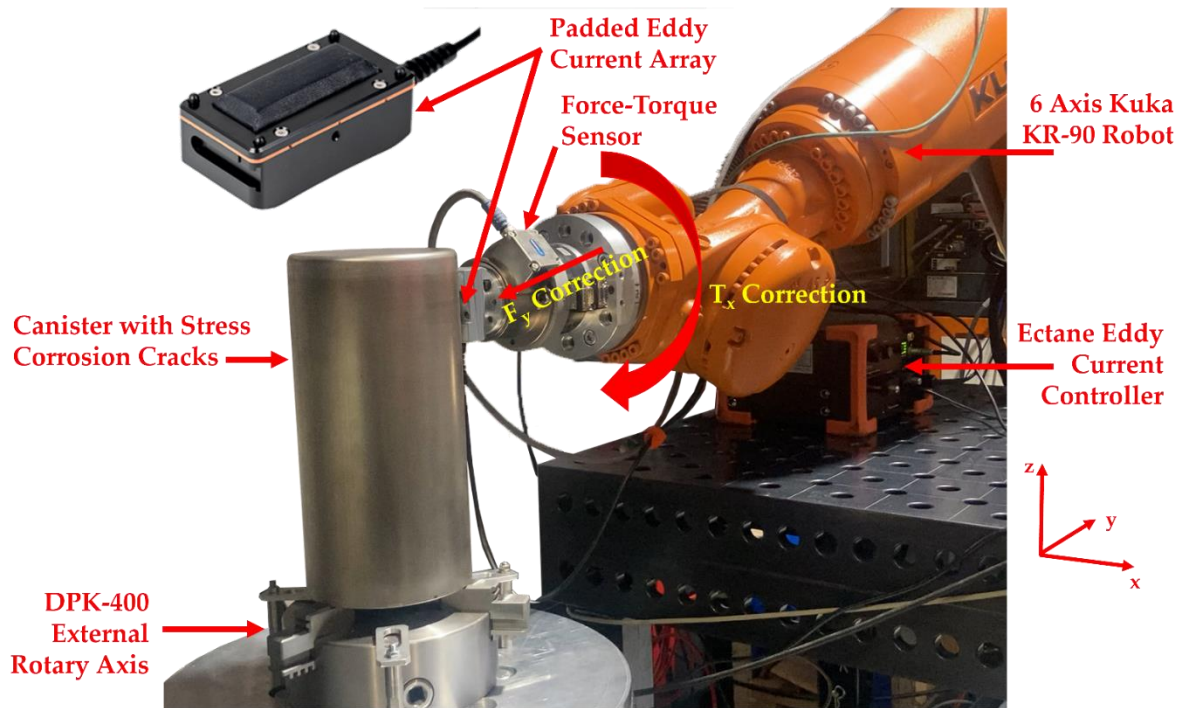
Figure 59. Eddy current inspection hardware with force (F_y) and torque (T_x) compensation annotated.

The eddy current array is deployed to the motion path start point via a LabVIEW program using a framework similar to previously published work [31]. Force and torque in and around all three axes shown in Figure 59 are sensed via the force-torque sensor and are transmitted to a LabVIEW program via the robot controller using the Kuka Robot Sensor Interface (RSI) [222]. The transmission of the force and torque characteristics allowed for: 1) the adaptive motion of the eddy current sensor during inspection; 2) the balancing of the eddy current probe and the subsequent triggering for the acquisition of the impedance data to begin; and 3) the triggering of the movement of the array relative to the sample, or the sample relative to the array. It is important to note that the force-torque sensor was calibrated with all hardware mounted prior to any automated inspection through a program provided by the manufacturer. The calibration enabled the net force and torque values being applied to the eddy current array and mounting assembly to be correctly sensed and subsequently transmitted to the LabVIEW control program for adaptive motion to be performed.

The KR-90 robot presented the eddy current array onto the surface of the component under inspection, and a target force and torque of 10 N & 0 Nm was met in the Y-direction and X-axis respectively for 3 seconds. Once this time period had past, the balancing of all coils within the eddy current array was performed when the probe was stationary. After a further 3 seconds, the impedance data acquisition along with the movement of the array relative to the sample, or the sample relative to the array, was triggered. This achieved the moment of the sample relative to the array or vice versa enabling a raster scan to be performed.

During the inspection, a Proportional Integral (PI) control system was used to monitor and correct both the force in the Y-direction and the torque around the X-axis at the previously mentioned target force and torque values. It was found that P and I values of 0.1 and 0.0 gave an adequate control response. Control of the eddy current probe's orientation in this manner allowed for minimal variations in the lift-off of the eddy current array throughout the inspection providing excellent coupling. Other previously published literature has shown that lift off can be reduced via advanced signal processing and

elaborate probe design [42]. These efforts are often particularly involved and particular to one sample/defect type. As a result, these lift-off compensation strategies are complex to deploy and benefit from. The approach used in this work of utilising a force-torque sensor in combination with a padded ECT array provides experimental flexibility and passively compensates for any lift-off variation at the point of acquisition giving wide reaching benefits.

The acquisition of the impedance data was stopped when the specified motion path had been completed. A singular scan can be summarised by the following process:

1. A connection with the eddy current Ectane device is made
2. The eddy current array is set up with the following parameters:
    a. Probe type
    b. Probe configuration (axial and/or transversal – See Section 4.2.1)
    c. Frequencies
    d. Voltages
    e. Gain
    f. Repetition rate
3. The robot and external rotary axis are set up with the following parameters:
    a. Linear speed of the KR-90 robot
    b. Approach speed of the KR-90 robot
    c. Angular/linear movement of the external rotary stage/KR-90 robot
    d. Angular/linear scan speed of the external rotary stage/KR-90 robot
    e. Target force for the KR-90 robot to apply the array onto the component.
4. The KR-90 robot places the probe against the component and the target force is reached
5. The target force is maintained for 3 seconds
6. The balancing of the eddy current array is performed
7. Wait a further 3 seconds
8. The acquisition of impedance data and the movement is triggered

9. Once the motion path has completed, the acquisition of impedance data is stopped

10. The KR-90 robot moves the eddy current array to a predetermined safe position

11. The acquired impedance data is saved to a binary file for post-processing in MATLAB

4.2.1.   Eddy current c-scan acquisition

Figure 60 shows a generic eddy current array layout along with illustrations of the transmit and receive pairings for the axial and transversal configurations. Depending on the probe geometry, there may or may not be an equal number of transversal and axial transmit and receive pairs. Each pairing in each configuration generates a data point of complex impedance data. The probe is linearly scanned perpendicular to the coil columns as noted in Figure 60, and the data points are logged into a complex 2D-array. The resulting complex arrays can then be post-processed, and the vertical component of the post-processed complex array can be plotted in a C-scan format to show any defective signals with maximum Signal to Noise Ratio (SNR).
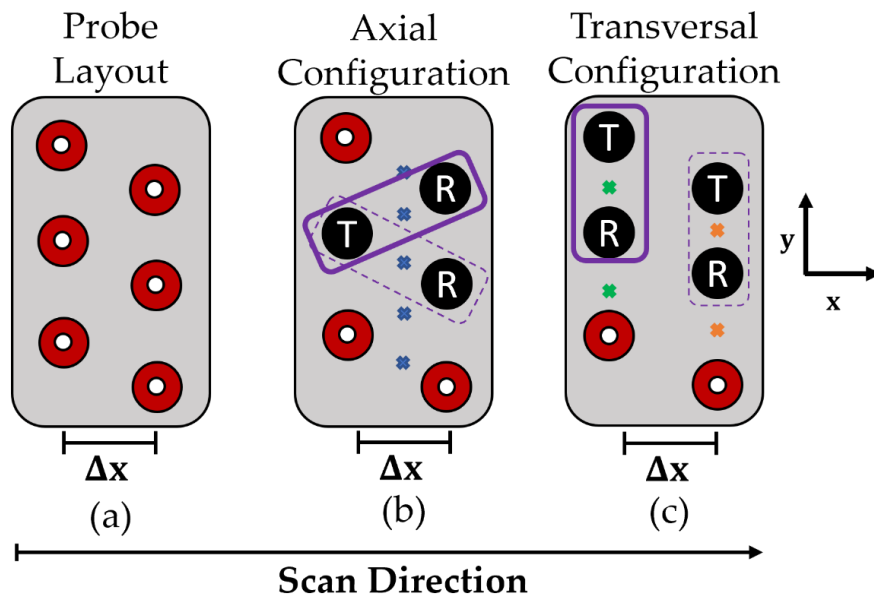
Figure 60. Eddy current array transmit and receive configurations. (a) Generic Eddy current array layout with two vertical columns of coils. (b) Axial transmit and receive configuration where x (in blue) correspond to the transmit/receive pair centres of the excited eddy current channels in the test part. (c) Transversal transmit and receive

configuration where x (in green) correspond to the transmit/receive pair centres of the excited eddy currents in the test part resulting from the first/odd column of coils, and where x (in orange) correspond to the transmit/receive pair centres of the excited eddy currents in the test part resulting from the second/even column of coils.

As can be seen in Figure 60 (b) for the axial configuration, coils in the array are excited in one column and reception of the impedance data is performed across the array in the second column. Conversely, the transversal configuration documented in Figure 60 (c) shows coils being excited and reception of the impedance data being performed within the same vertical column of coils.

The coil firing sequence is changed between the axial and transversal configurations to achieve greater sensitivity to differing defect orientations. With reference to the coordinate system in Figure 60, a larger change in impedance would be observed for a defect that is aligned with the X-axis for a transversal configuration over that of an axial configuration. This is due to the defect more severely intercepting the eddy current that exists between the two transmit and receive coils in the transversal configuration over that of the axial configuration. This greater compression of the eddy currents caused by the defect presence will have a large effect on the electromagnetic field and by proxy the sensed change in impedance. The opposite can be said to be true for a defect aligned in the Y-direction. For further reading, Ye et al. [153] provide a thorough theoretical and experimental investigation of this phenomenon.

It is also evident from Figure 60 that the centres of excitation are not aligned between the axial and transversal datasets in the X-direction. Moreover, for each coil column within the transversal dataset, the data centres are also misaligned. This positional misalignment is corrected for within the LabVIEW program and ensures that the resulting complex array for each dataset have the same spatial grid.

Key to the positional compensation is the acquisition rate of the eddy current array and the angular speed of the rotary stage, so that each acquisition point aligns with an integer number of divisions of half the array coil column pitch, Δx. The acquisition rate and number of divisions between half of the array column pitch are set by the user, and the coil pitch is defined by the geometry of the array. These three variables are used to set

the angular speed of the rotary stage. For example, if an eddy current array has a column coil pitch of $\Delta x = 7.00\ mm$, an acquisition rate of 50.00 Hz, and 50 divisions, the linear speed would need to be $\left(\frac{7}{2} \times \frac{1}{50}\right) / \left(\frac{1}{50}\right) = 3.5\ \text{mm/s}$. This linear speed can then be converted to rotational speed by dividing by the diameter of the canister at 150.00 mm to give the angular speed of the rotary stage at 1.34 deg/s. Whilst individual datapoints are not positionally-encoded, the positional location is extrapolated from setting the angular speed relative to the eddy current probe geometry and acquisition rate as mentioned above. By doing so, it ensures that data is acquired at both the axial and transversal data centre points in the x-axis as the array is linearly scanned.

In order to ensure a common spatial grid, the first and last impedance data points corresponding to a distance of half the coil pitch are discarded within the axial complex array. By discarding the first set of data points that cover half the coil pitch, the axial complex array in the x-direction is synced with the first/odd column of the transversal dataset. Moreover, by discarding the last set of data points that cover half the coil pitch, the axial complex array in the x-direction is synced with the second/even column of the transversal complex array. This discarding of data is shown graphically in Figure 61 (a). The resulting data is then linearly interpolated in the y-direction to align with the y-coordinates of the transversal complex array.

The transversal C-scan array is similarly compensated by separating out the first/odd and second/even columns into separate arrays. Impedance data corresponding to a distance of a full coil pitch is discarded from the start of the odd array. Conversely, the opposite operation is performed on the even array where impedance data corresponding to a distance of a full coil pitch is discarded from the end of the array. This process is graphically illustrated in Figure 61 (b). Once all data is discarded, the odd and even arrays are interleaved together to make one C-scan array that is on the same positional grid as the axial C-scan array.

Once all data has been collected and positionally compensated, oversampling via interpolation is undertaken in the vertical direction of the array. No oversampling is

performed in the horizontal scan direction as this is controlled adequately through setting the rotational speed and acquisition rate of robot as described in the previous paragraphs. The oversampling is performed via linear interpolation of the raw impedance data. It was found that this linear interpolation was fast to implement and produced negligible errors with a maximum error of 2.12% and an average of 0.55% across both the axial and transversal datasets at 250.00 kHz.

By performing data compensation in this manner, a common spatial grid is established for each dataset configuration, enabling like for like comparison and further advanced post-processing techniques such as mixing of datasets.
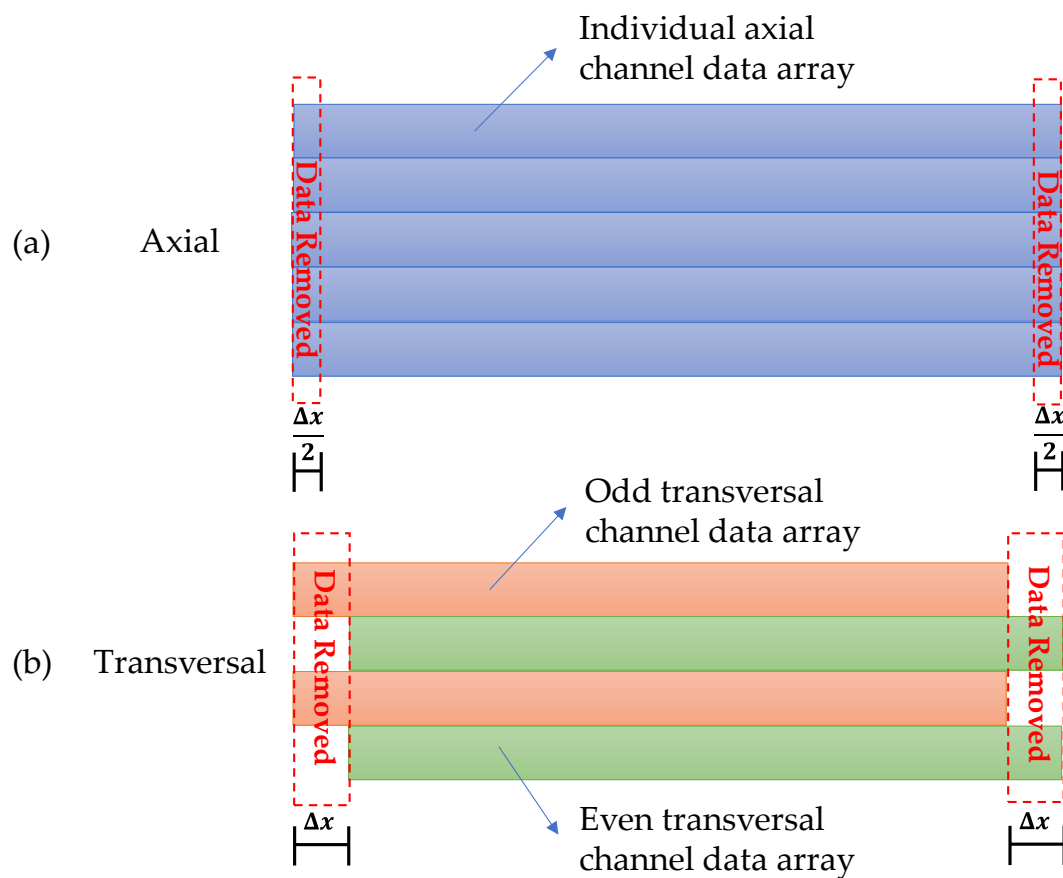
Figure 61. Illustration of complex impedance data positional compensation performed between axial and transversal configurations. (a) Axial complex array positional compensation. (b) Transversal complex array positional compensation

4.2.2. Software infrastructure

Extensive software infrastructure to control the eddy current Ectane device, as well as receive and process the acquired impedance data in real time was developed and is documented in Figure 62. Literature has previously well documented the robotic software infrastructure required [31], [32] and as a result the work presented herein will focus on the eddy current software development effort.
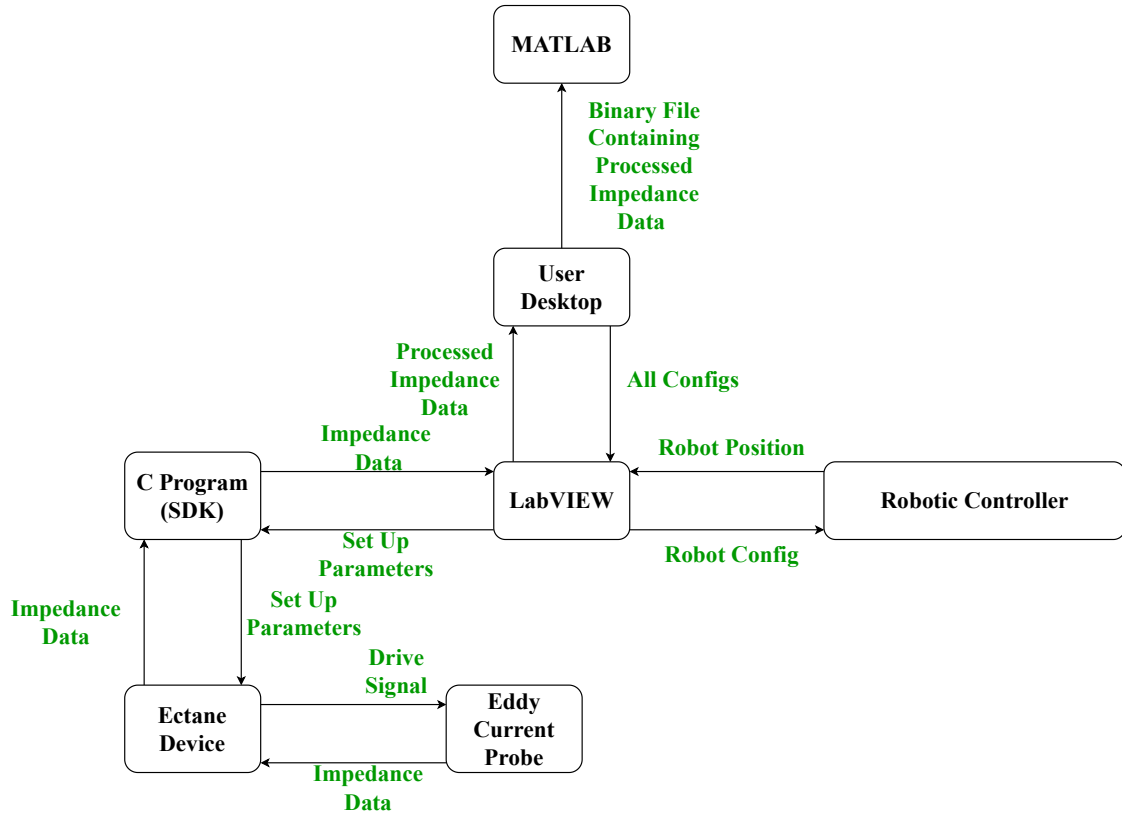
Figure 62. A flow chart showing the data transfer between different software and hardware elements

In total 3 programs were developed: 1) A C program that houses the Eddyfi Ectane 2 Software Development Kit (SDK); 2) A LabVIEW program that receives, post-processes and plots impedance data in real time as well as saving the data in a binary file format; and 3) A MATLAB reviewer program that reads in the binary file for further post-processing.

Both the C and LabVIEW programs are state machines. States within the C program are evaluated through a switch statement within a main while loop. In addition to the main while loop, the C program contains two threads that each have local host Transmission Control Protocol (TCP) connections. The first listens for standardised comma separated string commands from LabVIEW and the other sends 32-bit impedance data from the Ectane device to the LabVIEW program. The same infrastructure with reverse logic is mimicked within the LabVIEW program through JKI state machines [223]. The standardised comma separated string that is sent from LabVIEW is done so in the following format:

```
state, IPAddress, configuration, acquisitionRate, gain,
freq1, voltage1, freq2, voltage2, freq3, voltage3,
freq4, voltage4, freq5, voltage5
```

As can be seen, there are 15 variables housed within the standardised string command. The first of which is the state that the C program should execute, and these are summarised below.

1. Do Nothing
2. Connect to Device
3. Set Up
4. Balance
5. Acquire Data
6. Stop Data
7. Disconnect from Device

The second is the IP address of the Ectane device in order for the C program to connect to the Ectane device. Third is the configuration of the probe (i.e. will axial and/or transversal datasets be acquired? What probe is being used?). Next is the acquisition rate and gain of all Ectane channels. The final ten are the voltages and frequencies of each Ectane channel. As the Ectane device can acquire 5 datasets at different voltages and frequencies each of these must be specified even if some are unused.

The raw impedance data is received in the LabVIEW program as a series of 32-bit numbers and is immediately queued to be sequentially analysed in two additional threads. Using a 6 core, 2.60 GHz Intel i7-8850H processor, it was found that the queueing of the received data was performed in 1ms. Like previously, these threads are implemented via two JKI state machines.

The first thread takes each 32-bit number and separates out the first and last 16-bits of data as these correspond to the imaginary and real impedance components. Additionally, the first thread reformats the impedance data into geometric order as the coils are pulsed in a pseudo-random fashion to prevent crosstalk caused by mutual inductance. Moreover, the first thread compensates for offset in coil excitation in the X-direction. Further details of this coil excitation compensation are provided in Section 4.2.1. It was found that this process was executed in 1ms on a 6 core, 2.60 GHz Intel i7-8850H processor.

The second thread within the LabVIEW program is responsible for interpolation in the Y-direction between axial and transversal dataset configurations, oversampling, basic mixing of different datasets and live plotting of the impedance magnitude. As before, further details of this Y-direction interpolation and mixing of datasets are provided in 4.2.1 and 4.2.3 respectively. Likewise, it was found that this process was executed in 5ms on a 6 core, 2.60 GHz Intel i7-8850H processor. It is noted that the timings reported should be representative for any array used as the software infrastructure is built for the maximum number of elements, channel pairings, and number of frequencies.

This multithreaded approach is illustrated in Figure 63 and provides data acquisition, positional compensation, and interpolation of impedance data whilst displaying various impedance magnitude C-scans in real-time to the user, all within the LabVIEW software environment with minimal 7ms lag. The user can then select a directory to store the acquired data in a binary file format for future post-processing and analysis.

C Program

State machine setting the relevant variables and mode of operation on the eddy current controller

Listener loop

Data Sender Loop

TCP/IP Connection sending standardised string from LabVIEW to C Program

TCP/IP Connection sending impedance data from C Program to LabVIEW

LabVIEW

State machine sending parameters to C program

Data Receiver Loop

Data Formatter Loop

Image Processor Loop

Figure 63. Illustration of the multi-threaded C and LabVIEW programs

4.2.3. Image enhancement of impedance data

It has been shown in the literature that the impedance plane of the acquired data can be complex to interpret and variations in probe lift-off and wobble can commonly be mistaken as signals from defects [224], [225]. Therefore, great care was taken in this work to minimise these adverse effects. Methods such as optimal probe design [226], multi-frequency excitation [224], and phase rotation [225] have been shown to reduce such effects. Due to this work utilising commercial off the shelf (COTS) equipment, only multi-frequency excitation and phase rotation was performed. Multi-frequency excitation of 4 separate frequencies was conducted as the data was acquired and mixing of the datasets as described in Section 4.2.3.2 was performed in post-processing. Additionally, Phase rotation was performed on the acquired C-scan datasets. All post-processing was performed via the MATLAB review application mentioned in Section 4.2.2.

4.2.3.1. Phase Rotation

The signals produced by adverse effects such as lift-off and wobble experience a phase difference to the response caused by a defect on the impedance plane. It is therefore common to phase rotate the data so that the response from the lift-off aligns with the horizontal axis of the display impedance plane , and plot C-scan images of the resulting vertical component of the impedance [227]. Due to the phase difference observed between

the lift-off variations and that of a defect, the resulting C-scan will show any response from a defect clearly.

Mathematically this is described in Eq. 104 & Eq. 105. Eq. 104 describes the resulting acquired impedance array from Section 4.2.2, where the resistive and reactance components are represented by R and X respectively in Ohms (Ω). Eq. 105 describes the mathematical operation performed to phase rotate the data by an angle, θ. This can be done at the point of acquisition or in post-processing. For this study, the decision was taken to phase rotate the data in post-processing to maintain maximum flexibility with the acquired data.

$$Z = R + iX \qquad\qquad \text{Eq. 104}$$

$$Z_{rot} = Z\big(\cos(\theta) + i sin(\theta)\big) \qquad\qquad \text{Eq. 105}$$
$$= (R + iX)\big(\cos(\theta) + i sin(\theta)\big)$$

4.2.3.2. Mixing Eddy Current Datasets

As the impedance data has been acquired on to a common spatial grid, mixing of datasets recorded under differing configurations or frequencies can be performed by superimposing the impedance C-scan data. This is graphically illustrated in Figure 64.
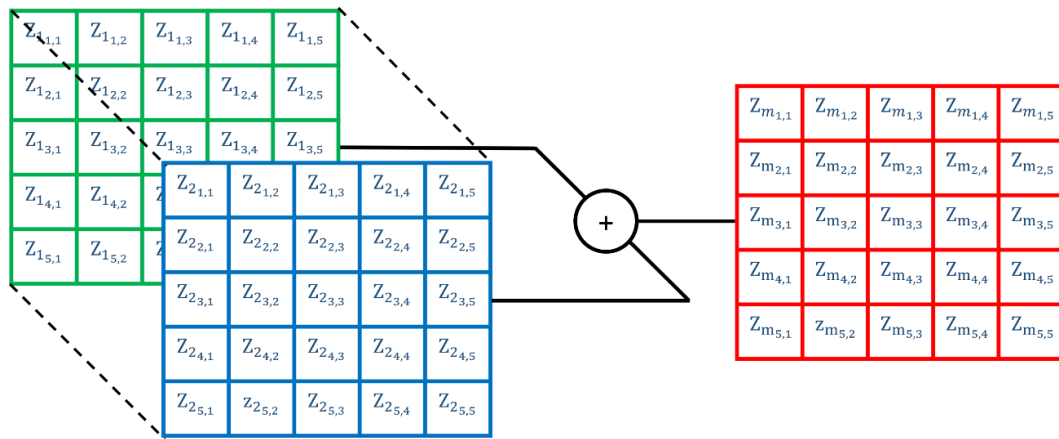
Figure 64. Illustration of mixing datasets Z_1 and Z_2 impedance data to make Z_m mixed data

Two differing mixing methodologies were performed with the first being a simple sum and the second being a selective sum and average. As the name implies, the simple sum, summates complex impedance datasets on pixel wise basis. For the selective sum and average, data above a defined noise floor was summated and everything below was averaged. The noise floor was defined as being 5 times the RMS values reported across a non-defective section of the one of the impedance datasets to be mixed.

4.3. Eddy current scanning of canister body

4.3.1.   Sample overview

As previously mentioned, Sellafield stores low-level waste in canisters made from 0.90 mm thick 1.4404 stainless steel. To allow for effective cooling, the canisters are stored in facilities that are partially open to the environment. Given the coastal location of the UK, stress corrosion cracking is a concern. To this effect, a canister matrix of 16 intentionally induced stress corrosion cracks, shown in Figure 64, were scanned using the automated eddy current platform previous described.

Matrix of 16 Stress Corrosion Cracks
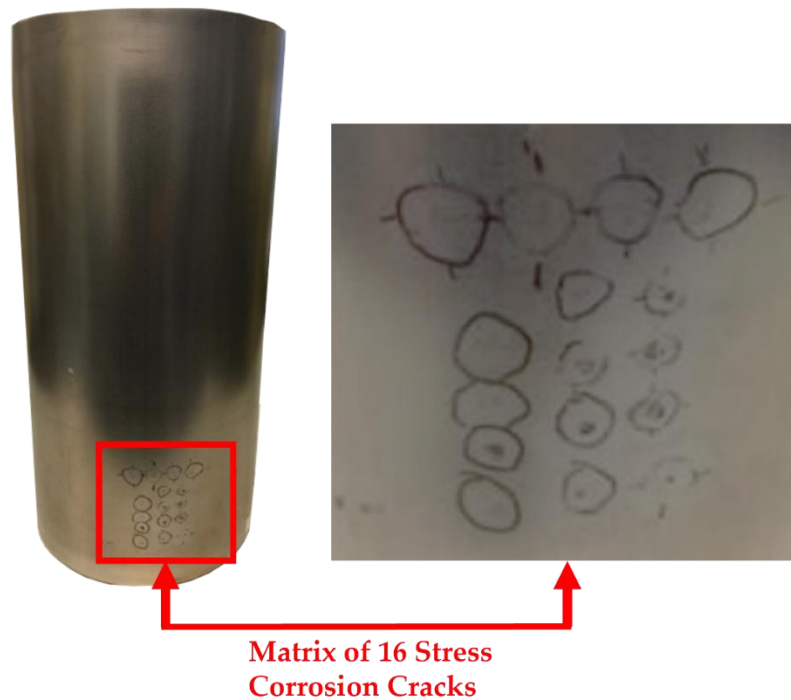
Figure 65. Canisters with a matrix of 16 stress corrosion cracks produced by the Corrosion and Protection Centre within the Research Centre for Radwaste and Decommissioning at the University of Manchester. Depositions of 5μL droplets of sea water, 3.03 g/L of MgCl2, 15.2 g/L of MgCl2 & 30.03 g/L of MgCl2 were used to induce the cracks in the top row, left, central and right columns respectively.

In order for the eddy current array to be pressed on to the canister surface in the direction of the canister' centre, a calibration tool was manufactured to teach the KR-90 robot a new base coordinate system. The calibration tool was made so that it would align the centre of the chuck to the centre of the rotary stage. Additionally, the calibration tool allowed for centring of the tool along with 4 concentric radial calibration points at 15.00 mm in 90.00° increments to be taught to the KR-90 robot. A schematic of the calibration toll is shown in Figure 66.
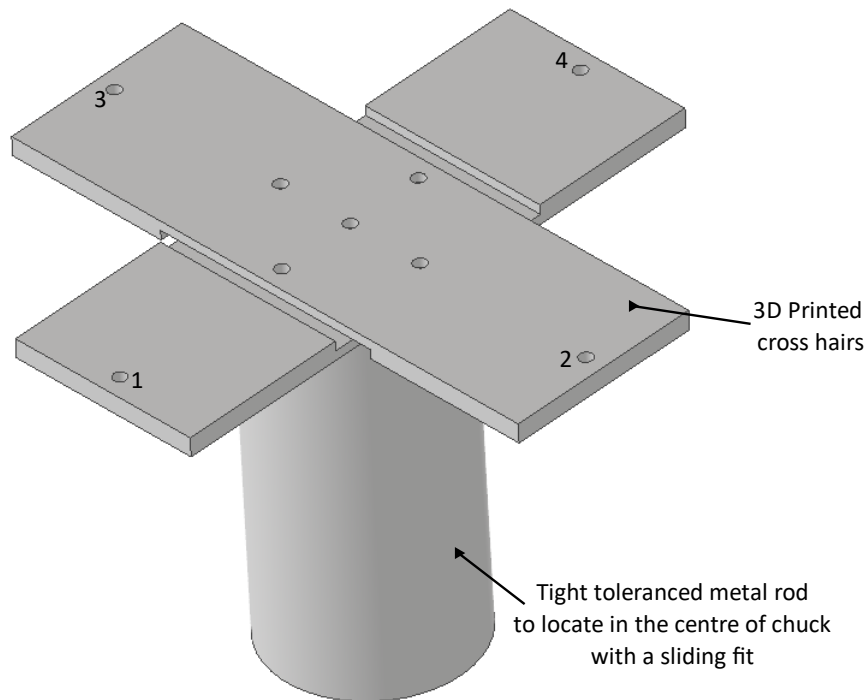
Figure 66: Schematic of calibration tool.

By teaching the KR-90 robot these points, it was able to know where the centre of the canister and rotary stage was relative to its own coordinate system, and ensure motion was performed relative to this point. This effort guaranteed that the eddy current array was always pressed against the canister surface in the direction of the canister's axial centre and helped establish good electromagnetic coupling during the automated inspection.

149

4.3.2.　　Results

　　　　Three 180-degree scans at different heights on the canister shown in Figure 65 were undertaken with both transversal and axial datasets being simultaneously acquired at frequencies of 250.00, 300.00, 400.00, & 450.00 kHz with an amplitude of 2.00 volts for each frequency channel, 30.00 dB of gain, an acquisition rate of 40.00 Hz, and a rotational speed of 1.72 deg/s. Each scan covered an area of 7,687.10 mm^2 (Array Height of 32.63 mm x half the circumference of a 150.00 mm canister equating to 235.62 mm) making the final stitched image representative of an area of 23,061.30 mm^2. The interpolation was set to 5, and the increments between half a coil pitch was specified at 20, giving a spatial resolution of 0.23 mm and 0.056 mm in the vertical and horizontal direction respectively. Positions were chosen for each scan so that they were acquired one array coil vertically above each other with no overlap. The impedance data for all three scans were vertically stitched together and axial channel C-scans of the vertical impedance component from the impedance vector are shown in Figure 67. One of the stress corrosion cracks in the centre of the far-right column is highlighted. To the right of each C-scan, the impedance plane Lissajous for the highlighted defect is also shown along a horizontal cursor passing through the maximum intensity of the defect indication in the C-scan. A Lissajous figure is the variation in impedance observed in the impedance plane and is typically shaped like a "figure of eight" [228]. It can be seen, that the impedance plane response of the same defect for different frequencies varies drastically in amplitude and phase due to the differing interaction depth of the eddy currents with the defect [225].
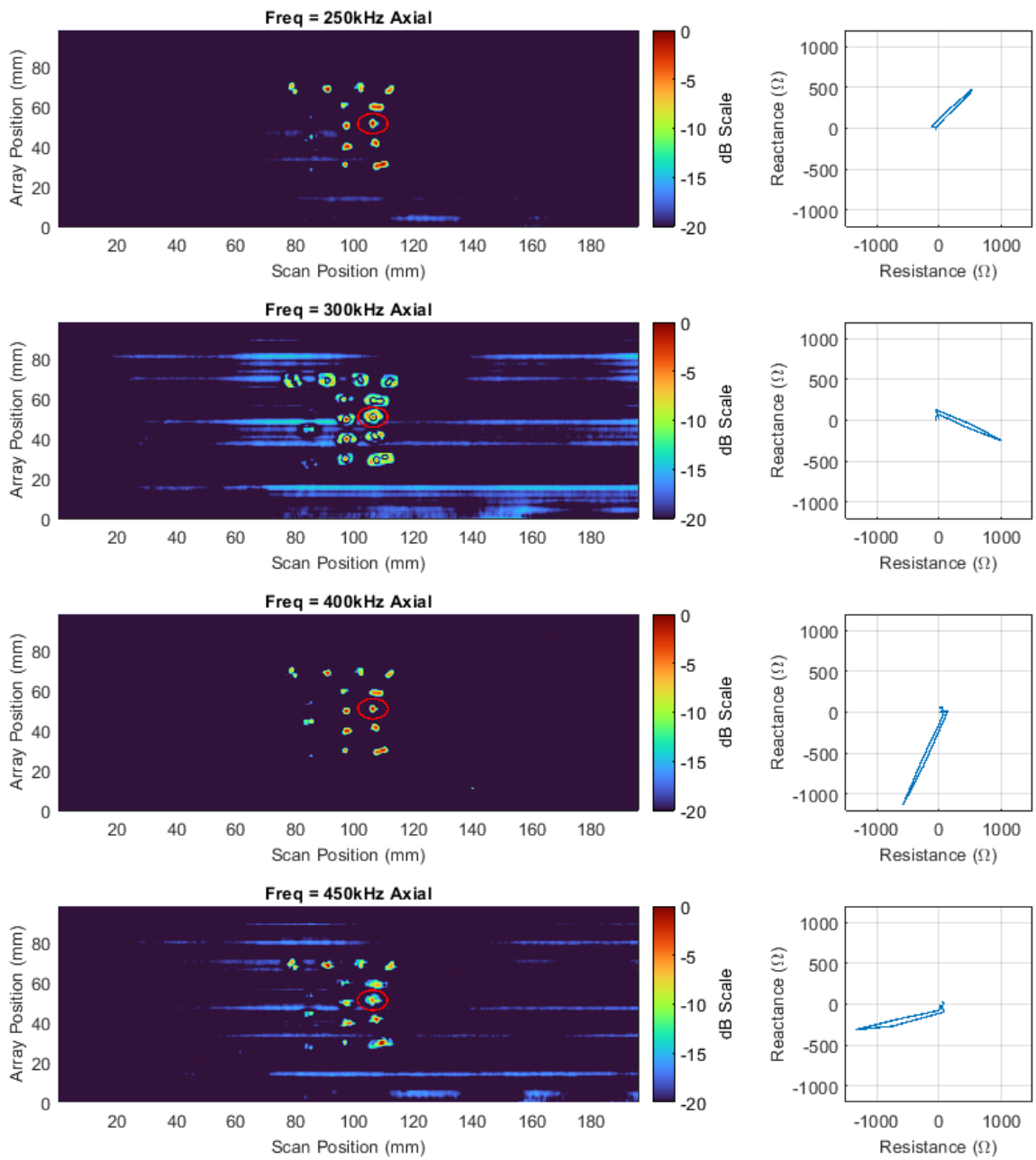
Figure 67. Axial vertical impedance component C-scan images at 250.00, 300.00, 400.00, & 450.00 kHz on a dB scale alongside impedance plane plots of the response from the highlighted defect.

Additionally, Figure 67 also shows that at 250.00 kHz and 450.00 kHz, the impedance plane contains a large horizontal component and as such the resulting image contains a large amount of noise. In order to compensate for this effect, the impedance data at each frequency was phase rotated so that the SNR of the highlighted defect was maximised as is shown in Figure 68.
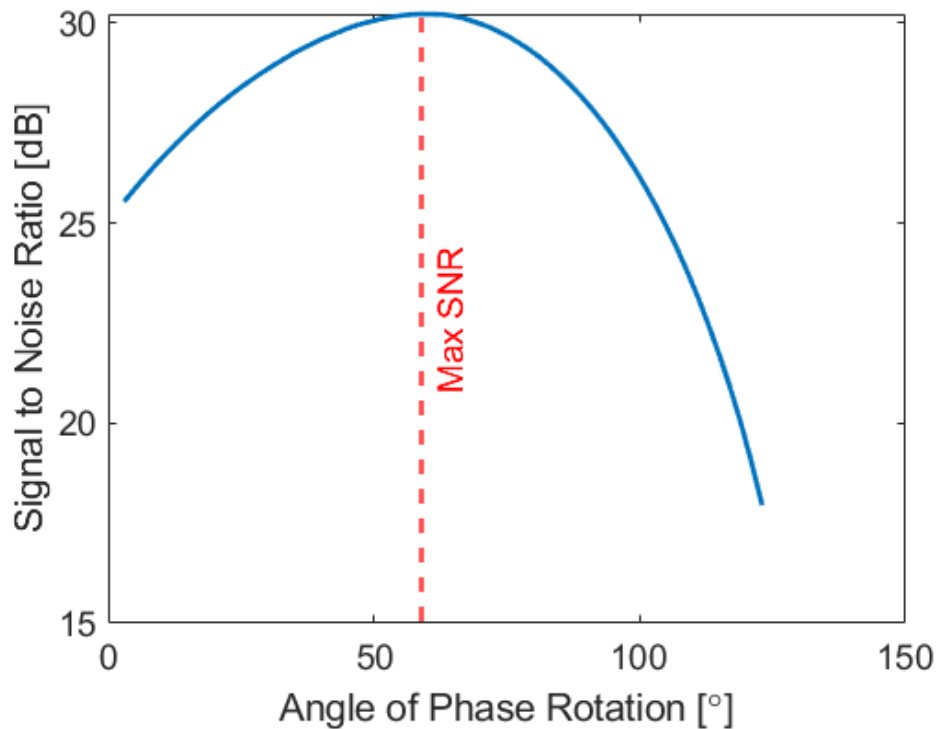
Figure 68: SNR Vs Angle of phase rotation for the axial dataset acquired at 250.00 kHz

Figure 69, shows example Lissajous plots of eddy current data arising from a defect and noise. Figure 69 (a) documents raw eddy current data that has not been phase rotated since acquisition. If we plot the vertical component of the impedance data in Figure 69 (a), a large signal would be recorded for both the noise and defect. In contrast to this, Figure 69 (b) shows data that has been phase rotated so that the noise is approximately horizontal. It is clear that if a plot of the vertical component the impedance data is taken, a large signal from the defect would be registered with a minimal amount of noise. This is the basis for the increase in SNR seen in Figure 68
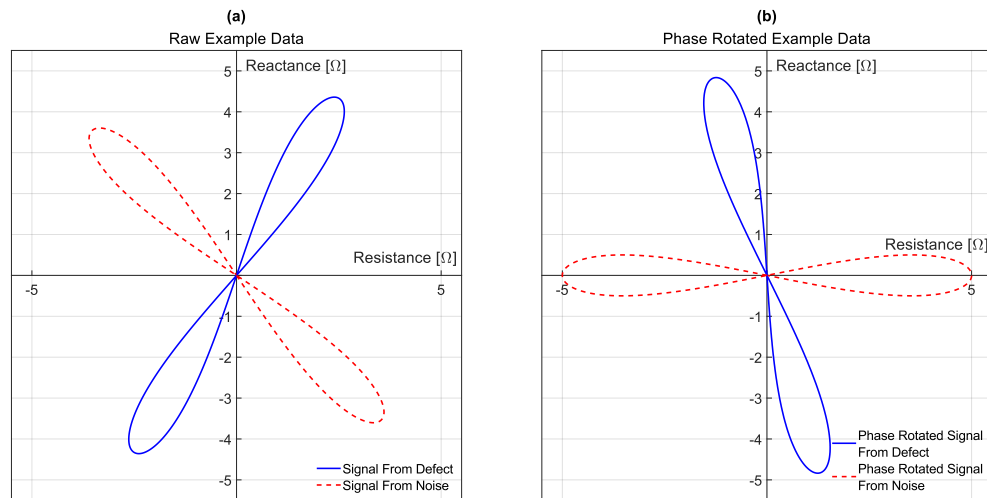
Figure 69: Example eddy current Lissajous plots, (a) raw eddy current data from a defect and noise that has not been phase rotated, (b) eddy current data from a defect and noise that has been phase rotated.

Figure 70 shows C-scan images of the optimised phase rotated axial data, while Table 3 denotes the SNR increases for both axial and transversal datasets at all frequencies recorded for the target defect. The increase in SNR for all defect is visually evident from Figure 70, and on average the SNR was increased by 4.56 decibels for the targeted defect. This result illustrates the effectiveness that phase rotation can have on increasing the image performance of C-scans and the benefit of being able to flexibly perform such a task in post-processing.

Table 3. SNR Values of original and phase rotated data

	250 kHz		300 kHz		400 kHz		450 kHz	
	Original SNR [dB]	Phase Rotated SNR [dB]	Original SNR [dB]	Phase Rotated SNR [dB]	Original SNR [dB]	Phase Rotated SNR [dB]	Original SNR [dB]	Phase Rotated SNR [dB]
Axial	25.02	30.23	20.19	31.22	29.86	31.27	21.11	31.27
Transversal	30.62	32.19	27.43	32.23	31.72	32.28	30.47	32.20
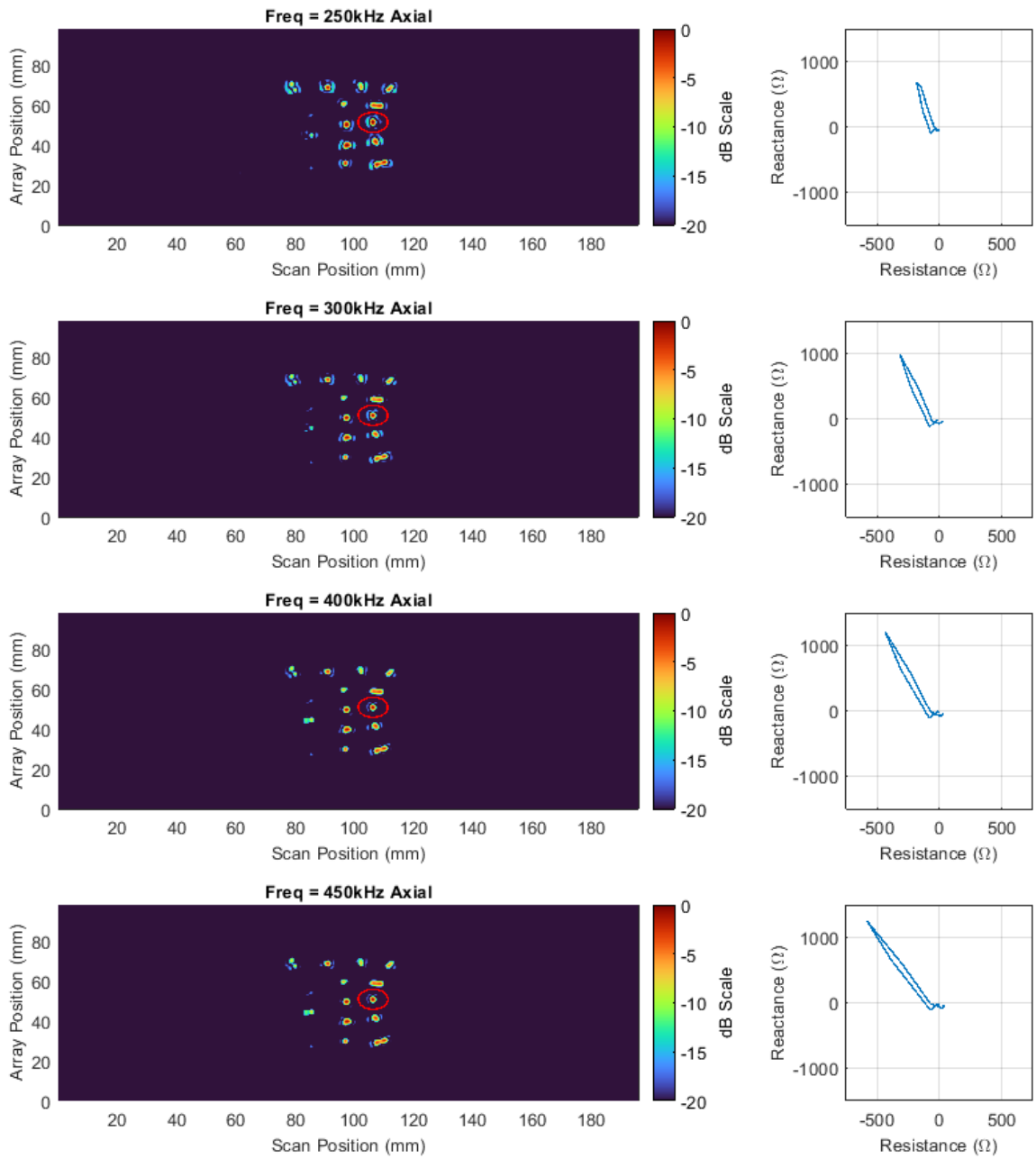
Figure 70. Phase rotated axial vertical impedance component C-scan images at 250.00, 300.00, 400.00 & 450.00 kHz on a dB scale alongside impedance plane plots of the response from the highlighted defect.

To further enhance image quality and reveal more about the nature of the defect, mixing of differing datasets as described in Section 4.2.3.2 was performed. The optimised transversal and axial datasets at 250.00 & 450.00 kHz were mixed together, as the dissimilar frequencies would produce differing eddy current penetration depths and thus be influenced in differing manners. Eq. 106 mathematically describes the penetration depth of an eddy current for a given material, where f is the frequency of the voltage being excited in the array coils in hertz (Hz), μ is the magnetic permeability of the component under test in henries per meter (H/m), and σ is the electrical conductivity of the component under test in siemens per meter (S/m).

$$\delta = \frac{1}{\sqrt{\pi f \mu \sigma}} \qquad\qquad \text{Eq. 106}$$

For stainless steel, with an electrical conductivity of 1.08×10^6 S/m, and a relative magnetic permeability of 1.0025, a frequency of 250.00 kHz would produce a penetration depth of 0.97 mm, while a frequency of 450.00 kHz would produce a penetration depth of 0.72 mm.
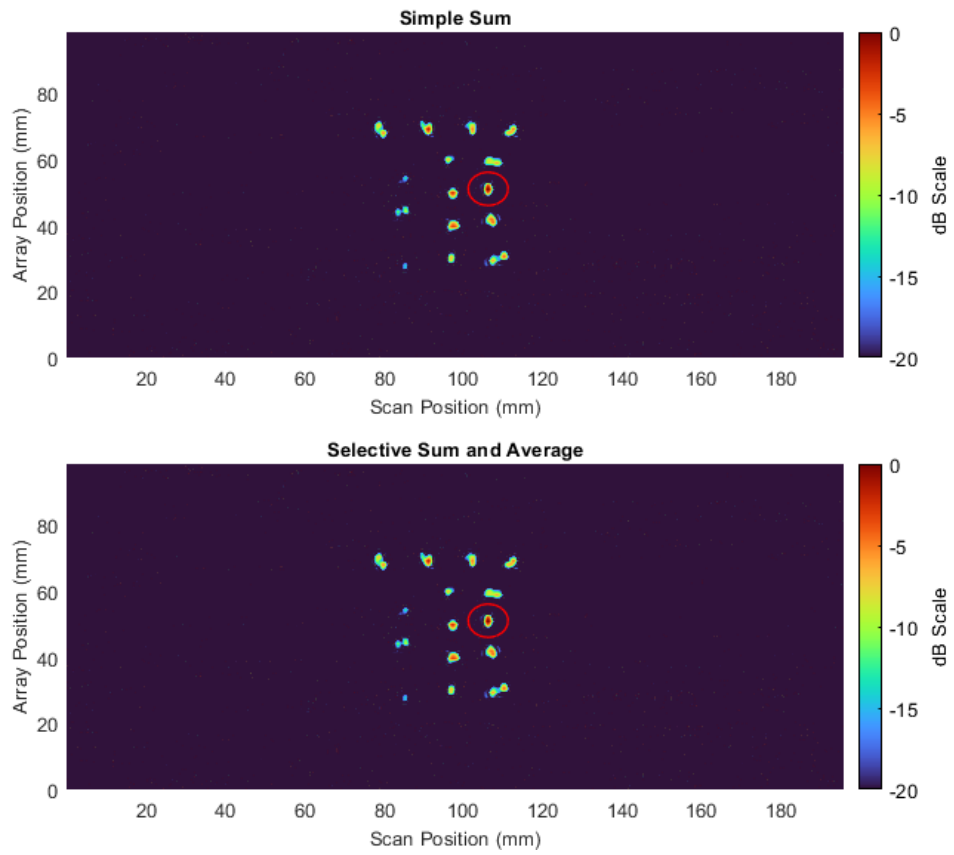
Figure 71. Mixed vertical impedance component C-scan

Table 4. Mixed Image SNR

	250 kHz	450 kHz	Mixed Data Simple Sum	Mixed Data Selective Sum
	Phase Rotated SNR [dB]	Phase Rotated SNR [dB]	Phase Rotated SNR [dB]	Phase Rotated SNR [dB]
Axial	30.22	31.27	31.85	32.66
Transversal	32.19	32.20		

The resulting mixed C-scan image is shown in Figure 71. Like before Table 4, documents the SNR of the highlighted defect. As is shown from Table 4, the SNR of the defect for the simple sum approximates to be the average across all four datasets that contributed to the mixed image, and as such it can be said the imaging performance has not been improved by this mixing methodology. Interestingly, this is a result that is also observed in ultrasound when fusing multi-modal Total Focused Method (TFM) images [81]. By contrast, the selective sum and average technique was able to boost the SNR by an average of 1.19 dB demonstrating an increase in imaging performance.

It is acknowledged that in this study SNR is the only metric being used to evaluate the eddy current detection system. A better metric would be a physical parameter related to the geometry of the defect itself (i.e. crack extent, crack depth) and whether this is better reflected in the mixing of datasets. As reported in the literature, this is a highly complex inversion problem, with successful inversions demonstrated on only simple geometries [229]–[232] or overall dimensions such as the depth or extent on complex defect geometries [233], [234]. In all these studies, the defects were manufactured to specified geometries before eddy current testing which is somewhat removed from a real inspection scenario where prior knowledge of the defect geometry is not known. In addition, the sizing algorithms used vary drastically from defect to defect making the inversion of defect size somewhat deterministic and not well suited to automated deployment and analysis of which this chapter is primarily concerned with. While the current system and signal processing cannot currently invert physical defect size, it has been shown on another sample and different probe better suited to low frequency operation, that the system is able to defect embedded defects ~3.00 mm below the inspection surface.

To understand more about the physical geometry of the highlighted stress corrosion crack, a macrograph of was taken at 96 times zoom and is shown in Figure 72. It can be seen that the defect under inspection is a multifaceted stress corrosion crack. Due to its multifaceted nature, the interaction with the induced eddy current will be highly complex and therefore inversion of the physical geometry would be highly challenging. It is expected that for a simple linear defect, such as a fatigue crack, mixing of datasets would

lead to benefits in defect characterisation even if the SNR was adversely affected. This issue is subject to future work and will be investigated at a later date.

Figure 72. Photo of crack matrix and micrograph (a) Photo of crack matrix with the defect of interest highlighted in a red circle (b) Micrograph of the defect of interest at 96x zoom with desaturated background

4.4. Targeted eddy current scanning based on FGW screening

4.4.1. Sample overview

The same 900.00 mm long flat plate used in Chapter 3 with a through thickness EDM notch in the centre of the RSW was used to illustrate the targeted automated eddy current deployment and assess the benefits of doing so. Figure 73 shows an illustration of the defective sample where the EDM notch is the full weld width at 4.18mm, 0.50 mm long, and through thickness.

Figure 73: Illustration of EDM notched flat plate RSW sample

Few publications try to localise defects via guided wave testing and characterise the detected defects in a more in-depth manner via additional NDE modalities within the same experimental set up. The latter point is commonly unfeasible, as guided wave testing is frequently used when other NDE modalities cannot be due to accessibility issues [235], [236]. However, as businesses seek increasing use of automation, one can visualise a multi sensor automated cell that performs both screening and characterisation, which results in decreased operator requirements and delivers economic efficiencies. This section therefore explores the use of a FGW documented in Chapter 3 to localise and detect defects in order to allow for targeted eddy current deployment and characterisation of the detected defect. Figure 74 shows a modified experimental setup to the one covered in Section 4.2 that integrates the FGW hardware within the eddy current and robotic cell. The readings from the oscilloscope are read into LabVIEW and are used to inform the robot of the approximate position of the defect. The robot then begins the motion path and scans a length of 75.00 mm before the indicated defect and 75.00 mm after the indicated defect.
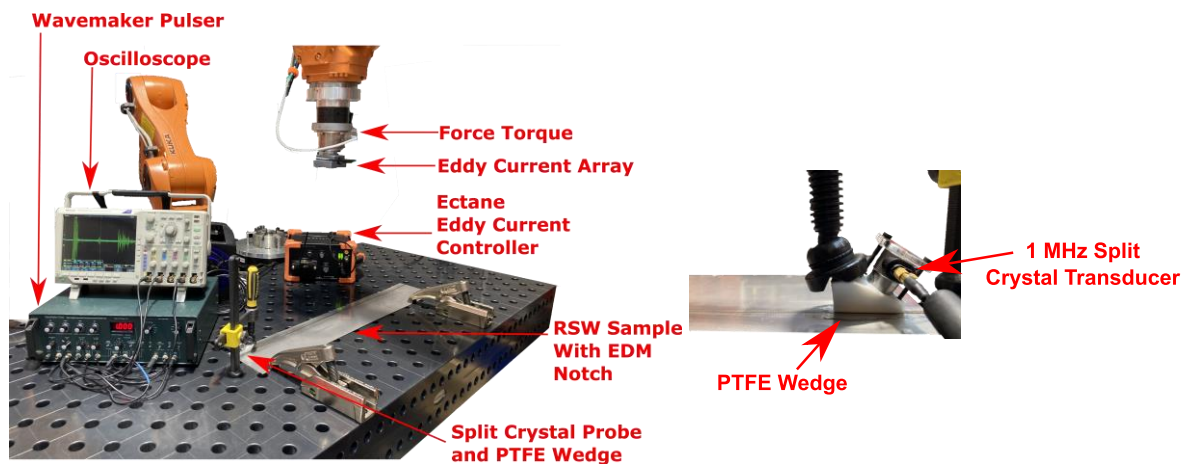
Figure 74: Illustration of the targetted eddy current deployment experimental set up

4.4.2.   Results

Scans on a resistance seam welded flat plate with a through wall defect shown in Figure 73 were performed with the same padded eddy current array noted in Section 4.2. The same FGW experiment documented in Section 3.2.3.2.2 was used and the experimental data reported is representative of the data used to localise the defect. The same set up Impedance data in both transversal and axial configurations were acquired at frequencies of 250.00, 300.00, 400.00, & 450.00 kHz with an amplitude of 2.00 volts for each frequency channel, 30.00 dB of gain, an acquisition rate of 40.00 Hz, and a linear speed of 4.50 mm/s.

Figure 75 shows vertical impedance component C-scans of the axial and transversal datasets acquired at 250.00 kHz. In order to estimate the width of the EDM notch, the -6.00 dB point from the maximum impedance response caused by the defect was monitored. The points highest and lowest -6.00 dB points in the array coil direction was logged and is illustrated by crosses on Figure 75. From monitoring these points in the data produced, the crack length was estimated to be 4.03 mm and 2.20 mm from the axial and transversal dataset respectively. When compared to Figure 73, this represents an error of 3.60% & 47.30% for the axial and transversal datasets when attempting to estimate the width of the EDM notch in this manner. The higher error associated with the transversal dataset is thought to be down to the orientation of the defect with respect to the coil transmit and receive direction as explained in Section 4.2.1. The less severe interruption of the eddy current signal observed in the transversal dataset, leads to it significantly underestimating the EDM notch width while the greater disruption observed in the axial dataset, leads to significantly more accurate EDM notch width predictions.
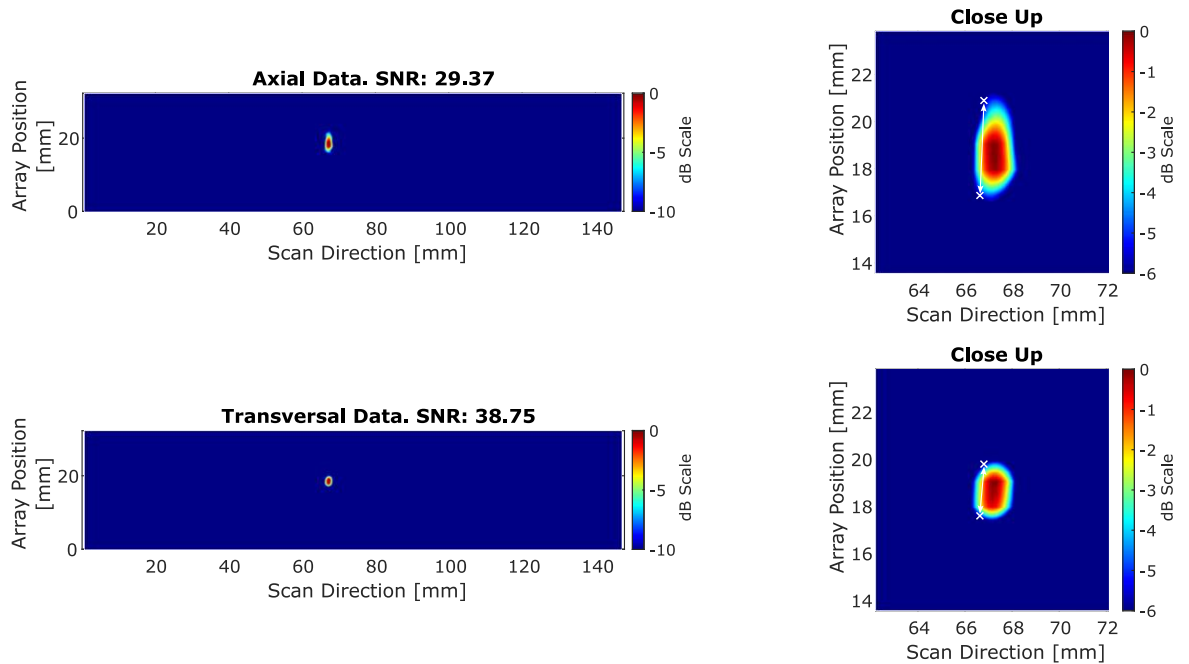
Figure 75: Axial and transversal vertical impedance component C-scan images at 250.00 kHz on a dB scale

In order, to assess the commercial benefits of performing targeted eddy current deployment in combination with a FGW, a series of experiments were timed, and are detailed in Table 5. The series comprised of: 1) raster scanning the entire flat plate; 2) just the RSW; and 3) the 150.00 mm targeted defective region identified by the FGW. It can be seen that by targeting the eddy current deployment to defective regions time savings of ~95% can be realised. For an operator such as Sellafield with several thousand assets requiring inspection, these benefits will further compound and represent sizable operational efficiencies.

162

Table 5: Timed automated eddy current deployment comparison

Scan Type	Time (s)	Percentage Reduction
Full Component	675.6	0%
Full Weld	168.9	75%
Targeted	33.3	95.1%

4.5. Summary

This chapter demonstrates for the first time how eddy current inspection with full image post processing functions can be robotically deployed, showing a significant step closer to Industry 4.0 applications, and addressing the ex-situ inspection scenario. Variations in the lift-off of the eddy current array were compensated for by the use of a PI control system and a force-torque sensor ensuring excellent low-noise coupling throughout the inspection. Extensive software infrastructure was developed that allowed for the eddy current data to be post-processed to enhance the generated images and reveal more about the nature of the defects under inspection.

The capability of the eddy current inspection system was demonstrated by inspecting a nuclear canister with a matrix of 16 stress corrosion cracks and was combined with the FGW work documented in Chapter 3 to inspect the RSWs that seal the canister body to the lid.

Three 180-degree scans were conducted, gathering axial and transversal datasets at 4 different frequencies simultaneously – 250.00, 300.00, 400.00, & 450.00 kHz – detecting 15/16 stress corrosion cracks. In the resulting data, one defect was highlighted, and various post-processing techniques were employed to increase the image quality. It was shown that, by phase rotation alone, the SNR could be increased by an average of 4.56 decibels. Dataset mixing was also attempted, and it was shown that a selective sum and average could boost the SNR by an average of 1.19 dB. The multifaceted nature of the stress corrosion crack under inspection created a complex eddy current interaction, making it difficult to invert the physical geometry of the crack. It is expected that for simpler defect geometries a benefit in defect characterization would be observed through dataset mixing.

Further scans were conducted on a flat plate RSW with a through thickness EDM notch present. The location of the defect was extrapolated via the FGW documented in Chapter 3. Given the simplistic nature of the defect, simple inversion was performed with an error of only 3.6% being report on the crack width for the axial dataset. Commercial

benefits were assessed and it was shown that by performing targeted eddy current raster scans time savings of ~95% could be achieved.

This work demonstrated the detection of defects in real time via eddy current data and showed the ability to further post-process the acquired data to enhance image quality. The benefit of being able to post-process the acquired data in such a manner should not be understated, and it is hoped that similar studies like this can be used to further develop the post-processing of eddy current data to the standard achieved in ultrasonic NDE.

Chapter 5

Ultrasonic Inspection at the Point of Manufacture

The design for the canister of the future is yet to be finalised, but it is envisaged that a GTAW process would be used with significantly larger wall thicknesses (3.00-10.00 mm – see Figure 4) when compared to the RSW on the legacy canister (1.00-2.00 mm). Thick fusion welding produced from GTAW is well suited to ultrasonic inspection [37]. However, considerable delays, often in several days, are encountered from the point of manufacture to the point of inspection to allow for the component to cool and the removal of additional unwanted thermal effects. If inspection at the point of manufacture were to be realised, intervention could be taken to rectify for defects earlier in the manufacturing process, production volumes could be optimised, and lead times would be decreased. There is also quality benefit as inspection records over time can be compared from cradle to grave and establish a "digital twin" [43], [237].

This chapter therefore explores the challenges of inspecting at the point of manufacture, and compensating for the harsh environmental factors, namely temperature. As the canister of the future design is not yet finalised, the hypotheses within this chapter are tested on a 21-pass 16.00 mm thick S275 carbon steel GTAW procedure. Thermal simulations are developed that document the thermal gradients experienced during the GTAW procedure, and the resulting thermal datasets are validated to experiments. It is shown that by using these thermal datasets in combination with advanced path finding algorithms, the positional accuracy of any detected defects is significantly improved, enabling inspection at the point of manufacture.

5.1. Introduction

Ultrasonic phased arrays have become increasingly popular in many NDE applications due to their flexibility, quality, and reduced inspection times [58], [73]. Flexibility in the acquisition of data is ensured since the same array can be used for various differing inspections, while flexibility in post-processing arises from the variety of imaging algorithms that can be applied to the rich ultrasonic datasets acquired by arrays. Advanced array data acquisition strategies, including Full Matrix Capture (FMC) [77] and plane wave [74], have enabled various images to be generated through algorithms, such as the Total Focusing Method (TFM) [78], Phase Coherence Imaging (PCI) [238], the wavenumber algorithm [239], and Inverse Wave Field Extrapolation (IWEX) [240], and have allowed for optimised geometries and features to be detected.

Full Matrix Capture (FMC) datasets, where a complete set of time domain A-scan data is acquired from all combinations of transmit/receive elements, have widely become the *de facto* standard to which imaging algorithms are applied [77]. It is necessary for these imaging algorithms to incorporate some element of *a priori* knowledge in order to accurately detect and characterise any present defects. One such imaging algorithm is the Total Focusing Method (TFM) [78]. In TFM, *a priori* knowledge of the ultrasonic velocity within the component is used in a forward model to create a Time of Flight (ToF) map from each transmit/receive pair to each pixel in the imaging domain. The amplitude corresponding to each of the times in the ToF map is extracted, and the results from every transmit/receive pair in the FMC dataset are then summed. This creates an image that is synthetically focused across the entire domain, leading to increased defect detection and improved characterisation [79]–[82]. Furthermore, as the cost of array electronics continues to decrease and the speed of computation increases, FMC acquisition and TFM imaging is becoming more widespread.

There have been various adaptations of the TFM algorithm from the basic single domain embodiment described in the previous paragraph. Recent innovations include: 1) adapting FMC acquisition and TFM imaging for laser induced ultrasound [241]–[243]; 2)

introducing iterative "ray tracing" algorithms in the forward model to calculate the required ToF maps for multiple material layers [72], [244] and anisotropic materials [245], [246], as well as; 3) incorporating "path finding" algorithms [247]–[249] in the forward model to likewise calculate complex ToF maps. Many industrially relevant applications are realised by the expansion of TFM imaging to multiple material layers and anisotropic materials, especially in relation to the in-process inspection of challenging multi-pass weld geometries [250] and Wire Arc Additive Manufactured (WAAM) components [251]–[253]. Ray tracing algorithms typically rely on an iterative solution of the wave equation via Fermat's principle of minimum time to generate a ray path and subsequent ToF map. Due to their iterative nature, these algorithms have been shown in the literature to be computationally demanding [247] and as a result slow. In order to address these issues, path finding algorithms, that have their origin in computer science [254]–[256] , have been introduced to great effect. Tant *et al.* [248], [249] & Bourne *et al.* [257] have demonstrated that by deploying path finding algorithms, the grain orientation maps for anisotropic media can be efficiently determined. More recently, Singh *et al.* [258] demonstrated that FE datasets in combination with path finding algorithms can be used to train deep learning models to enable real time inversion of microstructural maps.

It is well documented how temperature can affect the ultrasonic velocity within a component made from a specific material [259], and how thermal effects can pose challenges when characterising defects [69], [197], [198], [260], [261]. A thermal gradient within a component can be regarded as a multi layered or anisotropic component with each thermal zone being a different material or phase in the component. These different thermal zones introduce "beam bending" effects arising from refraction and represent some of the hardest inspection scenarios in ultrasonic imaging. The usual *a priori* assumption utilised in imaging algorithms of the ultrasonic velocity being constant within the domain is therefore invalid and needs to be addressed for imaging algorithms to allow for in-process inspection of the canister of the future. These challenging environments are encountered at the point of manufacture for multi-pass welded components. Due to the challenges associated with inspecting at temperature, in high electrical noise environments

168

and the delayed onset of certain defects, industry standards dictate that inspection is carried out after the final deposition and when the sample has cooled to ambient temperature [36]–[38]. This approach makes correcting any defects found post manufacture more complex and expensive, with delays contributing to uncertainty in the manufacturing schedule, with scrapping of the entire component not being uncommon [262], [263]. As businesses shift towards Industry 4.0, there is a demand for automated integration of inspection within the manufacturing process [43], [237]. If inspection of multi-pass welded components were to be performed in-process at the point of manufacture, huge economic benefits would be realised in being able to rectify for defects earlier in the manufacturing process, optimising production volumes, and decreasing lead times. Overcoming these challenges and providing high resolution ultrasonic images of welds at the point of manufacture is therefore highly desirable for many industrial sectors, such as nuclear and, specifically, in the manufacture of the envisaged canister of the future intended for use at Sellafield.

In this chapter, the theoretical approach and experimental verification for the correction of the thermal effects observed in ultrasonic imaging of welded components at the point of manufacture is presented.

Initially, an accurate FE simulations of the thermal environment which mimicked the GTAW procedure specification of a 21-pass, 7-layer, 16.00 mm thick S275 carbon steel weld with a 90° included bevel was created. This thermal dataset was then verified through extensive experimentation in a flexible robotic cell which automatically performed the weld procedure [31], [32], [198] and logged the temperature over time using 13 K-type thermocouples through a National Instruments 9214 temperature module [264]. The results demonstrated that the simulated dataset was in excellent alignment with the experimental thermocouple data with an average error of 1.80%.

With confidence that the simulated thermal data across the full domain was valid and accurate, several 2D ultrasonic FE models were created that produced FMC data representative of a Commercial Off The Shelf (COTS) 64-element array. The FE model domain comprised: an inhomogeneous steel welded plate that allowed for variations in the

169

ultrasonic velocity with a single reflector present in the centre of the weld; a wedge typically used in weld inspection; and absorbing regions to limit the domain size. By using the well documented material properties of S275 steel that vary over temperature, differing thermal zones were able to be replicated within the FE models [64], [265]. The Multi-Stencils Fast Marching Method (MSFMM), a path finding algorithm, was then deployed to compute the necessary ToF maps for the TFM algorithm [71]. It was shown that by compensating for thermal gradients in the simulated datasets, the reflector's indication positional error was reduced by ~3 mm while the focusing performance was negligibly altered. A positional shift of this magnitude is in the order of a weld pass width and thickness which would change the required rework operation to remedy. This result demonstrates the efficacy of the proposed thermal compensation scheme as accurate and fast detection is key for partially filled weld geometries associated with in-process inspection.

Experimental validation was achieved via an autogenous weld being deposited on top of a 16.00 mm thick S275 carbon steel plate with two 2.00 mm Side-Drilled Hole (SDH) reference reflectors positioned to match the fusion interface. The experimental results showed that performing thermal compensation produced no meaningful difference in SNR, but the positional error was reduced by 63.60%. The results presented in this chapter show a significant step towards industrially desirable inspection at the point of manufacture that is highly relevant to the manufacture of the canister of the future.

5.2. Methodology

The exchange of information that underpins the flow of this chapter is depicted in Figure 76. An overview of the theory underpinning the TFM and the MSFMM is given in Section 5.2.1 & 5.2.2 respectively. Further details are then provided for thermal validation (Section 5.3), ultrasonic simulations (Section 5.4), as well as the experimental validation (Section 5.5).
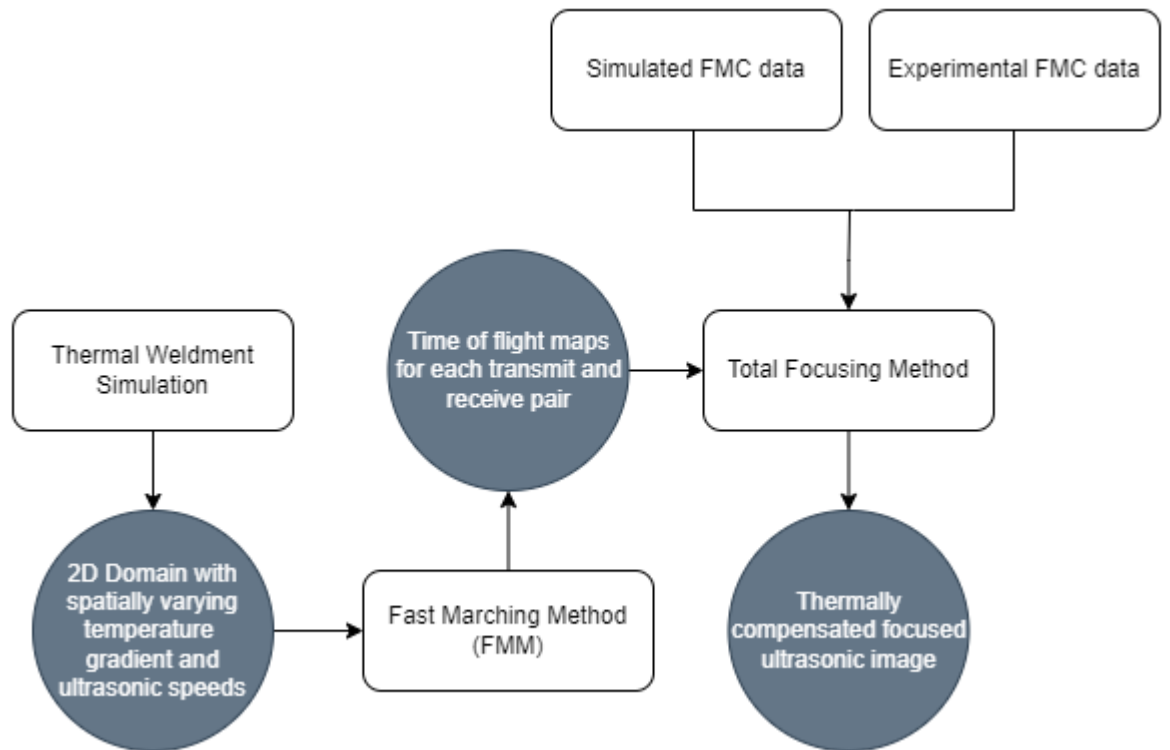
Figure 76: Flowchart showing the various modelling techniques and algorithms used within this study

5.2.1. Total focusing method

The TFM is a standard imaging algorithm for detecting and characterising defects used widely across the NDE community. TFM uses the FMC dataset, consisting of recorded signals, referred to as A-scans, transmitted at each element of an ultrasonic array, s_{xy}, and received at all elements of the ultrasonic array, $r_{x,y}$, over time, t. Each recorded A-scan can therefore be denoted as $A_{s_{x,y}r_{x,y}}(t)$.

Conventional TFM algorithms assume a constant wave speed, c, throughout the entire domain, and calculates the distances from each transmitting element, s_{xy}, to each receiving element, $r_{x,y}$, to every imaging point. With the distance and speed known, this enables the calculation of the travel times in the imaging domain and be related to an amplitude in the corresponding A-scan. The intensity of each pixel in the TFM imaging domain, $I(x_i, y_i)$, is the sum of all amplitudes in each A-scan of the FMC dataset. This is mathematically described in Eq. 107, where x_{s_x} and y_{s_y} are the x and y coordinates of the transmitting ultrasonic array element, and x_{r_x} and y_{r_y} are the x and y coordinates of the receiving ultrasonic array element.

$$I(x_i, y_i) =$$

$$\left| \sum_{s_{x,y}=1}^{N} \sum_{s_{x,y}=1}^{N} \left(\frac{A_{s_{x,y}r_{x,y}} *}{\left(\sqrt{(x_{s_x} - x_i)^2 + (y_{s_y} - y_j)^2} + \sqrt{(x_{r_x} - x_i)^2 + (y_{r_y} - y_j)^2} \right)}{c} \right) \right| \qquad \text{Eq. 107}$$

The mathematical description contained within Eq. 107, is accurate for an isotropic domain which has constant material properties that are spatially invariant. As alluded to previously, an isotropic material in the presence of a thermal gradient introduces spatial variations in the ultrasonic velocity as a function of the applied thermal gradient. It is

therefore necessary to incorporate an approach where the simplistic geometric forward model is replaced with one that is more complex and can account for spatial changes in material properties. This generalised ToF map could be calculated by any forward modelling technique, however, for this study, the MSFMM was used to compute the required ToF maps by solving the Eikonal equation. Implementation of the TFM algorithm in conjunction with the MSFMM has been previously referred to as TFM+ in previously published work [248], [249]. By using the MSFMM in this manner, it can be said that for an array of N elements, N ToF maps are generated from each source to each pixel in the domain. Assuming a pulse-echo set-up, source-receiver reciprocity can be invoked, where the travel time for a wave to travel from each transmitting element to each pixel can be assumed to be the same as the travel time from each pixel to each receiving element. Therefore, the TFM image intensity can be calculated through Eq. 108 with the introduction of, τ, to represent a generalised ToF map. This generalised ToF map is expanded upon in Section 5.2.2 and is formally documented within Eq. 109.

$$I(x_i, y_i) = \left| \sum_{s_{x,y}=1}^{N} \sum_{s_{x,y}=1}^{N} A_{s_{x,y}r_{x,y}}\big(\tau_s(x_i.y_i) + \tau_r(x_i.y_i)\big) \right| \qquad \text{Eq. 108}$$

5.2.2. Multi-stencils fast marching method

To calculate the travel times through spatially varying medium, forward model must be used. The MSFMM is used as the forward model to simulate the wave front propagation in the heterogenous steel domain and to provide accurate estimates of travel times, accounting for the varying velocities and resulting wave refraction caused by the presence of thermal gradients. The MSFMM is an adaptation of the original Fast Marching Method (FMM) first proposed in [71] for generating computational solutions to the nonlinear Eikonal equation, and by extension related static Hamilton-Jacobi equations. FMMs make use of entropy satisfying upwind schemes and fast sorting techniques to produce highly accurate, repeatable, and efficient results. The FMM discretises the domain into a grid and uses computational methods to find the fastest ray path to each pixel in the domain from

each element in the ultrasonic array. The traditional FMM has been shown to be inaccurate along diagonal trajectories on coarsely discretised domains as only the nearest neighbours in each node are considered. As the wavefront propagates through the discretised domain, errors accumulate and compound along the directions between axis vectors. To avoid this issue, the MSFMM [266] is used in this study which adds the diagonals to the shortest time calculation by performing a 45° rotation to the original four-point stencil. This higher order fast marching method (on which MSFMM is based) has been shown to diminish the grid bias and converge to the underlying geodesic distance when the grid step size tends to zero [267]. The MSFMM is shown graphically for one nodal search point in Figure 77. Various differing embodiments of the MSFMM have been developed and successfully been deployed in similar studies to account for refraction in isotropic [248] and anisotropic media [249]. For this work, only spatially-varying isotropic media is considered.
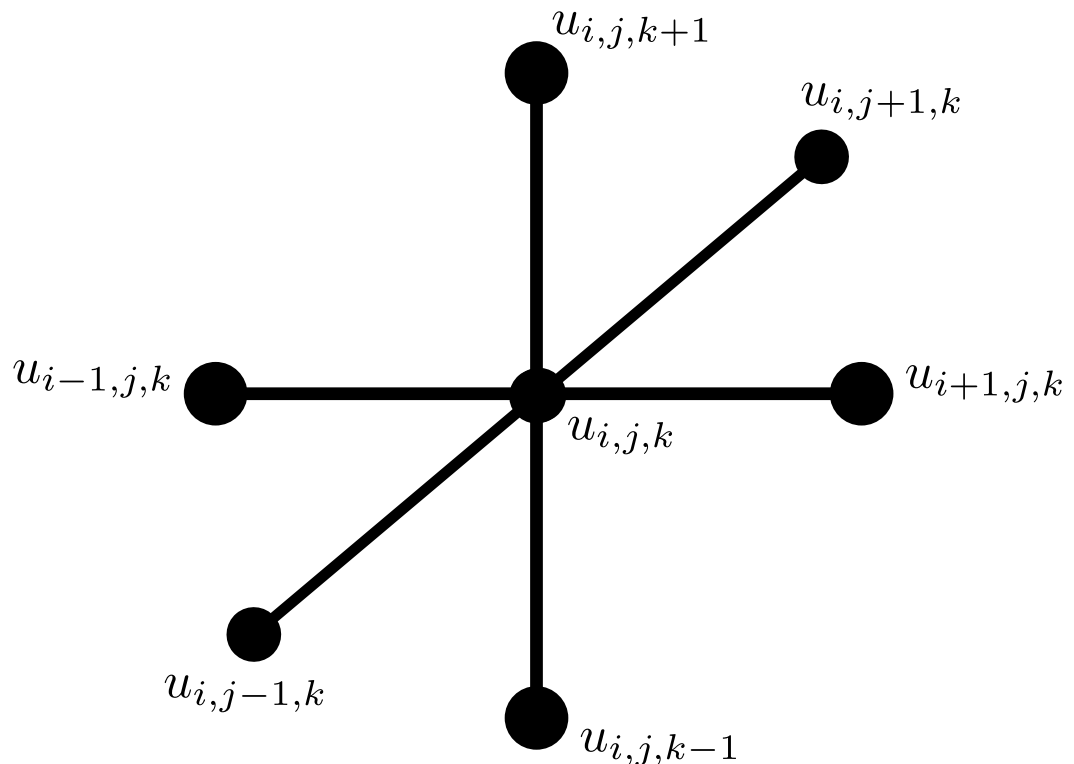
Figure 77. MSFMM schematic of a single nodal search in 3D space.

The MSFMM solves the Eikonal equation stated in Eq. 109. $\tau(x_i, y_i, s_{xy})$ denotes the minimum travel time for a wave to travel from the transmitter $s \in \partial I$, on the boundary of the discretised image domain $I = x \times y$, to the point $(x_i, y_i) \in I$. An upwind finite difference scheme is used to solve for $\Delta\tau(x_i, y_i, s_{xy})$ [268], where $V(x_i, y_i)$ is the velocity model depicting the velocity at point (x_i, y_i).

$$\left|\Delta\tau(x_i, y_i, s_{xy})\right| = \frac{1}{V(x_i, y_i)}$$

Eq. 109

Solving Eq. 109 over a regular grid with an associated velocity field, the shortest travel-time between each transmitter, $s_{x,y}$ and receiver $r_{x,y} \in \partial I$ can be calculated, and the travel time matrix constructed. An example TOF map produced from the MSFMM is documented in Figure 78
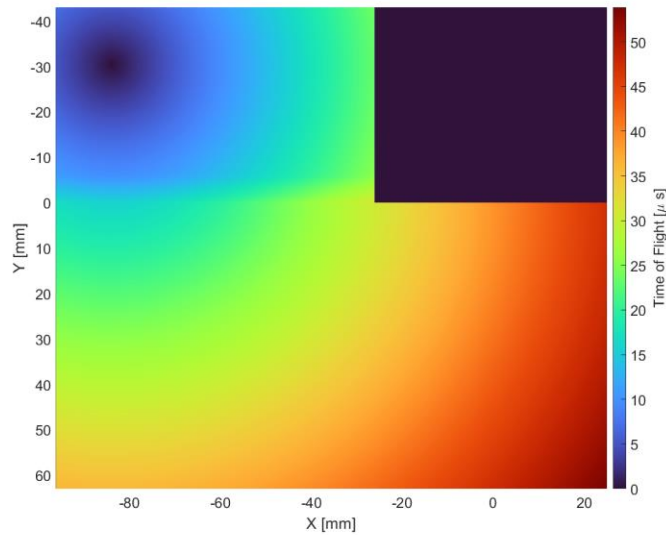
Figure 78: Example ToF Map produced by the MSFMM

It is noted that other physical phenomena such as scattering, attenuation and dispersion are ignored and only the travel time information is modelled. FMM algorithms such as the MSFMM have been shown to be an efficient, robust, and fast method for computing travel times for complex spatially-varying media [269]. Thus, imaging techniques, like TFM, that require a time-of-flight for many pixels in an imaging domain, prosper from the use of such an algorithm. A more thorough theoretical overview of the MSFMM is outside the scope of this work but readers are referred to Hassouna & Farag [266] for further information and discourse.

5.3. Thermal simulation & experimental validation

In order to quantify the thermal gradients that could be experienced during in-process inspection, several 3D thermal simulations of a 21 pass, 7-layer, 16.00 mm thick carbon steel S275 weld with a 90.00^o included bevel were performed in the commercial FE package, COMSOL [175]. A total of 7 models (see Figure 80 (b) & Table 6) were produced to mimic the thermal gradient observed for each layer during a GTAW process. An ambient convection and radiation boundary condition was applied of 20^oC at the surface of the steel for all models. The steel was modelled with a specific heat capacity of $475 \frac{J}{kgK}$ and a thermal conductivity of $44.5 \frac{W}{mK}$. Each model domain was 600 x 16 x 400 mm, comprised ~15,605 tetrahedral elements and is shown in Figure 79.
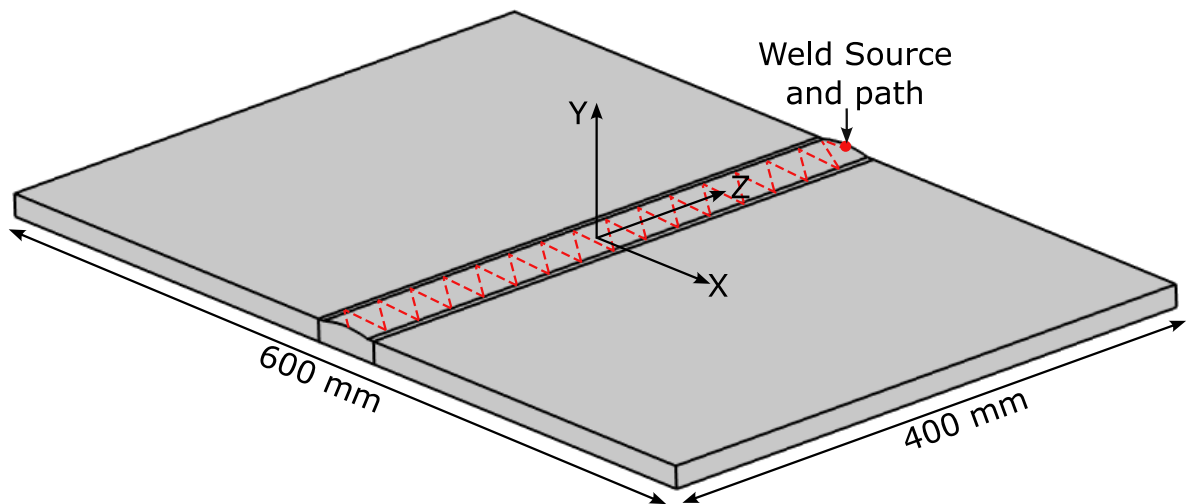
Figure 79: Schematic of COMSOL domain for the final pass with co-ordinate system marking the centre of the domain

Experimental verification of the simulations was undertaken in tandem. Two steel plates 300.00x16.00x400.00 mm in size with a 90° included bevel were fabricated as shown in Figure 80 (a). The weld procedure is documented in Figure 80 (b) with each pass sequentially numbered. Pass 1 and 2 refers to layers 1 and 2 respectively, while passes 3-4, 5-7, 8-11, 12-16, 17-21 refer to layers 3, 4, 5, 6 & 7, respectively.
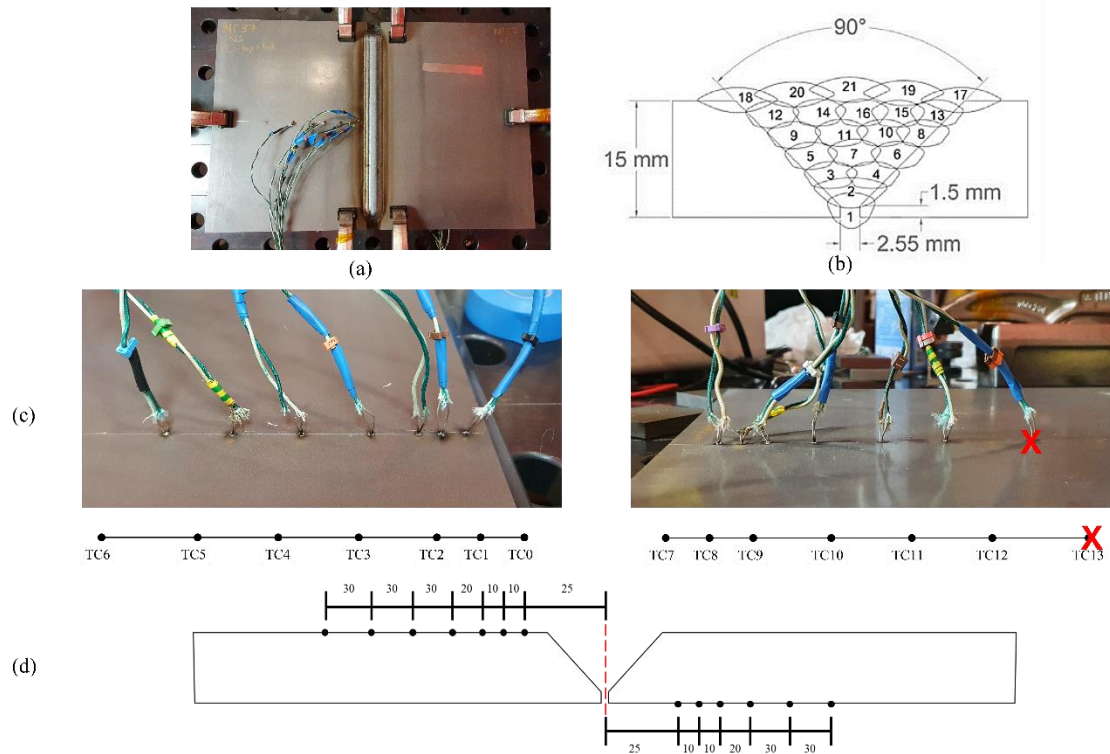
Figure 80: Schematics describing the experimental setup. (a) A photograph showing the completed welded assembly of two 300.00x16.00x400.00 mm S275 carbon steel plates, (b) A cross-sectional schematic of the welded fabrication documenting the weld procedure specification where the numbers refer to the sequential order of each weld pass, (c) Photographs showing the experimental thermocouple placement along with their respective label where faulty thermocouples are denoted with a X (in red), (d) A schematic denoting the thermocouple placement with respect to the centre of the weld. Note: The distances shown are not to scale but occur in the same order as documented in Figure 3(c). TC = Thermocouple.

A total of 13 K-type thermocouples were attached to the plates prior to welding. Seven were attached to the upper surface of the left-hand plate and six were attached to the bottom of the right-hand plate, as shown in Figure 80 (c) & (d). For the last pass in each layer, the temperature was recorded for a total of 380 seconds.

A robotic cell as described in previously published work was used to automatically perform the welding procedure [31], [32]. For all passes performed by the robotic system, the welding parameters documenting the welding current, voltage, travel speed, weave amplitude and frequency are given in Table 6.

178

*Table 6: Welding Parameters. * Automatic Voltage Correction (AVC) used in the robotically deployed weld process.*

	AVC set voltage (V) *	Current (A)	Travel Speed (mm/min)	Wire Feed Speed (mm/min)	Weaving Amplitude (mm)	Weaving Frequency (Hz)
Pass 1	12.00	120.00	50.00	910.00	2.00	0.30
Pass 2	13.50	220.00	100.00	1225.00	4.00	0.60
Pass 3-16	13.50	210.00	120.00	1470.00	3.00	0.55
Pass 17-21	13.50	240.00	100.00	1225.00	4.00	0.60

After each layer, a laser scan with a 2910-100 Micro-Epsilon laser scanner [270] was performed to document each layer's geometry. These scanned cross sections were used to generate CAD models for the thermal simulations and are shown in Figure 81.
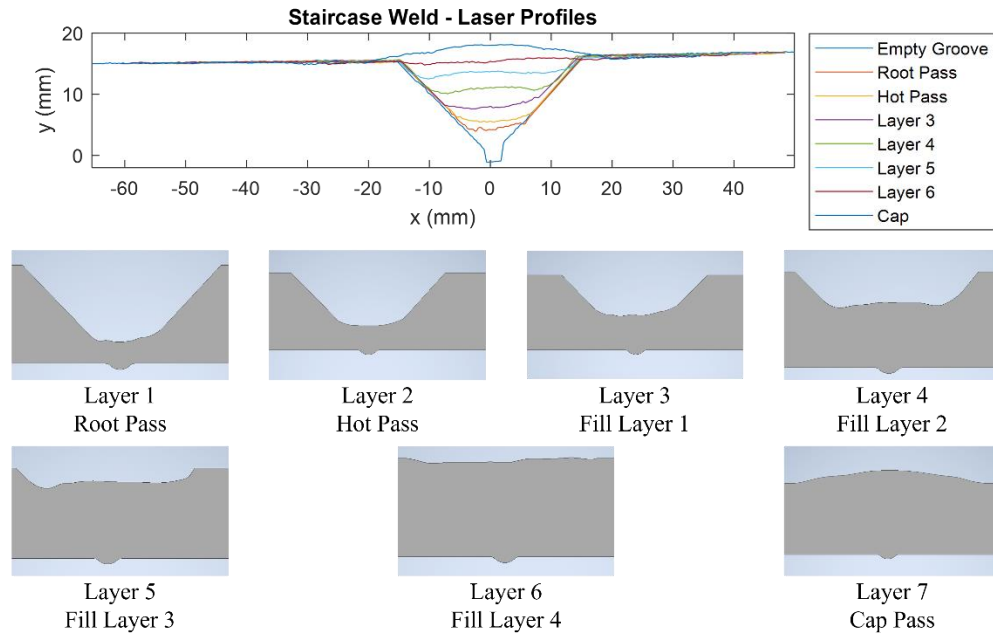
Figure 81: Laser profiles of each layer along with 2D CAD schematics.

For the thermal simulations, the welding source was modelled as a confined gaussian heat source [271], [272] as defined in Eq. 110. Where φ_q is the heat flux in W/m^2, η is the weld efficiency factor, P is the weld power, r_{spot} is the arc radius, and r_{focus} is the spatially and temporally dependent centre of the gaussian function. A weld efficiency

179

factor of 0.7 and spot size of 3.00 mm were used in this study. The weld power was determined by the multiplication of the voltage and the current for each pass as described in Table 6.

$$\varphi_q(x,z,t) = \frac{2\eta P}{\pi r_{spot}^2} e^{-\left(\frac{2r_{focus}^2}{r_{spot}^2}\right)}, \qquad t < t_{pass} \qquad \text{Eq. 110}$$

$$r_{focus}(x,z,t) = \sqrt{\left(x - x_{focus}\right)^2 + \left(z - z_{focus}\right)^2} \qquad \text{Eq. 111}$$

$$z_{focus}(t) = \left(a_z - \left(\frac{2a_z}{\pi} m \cos^{-1}\left(\cos\left(\frac{2\pi}{p_z}t\right)\right)\right)\right), \qquad t < t_{pass} \qquad \text{Eq. 112}$$

$$x_{focus}(t) = \frac{A_x}{2} \sin^{-1}\left(\sin\left(\frac{2\pi}{p_x}t\right)\right) + x_{offset}, \qquad t < t_{pass} \qquad \text{Eq. 113}$$

With reference to the co-ordinate system in Figure 79, Eq. 111-68 mathematically describe the spatial and temporal variation in x_{focus} & z_{focus} which contribute to the vector sum of r_{focus}. x_{focus} is a triangular wave which describes the weaving pattern of the weld torch centre in the x-direction over time. The weave had an amplitude, A_x, and a period, p_x, that corresponded to the weld variables given in Table 6, while x_{offset} was adjusted to align with the centre of the next deposited weld pass – see Figure 80(b). For layer 7, the weave pattern is annotated in Figure 82 for the first 20 periods. It is important to note that the weave pattern will vary throughout the welding process according to Table 6.
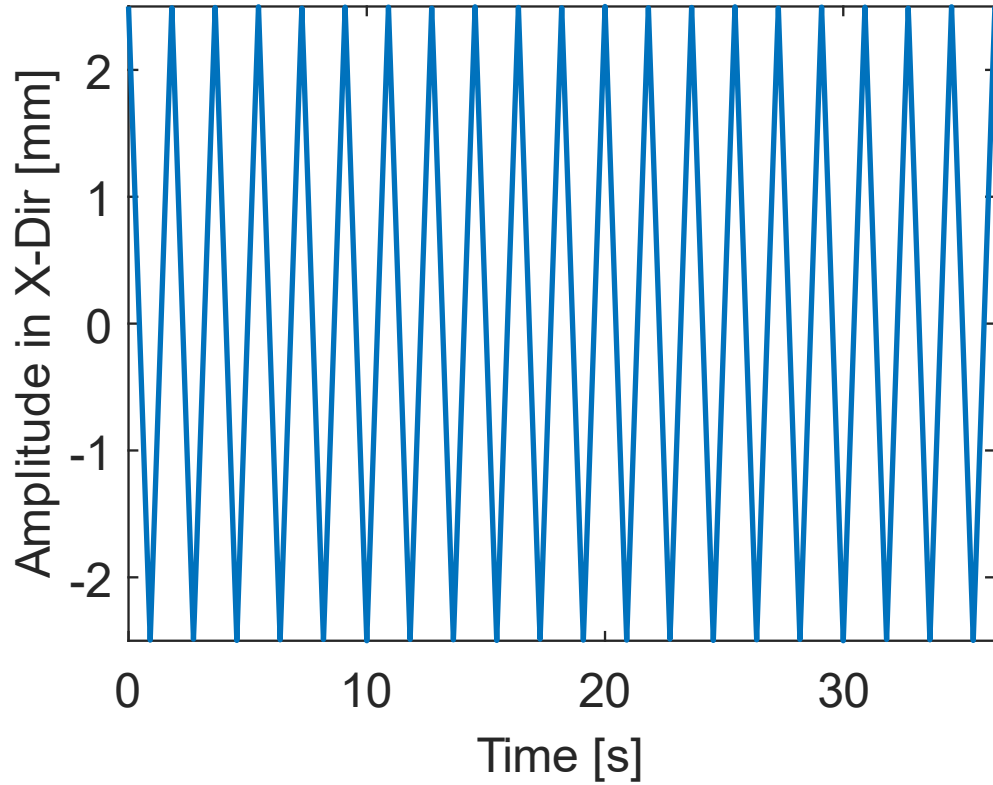
Figure 82: X-Position of the centre of the weld torch describing the weaving pattern over time

Likewise, z_{focus} is a truncated triangular wave for half a period that describes the linear progression of the weld torch centre as the weld is progressed in the z-direction over time. The amplitude, A_z, corresponds to the maximum and minimum z position in relation to Figure 83, and the period, p_z, was set to be double the pass time which is itself a function of linear velocity and weave frequency and alters for differing passes according to Table 6.. By setting the variables in this manner, a linear progression in the centre of the z-direction was obtained and is annotated in Figure 83.
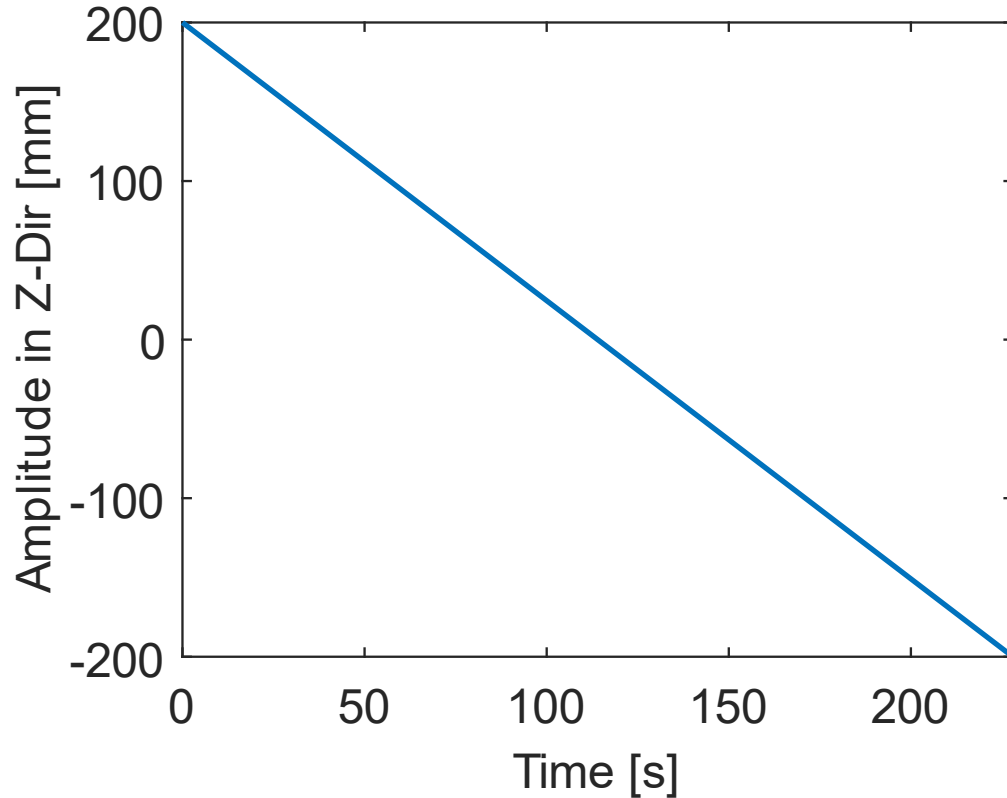
Figure 83: Z-Position of the centre of the weld torch over time

With all welding parameters defined, each model was run for double the time of a weld pass to observe how the thermal gradient changed over the domain during and after welding. Each model was solved in approximately 6 mins and 48 seconds on a PC with a 3.8Hz 24 core 3960X AMD thread ripper processor [273] and 128Gb of RAM. The temperature was logged at each nodal point of the mesh over the entire domain shown in Figure 79, and interpolated to the positions of the thermocouples noted in Figure 80.

As both simulated and experimental data had been collected, it was possible to compare the two datasets. Temperature data from the simulated datasets were extracted at points corresponding to the placement of the thermocouples in the experiment and both the simulated and experimental data is shown in Figure 84. With reference to Figure 80, thermocouples were chosen to be plotted at various distances from the centre of the weld and at the top and the bottom of the plate in order to validate the observed thermal gradient

at various points. Strong agreement between the experimental and simulated datasets is observed with an average error of 1.80% (mean error: 4.1ºC, max error: 19.2ºC). The variations from the simulation to what was observed were thought to be due to: 1) The positional error in mounting the thermocouples not exactly aligning with the exact points requested in the simulation; 2) the quality of the thermocouple attachment. The thermocouples are attached via spot welding and the quality of this bond influences the temperature reading; 3) Differences in the material properties; & 4) Differences in welding process parameters.
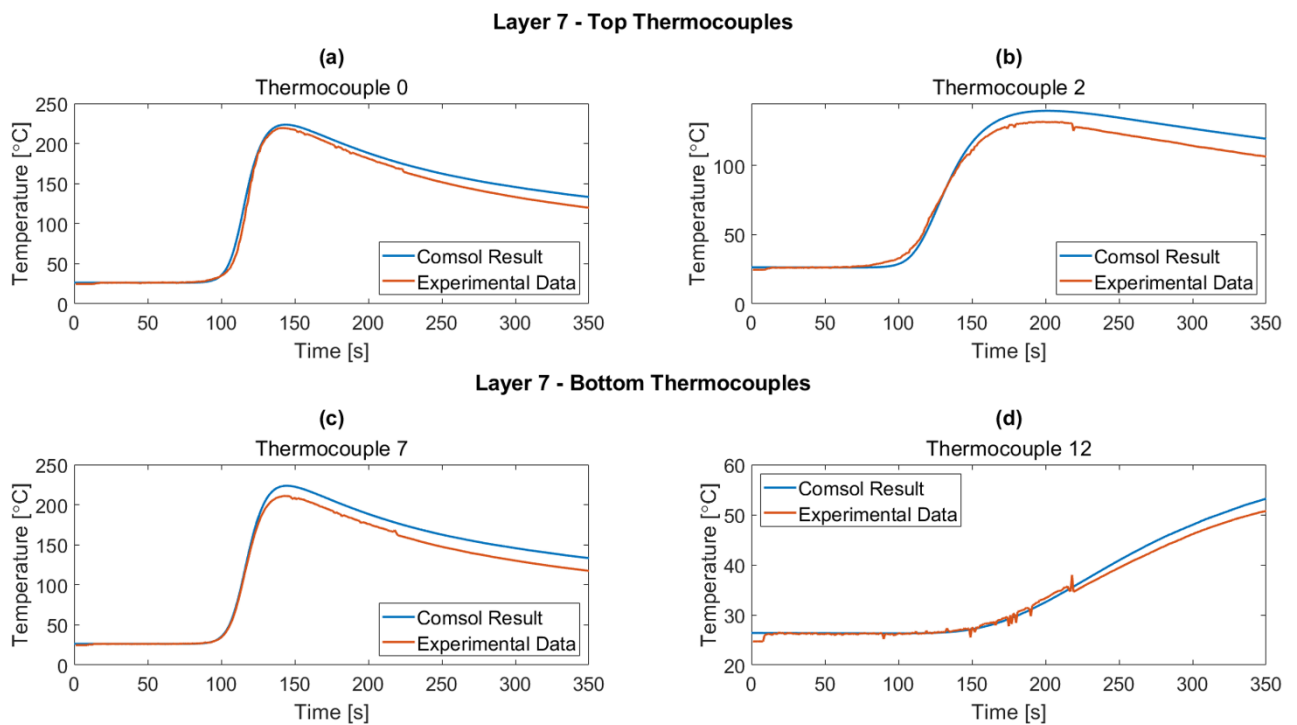
Figure 84: Experimental and simulated thermal data comparison

From the validation of the simulated data with the experimental data, the well-documented properties of S275 steel over temperature could be leveraged to create a spatially-varying material property map [259]. This spatial variation in material properties can be interpreted into a similar variation in ultrasonic velocity through the square root of the materials stiffness divided by its density [274], as documented in Eq. 114 & Eq. 115,

and thus be used by any forward model to compute the necessary travel times as described in Section 5.2. It was thus hypothesised that these thermal models could be the *a priori* knowledge needed to accurately image ultrasonic datasets at the point of manufacture welded components.

$$c_l = \frac{\sqrt{E(1-v)}}{\rho(1+v)(1-2v)} \qquad \text{Eq. 114}$$

$$c_s = \sqrt{\frac{E}{2\rho(1+v)}} \qquad \text{Eq. 115}$$
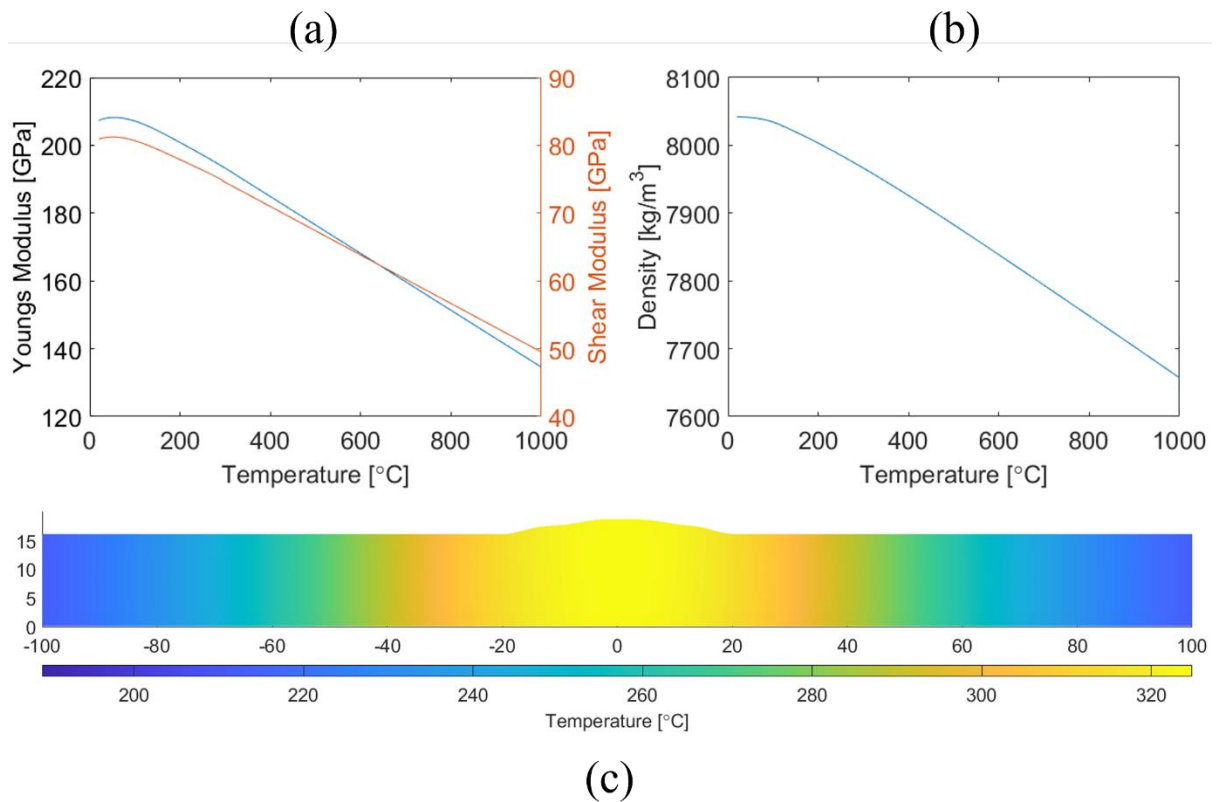
Figure 85: S275 Material properties against temperature and thermal gradient from COMSOL simulation. (a) S275 Young's and Shear Modulus against temperature [259], (b) S275 Density against temperature [259], (c) Thermal gradient 100.00 mm behind the weld torch.

5.4. Simulated thermal compensation

To prove the hypothesis that the validated thermal simulations could be used to accurately image high temperature welded components at the point of manufacture, several explicit FEA proof-of-concept models producing FMC datasets were developed. These models were created and solved in the accelerated high-fidelity GPU-based FEA package, Pogo, and were subsequently visualized using PogoPro [176].

The same standardised weld geometry used in Section 5.3 was modelled along with a 5.00 MHz COTS Olympus 5L32-A32 1D linear phased array [275] and a high temperature Olympus SA32C-ULT-N55SIHC ULTEM™ wedge [276] as shown in Figure 86 (a). A 3.00 mm Side Drilled Hole (SDH) was modelled in the centre of the weld to assess the thermal compensation strategy. The mechanical properties for the ULTEM™ wedge were kept constant ($\rho = 1270.00 \frac{kg}{m^3}, E = 2.89 GPa, G = 1.04 GPa$), whilst the steel material properties were allowed to vary with respect to temperature. It is important to note for an ultrasonic FE model in the presence of a thermal gradient, a spatially varying material property map needs to be created. This is done by leveraging the previously documented thermal gradient maps described in Section 5.3. Therefore, the temperature was interpolated from the nodal points of the mesh used in the FE model of the thermal environment to the nodal points of the mesh used in the ultrasonic FE model. Each unique temperature was modelled as a different material of the steel properties relating to their temperature as described in Figure 85. To lower computational demands, a variable mesh was obtained via Pogo's internal mesher, pogoMesh, where the mesh element size was 1/16th of the slowest wavelength in each medium. This is illustrated in Figure 86 (b). The full length of the welded plate was not modelled, and the domain was limited by Absorbing Layers with Increasing Damping (ALID) [221] as shown in Figure 9 (c). This effectively stopped any reflections from boundaries being seen in the imaging algorithm.

To aid development, each model was solved at 2.00 MHz initially, due to the lower mesh size and smaller computational domain associated with lower frequency simulations. When the 2.00 MHz modelling data had been validated, the frequency was increased to

5.00 MHz to match the centre frequency of the transducer itself. Each model was solved with and without a thermal gradient being imposed on the steel domain creating a total of 4 models. The 2.00 MHz & 5.00 MHz models contained 18,069,054 & 117,729,711 C3D6R elements respectively. The 2.00 MHz and 5.00 MHz models were solved in ~80 mins and ~20hrs respectively on a HPC that contained two Nvidia GeForce RTX 3090 graphics cards [277].
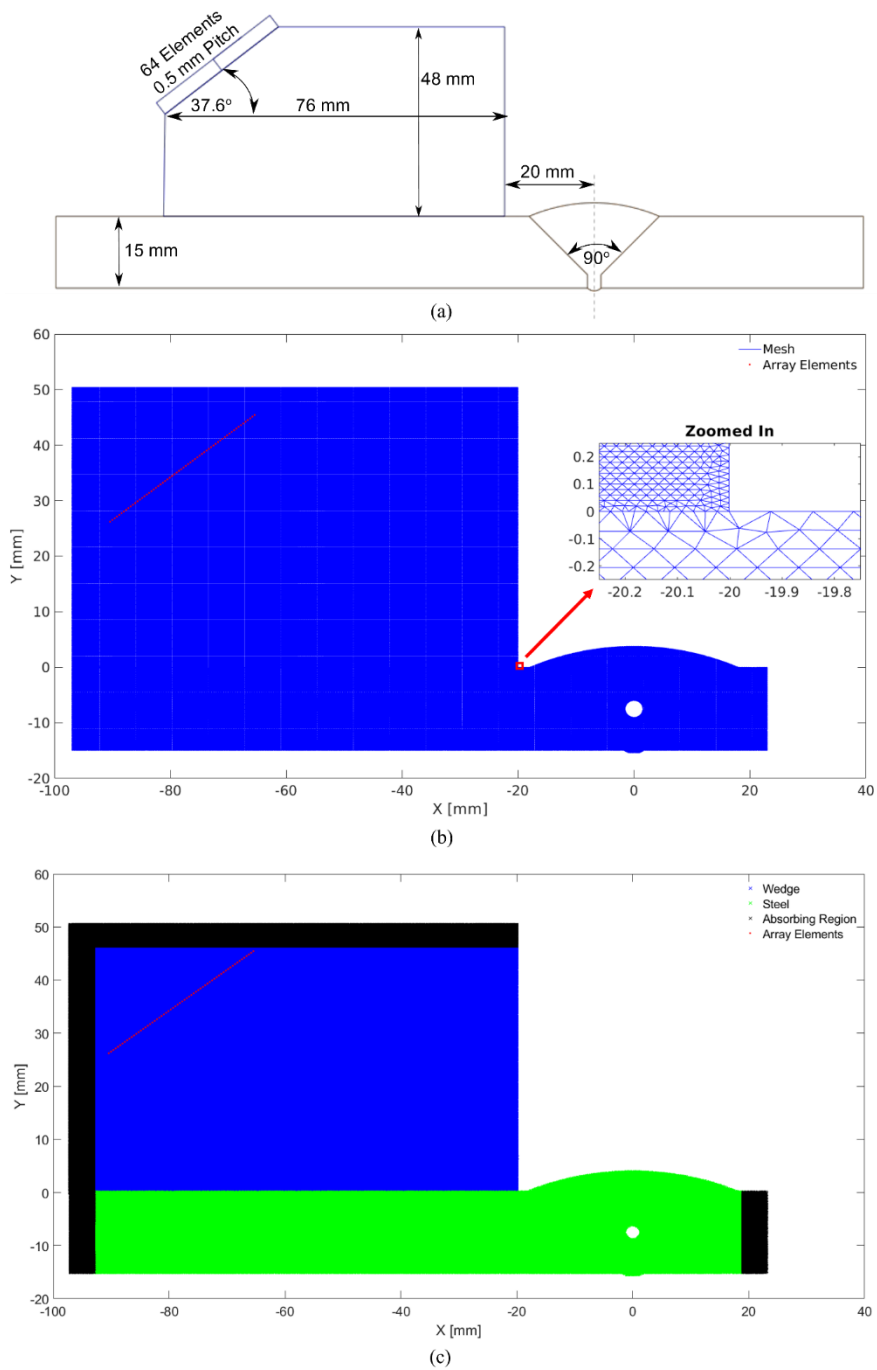
Figure 86: Schematics of proof-of-concept FEA models (a) Overall geometric domain, size, and positioning, (b) Variable mesh size created in pogoMesh, (c) Overall FEA domain showing the wedge, steel, and absorbing regions as well as the 3.00 mm SDH and array element positions.

187

The resulting generated FMC datasets were imaged using the TFM algorithm in combination with the MSFMM as described in Section 5.2. For each frequency, three images were created: 1) An ambient image that used the room temperature (20°C) FMC dataset and a room temperature ToF Map; 2) An uncompensated image that used a welded thermal gradient FMC dataset and a room temperature ToF map; and 3) A compensated image that used a welded thermal gradient FMC dataset and a welded thermal gradient ToF map.

Great effort was taken to ensure fast processing of the data. For each image, the MSFMM produced ToF maps using MATLABs parallel computing toolbox [278] in ~31.00 s on a HPC that housed two Intel Xeon Gold 6248R 48 core 3.00 GHz processors [279] with 192 Gb of RAM, while the TFM was performed in MATLABs GPU coder [280] in 1.60 s on the same HPC that housed two Nvidia GeForce RTX 3090 graphics cards [277]. Additionally, each image was formed on a spatial grid with a resolution of 20 pixels per millimetre. It has been shown in previously documented work [281] that for the frequencies and array used in this work, the Point Spread Function (PSF) of the array would limit the resolution to 0.08 mm, so the chosen value of 0.05 mm was well suited. The ToF calculation was bench marked against an Eikonal solver developed by the Consortium for Research in Elastic Wave Exploration Seismology (CREWES) [282] at the University of Calgary and provided accurate ToF maps in ~ 4 hours. This result demonstrates the benefits of using the MSFMM due its inherently fast solve times no noticeable image degradation as documented in Section 5.1.

The results for the 2.00 MHz and 5.00 MHz models are shown in Figure 87 and Figure 88 respectively where each image derived from each transversal half skip is displayed above each other [283]. The SNR was very similar across all three images for both the 2.00 MHz & 5.00 MHz datasets, as documented in Table 7. This implies that the thermal gradient has little defocusing effect. To quantify the improvement in the detected reflector position, the position of the maximum amplitude was recorded and compared across all the three images for both the 2.00 MHz and 5.00 MHz datasets. It was shown that by not compensating for the thermal effects associated with a typical welding process,

188

a maximum positional error of 4.34 mm & 3.81 mm was introduced for the 2.00 MHz and 5.00 MHz datasets respectively – see the images in Figure 87 (b) & Figure 88 (b). By compensating, the maximum error in the reflector's position was reduced to maximum of 0.20 mm & 0.46 mm for the 2.00 MHz and 5.00 MHz datasets respectively representing a ≥ 85% decrease in positional error across all images – see the images in Figure 87 (c) & Figure 88 (c). These results are summarised in Table 7.
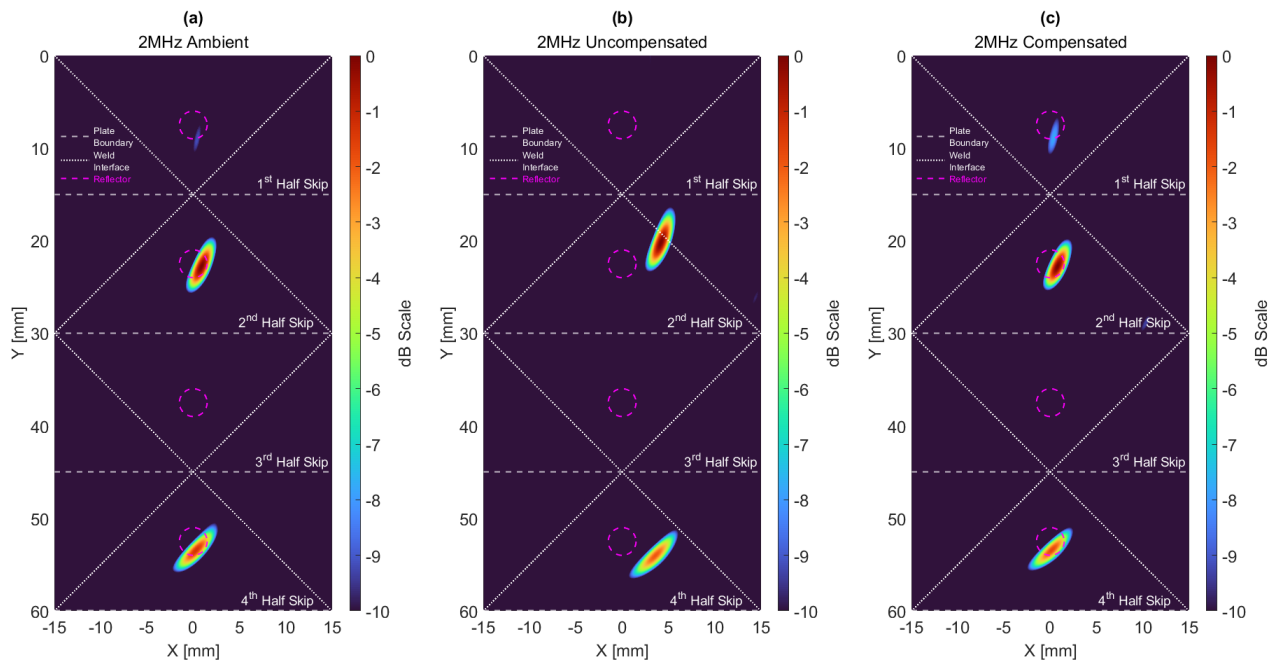
Figure 87: TFM images formed with ToF maps from the MSFMM. (a) TFM image constructed with FMC data simulated at 2.00 MHz ambient room temperature material properties and an ambient room temperature ToF map, (b) TFM image constructed with FMC data simulated at 2.00 MHz with thermally varying material properties over the steel domain and an ambient room temperature ToF map, & (c) TFM image constructed with FMC data simulated at 2.00 MHz with thermally varying material properties and ToF map over the steel domain.
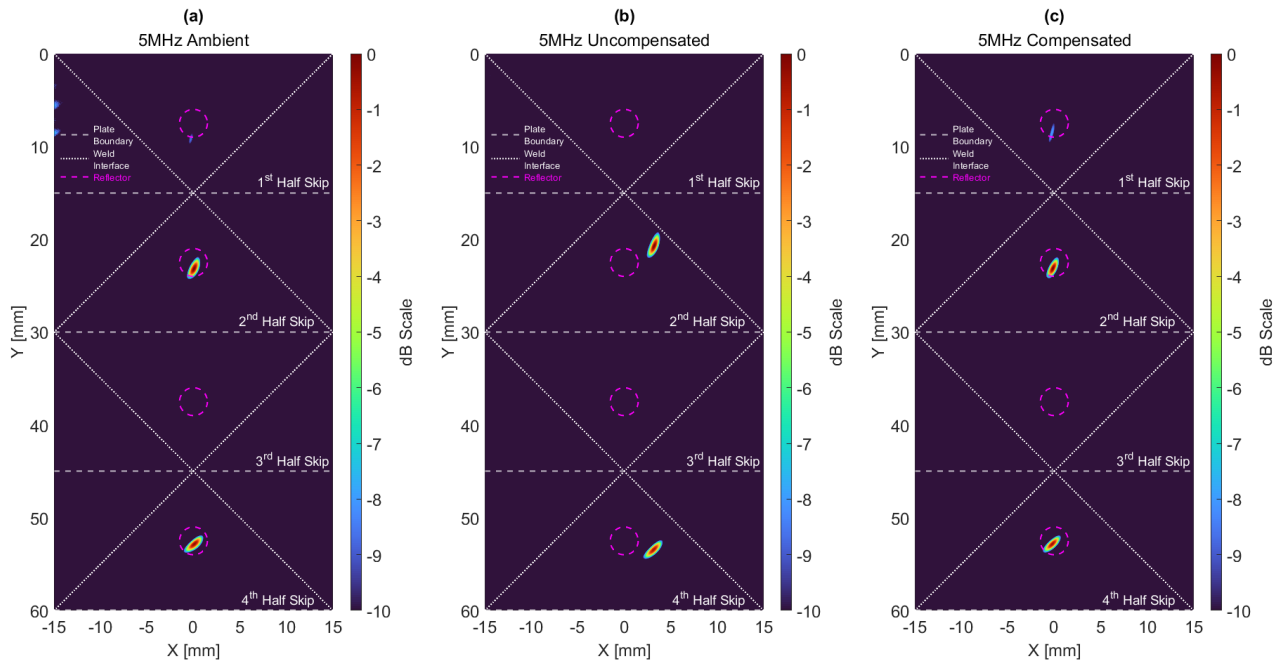
Figure 88: TFM images formed with ToF maps from the MSFMM. (a) TFM image constructed with FMC data simulated at 5.00 MHz ambient room temperature material properties and an ambient room temperature ToF map, (b) TFM image constructed with FMC data simulated at 5.00 MHz with thermally varying material properties over the steel domain and an ambient room temperature ToF map, & (c) TFM image constructed with FMC data simulated at 5.00 MHz with thermally varying material properties and ToF map over the steel domain.

This result is further emphasised in the averaged ToF maps from every transmit receive pair 15 mm either side of the reflector as shown in Figure 89. Between the high temperature and ambient ToF maps documented Figure 89 (a) and (b) respectively, a difference of 1.34 µs is reported at the reflector location. This represents a 4 mm positional shift for an assumed constant transverse ultrasonic velocity of 3000 m/s. A 4mm positional shift in the reflector location estimated in this manner is of the same order of magnitude observed in Table 7. Furthermore, the ToF map illustrated in Figure 89 (a) shows the correct reflector contour pulling the defect position towards the left of the imaging domain. This is expected and counteracts the shift to the right documented in the uncompensated images in Figure 87 (b) and Figure 88 (b). Therefore, by comparing ToF maps in this manner, an approximate positional shift magnitude and direction can be estimated.
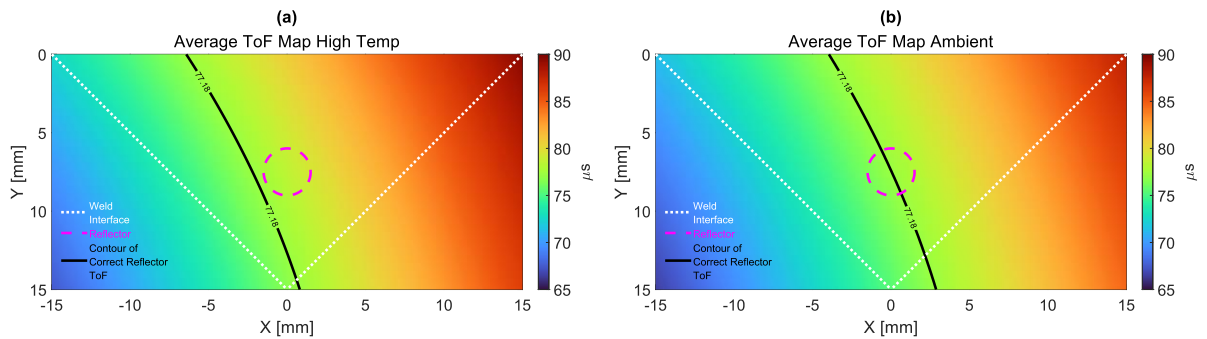
Figure 89: Zoomed in ToF maps, (a) 5MHz ambient ToF map 15 mm either side of the reflector. (b) 5MHz high temp ToF map 15 mm either side of the reflector

191

These results confirm that for a simulated noise-free environment, the proposed thermal compensation strategy has a positive effect on imaging performance. To confirm these results and trends hold true in a realistic setting at the point of manufacture, several experiments were conducted.

Table 7: Imaging performance summary for the simulated datasets stating the positional error and SNR observed in the TFM images.

	Reflector in 2nd Half Skip		Reflector in 4th Half Skip	
	SNR (dB)	Location Shift (mm)	SNR (dB)	Location Shift (mm)
2.00 MHz – Room Temp	23.30	0	21.70	0
2.00 MHz – High Temp – Uncompensated	23.50	4.34	22.00	3.81
2.00 MHz – High Temp – Compensated	24.00	0.20	22.60	0.32
5.00 MHz – Room temp	27.10	0	33.50	0
5.00 MHz – High Temp – Uncompensated	27.00	3.44	33.50	3.06
5.00 MHz – High Temp – Compensated	25.90	0.11	34.30	0.46

5.5. Experimental thermal compensation

5.5.1.   Initial experimental results

To further prove our hypothesis that the validated thermal simulations could be used to accurately image welded components at the point of manufacture with thermal gradients present, several experiments were conducted. A 15.80 mm thick carbon steel sample with two 2.00 mm SDHs machined along the weld groove interface at one third and two thirds the thickness to act as reflectors, was procured for an autogenous weld to be applied. Here, an autogenous weld refers to the application of a GTAW welding heat source on the surface of the plate without the addition of any filler material. The position of these reflectors was selected to mimic lack of sidewall fusion defects. The acquisition set up involved the use of two robots. A KUKA Quantec Extra HA KR-90 R3100 [216] was used to perform the welding sequence and a Kuka KR6 R900 Agilus [284] in combination with a IP-65 rated gamma force-torque sensor from ATI Industrial Automation [220] was used to record the ultrasonic data. Both robots were controlled via a KRC 4 controller [221] using the Kuka Robot Sensor Interface (RSI) [222]. The force torque sensor was used to apply a force of 120N in the Z-direction during the ultrasonic data acquisition to ensure consistent coupling. High temperature liquid polymer couplant [285] was applied between the transducer and wedge as well as between the wedge and sample. The FMC data was captured using a PEAK NDT LTPA 64+64 phased array controller [286] from an Olympus 5.00 MHz 5L32-A32 1D linear phased array and an Olympus SA32C-ULT-N55SIHC ULTEM™ wedge along with a 6.00 mm thick polymer coupling medium. To reduce the presence of artefacts, all FMC datasets were filtered around the centre frequency of the transducer in the model using a Hann window with a bandwidth of 60% of the centre frequency. The experimental setup is illustrated in Figure 90.
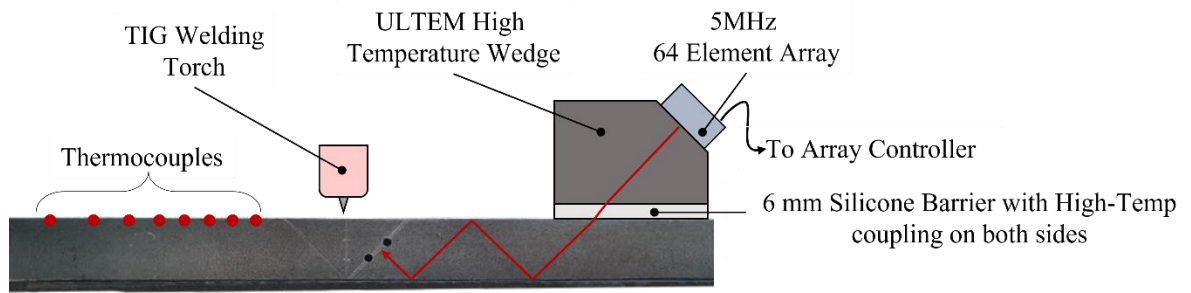
Figure 90: Experimental setup depicting the approximate location of the thermocouples, weld torch, polymer coupling medium, ultrasonic wedge, and array on top of the carbon steel component.

Initially, an FMC dataset was acquired and imaged at room temperature prior to the deposition of the autogenous weld for simplicity and comparison. The acquired room temperature data was imaged using the same code as in Section 5.4 and is shown in Figure 91 where each image derived from each transversal half skip is displayed above each other [283].
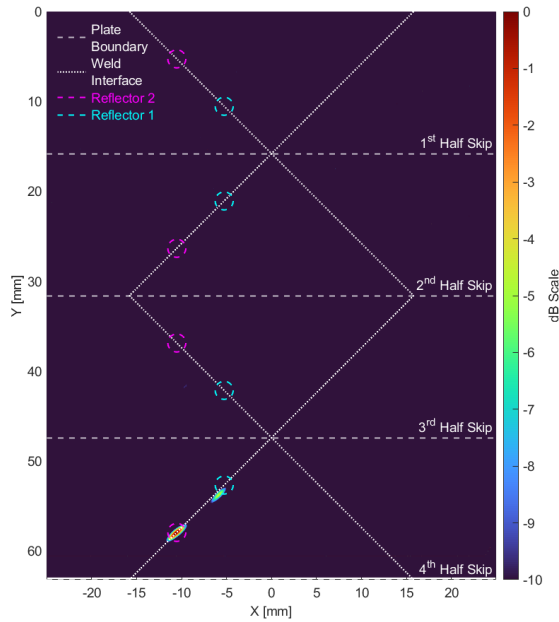
Figure 91: Experimental ambient temperature TFM image created with ToF maps from the MSFMM

With datasets acquired and successfully imaged under ambient conditions, the autogenous weld was then deposited. As the autogenous weld was laid, a thermal gradient was induced into the steel and was again logged via K-type thermocouples as in Section 5.3. The original COMSOL thermal models were altered slightly to account for the use of an autogenous weld in the experimental procedure and strong agreement (mean error: 4.6°C, max error: 8.6°C) was again observed between the thermally simulated and experimentally recorded thermal datasets. As the acquisition of thermal and ultrasonic datasets was performed in a semi-autonomous fashion, each dataset could be matched with ease by analysing their timestamp. FMC datasets were acquired after the maximum temperature recorded by the thermocouples was less than 150°C. This conservative criterion was used to avoid hardware failure as the ULTEM™ wedge has an operating temperature of ~150°C as recommended by the wedge manufacturer. Beamformed images were displayed in real time at the point of acquisition showed that the coupling had stabilised. An FMC dataset with stable coupling was then elected for compensation, and

195

a thermal gradient corresponding to this was selected from the COMSOL model and is shown in Figure 92. In this part of the work, the silicone coupling medium and ULTEM™ wedge were not modelled in the thermal simulations, and as a result they have an assumed ambient temperature of 20°C across their entire domains.
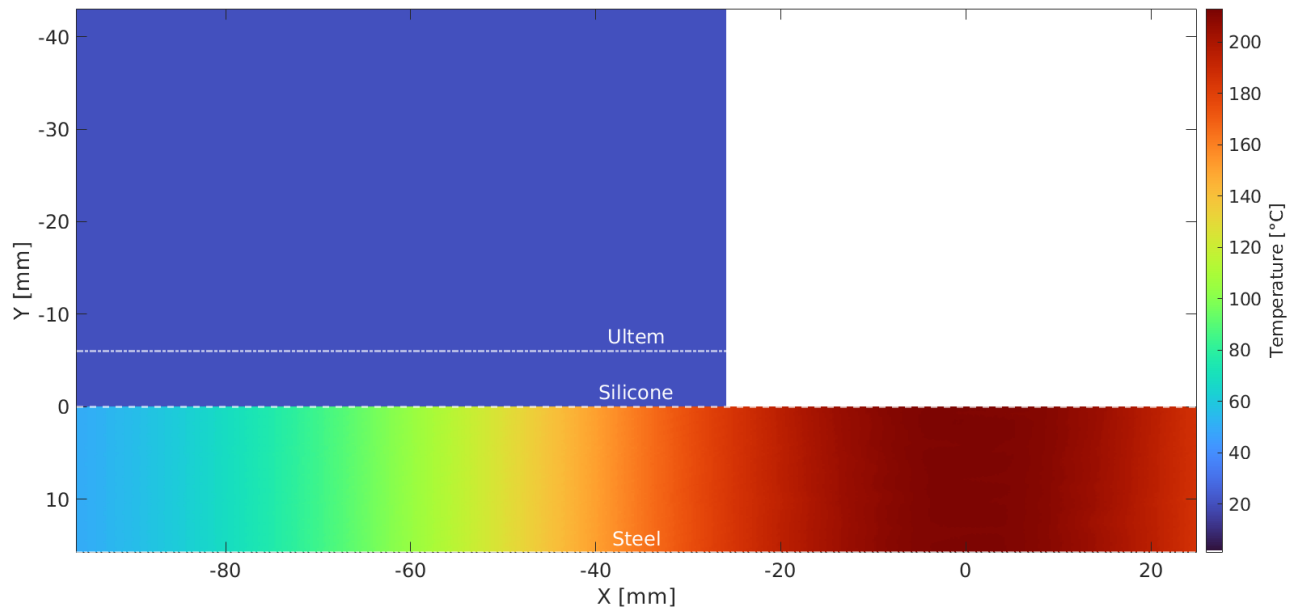
Figure 92: Extrapolated 2D thermal gradient from the COMSOL model that mimicked the experimental autogenous weld procedure

The uncompensated and steel gradient-compensated TFM images produced from the FMC data and initial thermal gradient are shown in Figure 93 (a) and (b) respectively, where each image derived from each transversal half skip is displayed above each other [283]. A SNR of 18.60 dB was reported for Reflector 2 in the uncompensated high-temperature image, and a very similar SNR of 16.70 dB was reported for Reflector 2 in the steel gradient-compensated high-temperature TFM images. This agrees with the trend observed in the simulated data where comparable SNRs are reported for uncompensated and compensated images. Like the simulated datasets, a positive benefit was observed when the uncompensated and steel gradient-compensated reflector positions were compared. A 20.5% reduction in positional error was reported between the

196

uncompensated and steel gradient-compensated high-temperature images, with an absolute positional error of 4.49 mm and 3.57 mm for Reflector 2 respectively.
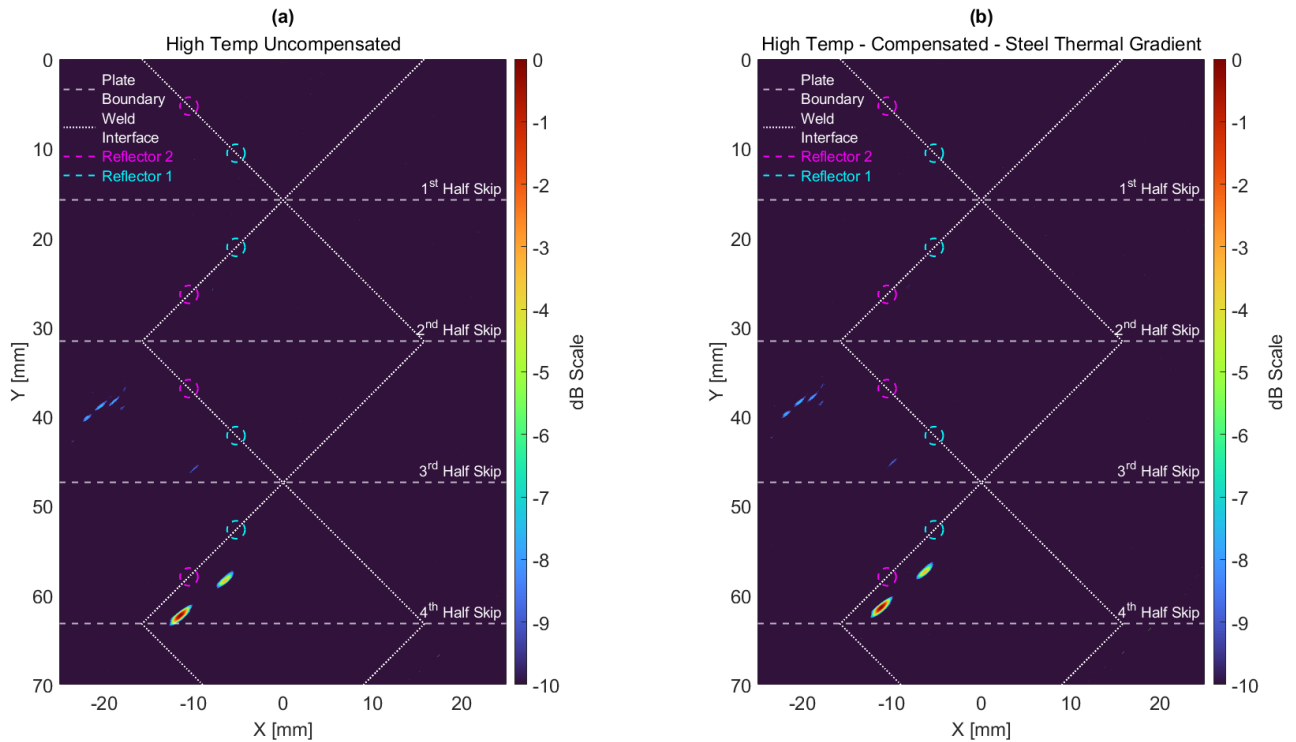
Figure 93: Experimental high temperature TFM Images created with ToF maps from the MSFMM (a) Uncompensated TFM image showing a positional error with respect to Reflector 2 of 4.49 mm, & (b) Thermally compensated TFM image using a thermal gradient only in the steel plate showing a positional error with respect to Reflector 2 of 3.57 mm.

5.5.2. Incorporating coupling & wedge thermal gradients

While the initial experimental results at the point of manufacture demonstrated an improvement in the position of the reflector, these did not incorporate thermal gradients within the wedge and coupling medium.

A further series of experiments were performed to understand how the ultrasonic velocity varied within the polymer coupling medium and ULTEM™ wedge with temperature. Experimental pulse-echo time of flight measurements, across known depth

samples of each material were undertaken across the working temperature range. The COMSOL models were then updated to incorporate the thermal gradient in the wedge and coupling medium. Isothermal boundary conditions were applied at the steel-silicone and silicone- ULTEM™ interfaces, while ambient convection and radiation boundary conditions of 20°C were applied at all air interfaces. The ULTEM™ wedge and silicone polymer coupling medium were modelled with a specific heat capacity of $2,000 \frac{J}{kgK}$ & $1430.15 \frac{J}{kgK}$ and thermal conductivity of $0.22 \frac{W}{mK}$ & $0.143 \frac{W}{mK}$, respectively. The updated thermal gradient is shown in Figure 94 with an average predicted temperature in the polymer coupling medium and wedge of 29.15°C and 20°C, respectively.
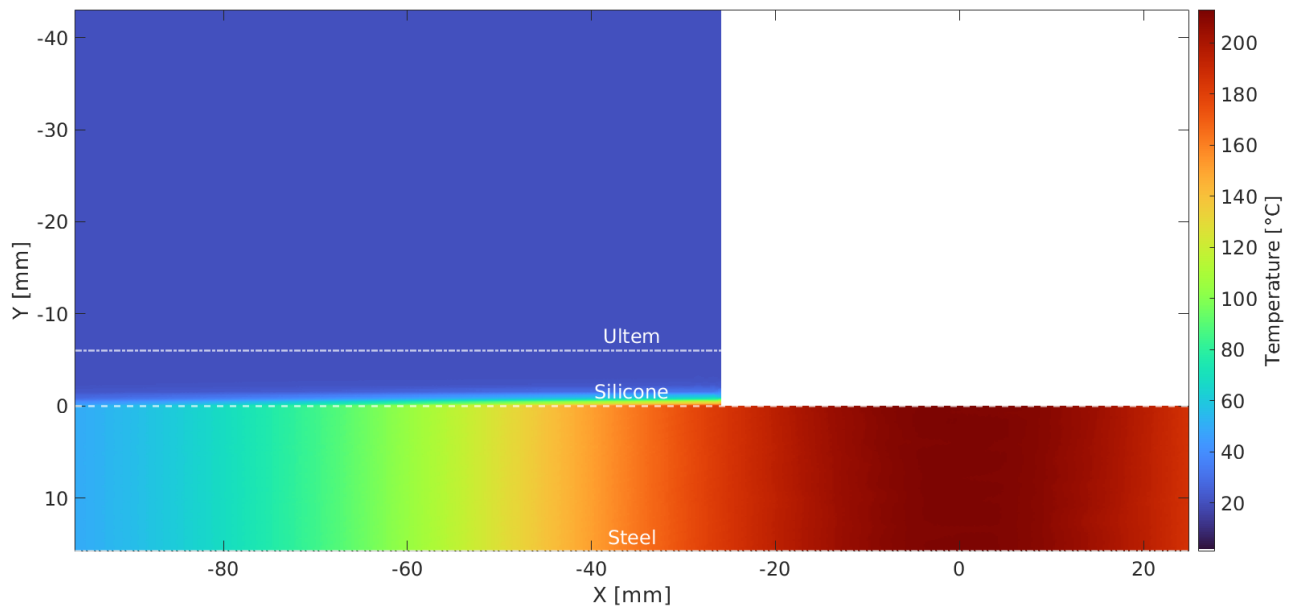
Figure 94: Updated thermal gradient in the steel, silicone polymer coupling medium and ULTEM™ wedge 100.00 mm behind weld torch.

The updated thermal gradient was used to produce a new ToF map through the MSFMM and the TFM images were reconstructed once more. The updated TFM image is shown in Figure 95 (d) along with comparisons to images formed with: 1) ambient FMC data and an ambient thermal gradient (Figure 95 (a)); 2) high temperature FMC data and

an ambient thermal gradient (Figure 95 (b)); 3) high temperature FMC data corrected with a thermal gradient only in the steel domain (Figure 95 (c)). The imaging performance is summarised in Table 8. It is again noted that the updated image in Figure 95 (d) produced a comparable SNR to the other images formed from the same FMC dataset in line with previous results documented in this study. A positive increase in positional accuracy is also observed, with the reflector position error decreasing by a further 53% from the initial steel-compensation attempt – see Figure 93 (b)/Figure 95 (c) – to an absolute error of 1.68 mm. It is thought that the remaining 1.68 mm positional error can be attributed to errors in the thermal gradient, errors in our understanding of how the ultrasonic velocity varies over temperature, and positional inaccuracies between the modelling domains and reality. When the updated thermal compensation strategy is compared to the uncompensated case, a 63.6% reduction in absolute positional error is observed, proving the efficacy of using this strategy to inspect at the point of manufacture in the presence of high-temperature gradients, and aiding industry as it moves towards higher throughput production lines associated with Industry 4.0.
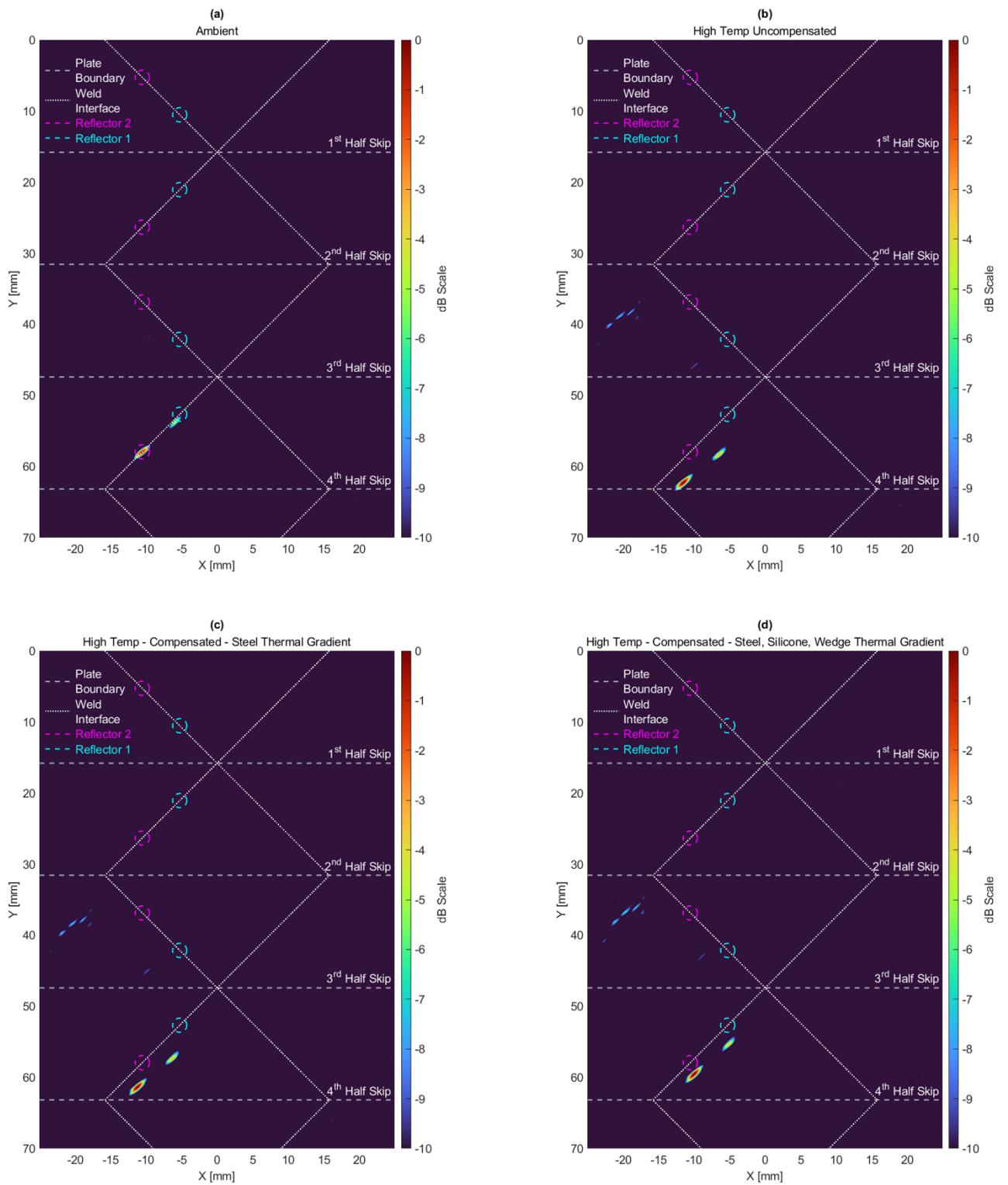
Figure 95: Experimental TFM images created with ToF maps from the MSFMM (a) TFM image of ambient FMC data, (b) Uncompensated TFM image of high temperature

FMC data showing a positional error with respect to Reflector 2 of 4.49 mm, (c) Thermally compensated TFM image of high temperature FMC data using a thermal gradient only in the steel plate showing a positional error with respect to Reflector 2 of 3.57 mm, & (d) Thermally compensated TFM image of high temperature FMC data using a thermal gradient only in the steel, silicone, and ULTEM™ domains showing a positional error with respect to Reflector 2 of 1.68 mm

Table 8: Imaging performance summary for the experimental datasets stating the positional error and SNR observed for Reflector 2 in the 4th half skip of the TFM images.

Dataset	SNR (dB) of Reflector 2	Location Shift (mm) of Reflector 2
Ambient	18.60	0
High Temp - Uncompensated	16.70	4.49
High Temp - Steel Gradient - Compensated	16.50	3.57
High Temp - Full Domain-Gradient-Compensated	16.40	1.68

5.6. Summary

Traditionally, ultrasonic inspection of welded components has been performed after the component has been manufactured due to industrial protocol and the technical challenges associated with inspecting at the point of manufacture. As businesses seek continual process improvements as they move towards Industry 4.0, the time lost due to this practice is now undesirable and there is a desire to move inspection to the point of manufacture. Technically, inspecting welded components at the point of manufacture is challenging due to the elevated temperature and resulting thermal gradients in the component introducing beam bending effects due to refraction and positional inaccuracies in the ultrasonic data. In this chapter, a generalised time of flight maps to be created via the Multi-Stencils Fast Marching Method (MSFMM), incorporating thermal gradient information from the welding process and compensating for positional inaccuracy in defect location in resultant TFM images is presented for the first time.

To document the thermal gradients experienced during a standard GTAW procedure, various 3-dimensional thermal simulations were developed and experimentally validated with an average error of 1.8%. The resulting thermal information of the welding domain along with well-defined material properties that varied over temperature allowed for the generation of generic ToF maps through the MSFMM, and the ultrasonic data to be imaged by the TFM. The proposed thermal compensation strategy was initially evaluated on synthetically generated finite element data and showed an improvement in positional accuracy of reflectors of at least 85%. Experimental results also showed a similar trend with a 63.6% improvement in reflector positional accuracy. The results show how high-quality ultrasonic images can be generated in process and demonstrate a significant step closer to inspection at the point of manufacture which could be used in the manufacture of the canister of the future at Sellafield.

5.7. Author Statement

It is acknowledged that this chapter was highly collaborative and could not have been possible without the technical expertise of many academic collaborators. While this work was led by the author, the following authors statement is given to cite each individual's effort in this chapter.

Euan Foster: Data curation, Original draft preparation, Reviewing and editing, Software, Formal Analysis, Investigation

Charles MacLeod: Supervision, Reviewing and editing, Conceptualization, Methodology

Ehsan Mohseni: Supervision, Reviewing and editing, Investigation

Anthony Gachagan: Supervision, Reviewing and editing

Gareth Pierce: Supervision, Reviewing and editing

Katherine Tant: Software, Supervision, Reviewing and editing, Conceptualization, Methodology

Muhammad K. Rizwan: Supervision, Reviewing and editing, Investigation.

Ewan Nicolson: Software, Formal Analysis, Investigation, Reviewing and editing, Validation

Nina E. Sweeney: Reviewing and editing, Software, Formal Analysis, Investigation, Validation

David Lines: Supervision, Reviewing and editing, Software, Formal Analysis, Investigation

Jonathan Singh: Reviewing and editing, Software, Formal Analysis, Investigation

Chapter 6

Summary, key findings, and future work

6.1. Summary

This thesis presented NDE solutions to inspect the body and welds for low-level nuclear waste canisters in the context of three scenarios specific to the challenges faced by Sellafield Ltd, the theoretical background behind each as well as validation by simulation and/or experimental methods. The three scenarios covered were: 1) In-situ screening of legacy canisters sealed by RSWs while on a racking system with considerable accessibility constraints; 2) Ex-situ characterisation of legacy canisters sealed by RSWs; & 3) Inspection of fusion welds performed via Gas Tungsten Arc Welding (GTAW) for an upgraded canister of the future design at the point of manufacture. The in-situ challenge was addressed by a novel FGW which could be used to screen the RSW on specific canisters to allow for targeted removal and repackaging. The ex-situ challenge was resolved by developing a data rich eddy current platform to characterise defects on the canister body as well as the RSW sealing the canister. The canister of the future challenge was alleviated by developing an innovative thermal compensation strategy to enable inspection as the weld was being manufactured enabling the creating of a NDE digital twin throughout the canister's lifetime.

Chapter 1 began with an overview of the industrial motivation that highlighted the role of nuclear power within the UK and the importance of ensuring safe storage of nuclear assets. It was clear that due to complex issues and various differing stakeholders, ranging from political entities to power providers, a need to increase the lifetime of nuclear infrastructure further than its original design intent frequently arises. This leads to a reactionary requirement to integrate NDE methods to ensure continuous safe operation. The reader is introduced to the wide array of academic work undertaken by Sellafield to address their inspection challenges arising from this dilemma and to upgrade their

capabilities as technology advances. Inspection of three different canister variants were then highlighted and emphasis was placed on the importance of inspecting the welds and to a lesser degree, the overall canister body. Three inspection scenarios specific to inspection of the canisters and their welds were introduced. The in-situ and ex-situ challenges were related to a legacy canister design that was soon to go out of manufacture and was sealed with thin RSWs. The final inspection challenge was related to the canister of the future - a canister that was not yet fully designed but a thicker weld and overall canister design was envisaged. In all three scenarios, it was clear that the lack of inspection data was prohibitive to making timely decisions over safe and continuous storage of these nuclear assets. Subsequently, the main aims and objectives of this thesis were laid out, concluding with the contributions to academia and industry and the publications generated from this work.

Chapter 2 provided an overview of the welding techniques used on the legacy canister and canister of the future design. Specific methods of NDE were introduced to the reader that are well suited to addressing the three aforementioned inspection scenarios in line with any limitation placed on them from their specific welding technique. The three NDE techniques covered in detail are bulk ultrasonic inspection, ultrasonic guided waves, and eddy current testing. The first technique covered in detail is bulk ultrasound starting with an in-depth theoretical overview of wave propagation in infinite isotropic solids. Additional fundamentals were also covered including differing attenuation models, wave refraction, reflection, and mode conversion. Recent technological developments associated with phased arrays are summarised and emphasis on the flexibility associated with the datasets they gather is given. In line with industrial standards, it was concluded that phased array bulk ultrasound would be well suited to inspecting the thicker tungsten arc welds in the canister of the future. The next topic covered was guided waves due to their theoretical similarities to bulk ultrasonic waves. Unique features associated with guided waves such as their dispersive properties, mode shapes, and attenuation due to leakage were covered. The concepts of guided waves are then expanded upon with FGWs that propagate with their energy confined to a topological feature, such as a weld. The

complex theory and mathematics contributing to the SAFE method that allows for FGWs to predicted and studied are covered in depth. Nuances in identifying suitable FGWs for NDE purposes are highlighted that allow for proper mode selection and transduction strategies to be developed. It was concluded that for the in-situ inspection, FGWs would be an ideal solution to screen the thin RSWs that seal the canister body and the lid whilst on a racking system with considerable accessibility issues. The final topic covered is eddy current testing starting with an overview of differing types of eddy current testing and electromagnetic theory. Near field testing was documented to be the most relevant form of eddy current testing with emphasis being placed in the theory on the skin depth which is primarily controlled by the frequency of operation. Eddy current arrays were also briefly covered, and their advantages highlighted. It was concluded that eddy current array testing was well suited to further inspecting the canister body and RSWs of the legacy canister due to their ability to saturate the thin wall thicknesses.

Chapter 3 began the exploration of discovering a FGW and exploiting it on the RSW sealing the body to the lid on the legacy canister design. It was evident from Chapter 2, that applying the SAFE method in this manner was highly complex, and care would be needed. To this effect, literature replication of work done by Yu *et al.* [115] was performed. All the documented simulated results were able to be replicated with reflection coefficients being reproduced with 99% accuracy. With confidence established in the theoretical implementation of the SAFE method, adaptation to the RSW geometry was undertaken. Four weld-guided wave modes were identified, and the fundamental flexural (F_0) weld guided mode was down selected. Several FE models explored applicable transduction strategies and documented reflection coefficients to transversal cracks. Multiple experiments were conducted on pseudo RSW structures as well as flat plate and cylindrical RSWs. For the pseudo weld experiments, it was shown that FGWs, like that of the analytical free plate counterparts, could easily be excited in flat plate-like features with traditional transduction techniques. For the flat plate RSW experiments, it was shown that reflections from through wall and 1.00 mm deep defects could be observed with SNRs of 16.33 dB and 8.21 dB respectively. Lastly, it was shown that for cylindrical canister

like RSWs, reflections could also be observed from 1.00 mm deep defects with a SNR of 11.85 dB being reported. This work clearly showed the benefit of deploying such a system on-site at Sellafield as full circumferential screening of the RSW could be performed giving greater insight to the structural health of the canisters in-situ.

Chapter 4 focused on addressing the challenges associated with the ex-situ inspection of the legacy canisters. Without the accessibility constraints of the in-situ scenario, eddy current array testing was used as the eddy current could saturate the entire thickness of the canister and the welds. To facilitate the inspection in an autonomous fashion with little operator handling sought in the nuclear industry due to health and safety concerns, an automated robotic eddy current system was developed. The data rich platform allowed for a complete digital record to be established of the impedance data gathered and is well suited for further advancements in eddy current inversion to leverage in the future. The robotic deployment of the eddy current array is combined with force torque feedback and enables major sources of noise, resulting from lift-off and wobble, to be reduced. Two different datasets were reported on. The first being eddy current scans of canister bodies with known stress corrosion cracks. All of the stress corrosion cracks were detected, and the resulting SNR of images generated from the impedance data was increased through post processing of the eddy current data. The second dataset is concerned with eddy current scans of RSWs. These scans make use of the FGW, documented in Chapter 3, to localise defects and perform targeted raster scans in the area of concern. Basic inversion on the EDM notch width was shown to give results with 96.4% accuracy, and it was shown that time savings of up to ~95% could be realised by performing targeted eddy current raster scans. This work showed the benefit of performing ex-situ inspection in this manner due to the minimal levels of operator handling and time savings that can be realised on large production volumes like that at Sellafield.

Chapter 5 sought to address the challenges relating to the canister of the future and in particular inspecting at the point of manufacture. Inspecting at the point of manufacture is commercially desirable due to increases in operational efficiencies and the ability to be able to create an NDE digital twin to monitor the structural health of the component over

its lifetime. Technically, inspecting welded components at the point of manufacture is challenging due to the elevated temperature and resulting thermal gradients in the component introducing beam bending effects due to refraction and positional inaccuracies in the ultrasonic data. A novel thermal compensation strategy was developed that leveraged thermal weldment simulations, that were shown to be accurate with an average error of 1.8%, alongside the MSFMM and TFM to correct for positional inaccuracies of detected reflectors. Initially, the thermal compensation strategy was trialled on simulated data and the positional accuracy was shown to increase by at least 85%. Experimental results also showed a similar trend with a 63.6% improvement in reflector positional accuracy. Across both simulated and experimental datasets no significant improvement in SNR was shown. The results show how high-quality ultrasonic images can be generated at the point of manufacture and how a similar strategy could be deployed at Sellafield to establish an inspection record from manufacture until the asset is retired.

6.2. Key findings

The process of discovering, characterising, and experimentally exploiting a FGW within a RSW have been documented and studied. The use of an FGW has been demonstrated on a RSW through numerical, simulated, and experimental methods. Numerically, a FGW is predicted through the use of the SAFE method. The subsequent prediction is then validated via time-step FE models. Finally, the FGW is demonstrated experimentally on a simplified "pseudo weld" and representative flat and cylindrical RSWs. It is shown that on curved and flat RSW samples, reflections could be detected from 1.00 mm and through thickness transversal defects showing the efficacy of using this technique for screening canister welds in-situ on a storing rack.

A robotic system capable of automated eddy current inspection that could flexibly be programmed for differing component geometries and differing eddy current arrays was developed. Noise in the eddy current datasets resulting from variations in lift-off and wobble were greatly reduced due to the use of a force torque sensor for positional feedback. Substantial software infrastructure that allows for real-time acquisition, post processing, and display of the eddy current data to the user, was developed. Significant effort was put into developing software to a high standard to allow for further exploitation within our research group. So far, this software has aided in many demonstrations on large grants (NEWAM – EPSRC grant no: EP/R027218/1, RoboWAAM EPSRC grant no: EP/P030165/1, & Remote Inspection of SNM Cans GC_253) and at the BINDT & Material Testing 2022 conferences. The resulting data rich platform is well suited for further research focused on eddy current inversion.

The automated eddy current system was experimentally demonstrated on issues suited to the legacy canister in-situ inspection scenario at Sellafield. A canister with intentionally induced stress corrosion cracks was scanned and the software infrastructure showed successful detection and enhancement of all cracks on the canister. Additionally, the automated deployment allowed for targeted eddy current inspection of the RSW sealing the canister by leveraging the FGW development previously mentioned. By

combining both the FGW and automated eddy current deployment strategy, time savings of up to 95% can be realised.

Finally, a thermal compensation strategy was developed to enable inspection at the point of manufacture. This allows for Sellafield to inspect canister welds whilst they are manufactured as they shift their manufacturing process to thicker wall sections, generating substantial benefits. These benefits include the ability to correct for defects as they are manufactured, greater schedule certainty, and the ability to compare inspection records to the same points throughout the asset's life. It was shown that the proposed compensation strategy can increase reflector/defect positional accuracy by 63.6%, providing a significant step towards industrially desirable inspection at the point of manufacture.

6.3. Future work

Industrialisation and on-site integration

Various elements of the proof-of-concept FGW system investigated in this thesis could be improved upon to allow for industrialisation and on-site integration. These can be categorised into three categories: 1) removal of couplant; 2) radiation testing; and 3) integration to current on-site inspection hardware.

Couplant is predominantly water based, and water can act as a neutron moderator, slowing down fast-moving neutrons to make them more effective in fission chain reactions. In the storage of spent nuclear fuels, avoiding a chain reaction is key to safe storage and preservation of the surrounding infrastructure. From a risk reduction perspective there is therefore a desire to limit the presence of moderating materials and subsequently the use of ultrasonic couplant. This can be achieved my one of two means – through the use of dry coupling, or non-contact transduction techniques. Various studies have shown the use of dry coupling to be effective. Edwards *et al.* [287] showed how rubbers could be used for thickness gauging, corrosion monitoring, and air-coupled ultrasonic applications. Similarly, Robinson *et al.* [288] showed how rubbers could be used in a low frequency roller probe to enable adhesive bond layer quality assessment. It is thought that the current wedge transduction system described within this thesis could be altered to include dry coupling mediums within the wedge assembly removing the need for couplant.

Another pathway to the removal of couplant is through the design and implementation of a bespoke Electro-Magnetic Acoustic Transducer (EMAT). An EMAT comprises of a meandering wire of coil in the presence of a static magnetic field. When the EMAT is placed near a conductive test sample and pulsed with an alternating current at the desired frequency, eddy currents are introduced in the test sample. In turn, these eddy currents interact with the static magnetic field, and a Lorentz force is induced into the sample, which acts as the radiative ultrasonic source required for NDE applications [289], [290]. The meandering pattern of the coils can be altered to match the desired acoustic FGW wavelength. Many papers have used EMATs to successfully transduce

various guided wave types [291]–[293]. Moreover, flexible EMATs for the sole purpose of pipe inspection have also been developed [294]–[296] and similar designs are well suited to the FGW generation on the RSW observed in the legacy canister design.

Additionally, for successful on-site deployment in a radioactive environment, radiation testing is required to ensure that hardware can operate in this environment for a suitable amount of time. All equipment that has been used in this thesis has not had any radiation testing conducted, or alterations made to better accommodate such an environment. It has been shown in the literature, that substances such as PTFE used in the wedge of the FGW hardware, does not have a high tolerance to radiation. More expensive materials, such as PEEK, have been identified as a suitable replacement with a far higher tolerance to radiation [297]. Various different testing standards are available [298]–[301], and these are recommended to be reviewed and implemented to allow for effective onsite deployment.

Finally, it is necessary to integrate the FGW inspection hardware on to current on-site inspection and deployment mechanisms. As shown in Figure 3, the deployment of inspection hardware is accomplished via two openings on the storage infrastructure using a bespoke trolley system. It is recommended that a suitable contractor is hired to modify the inspection trolleys to accommodate the in-situ inspection hardware documented in this thesis.

Eddy current inversion

Interpretation of eddy current signals is typically done in a manual fashion by well-trained inspectors, and usually results in only detection of the defect with little characterisation of the defect size. There are two main types of inversion approaches that have been documented in the literature and these are phenomenological and empirical approaches [302], [303].

Phenomenological approaches rely on models that attempt to describe the underlying physics of the eddy current test being performed [302], [304]. However, this

kind of approach has reported limited success due to differences in probe designs, sample types, and the diffuse nature of the eddy current itself.

In contrast, empirical approaches have documented far more practical inversion through the use of pattern recognition techniques. These pattern recognition techniques make use of features that are extracted from eddy current signals that include Fourier descriptors [305]–[307], amplitudes [308], [309], phase angles [308], partial powers [309], and statistical moments [310]. Various different machine learning algorithms, such as k-means clustering [306], adaptive learning networks [311], linear discriminant functions [309], [310], k-nearest neighbour algorithms [309], [310], neural networks [307]–[310], [312], and fuzzy synthetic pattern recognition [313], have been deployed in the literature to classify and size any detected flaws.

It is clear that machine learning offers significant advantages when inverting the physical nature of any detected defect. A well-trained model can invert physical parameters in a fraction of the time than that associated with phenomenological approaches and can invert physical parameters of various defect types. Therefore, a next logical step with the data rich automated eddy current platform that has been developed, would be to integrate machine learning to classify and size detected defects.

Adaptation to austenitic steels and differing geometries

Whilst the work presented for the thermal compensation strategy was successfully performed on carbon steel welds, it is noted that austenitic welds associated with stainless steel welding produce several challenges due to high attenuation and backscattering caused by large grains within and around the HAZ [314]–[317].

There is no one definitive method for reducing these large attenuation and back scattering effects and it remains a highly active NDE research topic. However, these effects can be classified as coherent noise in which the same input will produce the same output. These properties make tackling such problems well suited to advanced pattern recognition techniques such as machine learning. Recently, machine learning has been deployed within NDE to alleviate another coherent noise issue observed in ultrasonic

images and effectively reduce artefacts generated from structural features [318]. Machine learning has also been deployed to reduce the noise resulting from the coarse grain structure in austenitic welds too. Li et al. have used k-means clustering and a machine learning auto encoder to denoise and drastically improve SNR on additive and welded components [319]. While Singh et al. have successfully deployed deep learning models to invert FE generated data, improving SNR of the detected defect and characterising the weld microstructure [258], [320]. The work performed by Singh et al. is of real benefit to the topics covered in this thesis as it would accurately provide accurate information of the grain microstructure and allow for defects to be detected. However, the work presented is only performed on simulated datasets and therefore experimental adaptation would be the logical and next feasible step recommended to advance the work presented in this thesis.

Other issues still to be overcome, would be adapting the geometry to that of the canister of the future once finalised and accelerating the code further so that real time imaging of the weld could take place. These next steps would provide an attractive and interesting follow up research topic.

Appendix A

The coefficients given in Eq. 80 are given below:

$$c = \begin{bmatrix} \mathbf{c}^{UU} & \mathbf{0} \\ \mathbf{0} & \mathbf{0} \end{bmatrix}; \; \alpha = \begin{bmatrix} 0 & I\alpha^{UV} \\ 0 & 0 \end{bmatrix};$$

$$r = \begin{bmatrix} \mathbf{0} \\ \mathbf{0} \end{bmatrix}; \; a = \begin{bmatrix} a^{UU} & Ia^{UV} \\ 0 & A^{VV} \end{bmatrix};$$

$$\beta = \begin{bmatrix} \boldsymbol{\beta}^{UU} & -I\beta^{UV} \\ 0 & 0 \end{bmatrix}; \; d_a = \begin{bmatrix} 0 & \mathbf{d}^{UV} \\ \mathbf{d}^{VU} & 0 \end{bmatrix};$$

$$d_a = \begin{bmatrix} 0 & \mathbf{d}^{UV} \\ \mathbf{d}^{VU} & 0 \end{bmatrix}; \; e_a = \begin{bmatrix} 0 & 0 \\ 0 & 0 \end{bmatrix}; \; f = \begin{bmatrix} \mathbf{0} \\ \mathbf{0} \end{bmatrix};$$

It is assumed that $\mathbf{0}$ represents a zero matrix of appropriate dimensions.

All other sub-matrices are given below:

$$\mathbf{c}^{UU} = \begin{bmatrix} c_{11}^{UU} & c_{12}^{UU} & c_{13}^{UU} \\ c_{21}^{UU} & c_{22}^{UU} & c_{23}^{UU} \\ c_{31}^{UU} & c_{32}^{UU} & c_{33}^{UU} \end{bmatrix};$$

$$c_{11}^{UU} = \begin{bmatrix} \left(\frac{1}{\gamma_1}\right)^2 C_{11} & \left(\frac{1}{\gamma_1\gamma_2}\right) C_{16} \\ \left(\frac{1}{\gamma_2\gamma_1}\right) C_{61} & \left(\frac{1}{\gamma_2}\right)^2 C_{66} \end{bmatrix}; \; c_{12}^{UU} = \begin{bmatrix} \left(\frac{1}{\gamma_1}\right)^2 C_{16} & \left(\frac{1}{\gamma_1\gamma_2}\right) C_{12} \\ \left(\frac{1}{\gamma_2\gamma_1}\right) C_{66} & \left(\frac{1}{\gamma_2}\right)^2 C_{62} \end{bmatrix};$$

$$c_{13}^{UU} = \begin{bmatrix} \left(\frac{1}{\gamma_1}\right)^2 C_{15} & \left(\frac{1}{\gamma_1\gamma_2}\right) C_{14} \\ \left(\frac{1}{\gamma_2\gamma_1}\right) C_{65} & \left(\frac{1}{\gamma_2}\right)^2 C_{64} \end{bmatrix}; \; c_{21}^{UU} = \begin{bmatrix} \left(\frac{1}{\gamma_1}\right)^2 C_{61} & \left(\frac{1}{\gamma_1\gamma_2}\right) C_{66} \\ \left(\frac{1}{\gamma_2\gamma_1}\right) C_{21} & \left(\frac{1}{\gamma_2}\right)^2 C_{26} \end{bmatrix};$$

$$c_{22}^{UU} = \begin{bmatrix} \left(\frac{1}{\gamma_1}\right)^2 C_{66} & \left(\frac{1}{\gamma_1\gamma_2}\right) C_{62} \\ \left(\frac{1}{\gamma_2\gamma_1}\right) C_{26} & \left(\frac{1}{\gamma_2}\right)^2 C_{22} \end{bmatrix}; \; c_{23}^{UU} = \begin{bmatrix} \left(\frac{1}{\gamma_1}\right)^2 C_{65} & \left(\frac{1}{\gamma_1\gamma_2}\right) C_{64} \\ \left(\frac{1}{\gamma_2\gamma_1}\right) C_{25} & \left(\frac{1}{\gamma_2}\right)^2 C_{24} \end{bmatrix};$$

215

$$c_{31}^{UU} = \begin{bmatrix} \left(\dfrac{1}{\gamma_1}\right)^2 C_{51} & \left(\dfrac{1}{\gamma_1\gamma_2}\right) C_{56} \\[3mm] \left(\dfrac{1}{\gamma_2\gamma_1}\right) C_{41} & \left(\dfrac{1}{\gamma_2}\right)^2 C_{46} \end{bmatrix}; \quad c_{32}^{UU} = \begin{bmatrix} \left(\dfrac{1}{\gamma_1}\right)^2 C_{56} & \left(\dfrac{1}{\gamma_1\gamma_2}\right) C_{52} \\[3mm] \left(\dfrac{1}{\gamma_2\gamma_1}\right) C_{46} & \left(\dfrac{1}{\gamma_2}\right)^2 C_{42} \end{bmatrix};$$

$$c_{33}^{UU} = \begin{bmatrix} \left(\dfrac{1}{\gamma_1}\right)^2 C_{55} & \left(\dfrac{1}{\gamma_1\gamma_2}\right) C_{54} \\[3mm] \left(\dfrac{1}{\gamma_2\gamma_1}\right) C_{45} & \left(\dfrac{1}{\gamma_2}\right)^2 C_{44} \end{bmatrix},$$

$$\alpha^{UV} = \begin{bmatrix} \begin{bmatrix} \left(\dfrac{1}{\gamma_1}\right) C_{15} \\[2mm] \left(\dfrac{1}{\gamma_2}\right) C_{65} \end{bmatrix} & \begin{bmatrix} \left(\dfrac{1}{\gamma_1}\right) C_{14} \\[2mm] \left(\dfrac{1}{\gamma_2}\right) C_{64} \end{bmatrix} & \begin{bmatrix} \left(\dfrac{1}{\gamma_1}\right) C_{13} \\[2mm] \left(\dfrac{1}{\gamma_2}\right) C_{63} \end{bmatrix} \\[6mm] \begin{bmatrix} \left(\dfrac{1}{\gamma_1}\right) C_{65} \\[2mm] \left(\dfrac{1}{\gamma_2}\right) C_{25} \end{bmatrix} & \begin{bmatrix} \left(\dfrac{1}{\gamma_1}\right) C_{64} \\[2mm] \left(\dfrac{1}{\gamma_2}\right) C_{24} \end{bmatrix} & \begin{bmatrix} \left(\dfrac{1}{\gamma_1}\right) C_{63} \\[2mm] \left(\dfrac{1}{\gamma_2}\right) C_{23} \end{bmatrix} \\[6mm] \begin{bmatrix} \left(\dfrac{1}{\gamma_1}\right) C_{55} \\[2mm] \left(\dfrac{1}{\gamma_2}\right) C_{45} \end{bmatrix} & \begin{bmatrix} \left(\dfrac{1}{\gamma_1}\right) C_{54} \\[2mm] \left(\dfrac{1}{\gamma_2}\right) C_{44} \end{bmatrix} & \begin{bmatrix} \left(\dfrac{1}{\gamma_1}\right) C_{53} \\[2mm] \left(\dfrac{1}{\gamma_2}\right) C_{43} \end{bmatrix} \end{bmatrix},$$

$$a^{UU} = \begin{bmatrix} -\rho\omega^2 & 0 & 0 \\ 0 & -\rho\omega^2 & 0 \\ 0 & 0 & -\rho\omega^2 \end{bmatrix}, \quad a^{VV} = \begin{bmatrix} -\rho\omega^2 & 0 & 0 \\ 0 & -\rho\omega^2 & 0 \\ 0 & 0 & -\rho\omega^2 \end{bmatrix},$$

$$a^{UV} = \begin{bmatrix} \left(\dfrac{1}{\gamma_1}\right)' C_{15} + \left(\dfrac{1}{\gamma_2}\right)' C_{65} & \left(\dfrac{1}{\gamma_1}\right)' C_{14} + \left(\dfrac{1}{\gamma_2}\right)' C_{64} & \left(\dfrac{1}{\gamma_1}\right)' C_{13} + \left(\dfrac{1}{\gamma_2}\right)' C_{63} \\[3mm] \left(\dfrac{1}{\gamma_1}\right)' C_{65} + \left(\dfrac{1}{\gamma_2}\right)' C_{25} & \left(\dfrac{1}{\gamma_1}\right)' C_{64} + \left(\dfrac{1}{\gamma_2}\right)' C_{24} & \left(\dfrac{1}{\gamma_1}\right)' C_{63} + \left(\dfrac{1}{\gamma_2}\right)' C_{23} \\[3mm] \left(\dfrac{1}{\gamma_1}\right)' C_{55} + \left(\dfrac{1}{\gamma_2}\right)' C_{45} & \left(\dfrac{1}{\gamma_1}\right)' C_{54} + \left(\dfrac{1}{\gamma_2}\right)' C_{44} & \left(\dfrac{1}{\gamma_1}\right)' C_{53} + \left(\dfrac{1}{\gamma_2}\right)' C_{43} \end{bmatrix},$$

$$\beta^{UU} = \begin{bmatrix} \beta_{11}^{UU} & \beta_{12}^{UU} & \beta_{13}^{UU} \\ \beta_{21}^{UU} & \beta_{22}^{UU} & \beta_{23}^{UU} \\ \beta_{31}^{UU} & \beta_{32}^{UU} & \beta_{33}^{UU} \end{bmatrix},$$

$$\beta_{11}^{UU} = \begin{bmatrix} \dfrac{1}{\gamma_1}\left(\dfrac{1}{\gamma_1}\right)' C_{11} + \dfrac{1}{\gamma_1}\left(\dfrac{1}{\gamma_2}\right)' C_{61} \\[3mm] \dfrac{1}{\gamma_2}\left(\dfrac{1}{\gamma_1}\right)' C_{16} + \dfrac{1}{\gamma_2}\left(\dfrac{1}{\gamma_2}\right)' C_{66} \end{bmatrix}; \quad \beta_{12}^{UU} = \begin{bmatrix} \dfrac{1}{\gamma_1}\left(\dfrac{1}{\gamma_1}\right)' C_{16} + \dfrac{1}{\gamma_1}\left(\dfrac{1}{\gamma_2}\right)' C_{66} \\[3mm] \dfrac{1}{\gamma_2}\left(\dfrac{1}{\gamma_1}\right)' C_{12} + \dfrac{1}{\gamma_2}\left(\dfrac{1}{\gamma_2}\right)' C_{62} \end{bmatrix};$$

$$\boldsymbol{\beta}_{13}^{UU} = \begin{bmatrix} \dfrac{1}{\gamma_1}\left(\dfrac{1}{\gamma_1}\right)' C_{15} + \dfrac{1}{\gamma_1}\left(\dfrac{1}{\gamma_2}\right)' C_{65} \\ \dfrac{1}{\gamma_2}\left(\dfrac{1}{\gamma_1}\right)' C_{14} + \dfrac{1}{\gamma_2}\left(\dfrac{1}{\gamma_2}\right)' C_{64} \end{bmatrix}; \; \boldsymbol{\beta}_{21}^{UU} = \begin{bmatrix} \dfrac{1}{\gamma_1}\left(\dfrac{1}{\gamma_1}\right)' C_{61} + \dfrac{1}{\gamma_1}\left(\dfrac{1}{\gamma_2}\right)' C_{21} \\ \dfrac{1}{\gamma_2}\left(\dfrac{1}{\gamma_1}\right)' C_{66} + \dfrac{1}{\gamma_2}\left(\dfrac{1}{\gamma_2}\right)' C_{26} \end{bmatrix};$$

$$\boldsymbol{\beta}_{22}^{UU} = \begin{bmatrix} \dfrac{1}{\gamma_1}\left(\dfrac{1}{\gamma_1}\right)' C_{66} + \dfrac{1}{\gamma_1}\left(\dfrac{1}{\gamma_2}\right)' C_{26} \\ \dfrac{1}{\gamma_2}\left(\dfrac{1}{\gamma_1}\right)' C_{62} + \dfrac{1}{\gamma_2}\left(\dfrac{1}{\gamma_2}\right)' C_{22} \end{bmatrix}; \; \boldsymbol{\beta}_{23}^{UU} = \begin{bmatrix} \dfrac{1}{\gamma_1}\left(\dfrac{1}{\gamma_1}\right)' C_{65} + \dfrac{1}{\gamma_1}\left(\dfrac{1}{\gamma_2}\right)' C_{25} \\ \dfrac{1}{\gamma_2}\left(\dfrac{1}{\gamma_1}\right)' C_{64} + \dfrac{1}{\gamma_2}\left(\dfrac{1}{\gamma_2}\right)' C_{24} \end{bmatrix};$$

$$\boldsymbol{\beta}_{31}^{UU} = \begin{bmatrix} \dfrac{1}{\gamma_1}\left(\dfrac{1}{\gamma_1}\right)' C_{51} + \dfrac{1}{\gamma_1}\left(\dfrac{1}{\gamma_2}\right)' C_{41} \\ \dfrac{1}{\gamma_2}\left(\dfrac{1}{\gamma_1}\right)' C_{56} + \dfrac{1}{\gamma_2}\left(\dfrac{1}{\gamma_2}\right)' C_{46} \end{bmatrix}; \; \boldsymbol{\beta}_{32}^{UU} = \begin{bmatrix} \dfrac{1}{\gamma_1}\left(\dfrac{1}{\gamma_1}\right)' C_{56} + \dfrac{1}{\gamma_1}\left(\dfrac{1}{\gamma_2}\right)' C_{46} \\ \dfrac{1}{\gamma_2}\left(\dfrac{1}{\gamma_1}\right)' C_{52} + \dfrac{1}{\gamma_2}\left(\dfrac{1}{\gamma_2}\right)' C_{42} \end{bmatrix};$$

$$\boldsymbol{\beta}_{33}^{UU} = \begin{bmatrix} \dfrac{1}{\gamma_1}\left(\dfrac{1}{\gamma_1}\right)' C_{55} + \dfrac{1}{\gamma_1}\left(\dfrac{1}{\gamma_2}\right)' C_{45} \\ \dfrac{1}{\gamma_2}\left(\dfrac{1}{\gamma_1}\right)' C_{54} + \dfrac{1}{\gamma_2}\left(\dfrac{1}{\gamma_2}\right)' C_{44} \end{bmatrix},$$

$$\boldsymbol{\beta}^{UV} = \begin{bmatrix} \begin{bmatrix} \left(\dfrac{1}{\gamma_1}\right) C_{51} \\ \left(\dfrac{1}{\gamma_2}\right) C_{56} \end{bmatrix} & \begin{bmatrix} \left(\dfrac{1}{\gamma_1}\right) C_{56} \\ \left(\dfrac{1}{\gamma_2}\right) C_{52} \end{bmatrix} & \begin{bmatrix} \left(\dfrac{1}{\gamma_1}\right) C_{55} \\ \left(\dfrac{1}{\gamma_2}\right) C_{54} \end{bmatrix} \\[3em] \begin{bmatrix} \left(\dfrac{1}{\gamma_1}\right) C_{41} \\ \left(\dfrac{1}{\gamma_2}\right) C_{46} \end{bmatrix} & \begin{bmatrix} \left(\dfrac{1}{\gamma_1}\right) C_{46} \\ \left(\dfrac{1}{\gamma_2}\right) C_{42} \end{bmatrix} & \begin{bmatrix} \left(\dfrac{1}{\gamma_1}\right) C_{45} \\ \left(\dfrac{1}{\gamma_2}\right) C_{44} \end{bmatrix} \\[3em] \begin{bmatrix} \left(\dfrac{1}{\gamma_1}\right) C_{31} \\ \left(\dfrac{1}{\gamma_2}\right) C_{36} \end{bmatrix} & \begin{bmatrix} \left(\dfrac{1}{\gamma_1}\right) C_{36} \\ \left(\dfrac{1}{\gamma_2}\right) C_{32} \end{bmatrix} & \begin{bmatrix} \left(\dfrac{1}{\gamma_1}\right) C_{35} \\ \left(\dfrac{1}{\gamma_2}\right) C_{34} \end{bmatrix} \end{bmatrix},$$

$$\boldsymbol{d}^{UV} = \begin{bmatrix} -C_{55} & -C_{54} & -C_{53} \\ -C_{45} & -C_{44} & -C_{43} \\ -C_{35} & -C_{34} & -C_{33} \end{bmatrix}, \; \boldsymbol{d}^{VU} = \begin{bmatrix} -\rho\omega^2 & 0 & 0 \\ 0 & -\rho\omega^2 & 0 \\ 0 & 0 & -\rho\omega^2 \end{bmatrix}$$

References

[1] 'About us', *GOV.UK*. https://www.gov.uk/government/organisations/sellafield-ltd/about (accessed Oct. 04, 2022).

[2] GOV.UK, 'Energy trends'. https://www.gov.uk/government/collections/energy-trends (accessed Mar. 03, 2019).

[3] GOV.UK, 'Table of past and present UK nuclear reactors'. https://assets.publishing.service.gov.uk/government/uploads/system/uploads/attachment_data/file/421705/Table_of_past_and_present_UK_nuclear_reactors.pdf (accessed Mar. 03, 2019).

[4] Nuclear Decommissioning Authority, 'Fact sheet: spent fuel reprocessing'. https://ukinventory.nda.gov.uk/wp-content/uploads/2014/01/Fact-sheet-spent-fuel-reprocessing.pdf (accessed Mar. 03, 2019).

[5] Nuclear Decommissioning Authority, 'End in sight for reprocessing nuclear fuel at Sellafield - Cleaning up our nuclear past: faster, safer and sooner'. https://nda.blog.gov.uk/2017/01/24/end-in-sight-for-reprocessing-nuclear-fuel-at-sellafield/ (accessed Mar. 03, 2019).

[6] 'Orano Melox - used fuel recycling and MOX fuel | Orano', *orano.group*. https://www.orano.group/en/nuclear-expertise/orano-s-sites-around-the-world/recycling-spent-fuel/melox/expertise (accessed Oct. 25, 2022).

[7] 'US MOX facility contract terminated : Uranium & Fuel - World Nuclear News'. https://world-nuclear-news.org/Articles/US-MOX-facility-contract-terminated (accessed Oct. 25, 2022).

[8] World Nuclear News, 'Reprocessing ceases at UK's Thorp plant - World Nuclear News'. http://www.world-nuclear-news.org/Articles/Reprocessing-ceases-at-UKs-Thorp-plant (accessed Mar. 03, 2019).

[9] The British Broadcasting Corporation, 'Sellafield Thorp site to close', Jun. 07, 2012. Accessed: Mar. 03, 2019. [Online]. Available: https://www.bbc.com/news/uk-england-cumbria-18353122

[10] 'Operations to end at Sellafield's Magnox Reprocessing Plant', *GOV.UK*. https://www.gov.uk/government/news/operations-to-end-at-sellafields-magnox-reprocessing-plant (accessed Dec. 15, 2022).

[11] U. of Sheffield, 'Professor Neil C Hyatt - Staff - Materials Science and Engineering - The University of Sheffield'. https://www.sheffield.ac.uk/materials/staff/nchyatt01 (accessed Apr. 01, 2019).

[12] N. C. Hyatt, 'Plutonium management policy in the United Kingdom: The need for a dual track strategy', *Energy Policy*, vol. 101, pp. 303–309, Feb. 2017, doi: 10.1016/j.enpol.2016.08.033.

[13] GOV.UK, 'Plutonium: Credible Options Analysis'. https://webarchive.nationalarchives.gov.uk/20150806125613/http://www.nda.gov.uk/publication/plutonium-credible-options-analysis-redacted-2010/ (accessed Mar. 03, 2019).

[14] 'Game Changers - Projects', *Game Changers*. https://www.gamechangers.technology/projects (accessed Oct. 14, 2022).

[15] 'Image Enhancement for Vault Store Visual Inspection', *Game Changers*. https://www.gamechangers.technology/projects/Image_Enhancement_for_Vault_Store_Visual_Inspection (accessed Oct. 14, 2022).

[16] 'Field assessment of granular materials', *Game Changers*. https://www.gamechangers.technology/projects/Field_assessment_of_granular_materials (accessed Oct. 14, 2022).

[17] 'Hyperspectral Imaging Corrosion Detection'. https://www.gamechangers.technology/projects/Hyperspectral_Imaging_Corrosion_Detection (accessed Oct. 14, 2022).

[18] '[3A3] Focused Lamb waves for sub-wavelength defect detection using EMATs'. https://www.bindt.org/events/ndt-2022/abstract-3a3/ (accessed Oct. 04, 2022).

[19] '[2A5] Non-contact pressure measurement of sealed units using acoustic methods'. https://www.bindt.org/events/ndt-2022/abstract-2a5/ (accessed Oct. 04, 2022).

[20] 'Atmospheric Corrosion of Aluminum Alloy 6063 Beneath Ferric Chloride Corrosion Product Droplets | CORROSION'. https://meridian.allenpress.com/corrosion/article/76/10/985/447117/Atmospheric-Corrosion-of-Aluminum-Alloy-6063 (accessed Oct. 04, 2022).

[21] S. Mahmood, C. Gallagher, and D. L. Engelberg, 'Application of X-Ray Computed Tomography to Assess the Effect of Elevated Temperature on Atmospheric Corrosion of Aluminum Alloy 6063 in Contact with FeCl3 Droplets', *Corrosion*, vol. 78, no. 7, pp. 650–660, May 2022, doi: 10.5006/4050.

[22] M. Kroening, D. Sednev, and D. Chumak, 'Nondestructive testing at nuclear facilities as basis for the 3S synergy implementation', 2012, pp. 1–4. doi: https://doi.org/10.1109/IFOST.2012.6357725.

[23] W. Lucas and S. Westgate, '10 - Welding and Soldering', in *Electrical Engineer's Reference Book (Sixteenth Edition)*, M. A. Laughton and D. J. Warne, Eds. Oxford: Newnes, 2003, pp. 10–1. doi: 10.1016/B978-075064637-6/50010-1.

[24] K. Weman, *Welding processes handbook*, 2nd ed. Oxford ; Philadelphia: Woodhead Pub, 2012.

[25] R. W. M. Jr, *Principles of Welding: Processes, Physics, Chemistry, and Metallurgy*. John Wiley & Sons, 2008.

[26] A. W. Society, *Welding Handbook: Welding processes*. American Welding Society, 2004.

[27] D. Y. You, X. D. Gao, and S. Katayama, 'Review of laser welding monitoring', *Sci. Technol. Weld. Join.*, vol. 19, no. 3, pp. 181–201, Apr. 2014, doi: 10.1179/1362171813Y.0000000180.

[28] M. St. Węglowski, S. Błacha, and A. Phillips, 'Electron beam welding – Techniques and trends – Review', *Vacuum*, vol. 130, pp. 72–92, Aug. 2016, doi: 10.1016/j.vacuum.2016.05.004.

[29] P. Kah, R. Suoranta, and J. Martikainen, 'Advanced gas metal arc welding processes', *Int. J. Adv. Manuf. Technol.*, vol. 67, no. 1, pp. 655–674, Jul. 2013, doi: 10.1007/s00170-012-4513-5.

[30] B. J. Kutelu, S. O. Seidu, G. I. Eghabor, and A. I. Ibitoye, 'Review of GTAW Welding Parameters', *J. Miner. Mater. Charact. Eng.*, vol. 06, no. 05, Art. no. 05, Aug. 2018, doi: 10.4236/jmmce.2018.65039.

[31] M. Vasilev, C. N. MacLeod, C. Loukas, Y. Javadi, R. K. W. Vithanage, D. Lines, E. Mohseni, S. G. Pierce, and A. Gachagan, 'Sensor-enabled multi-robot system for automated welding and in-process ultrasonic NDE', *Sensors*, vol. 21, no. 15, Jul. 2021, doi: 10.3390/s21155077.

[32] M. Vasilev, 'Sensor-enabled robotics for ultrasonic NDE', PhD Thesis, University of Strathclyde, Glasgow, 2021. [Online]. Available: https://doi.org/10.48730/wf52-x747

[33] '500i'. https://www.fronius.com/en/welding-technology/products/manual-welding/migmag/tpsi/tpsi/tps-500i (accessed Aug. 25, 2022).

[34] JESS WELDING, 'Products', Sep. 14, 2020. https://www.jess-welding.com/products/ (accessed Aug. 25, 2022).

[35] 'ISO 6520-1:2007 - Welding and allied processes — Classification of geometric imperfections in metallic materials — Part 1: Fusion welding', *Int. Stand. Organ.*, Accessed: Aug. 26, 2022. [Online]. Available: https://www.iso.org/cms/render/live/en/sites/isoorg/contents/data/standard/04/02/40229.html

[36] 'ISO 13588:2019 - Non-destructive testing of welds — Ultrasonic testing — Use of automated phased array technology', *Int. Stand. Organ.*, Accessed: Jul. 18, 2022. [Online]. Available: https://www.iso.org/cms/render/live/en/sites/isoorg/contents/data/standard/07/27/72747.html

[37] 'ISO 17640:2018 - Non-destructive testing of welds — Ultrasonic testing — Techniques, testing levels, and assessment', *Int. Stand. Organ.*, Accessed: Jul. 18, 2022. [Online]. Available: https://www.iso.org/cms/render/live/en/sites/isoorg/contents/data/standard/07/57/75737.html

[38] 'ISO 19285:2017- Non-destructive testing of welds — Phased array ultrasonic testing (PAUT) — Acceptance levels', *Int. Stand. Organ.*, Accessed: Jul. 18, 2022.

[Online]. Available: https://www.iso.org/cms/render/live/en/sites/isoorg/contents/data/standard/06/42/64 266.html

[39] 'BS EN ISO 17643:2015 - Non-destructive testing of welds. Eddy current examination of welds by complex plane analysis', *Int. Stand. Organ.*, Accessed: May 24, 2019. [Online]. Available: https://shop.bsigroup.com/ProductDetail/?pid=000000000030266748

[40] 'ISO 23864:2021(en), Non-destructive testing of welds — Ultrasonic testing — Use of automated total focusing technique (TFM) and related technologies', *Int. Stand. Organ.*, Accessed: Aug. 26, 2022. [Online]. Available: https://www.iso.org/obp/ui/#iso:std:iso:23864:ed-1:v1:en

[41] 'ISO 23277:2015 - Non-destructive testing of welds — Penetrant testing — Acceptance levels', *Int. Stand. Organ.*, Accessed: Aug. 26, 2022. [Online]. Available: https://www.iso.org/cms/render/live/en/sites/isoorg/contents/data/standard/06/23/62 315.html

[42] 'ISO 17637:2003(en), Non-destructive testing of welds — Visual testing of fusion-welded joints', *Int. Stand. Organ.*, Accessed: Aug. 26, 2022. [Online]. Available: https://www.iso.org/obp/ui/#iso:std:iso:17637:ed-1:v1:en

[43] L. Schulenburg, 'NDT 4.0: Opportunity or Threat?', *Mater. Eval.*, vol. 78, no. 7, pp. 852–860, Jul. 2020, doi: 10.32548/2020.me-04134.

[44] Resistance Welding Manufacturers' Association Alliance, *Resistance Welding Manufacturing Alliance (RWMA) - Resistance Welding Manual-American Welding Society (AWS) (2003).pdf*, Revised Fourth Edition.

[45] A. O'Brien and American Welding Society, Eds., *Welding handbook. Vol. 3: Welding processes, part 2*, 9. ed. Miami, Fla: American Welding Soc, 2007.

[46] Resistance Welder Manufacturers' Association, *Resistance Welding Manual*. Resistance Welder Manufactures assn, 2003.

[47] G. T. Meaden, *Electrical Resistance of Metals*. Springer, 2013.

[48] U. S. N. B. of Standards, *Copper Wire Tables*. U.S. Government Printing Office, 1956.

[49] AWS Committee on Methods of Inspection and American Welding Society, Eds., *Welding inspection handbook*, Fourth edition. Miami, Florida: American Welding Society, 2015.

[50] M. Ouisse and S. Cogan, 'Robust design of spot welds in automotive structures A decision-making methodology', *Mech. Syst. Signal Process.*, p. 19, 2010, doi: https://doi.org/10.1016/j.ymssp.2009.09.012.

[51] M. A. Fakih, 'Detection and assessment of flaws in friction stir welded joints using ultrasonic guided waves: experimental and finite element analysis', *Mech. Syst. Signal Process.*, p. 19, 2018, doi: https://doi.org/10.1016/j.ymssp.2017.09.003.

[52] H. Eisazadeh, M. Hamedi, and A. Halvaee, 'New parametric study of nugget size in resistance spot welding process using finite element method', *Mater. Des.*, vol. 31, no. 1, pp. 149–157, Jan. 2010, doi: 10.1016/j.matdes.2009.06.042.

[53] F. Qiuyue, X. Guocheng, and G. Xiaopeng, 'Ultrasonic Nondestructive Evaluation of Porosity Size and Location of Spot Welding Based on Wavelet Packet Analysis', *J. Nondestruct. Eval.*, vol. 39, no. 1, p. 7, Jan. 2020, doi: 10.1007/s10921-019-0650-1.

[54] J.-P. Kong and C.-Y. Kang, 'Effect of alloying elements on expulsion in electric resistance spot welding of advanced high strength steels', *Sci. Technol. Weld. Join.*, vol. 21, no. 1, pp. 32–42, Jan. 2016, doi: 10.1179/1362171815Y.0000000057.

[55] T. Mira-Aguiar, I. Galvão, C. Leitão, and D. M. Rodrigues, 'Analysis of weld defects in similar and dissimilar resistance seam welding of aluminium, zinc and galvanised steel', *Sci. Technol. Weld. Join.*, vol. 20, no. 5, pp. 409–417, May 2015, doi: 10.1179/1362171815Y.0000000031.

[56] R. Halmshaw, *Non-Destructive Testing*, 2nd Edition. Northampton: Edward Arnold, 2004.

[57]   'Non-Destructive Testing (NDT) Market Size, Growth Analysis 2029'. https://www.fortunebusinessinsights.com/non-destructive-testing-ndt-market-103596 (accessed Jun. 07, 2022).

[58]   B. W. Drinkwater and P. D. Wilcox, 'Ultrasonic arrays for non-destructive evaluation: A review', *NDT E Int.*, vol. 39, no. 7, pp. 525–541, Oct. 2006, doi: 10.1016/j.ndteint.2006.03.006.

[59]   J. L. Rose, *Ultrasonic Waves in Solid Media*. Cambridge University Press, 2004.

[60]   J. L. Rose, *Ultrasonic Guided Waves in Solid Media*. New York: Cambridge University Press, 2014. doi: 10.1017/CBO9781107273610.

[61]   L. Bjørnø, 'Forty years of nonlinear ultrasound', *Ultrasonics*, vol. 40, no. 1, pp. 11–17, May 2002, doi: 10.1016/S0041-624X(02)00084-7.

[62]   B. A. Auld, *Acoustic Fields and Waves in Solids*, 2nd ed., vol. 1, 2 vols. Malabar, Florida: Krieger Publishing Company, 1973.

[63]   J. D. Achenbach, *Wave propagation in elastic solids*. Amsterdam, New York: North-Holland Pub. Co.; American Elsevier Pub. Co, 1973.

[64]   H. M. Ledbetter, 'Stainless-steel elastic constants at low temperatures', *J. Appl. Phys.*, vol. 52, no. 3, pp. 1587–1589, Mar. 1981, doi: 10.1063/1.329644.

[65]   M. J. S. Lowe, 'Matrix techniques for modeling ultrasonic waves in multilayered media', *IEEE Trans. Ultrason. Ferroelectr. Freq. Control*, vol. 42, no. 4, pp. 525–542, Jul. 1995, doi: 10.1109/58.393096.

[66]   M. Castaings and B. Hosten, 'Delta operator technique to improve the Thomson–Haskell-method stability for propagation in multilayered anisotropic absorbing plates', *J. Acoust. Soc. Am.*, vol. 95, no. 4, pp. 1931–1941, Apr. 1994, doi: 10.1121/1.408707.

[67]   B. Hosten and M. Castaings, 'Transfer matrix of multilayered absorbing and anisotropic media. Measurements and simulations of ultrasonic wave propagation through composite materials', *J. Acoust. Soc. Am.*, vol. 94, no. 3, pp. 1488–1495, Sep. 1993, doi: 10.1121/1.408152.

[68]   S. Adhikar, 'Damping Models for Structural Vibration', PhD Thesis, Cambridge University Trinity College, 2000.

[69]   R. K. W. Vithanage, E. Mohseni, Z. Qiu, C. MacLeod, Y. Javadi, N. Sweeney, G. Pierce, and A. Gachagan, 'A Phased Array Ultrasound Roller Probe for Automated in-Process/Interpass Inspection of Multipass Welds', *IEEE Trans. Ind. Electron.*, vol. 68, no. 12, pp. 12781–12790, Dec. 2021, doi: 10.1109/TIE.2020.3042112.

[70]   N. H. Fletcher, *Acoustic Systems in Biology*. Oxford University Press, USA, 1992.

[71]   J. A. Sethian, *Level Set Methods and Fast Marching Methods: Evolving Interfaces in Computational Geometry, Fluid Mechanics, Computer Vision, and Materials Science*. Cambridge University Press, 1999.

[72]   C. Mineo, D. Lines, and D. Cerniglia, 'Generalised bisection method for optimum ultrasonic ray tracing and focusing in multi-layered structures', *Ultrasonics*, vol. 111, p. 106330, Mar. 2021, doi: 10.1016/j.ultras.2020.106330.

[73]   J. Krautkrämer and H. Krautkrämer, *Ultrasonic Testing of Materials*. Springer Science & Business Media, 2013.

[74]   L. Le Jeune, S. Robert, E. Lopez Villaverde, and C. Prada, 'Plane Wave Imaging for ultrasonic non-destructive testing: Generalization to multimodal imaging', *Ultrasonics*, vol. 64, pp. 128–138, Jan. 2016, doi: 10.1016/j.ultras.2015.08.008.

[75]   W. Kerr, S. G. Pierce, and P. Rowe, 'Investigation of synthetic aperture methods in ultrasound surface imaging using elementary surface types', *Ultrasonics*, vol. 72, pp. 165–176, Dec. 2016, doi: 10.1016/j.ultras.2016.08.007.

[76]   S. Cochran, 'Ultrasonics Part 12. Fundamentals of ultrasonic phased arrays', *Insight - Non-Destr. Test. Cond. Monit.*, vol. 48, no. 4, pp. 212–217, Apr. 2006, doi: 10.1784/insi.2006.48.4.212.

[77]   C. Fan, M. Caleap, M. Pan, and B. W. Drinkwater, 'A comparison between ultrasonic array beamforming and super resolution imaging algorithms for non-destructive evaluation', *Ultrasonics*, vol. 54, no. 7, pp. 1842–1850, Sep. 2014, doi: 10.1016/j.ultras.2013.12.012.

[78]   C. Holmes, B. W. Drinkwater, and P. D. Wilcox, 'Post-processing of the full matrix of ultrasonic transmit–receive array data for non-destructive evaluation', *NDT E Int.*, vol. 38, no. 8, pp. 701–711, Dec. 2005, doi: 10.1016/j.ndteint.2005.04.002.

[79]   J. Zhang, B. W. Drinkwater, P. D. Wilcox, and A. J. Hunter, 'Defect detection using ultrasonic arrays: The multi-mode total focusing method', *NDT E Int.*, vol. 43, no. 2, pp. 123–133, Mar. 2010, doi: 10.1016/j.ndteint.2009.10.001.

[80]   P. D. Wilcox, A. J. Croxford, N. Budyn, R. L. T. Bevan, J. Zhang, A. Kashubin, and P. Cawley, 'Fusion of multi-view ultrasonic data for increased detection performance in non-destructive evaluation', *Proc. R. Soc. Math. Phys. Sci.*, vol. 476, no. 2243, Nov. 2020, doi: 10.1098/rspa.2020.0086.

[81]   R. L. T. Bevan, N. Budyn, J. Zhang, A. J. Croxford, S. Kitazawa, and P. D. Wilcox, 'Data Fusion of Multiview Ultrasonic Imaging for Characterization of Large Defects', *IEEE Trans. Ultrason. Ferroelectr. Freq. Control*, vol. 67, no. 11, pp. 2387–2401, Nov. 2020, doi: 10.1109/TUFFC.2020.3004982.

[82]   N. S. Budyn, A. J. Croxford, R. L. T. Bevan, J. Zhang, and P. D. Wilcox, 'Characterisation of small embedded two-dimensional defects using multi-view Total Focusing Method imaging algorithm', *NDT E Int.*, vol. 119, no. 102413, Apr. 2021, doi: 10.1016/j.ndteint.2021.102413.

[83]   J. Zhang, A. Hunter, B. W. Drinkwater, and P. D. Wilcox, 'Monte carlo inversion of ultrasonic array data to map anisotropic weld properties', *IEEE Trans. Ultrason. Ferroelectr. Freq. Control*, vol. 59, no. 11, pp. 2487–2497, Nov. 2012, doi: 10.1109/TUFFC.2012.2481.

[84]   R. J. Pyle, R. L. T. Bevan, R. R. Hughes, R. K. Rachev, A. A. S. Ali, and P. D. Wilcox, 'Deep Learning for Ultrasonic Crack Characterization in NDE', *IEEE Trans. Ultrason. Ferroelectr. Freq. Control*, vol. 68, no. 5, pp. 1854–1865, May 2021, doi: 10.1109/TUFFC.2020.3045847.

[85]   S. N. Ramadas, R. L. O'Leary, and A. Gachagan, 'Ultrasonic Sensor Design for NDE Application: Design Challenges & Considerations'.

[86]   M. V. Predoi and C. C. Petre, 'Thin Wall Pipe Ultrasonic Inspection through Paint Coating', *Phys. Procedia*, vol. 70, pp. 287–291, Jan. 2015, doi: 10.1016/j.phpro.2015.08.156.

[87]   B. Pavlakovic, M. Lowe, D. Alleyne, and P. Cawley, 'Disperse: A General Purpose Program for Creating Dispersion Curves', in *Review of Progress in Quantitative Nondestructive Evaluation*, D. O. Thompson and D. E. Chimenti, Eds. Boston, MA: Springer US, 1997, pp. 185–192. doi: 10.1007/978-1-4615-5947-4_24.

[88]   P. Bocchini, A. Marzani, and E. Viola, 'Graphical User Interface for Guided Acoustic Waves', *J. Comput. Civ. Eng.*, vol. 25, no. 3, pp. 202–210, May 2011, doi: 10.1061/(ASCE)CP.1943-5487.0000081.

[89]   'Center for Lightweight-Production-Technology - The Dispersion Calculator: An open source software for calculating dispersion curves and mode shapes of guided waves'. https://www.dlr.de/zlp/en/desktopdefault.aspx/tabid-14332/24874_read-61142/ (accessed Sep. 07, 2022).

[90]   M. J. S. Lowe and P. Cawley, 'Long Range Guided Wave Inspection Usage – Current Commercial Capabilities and Research Directions', 2007.

[91]   P. D. Wilcox, 'A rapid signal processing technique to remove the effect of dispersion from guided wave signals', *IEEE Trans. Ultrason. Ferroelectr. Freq. Control*, vol. 50, no. 4, pp. 419–427, Apr. 2003, doi: 10.1109/TUFFC.2003.1197965.

[92]   A. Demma, P. Cawley, M. Lowe, A. G. Roosenbrand, and B. Pavlakovic, 'The reflection of guided waves from notches in pipes: a guide for interpreting corrosion measurements', *NDT E Int.*, vol. 37, no. 3, pp. 167–180, Apr. 2004, doi: 10.1016/j.ndteint.2003.09.004.

[93]   M. Castaings, D. Singh, and P. Viot, 'Sizing of impact damages in composite materials using ultrasonic guided waves', *NDT E Int.*, vol. 46, pp. 22–31, Mar. 2012, doi: 10.1016/j.ndteint.2011.10.002.

[94]   A. A. E. Zimmermann, P. Huthwaite, and B. Pavlakovic, 'High-resolution thickness maps of corrosion using SH1 guided wave tomography', *Proc. R. Soc. Math. Phys. Eng. Sci.*, vol. 477, no. 2245, p. 20200380, Jan. 2021, doi: 10.1098/rspa.2020.0380.

[95]   P. Huthwaite and F. Simonetti, 'High-resolution guided wave tomography', *Wave Motion*, vol. 50, no. 5, pp. 979–993, Jul. 2013, doi: 10.1016/j.wavemoti.2013.04.004.

[96]   J. Rao, M. Ratassepp, and Z. Fan, 'Guided Wave Tomography Based on Full Waveform Inversion', *IEEE Trans. Ultrason. Ferroelectr. Freq. Control*, vol. 63, no. 5, pp. 737–745, May 2016, doi: 10.1109/TUFFC.2016.2536144.

[97]   Lord Rayleigh, 'On Waves Propagated along the Plane Surface of an Elastic Solid', *Proc. Lond. Math. Soc.*, vol. s1-17, no. 1, pp. 4–11, 1885, doi: 10.1112/plms/s1-17.1.4.

[98]   P. Cawley and D. Alleyne, 'The use of Lamb waves for the long range inspection of large structures', *Ultrasonics*, vol. 34, no. 2, pp. 287–290, Jun. 1996, doi: 10.1016/0041-624X(96)00024-8.

[99]   N. Guo and P. Cawley, 'The interaction of Lamb waves with delaminations in composite laminates', *J. Acoust. Soc. Am.*, vol. 94, no. 4, pp. 2240–2246, Oct. 1993, doi: 10.1121/1.407495.

[100]   M. J. S. Lowe and O. Diligent, 'Low-frequency reflection characteristics of the s0 Lamb wave from a rectangular notch in a plate', *J. Acoust. Soc. Am.*, vol. 111, no. 1, pp. 64–74, Jan. 2002, doi: 10.1121/1.1424866.

[101]   M. J. S. Lowe, P. Cawley, J.-Y. Kao, and O. Diligent, 'The low frequency reflection characteristics of the fundamental antisymmetric Lamb wave a0 from a rectangular notch in a plate', *J. Acoust. Soc. Am.*, vol. 112, no. 6, pp. 2612–2622, Dec. 2002, doi: 10.1121/1.1512702.

[102]   W. Luo and J. L. Rose, 'Phased array focusing with guided waves in a viscoelastic coated hollow cylinder', *J. Acoust. Soc. Am.*, vol. 121, no. 4, pp. 1945–1955, Apr. 2007, doi: 10.1121/1.2711145.

[103]   F. H. Quintanilla, Z. Fan, M. J. S. Lowe, and R. V. Craster, 'Guided waves' dispersion curves in anisotropic viscoelastic single- and multi-layered media', *Proc. R. Soc. Math. Phys. Eng. Sci.*, vol. 471, no. 2183, p. 20150268, Nov. 2015, doi: 10.1098/rspa.2015.0268.

[104]   N. Ryden and M. J. S. Lowe, 'Guided wave propagation in three-layer pavement structures', *J. Acoust. Soc. Am.*, vol. 116, no. 5, pp. 2902–2913, Nov. 2004, doi: 10.1121/1.1808223.

[105] E. Leinov, M. J. S. Lowe, and P. Cawley, 'Investigation of guided wave propagation and attenuation in pipe buried in sand', *J. Sound Vib.*, vol. 347, pp. 96–114, Jul. 2015, doi: 10.1016/j.jsv.2015.02.036.

[106] 'Ultrasonic leaky waves in the presence of a thin layer: Journal of Applied Physics: Vol 52, No 8'. https://aip.scitation.org/doi/10.1063/1.329439 (accessed Sep. 15, 2022).

[107] R. Kumar, 'Dispersion of Axially Symmetric Waves in Empty and Fluid-Filled Cylindrical Shells', *Acta Acust. United Acust.*, vol. 27, no. 6, pp. 317–329, Dec. 1972.

[108] B. N. Pavlakovic, 'Leaky guided ultrasonic waves in NDT.', Jan. 1999, Accessed: Sep. 15, 2022. [Online]. Available: http://spiral.imperial.ac.uk/handle/10044/1/7907

[109] J. P. Sargent, 'Corrosion detection in welds and heat-affected zones using ultrasonic Lamb waves', *Insight - Non-Destr. Test. Cond. Monit.*, vol. 48, no. 3, pp. 160–167, Mar. 2006, doi: 10.1784/insi.2006.48.3.160.

[110] N. Juluri, M. Lowe, and P. Cawley, 'The Guiding of Ultrasound by a Welded Joint in a Plate', *AIP Conf. Proc.*, vol. 894, no. 1, pp. 1079–1086, Mar. 2007, doi: 10.1063/1.2718087.

[111] Z. Fan, 'Applications of guided wave propagation on waveguides with irregular cross-section', PhD Thesis, Imperial College London, 2010. Accessed: Jun. 02, 2022. [Online]. Available: http://spiral.imperial.ac.uk/handle/10044/1/5935

[112] X. Yu, Z. Fan, M. Castaings, and C. Biateau, 'Feature guided wave inspection of bond line defects between a stiffener and a composite plate', *NDT E Int.*, vol. 89, pp. 44–55, Jul. 2017, doi: 10.1016/j.ndteint.2017.03.008.

[113] Z. Fan and M. J. S. Lowe, 'Elastic waves guided by a welded joint in a plate', *Proc. R. Soc. Math. Phys. Eng. Sci.*, vol. 465, no. 2107, pp. 2053–2068, Jul. 2009, doi: 10.1098/rspa.2009.0010.

[114] Z. Fan and M. J. S. Lowe, 'Interaction of weld-guided waves with defects', *NDT E Int.*, vol. 47, pp. 124–133, Apr. 2012, doi: 10.1016/j.ndteint.2012.01.001.

[115] X. Yu, P. Zuo, J. Xiao, and Z. Fan, 'Detection of damage in welded joints using high order feature guided ultrasonic waves', *Mech. Syst. Signal Process.*, vol. 126, pp. 176–192, Jul. 2019, doi: 10.1016/j.ymssp.2019.02.026.

[116] A. Ramdhas, R. K. Pattanayak, K. Balasubramaniam, and P. Rajagopal, 'Antisymmetric feature-guided ultrasonic waves in thin plates with small radius transverse bends from low-frequency symmetric axial excitation', *J. Acoust. Soc. Am.*, vol. 134, no. 3, pp. 1886–1898, Sep. 2013, doi: 10.1121/1.4817878.

[117] P. Manogharan, X. Yu, Z. Fan, and P. Rajagopal, 'Interaction of shear horizontal bend (SHB) guided mode with defects', *NDT E Int.*, vol. 75, pp. 39–47, Oct. 2015, doi: 10.1016/j.ndteint.2015.06.004.

[118] P. Manogharan, P. Rajagopal, and K. Balasubramaniam, 'Longitudinal guided waves confined in radius filler regions of composite joints', *J. Acoust. Soc. Am.*, vol. 140, no. 1, pp. 334–343, Jul. 2016, doi: 10.1121/1.4955288.

[119] J. Corcoran, E. Leinov, A. Jeketo, and M. J. S. Lowe, 'A Guided Wave Inspection Technique for Wedge Features', *IEEE Trans. Ultrason. Ferroelectr. Freq. Control*, vol. 67, no. 5, pp. 997–1008, May 2020, doi: 10.1109/TUFFC.2019.2960108.

[120] W. Luo and J. L. Rose, 'Guided wave thickness measurement with EMATs', *Insight - Non-Destr. Test. Cond. Monit.*, vol. 45, no. 11, pp. 735–739, Nov. 2003, doi: 10.1784/insi.45.11.735.52961.

[121] S. Fletcher, M. J. S. Lowe, M. Ratassepp, and C. Brett, 'Detection of Axial Cracks in Pipes Using Focused Guided Waves', *J. Nondestruct. Eval.*, vol. 31, no. 1, pp. 56–64, Mar. 2012, doi: 10.1007/s10921-011-0120-x.

[122] J. O. Davies, 'INSPECTION OF PIPES USING LOW FREQUENCY FOCUSED GUIDED WAVES', Imperial College London, 2008. [Online]. Available: https://www.imperial.ac.uk/media/imperial-college/research-centres-and-groups/non-destructive-evaluation/Jacob_Davies_thesis_corrected_aug08.pdf

[123] X. Jian, Y. Fan, R. S. Edwards, and S. Dixon, 'Surface-breaking crack gauging with the use of laser-generated Rayleigh waves', *J. Appl. Phys.*, vol. 100, no. 6, p. 064907, Sep. 2006, doi: 10.1063/1.2353892.

[124] X. Jian, S. Dixon, N. Guo, and R. Edwards, 'Rayleigh wave interaction with surface-breaking cracks', *J. Appl. Phys.*, vol. 101, no. 6, p. 064906, Mar. 2007, doi: 10.1063/1.2435803.

[125] R. S. Edwards, S. Dixon, and X. Jian, 'Depth gauging of defects using low frequency wideband Rayleigh waves', *Ultrasonics*, vol. 44, no. 1, pp. 93–98, Jan. 2006, doi: 10.1016/j.ultras.2005.08.005.

[126] B. Aalami, 'Waves in Prismatic Guides of Arbitrary Cross Section', *J. Appl. Mech.*, vol. 40, no. 4, pp. 1067–1072, Dec. 1973, doi: 10.1115/1.3423127.

[127] P. E. Lagasse, 'Higher-order finite-element analysis of topographic guides supporting elastic surface waves', *J. Acoust. Soc. Am.*, vol. 53, no. 4, pp. 1116–1122, Apr. 1973, doi: 10.1121/1.1913432.

[128] L. Gavric, 'Computation of propagative waves in free rail using a finite element technique', 1995, doi: 10.1006/JSVI.1995.0398.

[129] T. Hayashi, W.-J. Song, and J. L. Rose, 'Guided wave dispersion curves for a bar with an arbitrary cross-section, a rod and rail example', *Ultrasonics*, vol. 41, no. 3, pp. 175–183, May 2003, doi: 10.1016/S0041-624X(03)00097-0.

[130] P. Wilcox, M. Evans, O. Diligent, M. Lowe, and P. Cawley, 'Dispersion and excitability of guided acoustic waves in isotropic beams with arbitrary cross section', *AIP Conf. Proc.*, vol. 615, no. 1, pp. 203–210, May 2002, doi: 10.1063/1.1472800.

[131] U. Orrenius and S. Finnveden, 'CALCULATION OF WAVE PROPAGATION IN RIB-STIFFENED PLATE STRUCTURES', *J. Sound Vib.*, vol. 198, no. 2, pp. 203–224, Nov. 1996, doi: 10.1006/jsvi.1996.0565.

[132] I. Bartoli, A. Marzani, H. Matt, and F. L. di Scalea, 'Modeling wave propagation in damped waveguides of arbitrary cross-section', p. 13.

[133] M. Castaings and M. Lowe, 'Finite element model for waves guided along solid systems of arbitrary section coupled to infinite solid media', *J. Acoust. Soc. Am.*, vol. 123, no. 2, pp. 696–708, Feb. 2008, doi: 10.1121/1.2821973.

[134] F. Tisseur and K. Meerbergen, 'The Quadratic Eigenvalue Problem', *SIAM Rev.*, vol. 43, no. 2, pp. 235–286, 2001, doi: 10.1137/S0036144500381988.

[135] 'COMSOL Multiphysics® Modeling Software'. https://uk.comsol.com/ (accessed Mar. 26, 2019).

[136] M. V. Predoi, M. Castaings, B. Hosten, and C. Bacon, 'Wave propagation along transversely periodic structures', *J. Acoust. Soc. Am.*, vol. 121, no. 4, pp. 1935–1944, Apr. 2007, doi: 10.1121/1.2534256.

[137] P. Zuo, X. Yu, and Z. Fan, 'Numerical modeling of embedded solid waveguides using SAFE-PML approach using a commercially available finite element package', *NDT E Int.*, vol. 90, pp. 11–23, Sep. 2017, doi: 10.1016/j.ndteint.2017.04.003.

[138] M. Castaings, C. Bacon, B. Hosten, and M. V. Predoi, 'Finite element predictions for the dynamic response of thermo-viscoelastic material structures', *J. Acoust. Soc. Am.*, vol. 115, no. 3, pp. 1125–1133, Mar. 2004, doi: 10.1121/1.1639332.

[139] F. Treyssède, K. L. Nguyen, A.-S. Bonnet-BenDhia, and C. Hazard, 'Finite element computation of trapped and leaky elastic waves in open stratified waveguides', *Wave Motion*, vol. 51, no. 7, pp. 1093–1107, Nov. 2014, doi: 10.1016/j.wavemoti.2014.05.003.

[140] K. L. Nguyen, F. Treyssède, and C. Hazard, 'Numerical modeling of three-dimensional open elastic waveguides combining semi-analytical finite element and perfectly matched layer methods', *J. Sound Vib.*, vol. 344, pp. 158–178, May 2015, doi: 10.1016/j.jsv.2014.12.032.

[141] F. L. Teixeira and W. C. Chew, 'Complex space approach to perfectly matched layers: a review and some new developments', *Int. J. Numer. Model. Electron. Netw. Devices Fields*, vol. 13, no. 5, pp. 441–455, 2000, doi: 10.1002/1099-1204(200009/10)13:5<441::AID-JNM376>3.0.CO;2-J.

[142] D. S. Jones, *Acoustic and Electromagnetic Waves*. Clarendon University Press, 1986.

[143] P. Cawley, 'Non-destructive testing—current capabilities and future directions', *Proc. Inst. Mech. Eng. Part J. Mater. Des. Appl.*, vol. 215, no. 4, pp. 213–223, Oct. 2001, doi: 10.1177/146442070121500403.

[144] D. L. Atherton, 'Remote field eddy current inspection', *IEEE Trans. Magn.*, vol. 31, no. 6, pp. 4142–4147, Nov. 1995, doi: 10.1109/20.489888.

[145] A. Sophian, G. Tian, and M. Fan, 'Pulsed Eddy Current Non-destructive Testing and Evaluation: A Review', *Chin. J. Mech. Eng.*, vol. 30, no. 3, pp. 500–514, May 2017, doi: 10.1007/s10033-017-0122-4.

[146] J. C. Maxwell, 'VIII. A dynamical theory of the electromagnetic field', *Philos. Trans. R. Soc. Lond.*, vol. 155, pp. 459–512, Jan. 1865, doi: 10.1098/rstl.1865.0008.

[147] E. Lenz, 'Ueber die Bestimmung der Richtung der durch elektrodynamische Vertheilung erregten galvanischen Ströme', *Ann. Phys.*, vol. 107, no. 31, pp. 483–494, 1834, doi: 10.1002/andp.18341073103.

[148] M. Wright, *Eddy Current Array Technology: Fundamentals & Applications for Non-destructive Testing*. Eclipse Scientific Products Incorporated, 2014.

[149] J.-F. Bureau, R. Ward, and W. Jenstead, 'Advances in Eddy Current Array Sensor Technology', p. 4.

[150] 'Padded ECA Probes | Eddyfi'. https://www.eddyfi.com/en/product/padded-eca-probes (accessed Sep. 20, 2022).

[151] 'Sharck Probes | Eddyfi'. https://www.eddyfi.com/en/product/sharck-probes (accessed Sep. 20, 2022).

[152] E. Mohseni, H. Habibzadeh Boukani, D. Ramos França, and M. Viens, 'A Study of the Automated Eddy Current Detection of Cracks in Steel Plates', *J. Nondestruct. Eval.*, vol. 39, no. 1, p. 6, Dec. 2019, doi: 10.1007/s10921-019-0647-9.

[153] C. Ye, N. Zhang, L. Peng, and Y. Tao, 'Flexible Array Probe With In-Plane Differential Multichannels for Inspection of Microdefects on Curved Surface', *IEEE*

Trans. Ind. Electron., vol. 69, no. 1, pp. 900–910, Jan. 2022, doi: 10.1109/TIE.2021.3050376.

[154] P. Gao, C. Wang, Y. Li, and Z. Cong, 'Electromagnetic and eddy current NDT in weld inspection: a review', *Insight - Non-Destr. Test. Cond. Monit.*, vol. 57, no. 6, pp. 337–345, Jun. 2015, doi: 10.1784/insi.2015.57.6.337.

[155] 'ndtatbristol/mfmc'. Ultrasonics and Non-destructive Testing Group, Oct. 05, 2020. Accessed: Jun. 20, 2022. [Online]. Available: https://github.com/ndtatbristol/mfmc

[156] M. Farley, '40 years of progress in NDT - History as a guide to the future', Baltimore, Maryland, USA, 2014, pp. 5–12. doi: 10.1063/1.4864796.

[157] 'Watertown Arsenal'. https://www.asce.org/about-civil-engineering/history-and-heritage/historic-landmarks/watertown-arsenal (accessed Jan. 11, 2023).

[158] H. H. Lester, 'The X-Ray Testing of Metals at Watertown Arsenal', *SAE Trans.*, vol. 22, pp. 64–68, 1927, Accessed: Jan. 11, 2023. [Online]. Available: https://www.jstor.org/stable/44434019

[159] C. J. Hellier, 'Handbook of Nondestructive Evaluation, Second Edition', *AccessEngineering | McGraw-Hill Education - Access Engineering*, 2013. https://www.accessengineeringlibrary.com/content/book/9780071777148 (accessed Jan. 11, 2023).

[160] S. Sokolov, 'On the problem of the propagation of ultrasonic oscillations in various bodies', *Elek Nachr Tech*, vol. 6, pp. 454–460, 1929.

[161] S. J. Sokolov, 'Ultrasonic oscillations and their applications', *Tech Phys USSR*, vol. 2, p. 522, 1935.

[162] S. Y. Sokolov, 'The practical utilization of the diffraction of light by ultrasonic waves', *Phys. Z*, vol. 36, no. 4, p. 142, 1935.

[163] S. Y. Sokolov, 'Ultrasonic methods of detecting internal flaws in metal articles', *Zavod. Lab.*, vol. 4, no. 1468–1472, 1935.

[164] 'Nondestructive Evaluation Techniques : Radiography'. https://www.nde-ed.org/NDETechniques/Radiography/TechCalibrations/definition.xhtml (accessed Jan. 11, 2023).

[165] 'The Fascinating History of Radiography - X Ray Academy', Nov. 22, 2021. https://xrayacademy.com/the-fascinating-history-of-radiography/ (accessed Jan. 11, 2023).

[166] 'Standard Practice for Radiographic Examination of Weldments Using Industrial X-Ray Film'. https://www.astm.org/e1032-19.html (accessed Jan. 11, 2023).

[167] 'Standard Practice for Radioscopic Examination of Weldments'. https://www.astm.org/e1416-16a.html (accessed Jan. 11, 2023).

[168] 'Standard Practice for Examination of Carbon Steel Welds Using An Eddy Current Array'. https://www.astm.org/e3052-21.html (accessed Jan. 11, 2023).

[169] M. M. Nadrljanski, 'History of ultrasound in medicine | Radiology Reference Article | Radiopaedia.org', *Radiopaedia*. https://radiopaedia.org/articles/history-of-ultrasound-in-medicine?lang=gb (accessed Jan. 11, 2023).

[170] 'DGS'. https://www.bindt.org/What-is-NDT/Index-of-acronyms/D/DGS/ (accessed Jan. 11, 2023).

[171] 'DAC'. https://www.bindt.org/What-is-NDT/Index-of-acronyms/D/DAC/ (accessed Jan. 11, 2023).

[172] M. G. Silk and B. H. Lidington, 'The potential of scattered or diffracted ultrasound in the determination of crack depth', *Non-Destr. Test.*, vol. 8, no. 3, pp. 146–151, Jun. 1975, doi: 10.1016/0029-1021(75)90024-9.

[173] 'BS EN ISO 10863:2011 - Non-destructive testing of welds. Ultrasonic testing. Use of time-of-flight diffraction technique (TOFD)'. https://shop.bsigroup.com/ProductDetail/?pid=000000000030187581 (accessed May 24, 2019).

[174]   D. Alleyne and P. Cawley, 'A two-dimensional Fourier transform method for the measurement of propagating multimode signals', *J. Acoust. Soc. Am.*, vol. 89, no. 3, pp. 1159–1168, Mar. 1991, doi: 10.1121/1.400530.

[175]   'COMSOL 5.6 Multiphysics Reference Manual'. https://doc.comsol.com/ (accessed Nov. 03, 2021).

[176]   P. Huthwaite, 'Accelerated finite element elastodynamic simulations using the GPU', *J. Comput. Phys.*, vol. 257, pp. 687–707, Jan. 2014, doi: 10.1016/j.jcp.2013.10.017.

[177]   P. Rajagopal, M. Drozdz, E. A. Skelton, M. J. S. Lowe, and R. V. Craster, 'On the use of absorbing layers to simulate the propagation of elastic waves in unbounded isotropic media using commercially available Finite Element packages', *NDT E Int.*, vol. 51, pp. 30–40, Oct. 2012, doi: 10.1016/j.ndteint.2012.04.001.

[178]   Abaqus, 'Abaqus Analysis User's Guide, Version 6.13', *Dassault Systèmes*, Apr. 28, 2022. https://www.3ds.com/ (accessed Sep. 27, 2022).

[179]   S. Choi, H. Cho, and C. J. Lissenden, 'Nondestructive inspection of spent nuclear fuel storage canisters using shear horizontal guided waves', *Nucl. Eng. Technol.*, vol. 50, no. 6, pp. 890–898, Aug. 2018, doi: 10.1016/j.net.2018.04.011.

[180]   W. Luo, X. Zhao, and J. L. Rose, 'A Guided Wave Plate Experiment for a Pipe', *J. Press. Vessel Technol.*, vol. 127, no. 3, p. 345, 2005, doi: 10.1115/1.1989351.

[181]   H. M. Ledbetter, 'Monocrystal elastic constants in the ultrasonic study of welds', *Ultrasonics*, vol. 23, no. 1, pp. 9–13, Jan. 1985, doi: 10.1016/0041-624X(85)90005-8.

[182]   J. Combaniere, P. Cawley, K. McAughey, and J. Giese, 'Interaction Between SH0 Guided Waves and Tilted Surface-Breaking Cracks in Plates', *IEEE Trans. Ultrason. Ferroelectr. Freq. Control*, vol. 66, no. 1, pp. 119–128, Jan. 2019, doi: 10.1109/TUFFC.2018.2876723.

[183]   A. De Luca, D. Perfetto, A. De Fenza, G. Petrone, and F. Caputo, 'Guided waves in a composite winglet structure: Numerical and experimental investigations',

Compos. Struct., vol. 210, pp. 96–108, Feb. 2019, doi: 10.1016/j.compstruct.2018.11.048.

[184] Y. Ma, Z. Yang, J. Zhang, K. Liu, Z. Wu, and S. Ma, 'Axial stress monitoring strategy in arbitrary cross-section based on acoustoelastic guided waves using PZT sensors', *AIP Adv.*, vol. 9, no. 12, p. 125304, Dec. 2019, doi: 10.1063/1.5130723.

[185] M. B. Drozdz, 'Efficient finite element modelling of ultrasound waves in elastic media', PhD Thesis, Imperial College London (University of London), 2008. Accessed: Nov. 02, 2021. [Online]. Available: http://spiral.imperial.ac.uk/handle/10044/1/7974

[186] P. D. Wilcox, M. J. S. Lowe, and P. Cawley, 'Mode and Transducer Selection for Long Range Lamb Wave Inspection', *J. Intell. Mater. Syst. Struct.*, vol. 12, no. 8, pp. 553–565, Aug. 2001, doi: 10.1177/10453890122145348.

[187] G. Dobie, G. Hayward, and G. Pierce, 'Ultrasonic sensor platforms for non-destructive evaluation', PhD Thesis, University of Strathclyde, Glasgow, 2010. Accessed: Nov. 03, 2021. [Online]. Available: https://strathprints.strath.ac.uk/59953/

[188] A. Van Pamel, 'Ultrasonic inspection of highly scattering materials', PhD Thesis, Imperial College London, 2015. Accessed: Apr. 21, 2022. [Online]. Available: http://spiral.imperial.ac.uk/handle/10044/1/29423

[189] 'SuperSoniX[TM] - Highest Performance Ultrasonic Couplant - Echo Ultrasonics'. https://www.echoultrasonics.com/product/supersonix-ultrasoinc-couplant/ (accessed Jun. 02, 2022).

[190] E. A. Foster, R. Bernard, G. Bolton, J. C. Jackson-Camargo, A. Gachagan, E. Mohseni, and C. N. MacLeod, 'Inspection of nuclear assets with limited access using feature guided waves', *NDT E Int.*, vol. 131, no. 102695, Jun. 2022, doi: 10.1016/j.ndteint.2022.102695.

[191] 'Aptflex F48', *Precision Acoustics*. https://www.acoustics.co.uk/product/aptflex-f48/ (accessed Apr. 21, 2022).

[192] C. Mineo, C. MacLeod, M. Morozov, S. G. Pierce, T. Lardner, R. Summan, J. Powell, P. McCubbin, C. McCubbin, G. Munro, S. Paton, D. Watson, and D. Lines,

'Fast ultrasonic phased array inspection of complex geometries delivered through robotic manipulators and high speed data acquisition instrumentation', in *2016 IEEE International Ultrasonics Symposium (IUS)*, Sep. 2016, pp. 1–4. doi: 10.1109/ULTSYM.2016.7728746.

[193]   C. Mineo, C. N. MacLeod, R. Su, D. Lines, S. Davi', B. Cowan, S. Pierce, S. Paton, G. Munro, C. McCubbin, D. Watson, and W. Kerr, 'Robotic geometric and volumetric inspection of high value and large scale aircraft wings: 2019 IEEE International Workshop on Metrology for AeroSpace', Jun. 2019. Accessed: Jun. 07, 2022. [Online]. Available: http://www.metroaerospace.org/

[194]   C. Mineo, M. Vasilev, B. Cowan, C. N. MacLeod, S. G. Pierce, C. Wong, E. Yang, R. Fuentes, and E. J. Cross, 'Enabling robotic adaptive behaviour capabilities for new industry 4.0 automated quality inspection paradigms', *Insight J. Br. Inst. Non-Destr. Test.*, vol. 62, no. 6, pp. 338–344, Jun. 2020, doi: 10.1784/insi.2020.62.6.338.

[195]   S. M. Tabatabaeipour, O. Trushkevych, G. Dobie, R. Edwards, C. N. MacLeod, and G. Pierce, 'Guided wave based-occupancy grid robotic mapping: European Workshop on Structural Health Monitoring', *Eur. Workshop Struct. Health Monit.*, pp. 267–275, Jan. 2021, doi: 10.1007/978-3-030-64908-1_25.

[196]   Y. Javadi, C. N. MacLeod, S. G. Pierce, A. Gachagan, D. Lines, C. Mineo, J. Ding, S. Williams, M. Vasilev, E. Mohseni, and R. Su, 'Ultrasonic phased array inspection of a Wire + Arc Additive Manufactured (WAAM) sample with intentionally embedded defects', *Addit. Manuf.*, vol. 29, no. 100806, Oct. 2019, doi: 10.1016/j.addma.2019.100806.

[197]   Y. Javadi, E. Mohseni, C. N. MacLeod, D. Lines, M. Vasilev, C. Mineo, E. Foster, S. G. Pierce, and A. Gachagan, 'Continuous monitoring of an intentionally-manufactured crack using an automated welding and in-process inspection system', *Mater. Des.*, vol. 191, no. 108655, Jun. 2020, doi: 10.1016/j.matdes.2020.108655.

[198]   D. Lines, Y. Javadi, E. Mohseni, M. Vasilev, C. N. MacLeod, C. Mineo, R. K. Wathavana Vithanage, Z. Qiu, R. Zimermann, C. Loukas, E. Foster, G. Pierce, and A. Gachagan, 'A flexible robotic cell for in-process inspection of multi-pass welds', *Insight J. Br. Inst. Non-Destr. Test.*, vol. 62, no. 9, pp. 526–532, Sep. 2020, doi: 10.1784/insi.2020.62.9.526.

[199] E. Mohseni, R. K. Wathavana Vithanage, Z. Qiu, C. N. MacLeod, Y. Javadi, D. Lines, R. Zimermann, G. Pierce, A. Gachagan, J. Ding, and S. Williams, 'A high temperature phased array ultrasonic roller probe designed for dry-coupled in-process inspection of wire + arc additive manufacturing: 47th Annual Review of Progress in Quantitative Nondestructive Evaluation', Aug. 2020. Accessed: Jun. 07, 2022. [Online]. Available: https://event.asme.org/QNDE

[200] Y. Javadi, E. Mohseni, C. N. MacLeod, D. Lines, M. Vasilev, C. Mineo, S. G. Pierce, and A. Gachagan, 'High-temperature in-process inspection followed by 96-h robotic inspection of intentionally manufactured hydrogen crack in multi-pass robotic welding', *Int. J. Press. Vessels Pip.*, vol. 189, no. 104288, Feb. 2021, doi: 10.1016/j.ijpvp.2020.104288.

[201] M. Vasilev, C. MacLeod, W. Galbraith, Y. Javadi, E. Foster, G. Dobie, G. Pierce, and A. Gachagan, 'Non-contact in-process ultrasonic screening of thin fusion welded joints', *J. Manuf. Process.*, vol. 64, pp. 445–454, Apr. 2021, doi: 10.1016/j.jmapro.2021.01.033.

[202] D. Zhang, R. Watson, C. MacLeod, G. Dobie, W. Galbraith, and G. Pierce, 'Implementation and evaluation of an autonomous airborne ultrasound inspection system', *Nondestruct. Test. Eval.*, vol. 37, no. 1, pp. 1–21, Jan. 2022, doi: 10.1080/10589759.2021.1889546.

[203] R. Watson, M. Kamel, D. Zhang, G. Dobie, C. MacLeod, S. G. Pierce, and J. Nieto, 'Dry coupled ultrasonic non-destructive evaluation using an over-actuated unmanned aerial vehicle', *IEEE Trans. Autom. Sci. Eng.*, Jul. 2021, doi: 10.1109/TASE.2021.3094966.

[204] R. J. Watson, S. G. Pierce, M. Kamel, D. Zhang, C. N. MacLeod, G. Dobie, G. Bolton, T. Dawood, and J. Nieto, 'Deployment of contact-based ultrasonic thickness measurements using over-actuated UAVs: European Workshop on Structural Health Monitoring', *Eur. Workshop Struct. Health Monit. EWSHM 2020*, pp. 683–694, Jan. 2021, doi: 10.1007/978-3-030-64594-6_66.

[205] D. Zhang, R. Watson, G. Dobie, C. N. MacLeod, and G. Pierce, 'Autonomous ultrasonic inspection using unmanned aerial vehicle: 2018 IEEE International Ultrasonics Symposium', *2018 IEEE Int. Ultrason. Symp. IUS*, Dec. 2018, doi: 10.1109/ULTSYM.2018.8579727.

[206] K. Prashar, M. Weston, and B. Drinkwater, 'Comparison and optimisation of fast array-based ultrasound testing', *Insight - Non-Destr. Test. Cond. Monit.*, vol. 63, pp. 209–218, Apr. 2021, doi: 10.1784/insi.2021.63.4.209.

[207] R. Zimermann, E. Mohseni, R. K. W. Vithanage, D. Lines, E. Foster, C. N. Macleod, S. Gareth Pierce, G. Marinelli, S. Williams, and J. Ding, 'Increasing the speed of automated ultrasonic inspection of as-built additive manufacturing components by the adoption of virtual source aperture', *Mater. Des.*, vol. 220, p. 110822, Aug. 2022, doi: 10.1016/j.matdes.2022.110822.

[208] R. J. Pyle, R. L. T. Bevan, R. R. Hughes, A. A. S. Ali, and P. D. Wilcox, 'Domain Adapted Deep-Learning for Improved Ultrasonic Crack Characterization Using Limited Experimental Data', *IEEE Trans. Ultrason. Ferroelectr. Freq. Control*, vol. 69, no. 4, pp. 1485–1496, Apr. 2022, doi: 10.1109/TUFFC.2022.3151397.

[209] R. J. Pyle, R. R. Hughes, A. A. S. Ali, and P. D. Wilcox, 'Uncertainty Quantification for Deep Learning in Ultrasonic Crack Characterization', *IEEE Trans. Ultrason. Ferroelectr. Freq. Control*, vol. 69, no. 7, pp. 2339–2351, Jul. 2022, doi: 10.1109/TUFFC.2022.3176926.

[210] M. N. O. Sadiku, *Elements of Electromagnetics*. Oxford University Press, 2001.

[211] H. A. Wheeler, 'Formulas for the Skin Effect', *Proc. IRE*, vol. 30, no. 9, pp. 412–424, Sep. 1942, doi: 10.1109/JRPROC.1942.232015.

[212] L. D. Mackenzie, S. G. Pierce, and G. Hayward, 'Robotic inspection system for non-destructive evaluation (nde) of pipes', *AIP Conf. Proc.*, vol. 1096, no. 1, pp. 1687–1694, Mar. 2009, doi: 10.1063/1.3114161.

[213] R. Summan, G. Pierce, C. Macleod, C. Mineo, J. Riise, M. Morozov, G. Dobie, G. Bolton, A. Raude, C. Dalpé, and J. Braumann, 'Conformable eddy current array delivery', *AIP Conf. Proc.*, vol. 1706, no. 1, p. 170003, Feb. 2016, doi: 10.1063/1.4940626.

[214] M. Morozov, S. G. Pierce, C. N. MacLeod, C. Mineo, and R. Summan, 'Off-line scan path planning for robotic NDT', *Measurement*, vol. 122, pp. 284–290, Jul. 2018, doi: 10.1016/j.measurement.2018.02.020.

[215] W. Zhang, C. Wang, F. Xie, and H. Zhang, 'Defect imaging curved surface based on flexible eddy current array sensor', *Measurement*, vol. 151, p. 107280, Feb. 2020, doi: 10.1016/j.measurement.2019.107280.

[216] Kuka, 'Kuka Industrial Robots High Payload Catalogue'. https://www.kuka.com/-/media/kuka-downloads/imported/9cb8e311bfd744b4b0eab25ca883f6d3/kuka_pb_hohe_tl_en.pdf (accessed Jun. 16, 2022).

[217] Kuka, 'DKP two-axis positioner', *KUKA AG*. https://www.kuka.com/en-gb/products/robotics-systems/robot-periphery/positionierer/dkp (accessed Jun. 16, 2022).

[218] 'CatalogEddyfi-Surface-ECA-Probes.pdf'. https://eddyfi.com/doc/Downloadables/CatalogEddyfi-Surface-ECA-Probes.pdf (accessed Jun. 16, 2022).

[219] EddyFi, 'Ectane 2 multi-technology tubing and surface test instrument', *Eddyfi*, 2019. http://www.eddyfi.com/products/ectane-2-test-instrument/ (accessed Jun. 26, 2019).

[220] ATI Industrial Automation, 'F/T Sensor Gamma IP65'. https://www.ati-ia.com/products/ft/ft_models.aspx?id=Gamma+IP65 (accessed Jun. 14, 2022).

[221] Kuka, 'KRC4'. https://www.kuka.com/en-gb/products/robotics-systems/robot-controllers/kr-c4 (accessed Jun. 16, 2022).

[222] Kuka, 'System Software'. https://www.kuka.com/en-us/products/robotics-systems/software/system-software/kuka_systemsoftware (accessed Jun. 14, 2022).

[223] 'JKI State Machine'. JKISoftware, Apr. 22, 2022. Accessed: Jun. 15, 2022. [Online]. Available: https://github.com/JKISoftware/JKI-State-Machine

[224] A. N. AbdAlla, M. A. Faraj, F. Samsuri, D. Rifai, K. Ali, and Y. Al-Douri, 'Challenges in improving the performance of eddy current testing: Review', *Meas. Control*, vol. 52, no. 1–2, pp. 46–64, Jan. 2019, doi: 10.1177/0020294018801382.

[225] P. J. Shull, Ed., *Nondestructive evaluation: theory, techniques, and applications*. New York: M. Dekker, 2002.

[226] B. A. Auld and J. C. Moulder, 'Review of Advances in Quantitative Eddy Current Nondestructive Evaluation', p. 34.

[227] G. Mook, F. Michel, and J. Simonin, 'Electromagnetic Imaging Using Probe Arrays', *Stroj. Vestn. – J. Mech. Eng.*, vol. 2011, no. 03, pp. 227–236, Mar. 2011, doi: 10.5545/sv-jme.2010.173.

[228] L. A. N. M. Lopez, D. K. S. Ting, and B. R. Upadhyaya, 'Removing Eddy-Current probe wobble noise from steam generator tubes testing using Wavelet Transform', *Prog. Nucl. Energy*, vol. 50, no. 7, pp. 828–835, Sep. 2008, doi: 10.1016/j.pnucene.2007.07.008.

[229] J. C. Aldrin, H. A. Sabbagh, C. Annis, E. B. Shell, J. Knopp, and E. A. Lindgren, 'Assessing inversion performance and uncertainty in eddy current crack characterization applications', *AIP Conf. Proc.*, vol. 1650, no. 1, pp. 1873–1883, Mar. 2015, doi: 10.1063/1.4914813.

[230] J. C. Aldrin, H. A. Sabbagh, E. Sabbagh, R. K. Murphy, M. Keiser, D. S. Forsyth, and E. A. Lindgren, 'Model-based inverse methods for bolt-holt eddy current (BHEC) inspections', *AIP Conf. Proc.*, vol. 1581, no. 1, pp. 1433–1440, Feb. 2014, doi: 10.1063/1.4864990.

[231] E. B. Shell, J. C. Aldrin, H. A. Sabbagh, E. Sabbagh, R. K. Murphy, S. Mazdiyasni, and E. A. Lindgren, 'Demonstration of model-based inversion of electromagnetic signals for crack characterization', *AIP Conf. Proc.*, vol. 1650, no. 1, pp. 484–493, Mar. 2015, doi: 10.1063/1.4914645.

[232] Y. Liu, G. Tian, B. Gao, X. Lu, H. Li, X. Chen, Y. Zhang, and L. Xiong, 'Depth quantification of rolling contact fatigue crack using skewness of eddy current pulsed thermography in stationary and scanning modes', *NDT E Int.*, vol. 128, p. 102630, Jun. 2022, doi: 10.1016/j.ndteint.2022.102630.

[233] L. Wang, W. Cai, and Z. Chen, 'Quantitative evaluation of stress corrosion cracking based on crack conductivity model and intelligent algorithm from eddy current testing signals', *Nondestruct. Test. Eval.*, vol. 35, no. 4, pp. 378–394, Oct. 2020, doi: 10.1080/10589759.2019.1699085.

[234] N. Yusa, 'Development of computational inversion techniques to size cracks from eddy current signals', *Nondestruct. Test. Eval.*, vol. 24, no. 1–2, pp. 39–52, Mar. 2009, doi: 10.1080/10589750802195469.

[235] L. Yibo, S. Liying, S. Zhidong, and Z. Yuankai, 'Study on energy attenuation of ultrasonic guided waves going through girth welds', *Ultrasonics*, vol. 44, pp. e1111–e1116, Dec. 2006, doi: 10.1016/j.ultras.2006.05.108.

[236] P. Belanger and P. Cawley, 'Feasibility of low frequency straight-ray guided wave tomography', *NDT E Int.*, vol. 42, no. 2, pp. 113–119, Mar. 2009, doi: 10.1016/j.ndteint.2008.10.006.

[237] N. Brierley, R. A. Smith, N. Turner, R. Culver, T. Maw, A. Holloway, O. Jones, and P. D. Wilcox, 'Advances in the UK Toward NDE 4.0', *Res. Nondestruct. Eval.*, vol. 31, no. 5–6, pp. 306–324, Nov. 2020, doi: 10.1080/09349847.2020.1834657.

[238] J. Camacho, M. Parrilla, and C. Fritsch, 'Phase Coherence Imaging', *IEEE Trans. Ultrason. Ferroelectr. Freq. Control*, vol. 56, no. 5, pp. 958–974, May 2009, doi: 10.1109/TUFFC.2009.1128.

[239] A. J. Hunter, B. W. Drinkwater, and P. D. Wilcox, 'The wavenumber algorithm for full-matrix imaging using an ultrasonic array', *IEEE Trans. Ultrason. Ferroelectr. Freq. Control*, vol. 55, no. 11, pp. 2450–2462, Nov. 2008, doi: 10.1109/TUFFC.952.

[240] N. Portzgen, D. Gisolf, and G. Blacquiere, 'Inverse wave field extrapolation: a different NDI approach to imaging defects', *IEEE Trans. Ultrason. Ferroelectr. Freq. Control*, vol. 54, no. 1, pp. 118–127, Jan. 2007, doi: 10.1109/TUFFC.2007.217.

[241] T. Stratoudaki, M. Clark, and P. Wilcox, 'Adapting the full matrix capture and the Total Focusing Method to laser ultrasonics for remote non destructive testing: 2017 IEEE International Ultrasonics Symposium, IUS 2017', *2017 IEEE Int. Ultrason. Symp. IUS 2017*, Oct. 2017, doi: 10.1109/ULTSYM.2017.8092900.

[242] T. Stratoudaki, M. Clark, and P. D. Wilcox, 'Full matrix capture and the total focusing imaging algorithm using laser induced ultrasonic phased arrays', *AIP Conf. Proc.*, vol. 1806, no. 1, p. 020022, Feb. 2017, doi: 10.1063/1.4974563.

[243] T. Stratoudaki, M. Clark, and P. D. Wilcox, 'Laser induced ultrasonic phased array using full matrix capture data acquisition and total focusing method', *Opt. Express*, vol. 24, no. 19, pp. 21921–21938, Sep. 2016, doi: 10.1364/OE.24.021921.

[244] C. Mineo, D. Cerniglia, and E. Mohseni, 'Solving ultrasonic ray tracing in parts with multiple material layers through Root-Finding methods', *Ultrasonics*, vol. 124, p. 106747, Aug. 2022, doi: 10.1016/j.ultras.2022.106747.

[245] O. Nowers, D. J. Duxbury, and B. W. Drinkwater, 'Ultrasonic array imaging through an anisotropic austenitic steel weld using an efficient ray-tracing algorithm', *NDT E Int.*, vol. 79, pp. 98–108, Apr. 2016, doi: 10.1016/j.ndteint.2015.12.009.

[246] G. D. Connolly, M. J. S. Lowe, J. a. G. Temple, and S. I. Rokhlin, 'Correction of ultrasonic array images to improve reflector sizing and location in inhomogeneous materials using a ray-tracing model', *J. Acoust. Soc. Am.*, vol. 127, no. 5, pp. 2802–2812, May 2010, doi: 10.1121/1.3372724.

[247] O. Nowers, D. J. Duxbury, J. Zhang, and B. W. Drinkwater, 'Novel ray-tracing algorithms in NDE: Application of Dijkstra and A∗ algorithms to the inspection of an anisotropic weld', *NDT E Int.*, vol. 61, pp. 58–66, Jan. 2014, doi: 10.1016/j.ndteint.2013.08.002.

[248] K. M. M. Tant, E. Galetti, A. J. Mulholland, A. Curtis, and A. Gachagan, 'A transdimensional Bayesian approach to ultrasonic travel-time tomography for non-destructive testing', *Inverse Probl.*, vol. 34, no. 9, p. 095002, Jun. 2018, doi: 10.1088/1361-6420/aaca8f.

[249] K. M. M. Tant, E. Galetti, A. J. Mulholland, A. Curtis, and A. Gachagan, 'Effective grain orientation mapping of complex and locally anisotropic media for improved imaging in ultrasonic non-destructive testing', *Inverse Probl. Sci. Eng.*, vol. 28, no. 12, pp. 1694–1718, Dec. 2020, doi: 10.1080/17415977.2020.1762596.

[250] Y. Javadi, M. Vasilev, C. N. MacLeod, S. G. Pierce, R. Su, C. Mineo, J. Dziewierz, and A. Gachagan, 'Intentional weld defect process: From manufacturing by robotic welding machine to inspection using TFM phased array', *AIP Conf. Proc.*, vol. 2102, no. 1, p. 040011, May 2019, doi: 10.1063/1.5099761.

[251] R. Zimermann, E. Mohseni, D. Lines, R. K. W. Vithanage, C. N. MacLeod, S. G. Pierce, A. Gachagan, Y. Javadi, S. Williams, and J. Ding, 'Multi-layer ultrasonic

imaging of as-built Wire + Arc additive manufactured components', *Addit. Manuf.*, vol. 48, no. Part A, Dec. 2021, doi: 10.1016/j.addma.2021.102398.

[252]   R. K. W. Vithanage, E. Mohseni, D. Lines, C. Loukas, E. Foster, C. N. MacLeod, S. G. Pierce, A. Gachagan, J. Ding, and S. Williams, 'Development of a phased array ultrasound roller probe for inspection of wire + arc additive manufactured components', *J. Manuf. Process.*, vol. 80, pp. 765–774, Aug. 2022, doi: 10.1016/j.jmapro.2022.06.045.

[253]   R. Zimermann, E. Mohseni, M. Vasilev, C. Loukas, R. K. W. Vithanage, C. N. Macleod, D. Lines, Y. Javadi, M. P. Espirindio E Silva, S. Fitzpatrick, S. Halavage, S. Mckegney, S. G. Pierce, S. Williams, and J. Ding, 'Collaborative Robotic Wire + Arc Additive Manufacture and Sensor-Enabled In-Process Ultrasonic Non-Destructive Evaluation', *Sensors*, vol. 22, no. 11, Art. no. 11, Jan. 2022, doi: 10.3390/s22114203.

[254]   R. H. Möhring, H. Schilling, B. Schütz, D. Wagner, and T. Willhalm, 'Partitioning Graphs to Speed Up Dijkstra's Algorithm', in *Experimental and Efficient Algorithms*, Berlin, Heidelberg, 2005, pp. 189–202. doi: 10.1007/11427186_18.

[255]   A. Crauser, K. Mehlhorn, U. Meyer, and P. Sanders, 'A parallelization of Dijkstra's shortest path algorithm', in *Mathematical Foundations of Computer Science 1998*, Berlin, Heidelberg, 1998, pp. 722–731. doi: 10.1007/BFb0055823.

[256]   B. Huang, Q. Wu, and F. B. Zhan, 'A shortest path algorithm with novel heuristics for dynamic transportation networks', *Int. J. Geogr. Inf. Sci.*, vol. 21, no. 6, pp. 625–644, Jul. 2007, doi: 10.1080/13658810601079759.

[257]   'An inverse problem for Voronoi diagrams: A simplified model of non-destructive testing with ultrasonic arrays - Bourne - 2021 - Mathematical Methods in the Applied Sciences - Wiley Online Library'. https://onlinelibrary.wiley.com/doi/10.1002/mma.6977 (accessed Jul. 15, 2022).

[258]   J. Singh, K. Tant, A. Curtis, and A. Mulholland, 'Real-time super-resolution mapping of locally anisotropic grain orientations for ultrasonic non-destructive evaluation of crystalline material', *Neural Comput. Appl.*, vol. 34, no. 6, pp. 4993–5010, Mar. 2022, doi: 10.1007/s00521-021-06670-8.

[259] C. B. Scruby and B. C. Moss, 'Non-contact ultrasonic measurements on steel at elevated temperatures', *NDT E Int.*, vol. 26, no. 4, pp. 177–188, Aug. 1993, doi: 10.1016/0963-8695(93)90472-7.

[260] F. A. Silber and C. Ganglbauer, 'Ultrasonic testing of hot welds', *Non-Destr. Test.*, vol. 3, no. 6, pp. 429–432, Dec. 1970, doi: 10.1016/0029-1021(70)90156-8.

[261] Y. Javadi, E. Mohseni, C. N. MacLeod, D. Lines, M. Vasilev, C. Mineo, S. G. Pierce, and A. Gachagan, 'High-temperature in-process inspection followed by 96-h robotic inspection of intentionally manufactured hydrogen crack in multi-pass robotic welding', *Int. J. Press. Vessels Pip.*, vol. 189, no. 104288, Feb. 2021, doi: 10.1016/j.ijpvp.2020.104288.

[262] Z. Wang, 'An Imaging and Measurement System for Robust Reconstruction of Weld Pool During Arc Welding', *IEEE Trans. Ind. Electron.*, vol. 62, no. 8, pp. 5109–5118, Aug. 2015, doi: 10.1109/TIE.2015.2405494.

[263] X. Li, X. Li, S. S. Ge, M. O. Khyam, and C. Luo, 'Automatic Welding Seam Tracking and Identification', *IEEE Trans. Ind. Electron.*, vol. 64, no. 9, pp. 7261–7271, Sep. 2017, doi: 10.1109/TIE.2017.2694399.

[264] 'National Instrument-9214 16-Channel Temperature Module'. https://www.ni.com/en-gb/support/model.ni-9214.html (accessed Jul. 18, 2022).

[265] S. S. Lee, U.-S. Min, B. Ahn, and S. H. Yoo, 'Elastic constants determination of thin cold-rolled stainless steels by dynamic elastic modulus measurements', *J. Mater. Sci.*, vol. 33, no. 3, pp. 687–692, Feb. 1998, doi: 10.1023/A:1004385611382.

[266] M. S. Hassouna and A. A. Farag, 'Multi-stencils fast marching methods: a highly accurate solution to the eikonal equation on cartesian domains', *IEEE Trans. Pattern Anal. Mach. Intell.*, vol. 29, no. 9, pp. 1563–1574, Sep. 2007, doi: 10.1109/TPAMI.2007.1154.

[267] A. M. Popovici and J. A. Sethian, '3-D imaging using higher order fast marching traveltimes', *GEOPHYSICS*, vol. 67, no. 2, pp. 604–609, Mar. 2002, doi: 10.1190/1.1468621.

[268] N. Rawlinson and M. Sambridge, 'Wave front evolution in strongly heterogeneous layered media using the fast marching method', *Geophys. J. Int.*, vol. 156, no. 3, pp. 631–647, Mar. 2004, doi: 10.1111/j.1365-246X.2004.02153.x.

[269] J. A. Sethian, 'Fast Marching Methods', *SIAM Rev.*, vol. 41, no. 2, pp. 199–235, Jan. 1999, doi: 10.1137/S0036144598347059.

[270] Micro-Epsilon Messtechnik, 'Compact laser scanner', *Micro-Epsilon Messtechnik*. https://www.micro-epsilon.co.uk (accessed Jul. 19, 2022).

[271] Y. A. Çengel and A. J. Ghajar, *Heat and Mass Transfer: Fundamentals & Applications*. McGraw-Hill Education, 2019.

[272] K. M. M. Prabhu, *Window Functions and Their Applications in Signal Processing*. CRC Press, 2018.

[273] 'AMD Ryzen Threadripper 3960X Desktop Processor'. https://www.amd.com/en/products/cpu/amd-ryzen-threadripper-3960x (accessed Jul. 20, 2022).

[274] P. Laugier and G. Haïat, *Bone Quantitative Ultrasound*. Springer Netherlands, 2010.

[275] 'New Weld Series Probes'. https://www.olympus-ims.com/en/probes/pa/weld-series/ (accessed Aug. 12, 2022).

[276] 'Ultrasonic phased array wedge for inspecting high-temperature parts'. https://www.olympus-ims.com/en/applications/ultrasonic-phased-array-wedge-for-inspecting-high-temperature-parts-up-to-150c/ (accessed Aug. 12, 2022).

[277] 'Nvidia GeForce 3090 & 3090 Ti Graphics Cards'. https://www.nvidia.com/en-gb/geforce/graphics-cards/30-series/rtx-3090-3090ti/ (accessed Aug. 15, 2022).

[278] MATLAB, 'Parallel Computing Toolbox'. https://uk.mathworks.com/products/parallel-computing.html (accessed Aug. 17, 2022).

[279] 'Intel Xeon Gold 6248R Processor Product Specifications'. https://www.intel.com/content/www/us/en/products/sku/199351/intel-xeon-gold-6248r-processor-35-75m-cache-3-00-ghz.html (accessed Aug. 15, 2022).

[280] MATLAB, 'GPU Coder'. https://uk.mathworks.com/products/gpu-coder.html (accessed Aug. 17, 2022).

[281] D. Lines, E. Mohseni, R. Zimermann, C. Mineo, C. N. MacLeod, G. Pierce, and A. Gachagan, 'Modelling of echo amplitude fidelity for transducer bandwidth and TFM pixel resolution', presented at the 47th Annual Review of Progress in Quantitative Nondestructive Evaluation, Virtual event, Aug. 2020. Accessed: Nov. 17, 2022. [Online]. Available: https://strathprints.strath.ac.uk/73720/

[282] 'CREWES'. https://www.crewes.org/ (accessed Nov. 22, 2022).

[283] 'Angle Probe Calculation for UT – welding & NDT'. https://www.weldingandndt.com/angle-probe-calculation-for-ut/ (accessed Nov. 17, 2022).

[284] Kuka, 'KR 6 R900'. https://www.kuka.com/-/media/kuka-downloads/imported/6b77eecacfe542d3b736af377562ecaa/0000205456_en.pdf (accessed Aug. 17, 2022).

[285] Echo Ultrasonics, 'High Temperature Ultrasonic Couplant'. https://www.echoultrasonics.com/product-category/high-temperature-ultrasonic-couplant/ (accessed Aug. 17, 2022).

[286] Peak NDT, 'LT-PA'. https://www.peakndt.com/products/ltpa/ (accessed Aug. 15, 2022).

[287] C. Edwards, 'Improvements to dry coupled ultrasound for wall thickness and weld inspection', in *AIP Conference Proceedings*, Montreal (Canada), 2000, vol. 509, pp. 1779–1786. doi: 10.1063/1.1306247.

[288] A. M. Robinson, B. W. Drinkwater, and J. Allin, 'Dry-coupled low-frequency ultrasonic wheel probes: application to adhesive bond inspection', *NDT E Int.*, vol. 36, no. 1, pp. 27–36, Jan. 2003, doi: 10.1016/S0963-8695(02)00056-7.

[289] M. Hirao and H. Ogi, *Electromagnetic Acoustic Transducers: Noncontacting Ultrasonic Measurements using EMATs*. Tokyo: Springer Japan, 2017. doi: 10.1007/978-4-431-56036-4.

[290] X. Jian, S. Dixon, and R. S. Edwards, 'Modelling ultrasonic generation for Lorentz force EMATs', *Insight - Non-Destr. Test. Cond. Monit.*, vol. 46, no. 11, pp. 671–673, Nov. 2004, doi: 10.1784/insi.46.11.671.52289.

[291] J. Isla and F. Cegla, 'Optimization of the Bias Magnetic Field of Shear Wave EMATs', *IEEE Trans. Ultrason. Ferroelectr. Freq. Control*, vol. 63, no. 8, pp. 1148–1160, Aug. 2016, doi: 10.1109/TUFFC.2016.2558467.

[292] P. Khalili and P. Cawley, 'Relative Ability of Wedge-Coupled Piezoelectric and Meander Coil EMAT Probes to Generate Single-Mode Lamb Waves', *IEEE Trans. Ultrason. Ferroelectr. Freq. Control*, vol. 65, no. 4, pp. 648–656, Apr. 2018, doi: 10.1109/TUFFC.2018.2800296.

[293] K. Rieger, D. Erni, and D. Rueter, 'Unidirectional emission and detection of Lamb waves based on a powerful and compact coils-only EMAT', *NDT E Int.*, vol. 122, p. 102492, Sep. 2021, doi: 10.1016/j.ndteint.2021.102492.

[294] H. Cho, S. Choi, C. J. Lissenden, and M. S. Lindsey, 'Electromagnetic Acoustic Transducer (EMAT) Development for Nondestructive Inspection of Spent Nuclear Fuel Storage Canisters', presented at the ASME 2017 Pressure Vessels and Piping Conference, Oct. 2017. doi: 10.1115/PVP2017-65926.

[295] C. Pei, P. Xiao, S. Zhao, Z. Chen, and T. Takagi, 'A flexible film type EMAT for inspection of small diameter pipe', *J. Mech. Sci. Technol.*, vol. 31, no. 8, pp. 3641–3645, Aug. 2017, doi: 10.1007/s12206-017-0701-4.

[296] T. Liu, C. Pei, R. Cai, Y. Li, and Z. Chen, 'A flexible and noncontact guided-wave transducer based on coils-only EMAT for pipe inspection', *Sens. Actuators Phys.*, vol. 314, p. 112213, Oct. 2020, doi: 10.1016/j.sna.2020.112213.

[297] U.S. Department of Energy, 'An Overview of Basic Radiation Effects on Polymers And Glasses'. Office of Scientific and Technical Information. Accessed: Oct. 17, 2022. [Online]. Available: https://www.osti.gov/servlets/purl/1671997

[298] 'MIL-HDBK-814 IONIZING DOSE NEUTRON HARDNESS ASSURANCE'. http://everyspec.com/MIL-HDBK/MIL-HDBK-0800-0999/MIL_HDBK_814_2106/ (accessed Oct. 17, 2022).

[299] 'Standard Guide for Neutron Irradiation of Unbiased Electronic Components'. https://www.astm.org/f1190-11.html (accessed Oct. 17, 2022).

[300] 'Standard Guide for the Measurement of Single Event Phenomena (SEP) Induced by Heavy Ion Irradiation of Semiconductor Devices'. https://www.astm.org/f1192-11r18.html (accessed Oct. 17, 2022).

[301] 'Standard Guide for Ionizing Radiation (Total Dose) Effects Testing of Semiconductor Devices'. https://www.astm.org/f1892-12r18.html (accessed Oct. 17, 2022).

[302] L. Udpa and S. S. Udpa, 'Solution of inverse problems in eddy-current nondestructive evaluation (NDE)', *J. Nondestruct. Eval.*, vol. 7, no. 1, pp. 111–120, Jun. 1988, doi: 10.1007/BF00565781.

[303] G. P. Singh and S. Udpa, 'The role of digital signal processing in NDT', *NDT Int.*, vol. 19, no. 3, pp. 125–132, Jun. 1986, doi: 10.1016/0308-9126(86)90100-8.

[304] M. Gramz and T. Stepinski, 'Eddy current imaging, array sensors and flaw reconstruction', *Res. Nondestruct. Eval.*, vol. 5, no. 3, pp. 157–174, Sep. 1994, doi: 10.1007/BF01606406.

[305] W. Lord and S. R. Satish, 'Fourier Descriptor Classification of Differential Eddy Current Probe Impedance Plane Trajectories', in *Review of Progress in Quantitative Nondestructive Evaluation: Volume 3A*, D. O. Thompson and D. E. Chimenti, Eds. Boston, MA: Springer US, 1984, pp. 589–603. doi: 10.1007/978-1-4684-1194-2_56.

[306] S. S. Udpa and W. Lord, 'FOURIER DESCRIPTOR CLASSIFICATION SCHEME FOR DIFFERENTIAL PROBE SIGNALS.', *Mater. Eval.*, vol. 42, no. 9, pp. 1136–1141, 1984.

[307] L. UDPA and S. S. UDPA, 'Eddy current defect characterization using neural networks', *Eddy Curr. Defect Charact. Using Neural Netw.*, vol. 48, no. 3, p. p.353[7 p.], 1990.

[308] J. M. MANN, L. W. SCHMERR, and J. C. MOULDER, 'Neural network inversion of uniform-field eddy current data', *Neural Netw. Inversion Unif.-Field Eddy Curr. Data*, vol. 49, no. 1, pp. 34–39, 1991.

[309] C. E. CHAPMAN, A. FAHR, A. PELLETIER, and D. R. HAY, 'Artificial intelligence in the Eddy current inspection of aircraft engine components', *Artif. Intell. Eddy Curr. Insp. Aircr. Engine Compon.*, vol. 49, no. 9, pp. 1090–1094, 1991.

[310] D. Forsyth, A. Fahr, and C. Chapman, 'An evaluation of artificial neural networks for the classification of eddy current signals', *Rev. Prog. Quant. Nondestruct. Eval. 13 A*, pp. 879–886, 1993.

[311] A. N. Mucciardi, 'Elements of learning control systems with applications to industrial processes', in *Proceedings of the 1972 IEEE Conference on Decision and Control and 11th Symposium on Adaptive Processes*, Dec. 1972, pp. 320–325. doi: 10.1109/CDC.1972.269012.

[312] S. J. Song, H. J. Park, Y. K. Shin, and H. B. Lee, 'Flaw Characterization in Tubes by Inversion of Eddy Current Signals Using Neural Networks Trained by Finite Element Model-Based Synthetic Data', in *Review of Progress in Quantitative Nondestructive Evaluation: Volume 18A–18B*, D. O. Thompson and D. E. Chimenti, Eds. Boston, MA: Springer US, 1999, pp. 881–888. doi: 10.1007/978-1-4615-4791-4_113.

[313] 'Fuzzy Syntactic Pattern Recognition Approach for Extracting and Classifying Flaw Patterns from and Eddy-Current Signal Waveform -Journal of Electrical Engineering and information Science | Korea Science'. https://koreascience.kr/article/JAKO199711920330167.page (accessed Oct. 18, 2022).

[314] B. L. Baikie, A. R. Wagg, M. J. Whittle, and D. Yapp, 'Ultrasonic inspection of austenitic welds', International Atomic Energy Agency (IAEA), 1976.

[315] A. H. Harker, J. A. Ogilvy, and J. A. G. Temple, 'Modeling ultrasonic inspection of austenitic welds', *J. Nondestruct. Eval.*, vol. 9, no. 2, pp. 155–165, Sep. 1990, doi: 10.1007/BF00566391.

[316] J. R. Tomlinson, A. R. Wagg, and M. J. Whittle, 'Ultrasonic inspection of austenitic welds', International Atomic Energy Agency (IAEA), 1980.

[317]   A. Bulavinov, M. Kröning, J. Liu, K. Reddy, J. Ribeiro, and F. Walte, 'Ultrasonic Inspection of Austenitic and Dissimilar Welds', p. 13.

[318]   S. Cantero-Chinchilla, P. D. Wilcox, and A. J. Croxford, 'A deep learning based methodology for artefact identification and suppression with application to ultrasonic images', *NDT E Int.*, vol. 126, no. 102575, Mar. 2022, doi: 10.1016/j.ndteint.2021.102575.

[319]   W. Xu, X. Li, J. Zhang, Z. Xue, and J. Cao, 'Ultrasonic signal enhancement for coarse grain materials by machine learning analysis', *Ultrasonics*, vol. 117, p. 106550, Dec. 2021, doi: 10.1016/j.ultras.2021.106550.

[320]   J. Singh, K. Tant, A. Mulholland, and C. MacLeod, 'Deep Learning Based Inversion of Locally Anisotropic Weld Properties from Ultrasonic Array Data', *Appl. Sci.*, vol. 12, no. 2, Art. no. 2, Jan. 2022, doi: 10.3390/app12020532.